

**IDENTIFIED PARTICLE PRODUCTION,
FLUCTUATIONS AND CORRELATIONS STUDIES
IN HEAVY ION COLLISIONS AT RHIC ENERGIES**

A THESIS

submitted to the

FACULTY OF SCIENCE

PANJAB UNIVERSITY, CHANDIGARH

for the degree of

DOCTOR OF PHILOSOPHY

2009

LOKESH KUMAR

DEPARTMENT OF PHYSICS

CENTRE OF ADVANCED STUDY IN PHYSICS

PANJAB UNIVERSITY, CHANDIGARH, INDIA

Dedicated
to
The Almighty God
and
My Beloved Family

Acknowledgements

First and foremost I would like to thank God. You have given me the power to believe in my passion and pursue my dreams. I could never have completed this thesis without the faith I have in you, the Almighty. Thank you for the strength and courage you provided me.

My deepest gratitude to Prof. M. M. Aggarwal, my supervisor, for his encouragement, tremendous support, guidance and patience during my research work. I am very thankful to him as because of him I was able to work in such a wonderful experiment and could contribute to many exciting STAR physics topics. A special thanks goes to my co-supervisor, Prof. A. K. Bhati. He was always there to listen to any of my problem whenever I approached him and was always willing to help whether it was an academic or non-academic issue. I found myself very fortunate to have worked with such good supervisors. They provided me opportunities to travel and discuss physics topics at National as well as International level.

It is my pleasure to have been associated with Department of Physics, Panjab University, Chandigarh. I would like to thank Prof. M. M. Gupta, Chairperson, Department of Physics, Panjab University, Chandigarh, for providing me various opportunities during my research. I would also like to thank Prof. R. C. Sobti, Vice-Chancellor, Panjab University, Chandigarh, for providing support during my research work.

I would like to express my sincere and heartfelt thanks to Dr. Bedangadas Mohanty, the STAR Physics Analysis Coordinator, Variable Energy Cyclotron Center, Kolkata. His help, support, guidance, and motivation were always there for me during my research career. I have greatly benefited from his deep knowledge and practical experiences of heavy-ion physics. During discussions with him, I learnt a lot about C++, ROOT, the STAR software, and the data analysis. He provided me support to work on the 9.2 GeV test run data, the lowest energy collisions at RHIC so far. The results (accepted for publication) from this data set will form the basis of RHIC Beam Energy Scan Program to search for the QCD critical point. We also worked together on the Photon Multiplicity Measurements leading to its successful publication. I am very fortunate to have worked

with such a wonderful physicist and a very nice person.

I would like to express my humble thanks to Dr. Y. P. Viyogi, Head, Experimental High Energy Physics and Applications Group (EHEPA), Variable Energy Cyclotron Center, Kolkata, as because of him and his team (the whole PMD group) efforts we could see an Indian detector (PMD) installed at the STAR experiment in USA. Dr. Viyogi has provided me many research opportunities during my Ph. D. career. I would like to sincerely thank Dr. S. Chattopadhyay, the STAR India group leader, for his unconditional support during my work in the STAR experiment. It was a nice experience working and interacting with Dr. T. K. Nayak, the ALICE India group leader. I cherish the discussions I had with him starting from the days when I was working for the hardware and software development in the ALICE experiment. It was equally interesting to work with and learn from so many experts in various areas working for PMD while at VECC. These include Dr. Z. Ahammed, Dr. A. Dubey, Dr. P. Ghosh, Mr. G. S. N. Murthy, Mr. M. R. Dutta Majumdar, Mr. S. Pal, Mr. R. N. Singaraju, Mr. V. Singhal, Mr. J. Saini and Mr. P. Bhaskar. They were always helpful specially for a new-comer in the group. I would like to express my humble thanks to Prof. B. Sinha, the ex-Director of VECC, for his unconditional support to the research and scholars coming to work in VECC.

I would like to take this opportunity to express my sincere thanks to the Brookhaven National Laboratory (BNL) colleagues. Dr. T. Hallman, the ex-BNL group leader and ex-STAR Spokesperson, has been very supportive for my work and visits to BNL. I would like to thank Dr. J. Laurete, Dr. G. V. Buren, and Dr. (Ms.) L. Didenko for the STAR software support. Special thanks goes to Dr. Didenko for generating simulation sample to obtain weak-decay pion contributions in Au+Au collisions at $\sqrt{s_{NN}} = 9.2$ GeV, which formed a part of my analysis. I would like to thank Dr. Z. Xu and Dr. (Ms.) L. Ruan, for some really nice physics discussions and help during my first stay at BNL. Dr. J. Dunlop, the STAR deputy spokesperson and BNL group leader, has always been approachable for any discussions and help. I would also like to thank Dr. W. Christie, Dr. R. Brown, Dr. B. Stringfellow, Dr. A. Lebedev and Dr. T. Ljubicic for their support during the STAR data taking period. I am thankful to Ms. C. Feliciano and Ms. L. Mogavero for their valuable help during my stay at BNL. It was a nice experience to discuss and interact

with several research scholars at BNL. These include Dr. J. Chen, Dr. Z. Tang, Mr. S. Shusu, Mr. Y. Pandit, Ms. J. Chen, Ms. N. Li, and Ms. Y. Xu.

It gives me immense pleasure to thank our STAR colleagues from the Lawrence Berkeley National Laboratory (LBNL) group. My special thanks goes to Dr. N. Xu, the STAR spokesperson, for his support, help and guidance during my research period. I would like to thank him and Dr. H. G. Ritter, the heavy-ion group leader at LBNL, for inviting me to the LBNL to work on the 9.2 GeV data analysis and embedding. A sincere thanks to Dr. N. Xu for inviting me to present a talk in Heavy Ion Tea Seminar at LBNL. I would also like to express my sincere thanks to Dr. A. Rose, the STAR embedding deputy, for generating the 9.2 GeV embedding data in a short time scale. Due to his efforts I was able to present first results from 9.2 GeV data at the Strange Quark Matter-2008 conference in Beijing, China. During my stay at LBNL, I was equally benefited from discussions with Dr. A. Poskanzer, Dr. E. Sichtermann, Dr. X. Dong, Dr. H. Masui, and Dr. (Ms.) G. Odyniec. Dr. Odyniec has been very instrumental in timely getting out the embedding data for 9.2 GeV and in various embedding discussions. It was a nice experience to interact with the several graduate students at LBNL. These include Mr. C. Jena, Mr. D. Kikola, and Mr. C. Powell. I would like to thank Ms. L. Bonifacio for helping me during my stay at LBNL. She was very helpful when I had to apply for Chinese visa during my stay at LBNL. I would like to mention here the Punjabi restaurant named Indian Palace, and Biryani house at Berkeley, where we would eat during the days of our stay at Berkeley. They reminded us of our Indian culture during our stay there. Still remember the Hindi song *...teri ore...oye rabba....* which we used to listen in the Biryani house during our dinner time.

I would like to thank the STAR physics working groups (PWG), their members, and the conveners for providing healthy physics discussions. These were very useful in understanding of the various physics issues, pursuing the analyses, and taking them up to publishable stage. It was a pleasure to have worked with Dr. (Ms.) L. Ruan and Dr. J. Takahashi, the LF spectra conveners; Dr. E. Finch, Prof. S. Raniwala, and Dr. P. Sorensen, the bulkcorr conveners; and Dr. D. Cebra, Dr. (Ms.) G. Odyniec, and Prof. D. Keane, the BES focus group conveners.

I would like to take this opportunity to thank the God Parent Committee (GPC) members and chairs of my papers. It is my pleasure to thank Dr. J. Hoffman (chair PMD paper) and Prof. D. Keane (chair 9.2 GeV paper) for their efforts to bring the papers to the publishable stage.

My sincere thanks are due to Collider-Accelerator Department at BNL. They were very accurate in providing us the 9.2 GeV collisions for the test run of Beam Energy Scan program. The 9.2 GeV is the lowest beam energy injected at RHIC so far and is lowest than the RHIC injection energy. This itself is a very difficult task which these people have accomplished with their hard work and efforts. Hats-off to them.

I would like to express my sincere thanks to Dr. S. Gupta, Department of Theoretical Physics, Tata Institute of Fundamental Research (TIFR), Mumbai, India, for inviting me to present our results on 9.2 GeV in the Free Meson Seminar at TIFR. This provided me an opportunity to interact with the theory group at TIFR and increase my theoretical knowledge.

It was a very nice experience to work in a team effort in the PMD group. I would like to thank our PMD collaborators with whom I was involved in many projects and discussions. These include Prof. S. Raniwala and his group at University of Rajasthan, Jaipur; Prof. (Ms.) A. Bhasin and her group at University of Jammu, Jammu; Prof. D. P. Mahapatra and his group at Institute of Physics, Bhubaneswar, Orissa; Prof. R. Varma and his group at Indian Institute of Technology Bombay, Mumbai.

I would like to acknowledge the support and encouragement of PMD research scholars during my research work. These include Mr. S. K. Prasad, Mr. M. M. Mondal, Mr. A. K. Dash, Mr. P. Pujahari, Ms. N. Shah, Ms. H. Bhatt, Dr. S. M. Dogra, Mr. S. Sharma, Dr. N. Gupta, and Dr. R. Datta. In addition I have always got help and guidance from the senior PMD research scholars Dr. P. K. Netrakanti, Dr. D. Das, Dr. (Ms.) M. Sharma, and Dr. (Ms.) S. Das. I cherish the moments spent with these guys.

I am very thankful to the research scholars within the Chandigarh group, Ms. Natasha Sharma and Mr. Navneet Pruthi, for their cordial and co-operative attitude throughout my stay at Chandigarh. I would like to specially thank Ms. Natasha Sharma for helping me during my synopsis and thesis submission. She was always willing to help

whenever I approached her.

My research work would not have been possible without the technical support provided by Mr. Ajit Singh, Mr. Dinesh Kumar Gupta, Mr. Satish Sharma, and all the members of purchase section in the Department of Physics, Panjab University, Chandigarh. I am very thankful to them for their help.

I would like to express my heartiest thanks to my friends Mr. Nitesh Sharma, Mr. Sushil Sharma, Mr. Lakhwinder Singh, Mr. Ashutosh Bilves, Mr. Rajesh Kumar, Mr. Ramji Gupta, Mr. Surinder Ranga, and Mr. Deepak Rawat. They were always there whenever I needed them. They always encouraged me, and believed in me and my capabilities. I will always remember the days I spent with these guys no matter wherever I go.

I would like to take this opportunity to express my humble thanks to all those who have contributed in some way or the other in my thesis completion. Here I could list only few names but of-course there are many more who have contributed and helped me till now and will continue to do so. I would like to thank all those my well wishers here.

I would like to gratefully acknowledge the financial support from the Department of Science & Technology and Department of Atomic Energy, Govt. of India, for my research career.

Last but not least, I would like to express my humble regards to my parents and sisters, for their continuous support, encouragement, love, patience, and blessings.

Date:

(Lokesh Kumar)

Abstract

The theory of strong interactions, Quantum Chromodynamics (QCD), predicts the formation of Quark-Gluon Plasma at sufficiently high density and/or temperature. The prime goal of the heavy-ion program at the Relativistic Heavy Ion Collider (RHIC) at Brookhaven National Laboratory is to search for the possible formation of Quark-Gluon Plasma. In heavy-ion collision experiments, we correlate information obtained from various observables (e.g. photon multiplicity, charged particles etc.) to understand the dynamics of particle production and evolution of the system.

In this thesis, we study and characterize the properties of photons and hadrons produced in heavy-ion collisions. Photons and hadrons are measured respectively by the Photon Multiplicity Detector (PMD) and the Time Projection Chamber (TPC) in the STAR experiment. The details of STAR detector and its subsystems are presented in this thesis.

We present the multiplicity and pseudorapidity distributions of photons produced in Au+Au and Cu+Cu collisions at $\sqrt{s_{NN}} = 62.4$ and 200 GeV. The photons are measured in the region $-3.7 < \eta < -2.3$ using the Photon Multiplicity Detector in the STAR experiment at RHIC. The photons are produced at all stages of the system created in heavy-ion collisions. They have large mean free paths and therefore, are good carriers of information about the history of collisions. The number of photons produced per average number of participating nucleon pairs increases with the beam energy and is independent of the collision centrality. For collisions with similar average numbers of participating nucleons the photon multiplicities are observed to be similar for Au+Au and Cu+Cu collisions at a given beam energy. The ratios of the number of charged particles to photons in the measured pseudorapidity range are found to be 1.4 ± 0.1 and 1.2 ± 0.1 for $\sqrt{s_{NN}} = 62.4$ GeV and 200 GeV, respectively. The energy dependence of this ratio could reflect varying contributions from baryons to charged particles, while mesons are the dominant contributors to photon production in the given kinematic region. The photon pseudorapidity distributions normalized by average number of participating nucleon pairs, when plotted as a function of $\eta - y_{beam}$, are found to follow a longitudinal

scaling independent of centrality and colliding ion species at both beam energies.

We also present the first measurements of identified hadron production from Au+Au collisions below the nominal injection energy at the Relativistic Heavy-Ion Collider (RHIC) facility. The data were collected using the large acceptance STAR detector at $\sqrt{s_{NN}} = 9.2$ GeV from a test run of the collider in the year 2008. Midrapidity results on multiplicity density (dN/dy) in rapidity (y), average transverse momentum ($\langle p_T \rangle$), average transverse mass ($\langle m_T \rangle$), and particle ratios are consistent with the corresponding results at similar $\sqrt{s_{NN}}$ from fixed target experiments. Furthermore, the collision centrality dependence of identified particle dN/dy , $\langle p_T \rangle$, and particle ratios are discussed. The chemical and kinetic freeze-out parameters are extracted for 9.2 GeV collisions and are presented in this thesis. These parameters are consistent with the observed energy dependence trend of freeze-out parameters. These results from $\sqrt{s_{NN}} = 9.2$ GeV collisions, also demonstrate the readiness of the STAR detector to undertake the proposed QCD critical point search and the exploration of the QCD phase diagram at RHIC.

We also present in this thesis, the results on measurement of event-by-event transverse momentum (p_T) fluctuations and two particle p_T correlations for Cu+Cu collisions at $\sqrt{s_{NN}} = 62.4$ and 200 GeV from STAR experiment at RHIC. These results are compared with those previously reported from Au+Au collisions at similar energies to study the system size dependence. We compare the $\langle p_T \rangle$ distributions of data and mixed events, and are compared with the corresponding Gamma distributions. We observe finite dynamical fluctuations in the data. These fluctuations are found to decrease with increasing collision centrality. The p_T correlations scaled by number of participating nucleon pair increases with collision centrality and then saturate in central Au+Au collision. It is also observed that square root of p_T correlations scaled by mean p_T is independent of beam energy as well as colliding ion size, but decrease with increase in collision centrality. We have investigated the dependence of p_T correlations on the azimuthal angle and pseudorapidity acceptance. The results on p_T correlation for forward and backward η regions and its dependence on the collision vertex are discussed. The dependence of p_T correlation on different p_T acceptances is also investigated.

List of Publications

- *1. **First results from Au+Au collisions at $\sqrt{s_{NN}} = 9.2$ GeV in STAR,**
Lokesh Kumar (for the STAR collaboration),
J. Phys. G: Nucl. Part. Phys. **36**, 064066 (2009).

- *2. **Center of mass energy and system-size dependence of photon production at forward rapidity at RHIC,**
B. I. Abelev *et al.* (STAR Collaboration),
Accepted in Nucl. Phys. A, arXiv:0906.2260v1 [nucl-ex].

- *3. **Identified particle production, azimuthal anisotropy, and interferometry measurements in Au+Au collisions at $\sqrt{s_{NN}} = 9.2$ GeV,**
B. I. Abelev *et al.* (STAR Collaboration),
Accepted in Phys. Rev. C, arXiv:0909.4131v1 [nucl-ex].

- 4. **First proton-proton collisions at LHC as observed with the ALICE detector: measurement of the pseudorapidity density at $\sqrt{s_{NN}} = 900$ GeV,**
K. Aamodt *et al.* (ALICE Collaboration),
Submitted to Eur. Phys. J. C, arXiv:0911.5430v2 [hep-ex].

- *5. **Bulk properties in Au+Au collisions at $\sqrt{s_{NN}} = 9.2$ GeV in STAR experiment at RHIC,**
Lokesh Kumar (for the STAR collaboration),
Nucl. Phys. A **830**, 275c (2009).

- 6. **Observation of an antimatter hypernucleus,**
B. I. Abelev *et al.* (STAR Collaboration),
Submitted to Science.

- *7. **Experimental study of the QCD phase diagram & search for the critical point: selected arguments for the Run-10 Beam Energy Scan,**
B. I. Abelev *et al.* (STAR Collaboration), STAR Internal Note - SN0493, 2009.

8. **Observation of charge-dependent azimuthal correlations and possible local strong parity violation in heavy ion collisions**
B. I. Abelev *et al.* (STAR Collaboration),
arXiv:0909.1717v1 [nucl-ex].

9. **Azimuthal charged-particle correlations and possible local strong parity violation,**
B. I. Abelev *et al.* (STAR Collaboration),
Accepted in Phys. Rev. Lett., arXiv:0909.1739v2 [nucl-ex].

10. **Long range rapidity correlations and jet production in high energy nuclear collisions,**
B. I. Abelev *et al.* (STAR Collaboration),
Submitted to Phys. Rev. C, arXiv:0909.0191 [nucl-ex].

11. **Neutral pion production in Au+Au collisions at $\sqrt{s_{NN}} = 200$ GeV,**
B. I. Abelev *et al.* (STAR Collaboration),
Phys. Rev. C **80**, 024905 (2009).

12. **Growth of long range forward-backward multiplicity correlations with centrality in Au+Au collisions at $\sqrt{s_{NN}} = 200$ GeV,**
B. I. Abelev *et al.* (STAR Collaboration),
Phys. Rev. Lett. **103**, 172302 (2009).

13. **System size dependence of associated yields in hadron-triggered jets,**
B. I. Abelev *et al.* (STAR Collaboration),
Submitted in Phys. Lett. B, arXiv:0904.1722v1 [nucl-ex].

- *14. **STAR measurement of system size and incident energy dependence of p_T correlations at RHIC,**
Lokesh Kumar (For the STAR collaboration),
Submitted to Indian J. Phys., arXiv:0806.3511 [nucl-ex].

15. **J/Ψ production at high transverse momentum in $p + p$ and Cu+Cu collisions at $\sqrt{s_{NN}} = 200\text{GeV}$,**
B. I. Abelev *et al.* (STAR Collaboration),
Phys. Rev. C **80**, 41903 (2009).

16. **Pion interferometry in Au+Au and Cu+Cu collisions at RHIC,**
B. I. Abelev *et al.* (STAR Collaboration),
Phys. Rev. C **80**, 024905 (2009).

17. **K/π fluctuations at relativistic energies,**
B. I. Abelev *et al.* (STAR Collaboration),
Phys. Rev. Lett. **103**, 092301 (2009).

18. **Measurement of D^* mesons in jets from $p + p$ collisions at $\sqrt{s_{NN}} = 200\text{GeV}$,**
B. I. Abelev *et al.* (STAR Collaboration),
Phys. Rev. D **79**, 112006 (2009).

19. **Observation of two-source interference in the photoproduction reaction $\text{Au}+\text{Au} \rightarrow \text{Au}+\text{Au}+\rho^0$,**
B. I. Abelev *et al.* (STAR Collaboration),
Phys. Rev. Lett. **102**, 112301 (2009).

20. **Energy and system size dependence of ϕ -meson production in Cu+Cu and Au+Au collisions,**
B. I. Abelev *et al.* (STAR Collaboration),
Phys. Lett. B **673**, 183 (2009).

21. **Measurements of ϕ -meson production in relativistic heavy-ion collisions at RHIC,**
B. I. Abelev *et al.* (STAR Collaboration),
Phys. Rev. C **79**, 034909 (2009).

22. **Systematic measurements of identified particle spectra in $p + p$, $d + \text{Au}$ and $\text{Au} + \text{Au}$ collisions from STAR,**
B. I. Abelev *et al.* (STAR Collaboration),
Phys. Rev. C **79**, 034906 (2009).

23. **Beam-energy and system-size dependence of dynamical net charge fluctuations,**
B. I. Abelev *et al.* (STAR Collaboration),
Phys. Rev. C **79**, 024906 (2009).

24. **System-size independence of directed flow at the Relativistic Heavy-Ion Collider,**
B. I. Abelev *et al.* (STAR Collaboration),
Phys. Rev. Lett. **101**, 0252301 (2008).

25. **Indications of conical emission of charged hadrons at RHIC,**
B. I. Abelev *et al.* (STAR Collaboration),
Phys. Rev. Lett. **102**, 052302 (2009).

26. **Centrality dependence of charged hadron and strange hadron elliptic flow from $\sqrt{s_{NN}} = 200\text{-GeV}$ $\text{Au} + \text{Au}$ collisions,**
B. I. Abelev *et al.* (STAR Collaboration),
Phys. Rev. C **77**, 054901 (2008).

27. **Forward neutral pion transverse single spin asymmetries in $p + p$ collisions at $\sqrt{s} = 200\text{ GeV}$,**
B. I. Abelev *et al.* (STAR Collaboration),
Phys. Rev. Lett. **101**, 222001 (2008).

28. **Spin alignment measurements of the $K^*(892)$ and $\phi(1020)$ vector mesons in heavy ion collisions at $\sqrt{s_{NN}} = 200\text{-GeV}$ $\text{Au} + \text{Au}$ collisions,**
B. I. Abelev *et al.* (STAR Collaboration),
Phys. Rev. C **77**, 061902 (2008).

29. **Hadronic resonance production in d +Au collisions at 200 GeV at RHIC,**
B. I. Abelev *et al.* (STAR Collaboration),
Phys. Rev. C **78**, 044906 (2008).

30. **Enhanced strange baryon production in Au+Au collisions compared to $p + p$ at $\sqrt{s_{NN}} = 200$ -GeV,**
B. I. Abelev *et al.* (STAR Collaboration),
Phys. Rev. C **77**, 044908 (2008).

31. **The ALICE experiment at the CERN LHC,**
K. Aamodt *et al.* (ALICE Collaboration),
JINST **0803**, S08002 (2008).

- *32. **Photon multiplicity measurements in Au+Au and Cu+Cu collisions at $\sqrt{s_{NN}} = 200$ and 62.4 GeV at RHIC,**
Lokesh Kumar (For the STAR Collaboration),
Proceedings of DAE Symposium **53**, 619 (2008).

- *33. **System size and incident energy dependence of p_T correlations at RHIC energies,**
Lokesh Kumar (For the STAR Collaboration),
Proceedings of DAE Symposium **52**, 551 (2007).

**Results from these publications are included in this thesis.*

Contents

1	INTRODUCTION	1
1.1	Quarks and Quark-Gluon Plasma (QGP)	1
1.2	Lattice QCD and Phase Transition	3
1.2.1	Phase Diagram	4
1.2.2	Equation of State	5
1.3	Nucleus-Nucleus Collisions	7
1.4	Probes of Quark-Gluon Plasma Formation	9
1.4.1	Strangeness Enhancement	9
1.4.2	J/Ψ Suppression	10
1.4.3	Direct Photons	13
1.4.4	Azimuthal Anisotropy or Flow	15
1.4.5	High p_T probes	19
1.4.6	Hanbury Brown-Twiss (HBT) Effect	22
1.4.7	Event-by-Event Fluctuations and Correlations	24
1.5	Photon Multiplicity Measurements	27
1.5.1	Photon Pseudorapidity Distribution	28
1.5.2	Scaling with Number of Participants	28
1.5.3	Longitudinal Scaling	29
1.6	Transverse Momentum Spectra	31
1.6.1	Yield and Ratios	32
1.6.2	Average Transverse Momentum and Mass	33
1.6.3	Freeze-Out Properties	35
1.7	Terminology and Kinematic Variables	37

1.8	Organization of Thesis	40
2	THE STAR EXPERIMENT	50
2.1	Relativistic Heavy Ion Collider (RHIC)	50
2.2	The STAR Detector	53
2.3	Trigger Detectors	56
2.3.1	Central Trigger Barrel	57
2.3.2	Zero Degree Calorimeter	58
2.3.3	Beam-Beam Counter	59
2.3.4	Electromagnetic Calorimeters	60
2.4	Trigger Levels and Data Acquisition	62
2.5	STAR Magnet	63
2.6	Time Of Flight Detector	64
2.7	Time Projection Chamber	65
2.7.1	Technical Design	66
2.7.2	Event Reconstruction in the TPC	70
2.7.3	Tracking Efficiency	72
2.7.4	Particle Identification	74
2.8	Forward Time Projection Chamber	76
2.9	Photon Multiplicity Detector	78
2.9.1	Front-End Electronics and Readout	84
2.9.2	PMD Trigger and Data Acquisition	88
3	PHOTON MULTIPLICITY MEASUREMENTS	94
3.1	Data Selection	95
3.2	Data Clean-up	100
3.3	Cell-to-Cell Gain Calibration	105
3.4	Occupancy	109
3.5	Clustering Algorithm	110
3.5.1	Physics Performance Criteria for PMD	113
3.5.2	Photon Conversion Efficiency	114

3.5.3	Clustering Efficiency	116
3.5.4	Cluster Properties and Optimization of Clustering Algorithm . . .	117
3.6	Efficiency and Purity	124
3.7	Photon Production	127
3.7.1	Systematic Errors	128
3.7.2	Multiplicity Distributions	128
3.7.3	Scaling of Photon Production	131
4	PARTICLE PRODUCTION AT $\sqrt{s_{NN}} = 9.2$ GeV	139
4.1	Introduction	139
4.2	STAR Detector for 9.2 GeV Run	140
4.3	Data Set Selection	141
4.3.1	Event Selection	142
4.3.2	Centrality Selection	143
4.3.3	Track Selection and Particle Identification	146
4.4	Correction Factors	147
4.5	Systematic Errors	153
4.6	Transverse Momentum Spectra	154
4.7	Centrality Dependence of Particle Production	155
4.8	Energy Dependence of Particle Production	159
4.9	Freeze-out Parameters and Phase Diagram	164
5	FLUCTUATIONS AND CORRELATIONS	173
5.1	Introduction	173
5.2	Data Selection	175
5.3	Transverse Momentum Fluctuations	181
5.4	Transverse Momentum Correlations	188
5.4.1	Scaling of p_T Correlations	192
5.5	Systematic Errors	194
5.6	η and ϕ -Dependence	198
5.7	Correlations in Forward and Backward η Regions	198

5.8	Correlations for Different p_T Bins	201
5.8.1	p_T Bin Effect Study	204
5.8.2	p_T Bin Effect Study using p_T Spectra	206
6	CONCLUSIONS	217

List of Figures

1.1	Schematic picture of the QCD phase diagram shown in $T - \mu_B$ space [9].	4
1.2	Energy density as a function of temperature as per the lattice QCD calculations [16].	6
1.3	Collision of two nuclei A and B, with a non-zero impact parameter. Number of participants and the spectators are also shown.	8
1.4	Space-time diagram and different evolution stages of a relativistic heavy-ion collision.	9
1.5	Upper panel: The ratio of the yields of K , ϕ , $\bar{\Lambda}$ and $\Xi + \bar{\Xi}$ normalized to $\langle N_{\text{part}} \rangle$ in Au+Au and Cu+Cu collisions to corresponding yields in inelastic $p + p$ collisions at 200 GeV. Lower panel: Same as above for only ϕ mesons at 200 and 62.4 GeV. The error bars shown represent the statistical and systematic errors added in quadrature.	11
1.6	The $(J/\Psi)/\text{Drell-Yan}$ cross-sections ratio as a function of N_{part} for three analyses of the Pb+Pb collisions at $\sqrt{s_{NN}} = 17.3$ GeV, divided by the normal nuclear absorption values. The data are from NA50 experiment at SPS.	12
1.7	Direct photon spectra at RHIC energies measured by PHENIX.	14
1.8	The invariant direct photon multiplicity for central Pb+Pb collisions at $\sqrt{s_{NN}} = 17.3$ GeV [30]. The model calculations [31] are shown in the form of lines.	15
1.9	Schematic diagram showing the initial spatial anisotropy created after the non-central heavy-ion collision, converted into the anisotropy in momentum space.	16

1.10	Top panel: Directed flow of charged particles as a function of pseudorapidity measured in STAR experiment [43]. Lower panel: mid-pseudorapidity region shown in more detail.	17
1.11	v_2 scaled by number of quarks (n_q) as a function of p_T scaled by n_q for various particles measured in the STAR experiment [50].	19
1.12	$R_{AA}(p_T)$ for charged hadrons for different centralities as measured in STAR experiment [58].	20
1.13	Schematic diagram showing jets produced from hard scattering.	21
1.14	Jet azimuthal correlations for Au+Au, d+Au and $p+p$ collisions at $\sqrt{s_{NN}} = 200$ GeV measured in STAR experiment [60].	21
1.15	Ratio R_O/R_S as function of lab frame energy (E_{lab}) for negatively charged pions as source [68].	24
1.16	Event-wise mean p_T distribution for top central Au+Au collisions at $\sqrt{s_{NN}} = 200$ GeV measured in STAR experiment [76].	26
1.17	Left panel: (a) Total number of charged particles detected within the range $ \eta < 5.4$, and (b)-(f) Centrality dependence of $dN_{ch}/d\eta$ for different ranges of $ \eta $, for Au+Au collisions at $\sqrt{s_{NN}} = 200$ GeV [87]. Right panel: Number of produced pions scaled by $\langle N_{part}/2 \rangle$ as a function of $\langle N_{part} \rangle$ for Au+Au and Cu+Cu collisions at $\sqrt{s_{NN}} = 62.4$ and 200 GeV at midrapidity measured at RHIC.	29
1.18	Charged particle multiplicities normalized to the number of participant nucleon pairs as a function of $\eta - y_{beam}$ for different collision centralities and different center of mass energies [94].	30
1.19	(a) Photon pseudorapidity density normalized to the number of participant nucleon pairs as a function of $\eta - y_{beam}$, for different collision energies and centralities [89]. Also shown $dN_\gamma/d\eta$ for $p + \bar{p}$ collisions. (b) Same as (a) but for charged particles.	31
1.20	Beam energy dependence of K/π ratio at midrapidity in heavy-ion collisions. The AGS, SPS, and RHIC data points are from the Refs. [95], [96], and [97], respectively.	32

1.21	Top panel: Mean p_T as a function of dN_{ch}/dy for Au+Au collisions at $\sqrt{s_{NN}} = 62.4, 130$ and 200 GeV [97]. Results from minimum bias $p+p$ and $d+\text{Au}$ collisions are also shown. Bottom panel: $\langle m_T \rangle - m$ as a function of center of mass energy for charged kaons [95–97].	34
1.22	Top panel: Baryon chemical potential extracted for central heavy-ion collisions as a function of the collision energy. Bottom panel: The extracted chemical (red points) and kinetic (black points) freeze-out temperatures for central heavy-ion collisions as a function of the collision energy. The figure is taken from the Ref. [97].	36
1.23	Coordinate system describing the heavy-ion collision system.	39
2.1	Layout picture of the RHIC collider shown along with four main experiments positions.	51
2.2	Diagram shows the RHIC complex. The various stages of acceleration of ions and the locations of four experiments at RHIC are also shown.	52
2.3	Perspective view of the STAR detector, with a cutaway for viewing inner detector systems [2].	54
2.4	Cross-sectional side view of the STAR detector [2].	55
2.5	CTB cylinder and detail of tray and slat.	57
2.6	Correlation of ZDC and CTB signals.	58
2.7	Schematic view of BBC, shown along with small (blue) and large (red) tiles. The beam pipe crosses BBC from the location designated by “B” at the center.	60
2.8	Schematic end view and side view of the STAR EMC showing the EMC Barrel and EMC Endcap [13].	61
2.9	Data flow through the trigger. See text for definition of acronyms.	63
2.10	Two side views of MRPC [22]. The upper (lower) is for long (short) side view. The two plots are not at the same scale.	65

2.11	The STAR TPC surrounds a beam-beam interaction region at RHIC. The collisions take place near the center of the TPC. Figure is taken from the Ref. [8].	66
2.12	A cut-away view of an outer subsector pad plane. The cut is taken along a radial line from the center of the TPC to the outer field cage so the center of the detector is to the right. The figure shows the spacing of the anode wires relative to the pad plane, the ground shield grid, and the gated grid. The bubble diagram shows additional detail about the wire spacing. . . .	67
2.13	The anode pad plane with one full sector shown [8]. The inner subsector is on the right and it has small pads arranged in widely spaced rows. The outer subsector is on the left and it is densely packed with larger pads. . .	69
2.14	Beam's eye (left) and side (right) views of a central event in Au+Au collisions at $\sqrt{s_{NN}} = 9.2$ GeV [30].	71
2.15	The pion tracking efficiency in STAR for central Au+Au events at RHIC [8]. The most central collisions are the highest multiplicity data, they are shown as black dots. The lowest multiplicity data are shown as open triangles. . .	74
2.16	The energy loss distribution for primary and secondary particles in the STAR TPC as a function of the p_T of the primary particle.	76
2.17	Schematic diagram of an FTPC for the STAR experiment.	77
2.18	Picture of the PMD after complete installation of electronics at the STAR experiment.	78
2.19	Cross-sectional schematic of the PMD [37] showing the veto plane, lead converter and preshower plane. SS is the support plane on which the lead plates and gas chambers are mounted.	79
2.20	Principle of Photon Multiplicity Detector. Single cell hit is due to hadron while the signal deposited in contiguous cells is due to photon.	80

2.21	(a) Unit cell schematic with cross-section showing the dimensions and the cathode extension, (b) Layout of the STAR PMD. Thick lines indicate supermodule boundaries. There are 12 supermodules each in the preshower plane and the veto plane. Divisions within a supermodule denote unit modules.	81
2.22	PMD support mechanism. The inner hexagonal part shows the two halves joined during data taking operation. The two halves, when separated for servicing, look as shown on the right and left.	83
2.23	Picture of the PMD after completion of data taking at STAR experiment. The PMD is disassembled so only one half is visible in the figure. Beam pipe can also be seen in the picture.	83
2.24	Block diagram of the front-end electronics readout system.	85
2.25	Photograph of a FEE board with four GASSIPLEX chips.	86
2.26	Chain configuration of the preshower plane of the PMD used during run 7 Au+Au collisions at $\sqrt{s_{NN}} = 200$ GeV. The view is from the tunnel side. .	87
2.27	Left panel: Pedestal minimum values (in mV) for 5000 chips. Right panel: Pedestal minimum vs. pedestal spread for these chips. Lines are drawn to suggest the grouping of chips for a uniform chain.	88
2.28	The PMD timing diagram is shown with different trigger signals arriving at the calculated times to record an event.	89
3.1	Flow chart for the photon reconstruction from PMD in real data and simulation.	95
3.2	Vertex- z range selected for the Au+Au 200 GeV analysis.	96
3.3	Top : XY display of hits on PMD (preshower plane) shown along with the supermodules which were working during the run time. The blank spaces are the dead areas during the run time. Bottom : XY display of PMD after the dead cell implementation and data clean-up. The supermodules shown here are used for data analysis.	97

3.4	Centrality selection for Au+Au collisions at $\sqrt{s_{NN}} = 200$ GeV. The uncorrected TPC track multiplicity measured within $ \eta < 0.5$, is shown. Vertical lines show the reference multiplicity cuts and the corresponding fraction of interaction cross-section. These multiplicity cuts decide the various centrality classes used in the analysis.	98
3.5	Top: Channel hit frequency of a typical chain over a large number of events. The peak reflects the hot channels for which the hit frequency is very high compared to rest of the channels in the chain for the same set of events. The channels not showing any hit frequency represent the dead or bad channels. Bottom: The cell ADC spectra for channels in a chain. The ADC spectra due to hot channels shows spikes.	100
3.6	The cell ADC spectra of isolated cells for a typical chain in PMD. The low ADC peak observed are due to noisy channels.	101
3.7	Problems in data due to bad run numbers and SMs before clean-up. (a) Correlation between the TPC track multiplicity and photon-like clusters in PMD. (b) Similar plot but after excluding bad runs from the analysis. (c) Correlation between the FTPC tracks and the PMD clusters. (d) Similar plot but after removing bad supermodules. See text for details.	102
3.8	Examples of problems in data before clean-up: (a) ADC distribution of cells in chain - 31, (b) Hit frequency distribution of channels in chain - 25 (c) Hit frequency distribution of channels in chain - 27, (d) Hit frequency distribution of channels in chain - 45, and (e) Total ADC per hits for chain - 39.	103
3.9	Global features of data after clean-up in Au+Au collisions at $\sqrt{s_{NN}} = 200$ GeV. Left-top plot shows the nice correlation between FTPC east track multiplicity and PMD photon-like clusters. Right-top plot shows a nice total ADC per hit distribution of a good chain. Left-bottom plot shows the hit frequency distribution of a good chain, and right-bottom plot shows the cleaned cell ADC spectra of a good chain.	104

3.10	Schematic diagram of an isolated cell in PMD. A cell is said to be isolated (shaded) if it has a non zero ADC content and its six neighboring cells (non shaded) have zero ADC content.	105
3.11	Typical isolated cell ADC spectra, along with fit to Landau distribution. .	106
3.12	Typical isolated cell ADC spectra for a cell with low gain in data.	107
3.13	Variation of most probable value and the mean of the isolated cell ADC spectra from real data. The correlation is linear.	108
3.14	Variation of mean of isolated cell ADC spectra for various SM-chains of PMD.	108
3.15	Occupancy of the STAR PMD as a function of η from real data for 0–5% central and 50–60% peripheral Au+Au collisions at $\sqrt{s_{NN}} = 200$ GeV. . .	110
3.16	Top panel: Cluster ADC distribution. Bottom panel: Number of cells in a cluster. Results are shown for Au+Au collisions at $\sqrt{s_{NN}} = 200$ GeV. . . .	111
3.17	Top panel: Total number of clusters on PMD event-by-event. Bottom panel: Correlation between total clusters on the PMD and the TPC track multiplicity from experimental data at $\sqrt{s_{NN}} = 200$ GeV.	112
3.18	Typical conversion efficiency for photons as a function of transverse momentum of incident photons in simulation.	114
3.19	Top panel: The photon conversion efficiency for many events in Au+Au collisions at $\sqrt{s_{NN}} = 200$ GeV. Middle panel: Correlation between number of incident photons on the PMD and number of photons detected within the PMD. Bottom panel: Variation of average photon conversion efficiency over a set of events as a function of photon multiplicity in the PMD acceptance.	115
3.20	Event-wise photon clustering efficiency.	117
3.21	Percentage of split clusters as a function of (a) photons incident in the PMD coverage for PMD only case (top panel), (b) photons incident in the PMD coverage for PMD+All detectors (middle panel), and (c) η for PMD+All detectors with refined clustering ON and OFF (bottom panel).	119

3.22	The difference between the incident track (η, ϕ) and its cluster (η, ϕ) positions for the PMD only (top) and for the PMD with all detectors case (bottom) for photons.	120
3.23	Total number of clusters (%) lying within certain $\Delta\eta$ and $\Delta\phi$ from its incident track for the PMD only case (top panels) and for PMD with all detectors case (bottom panels).	121
3.24	Efficiency (solid circles) and purity (solid squares) of photon counting as a function of MIP E_{dep} cut for Au+Au collisions at 200 GeV. One MIP E_{dep} value is ~ 2.5 keV.	123
3.25	Efficiency of photon counting (left panel) and purity of photon sample (right) as a function of pseudorapidity for PMD+All detectors in Au+Au 200 GeV collisions for refined clustering OFF and ON case.	124
3.26	Top panel: Photon reconstruction efficiency (ϵ_γ) (solid symbols) and purity of photon sample (f_p) (open symbols) for PMD as a function of pseudorapidity (η) for minimum bias Au+Au and Cu+Cu at $\sqrt{s_{NN}} = 200$ GeV. Bottom panel: Comparison between estimated ϵ_γ and f_p for PMD as a function of η for minimum bias Au+Au at $\sqrt{s_{NN}} = 62.4$ GeV using HIJING and AMPT models. The error bars on the AMPT data are statistical and those for HIJING are within the symbol size.	125
3.27	Event-by-event photon multiplicity distributions (solid circles) for Au+Au and Cu+Cu at $\sqrt{s_{NN}} = 62.4$ and 200 GeV. The distributions for top 0–5% central Au+Au collisions and top 0–10% central Cu+Cu collisions are also shown (open circles). The photon multiplicity distributions for central collisions are observed to be Gaussian (solid line). Only statistical errors are shown.	129
3.28	Photon pseudorapidity distributions for Au+Au and Cu+Cu at $\sqrt{s_{NN}} = 62.4$ and 200 GeV. The results for several centrality classes are shown. The solid curves are results of HIJING simulations for central (0–5% for Au+Au and 0–10% for Cu+Cu) and 30–40% mid-central collisions. The errors shown are systematic, statistical errors are negligible in comparison.	130

3.29	Top panel: The number of photons divided by $\langle N_{\text{part}} \rangle / 2$ as a function of average number of participating nucleons for Au+Au and Cu+Cu at $\sqrt{s_{NN}} = 62.4$ and 200 GeV for $-3.7 < \eta < -2.3$. Errors shown are systematic only and include those for $\langle N_{\text{part}} \rangle$. Results from HIJING are shown as lines (solid for Au+Au and dashed for Cu+Cu). Bottom panel: Same as above, for both photons and charged particles from PHOBOS [23].	132
3.30	Photon pseudorapidity distributions normalized by the average number of participating nucleon pairs for different collision centralities are plotted as a function of pseudorapidity shifted by the beam rapidity (-5.36 for 200 GeV and -4.19 for 62.4 GeV) for Au+Au and Cu+Cu collisions at $\sqrt{s_{NN}} = 62.4$ and 200 GeV. Errors are systematic only, statistical errors are negligible in comparison. For clarity of presentation, results for only four centralities are shown. The Cu+Cu data are shifted by 0.1 unit in $\eta - y_{\text{beam}}$. The solid line is a second order polynomial fit to the data (see text for details). . . .	134
3.31	Estimated $\frac{dN_{\pi^0}}{dy}$ from $\frac{dN_{\gamma}}{dy}$ normalized to N_{part} , as compared to $\frac{dN_{\pi^{\pm}}}{dy}$ normalized to N_{part} , as a function of $y - y_{\text{beam}}$ for central collisions at various collision energies.	135
4.1	Event-by-event distribution of the z -position of the primary vertex (V_z) in Au+Au collisions at $\sqrt{s_{NN}} = 9.2$ GeV. The vertical solid lines show the condition of $ V_z < 75$ cm for selected events.	141
4.2	The variation of x and y positions of event vertex. The events involving beam-gas and beam-pipe interactions are rejected by applying a cut of 2 cm on the event vertex radius for the present analysis. See text for details.	142
4.3	Typical event displays observed in TPC of STAR detector for Au+Au collisions at $\sqrt{s_{NN}} = 9.2$ GeV [16]. Upper plots show the view along z -axis (beam direction) and the lower plots show the view from the x -direction, perpendicular to the beam direction. Left plots in the two panel show a typical collision with low multiplicity, and right plots show a typical collision with high multiplicity.	143

4.4	Uncorrected charged particle multiplicity distribution (open circles) measured in the TPC within $ \eta < 0.5$ in Au + Au collisions at $\sqrt{s_{NN}} = 9.2$ GeV. The red-dashed line represents the simulated multiplicity distribution. Errors are statistical only.	144
4.5	The dE/dx of pion, kaon, proton and electron plotted as function of rigidity (charge \times momentum). Red band is for pion, blue is for kaon, magenta is for proton and green is for electron.	147
4.6	The dE/dx distribution for positively charged hadrons in the TPC, normalized by the expected pion dE/dx at $0.3 < p_T < 0.4$ GeV/ c and $ y < 0.5$ in Au+Au collisions at $\sqrt{s_{NN}} = 9.2$ GeV. The curves are Gaussian fits representing contributions from pions (dot-dashed, red), electrons (dashed, green), kaons (dot-dashed, blue), and protons (dotted, magenta). See text for details. Errors are statistical only.	148
4.7	(a) Distribution of distance of closest approach of proton tracks to the primary vertex. The embedded tracks are compared to the ones in real data at $0.4 < p_T < 0.7$ GeV/ c at midrapidity in Au+Au collisions at $\sqrt{s_{NN}} = 9.2$ GeV. The DCA distribution of anti-protons in a similar kinematic range is also shown for comparison. (b) Comparison between the distributions of number of fit points for pions from embedding and from real data for $0.4 < p_T < 0.7$ GeV/ c at midrapidity in Au+Au collisions at $\sqrt{s_{NN}} = 9.2$ GeV.	149
4.8	(a) Efficiency \times acceptance for reconstructed pions, kaons and protons in the TPC as a function of p_T at midrapidity in Au+Au collisions at $\sqrt{s_{NN}} = 9.2$ GeV. (b) Percentage of pion background contribution estimated from HIJING+GEANT as a function of p_T at midrapidity in Au+Au collisions at $\sqrt{s_{NN}} = 9.2$ GeV. The contributions from different sources and the total background are shown separately.	150
4.9	The p_T difference of reconstructed and embedded track plotted as function of p_T of embedded track for (a) kaons and (b) protons. See text for the details.	152

4.10	Transverse momentum spectra for (a) charged pions, (b) K^+ , (c) protons, and (d) K^- at midrapidity ($ y < 0.5$) in Au+Au collisions at $\sqrt{s_{NN}} = 9.2$ GeV for various centralities. The distributions for anti-protons were measured in this limited statistics data only for 0–60% centrality. The anti-proton yield shown in the figure is multiplied by a factor of 10. The errors are statistical and systematic errors added in quadrature.	155
4.11	dN/dy of (a) π^+ and (b) p , normalized by $\langle N_{\text{part}} \rangle$, for Au+Au collisions at $\sqrt{s_{NN}} = 9.2$ GeV, plotted as a function of $\langle N_{\text{part}} \rangle$. The lower energy results are compared to corresponding results for Au+Au collisions at $\sqrt{s_{NN}} = 62.4$ and 200 GeV [22, 25]. Errors shown are the quadrature sum of statistical and systematic uncertainties.	156
4.12	$\langle p_T \rangle$ for π^+ , K^+ , and p , plotted as a function of $\langle N_{\text{part}} \rangle$ for Au+Au collisions at $\sqrt{s_{NN}} = 9.2$ GeV and compared to corresponding results at $\sqrt{s_{NN}} = 62.4$ GeV (top panel) and $\sqrt{s_{NN}} = 200$ GeV (bottom panel). The 200 and 62.4 GeV results are from Refs. [4, 22, 25]. Errors shown are the quadrature sum of statistical and systematic uncertainties.	157
4.13	Variation of (a) K^-/K^+ , (b) p/π^+ , (c) K^-/π^- , and (d) K^+/π^+ ratios as a function of $\langle N_{\text{part}} \rangle$ for Au+Au collisions at $\sqrt{s_{NN}} = 9.2$ GeV. For comparison we also show the corresponding results from Au+Au collisions at $\sqrt{s_{NN}} = 62.4$ and 200 GeV [22, 25]. Errors shown are the quadrature sum of statistical and systematic uncertainties.	159
4.14	The midrapidity $dN_{\text{ch}}/d\eta$ normalized by $\langle N_{\text{part}} \rangle/2$ as a function of $\sqrt{s_{NN}}$. Au+Au collisions at $\sqrt{s_{NN}} = 9.2$ GeV are compared to previous results from AGS [26], SPS [27], and RHIC [22, 28]. Errors shown are the quadrature sum of statistical and systematic uncertainties.	160
4.15	Top panels: dN/dy normalized by $\langle N_{\text{part}} \rangle$ for (a) π^\pm and (b) K^\pm . Bottom panels: $\langle m_T \rangle - m$ of (c) π^\pm and (d) K^\pm . Results are shown for 0–10% central Au+Au collisions at $\sqrt{s_{NN}} = 9.2$ GeV, and are compared to previous results from AGS [26], SPS [27], and RHIC [22]. The errors shown are the quadrature sum of statistical and systematic uncertainties.	161

4.16	(a) π^-/π^+ , (b) K^-/K^+ , (c) \bar{p}/p , and (b) K/π ratios at midrapidity ($ y < 0.5$) for central 0–10% Au+Au collisions at $\sqrt{s_{NN}} = 9.2$ GeV compared to previous results from AGS [26], SPS [27], and RHIC [22]. Errors shown are the quadrature sum of statistical and systematic uncertainties.	162
4.17	Midrapidity transverse momentum distributions of pions, kaons and protons (no feed-down correction) for 0–10% most central Au+Au collisions at $\sqrt{s_{NN}} = 9.2$ GeV, fitted to blast-wave model calculations [33]. The extracted kinetic freeze-out parameters are $T_{\text{kin}} = 105 \pm 10$ (stat.) ± 16 (sys.) MeV and $\langle\beta_T\rangle = 0.46c \pm 0.01c$ (stat.) $\pm 0.04c$ (sys.).	164
4.18	Midrapidity particle ratios for 0–10% most central Au+Au collisions at $\sqrt{s_{NN}} = 9.2$ GeV, fitted to thermal model calculations. See text for details. The extracted chemical freeze-out temperature is $T_{\text{ch}} = 151 \pm 2$ (stat.) ± 7 (sys.) MeV and baryon chemical potential is $\mu_B = 354 \pm 7$ (stat.) ± 30 (sys.) MeV.	166
4.19	Temperature vs. baryon chemical potential (μ_B) from heavy-ion collisions at various $\sqrt{s_{NN}}$ [22]. The μ_B values shown are estimated at chemical freeze-out. The kinetic and chemical freeze-out parameters, extracted using models assuming thermal and chemical equilibrium from midrapidity measurement in central 0–10% Au+Au collisions at $\sqrt{s_{NN}} = 9.2$ GeV, are shown as star symbols. The range of critical temperatures (T_c) [39] of the cross-over quark-hadron phase transition at $\mu_B = 0$ [6] and the QCD critical point from two different calculations [9] from lattice QCD are also indicated. Model-based estimates of the range of initial temperature (T_{initial}) achieved in heavy-ion collisions based in part on direct photon data at top RHIC [37] and SPS [38] energies are also shown. The range of μ_B to be scanned in the upcoming RHIC critical point search and Beam Energy Scan program corresponding to $\sqrt{s_{NN}} = 5.5$ to 39 GeV is indicated by horizontal arrows near the μ_B axis [12].	167

5.1	Vertex distributions for Cu+Cu collisions at $\sqrt{s_{NN}} = 62.4$ (top) and 200 GeV (bottom). The vertex range selected for the analysis is within ± 30 cm along the beam axis. The plots are STAR preliminary.	176
5.2	Uncorrected charged track multiplicity (reference multiplicity) distributions for Cu+Cu collisions at $\sqrt{s_{NN}} = 62.4$ (top) and 200 GeV (bottom). Various centralities used for the analysis are shown with different colors. The plots are STAR preliminary.	177
5.3	Pseudorapidity (top) and azimuthal angle (bottom) distributions for Cu+Cu collisions. The distributions on left and right are for collision energies 62.4 and 200 GeV, respectively. The plots are STAR preliminary. . .	179
5.4	Quality assurance distributions for Cu+Cu collisions at 62.4 (left) and 200 GeV (right). Top, middle, and the bottom plots show the DCA, N_{Fit} points, and the p_T distributions, respectively. The plots are STAR preliminary. . .	180
5.5	Event-by-event $\langle p_T \rangle$ distributions for various centralities for data and mixed events in Cu+Cu collisions at $\sqrt{s_{NN}} = 62.4$ GeV. The lines represent the Γ distributions. The errors shown are statistical.	182
5.6	Event-by-event $\langle p_T \rangle$ distributions for various centralities for data and mixed events in Cu+Cu collisions at $\sqrt{s_{NN}} = 200$ GeV. The lines represent the Γ distributions. The errors shown are statistical.	183
5.7	The μ (top-left) and σ (top-right) from $\langle p_T \rangle$ distributions; α (bottom-left) and β (bottom-right) parameters in Γ distributions, plotted as a function of $\langle N_{\text{part}} \rangle$ for data and mixed events in Cu+Cu collisions at $\sqrt{s_{NN}} = 62.4$ and 200 GeV. The results are STAR preliminary.	187
5.8	Effect of η acceptance on parameters μ (top panels) and σ (bottom panels) in the $\langle p_T \rangle$ distributions for Cu+Cu collisions at 62.4 (left panels) and 200 GeV (right panels). The errors shown are systematic. The results are STAR preliminary.	188

5.9	Dynamical fluctuations in $\langle p_T \rangle$ as a function of $\langle N_{\text{part}} \rangle$ for Cu+Cu collisions at $\sqrt{s_{NN}} = 62.4$ and 200 GeV. Also shown are the results for Au+Au collisions at $\sqrt{s_{NN}} = 200$ GeV. The errors shown are systematic. The results are STAR preliminary.	189
5.10	Left panel: The $\langle \langle p_T \rangle \rangle$ as a function of average charged particle multiplicity, $\langle N_{\text{ch}} \rangle$ for Cu+Cu collisions at $\sqrt{s_{NN}} = 62.4$ GeV. Right panel: Same as above but for Cu+Cu collisions at $\sqrt{s_{NN}} = 200$ GeV. The results are STAR preliminary.	190
5.11	The p_T correlations as function of average number of participating nucleons. Top panels: Correlations shown for Cu+Cu collisions at 62.4 (left) and 200 GeV (right). Middle panels: Comparison of correlations in Cu+Cu collisions with those in Au+Au collisions at 62.4 (left) and 200 GeV (right). Bottom panels: Left plot shows the correlations in Cu+Cu collisions compared between 62.4 and 200 GeV. Right plot shows correlations as function of $\langle N_{\text{part}} \rangle$ for Au+Au and Cu+Cu collisions at 62.4 and 200 GeV.	191
5.12	The p_T correlations multiplied by $\langle N_{\text{part}} \rangle / 2$ as function of average number of participating nucleons for Cu+Cu and Au+Au collision at $\sqrt{s_{NN}} = 62.4$ and 200 GeV.	193
5.13	Square root of p_T correlations scaled by $\langle \langle p_T \rangle \rangle$ as function of average number of participating nucleons for Cu+Cu and Au+Au collision at $\sqrt{s_{NN}} = 62.4$ and 200 GeV.	193
5.14	Top panel: Comparison of HBT correlations with the overall p_T correlations. Bottom panel: Correlations between particle pairs with different charge combinations compared with correlation for inclusive charged particles to see the resonance effect on p_T correlations. The plots are shown for Cu+Cu collisions at $\sqrt{s_{NN}} = 62.4$ GeV. The results are STAR preliminary.	197

5.15	Left panels: The p_T correlations as function of collision centrality for different η regions. Right panels: Correlations plotted as function of $\Delta\eta$ for different collision centralities. Results are shown for Cu+Cu collisions at $\sqrt{s_{NN}} = 62.4$ (top panels) and 200 GeV (bottom panels). Results are STAR preliminary.	199
5.16	The p_T correlations as function of collision centrality for different ϕ acceptances. Results are shown for Cu+Cu collisions at $\sqrt{s_{NN}} = 62.4$ (left panel) and 200 GeV (right panel). Results are STAR preliminary.	199
5.17	The p_T correlations as function of collision centrality for different forward ($\eta > 0$), backward ($\eta < 0$), and combined η regions. Results are shown with $ v_z < 30$ cm for Cu+Cu collisions at $\sqrt{s_{NN}} = 62.4$ (top panel) and 200 GeV (bottom panel). Results are STAR preliminary.	200
5.18	Top panel: Same as Fig. 5.17, but for $ v_z < 10$ cm. Bottom panel: Correlations as function of N_{part} for $ v_z < 30$ cm and $ v_z < 10$ cm with $ \eta < 1$. Results are shown for Cu+Cu collisions at $\sqrt{s_{NN}} = 62.4$ and are STAR preliminary.	201
5.19	Top panel: p_T correlations for different p_T bins for Cu+Cu collisions at $\sqrt{s_{NN}} = 62.4$ GeV. Bottom panel: Same as above but shown in linear scale for clarity.	202
5.20	Top panel: p_T correlations for different p_T bins for Cu+Cu collisions at $\sqrt{s_{NN}} = 200$ GeV. Bottom panel: Same as above but shown in linear scale for clarity.	203
5.21	Top panel: The p_T correlations scaled by $\langle\langle p_T \rangle\rangle$ for different p_T bins in Cu+Cu collisions at $\sqrt{s_{NN}} = 200$ GeV. Bottom panel: same as above but y -axis is square root of correlations scaled by $\langle\langle p_T \rangle\rangle$. Left panels are shown in semi-log scale whereas right panels are in linear scale.	204
5.22	The p_T correlations scaled by the p_T bin sizes for different p_T bins in Cu+Cu collisions at $\sqrt{s_{NN}} = 200$ GeV. Left panel is shown in semi-log axis whereas right panel is in linear scale.	205

5.23	p_T correlations multiplied by $\langle N_{\text{ch}} \rangle$ for different p_T bins in Cu+Cu collisions at $\sqrt{s_{NN}} = 200$ GeV. Left panel is shown in semi-log axis whereas right panel is in linear scale.	206
5.24	Inclusive p_T -spectra for 0–10% central Cu+Cu collisions at $\sqrt{s_{NN}} = 200$ GeV. Spectra is fitted with the function, $F(p_T) = e^{-p_T/T}$ (red line), for the p_T range 0.2–2.0 GeV/ c . The errors are statistical.	208
5.25	p_T correlations divided by $[d\langle p_T \rangle/dT]^2$ for different p_T bins as function of $\langle N_{\text{part}} \rangle$ for Cu+Cu collisions at $\sqrt{s_{NN}} = 200$ GeV. Left panel is shown in semi-log axis whereas right panel is in linear scale.	209
5.26	Inclusive p_T -spectra for 0–10% central Cu+Cu collisions at $\sqrt{s_{NN}} = 200$ GeV. Spectra is fitted with the function, $F(p_T) = p_T e^{-p_T/T}$ (red line), for the p_T range 0.15–0.8 GeV/ c . The errors are statistical.	210
5.27	p_T correlations divided by $[d\langle p_T \rangle/dT]^2$ for different p_T bins as function of $\langle N_{\text{part}} \rangle$ for Cu+Cu collisions at $\sqrt{s_{NN}} = 200$ GeV. Left panel is shown in semi-log axis whereas right panel is in linear scale.	211
5.28	Inclusive p_T -spectra for 0–10% central Cu+Cu collisions at $\sqrt{s_{NN}} = 200$ GeV. Spectra is fitted with the function, $F(p_T) = p_T^2 e^{-p_T/T}$ (red line), for the p_T range 0.15–0.6 GeV/ c . The errors are statistical.	212
5.29	p_T correlations divided by $[d\langle p_T \rangle/dT]^2$ for different p_T bins as function of $\langle N_{\text{part}} \rangle$ for Cu+Cu collisions at $\sqrt{s_{NN}} = 200$ GeV. Left panel is shown in semi-log axis whereas right panel is in linear scale.	213

List of Tables

2.1	Nominal RHIC parameters for Au+Au collisions	53
2.2	Response of a photon and hadron in the PMD	80
2.3	Basic parameters of the STAR PMD	81
2.4	Specifications of a GASSIPLEX chip.	84
2.5	Electronic chain in STAR PMD.	86
3.1	Average number of participating nucleons ($\langle N_{\text{part}} \rangle$) for various collision centrality in Au+Au and Cu+Cu collisions at $\sqrt{s_{NN}} = 62.4$ and 200 GeV.	99
3.2	Global means of the isolated cell ADC distribution of cells for working SMs of PMD in Au+Au collisions at $\sqrt{s_{NN}} = 200$ GeV.	109
3.3	Gaussian fit parameters for photon multiplicity distributions for $-3.7 < \eta < -2.3$ for central Au+Au (0–5%) and Cu+Cu (0–10%) at $\sqrt{s_{NN}} = 62.4$ and 200 GeV.	130
4.1	Centrality selection, average number of participating nucleons ($\langle N_{\text{part}} \rangle$) and average number of binary collisions ($\langle N_{\text{coll}} \rangle$).	145
4.2	Track selection criteria for the analysis presented in this chapter.	146
4.3	Sources of systematic errors on yields of various produced hadrons.	153
4.4	Centrality dependence of $dN_{\text{ch}}/d\eta$ at midrapidity in Au+Au collisions at $\sqrt{s_{NN}} = 9.2$ GeV.	158
5.1	The $N_{\text{ch}}^{\text{TPC}}$ values, average number of participating nucleons ($\langle N_{\text{part}} \rangle$) and average number of binary collisions ($\langle N_{\text{coll}} \rangle$) for various collision centralities in Cu+Cu collisions at $\sqrt{s_{NN}} = 62.4$ GeV.	178

5.2	The $N_{\text{ch}}^{\text{TPC}}$ values, average number of participating nucleons ($\langle N_{\text{part}} \rangle$) and average number of binary collisions ($\langle N_{\text{coll}} \rangle$) for various collision centralities in Cu+Cu collisions at $\sqrt{s_{NN}} = 200$ GeV.	179
5.3	The μ and σ values in $\langle p_T \rangle$ distributions for various centralities for data and mixed events in Cu+Cu collisions at $\sqrt{s_{NN}} = 62.4$ GeV.	184
5.4	The μ and σ values in $\langle p_T \rangle$ distributions for various centralities for data and mixed events in Cu+Cu collisions at $\sqrt{s_{NN}} = 200$ GeV.	184
5.5	$\langle N_{\text{ch}} \rangle$, α and β parameters of Γ distributions for various centralities for data and mixed events in Cu+Cu collisions at $\sqrt{s_{NN}} = 62.4$ GeV.	185
5.6	$\langle N_{\text{ch}} \rangle$, α and β parameters of Γ distributions for various centralities for data and mixed events in Cu+Cu collisions at $\sqrt{s_{NN}} = 200$ GeV.	185
5.7	Systematic errors on μ and σ in event-wise $\langle p_T \rangle$ distributions due to different sources for various collision centralities in Cu+Cu collisions at $\sqrt{s_{NN}} = 62.4$ GeV.	195
5.8	Systematic errors on μ and σ in event-wise $\langle p_T \rangle$ distributions due to different sources for various collision centralities in Cu+Cu collisions at $\sqrt{s_{NN}} = 200$ GeV.	195
5.9	Systematic errors on p_T correlations due to different sources for various collision centralities in Cu+Cu collisions at $\sqrt{s_{NN}} = 62.4$ GeV.	196
5.10	Systematic errors on p_T correlations due to different sources for various collision centralities in Cu+Cu collisions at $\sqrt{s_{NN}} = 200$ GeV.	196
5.11	The inverse slope parameters obtained by fitting function - I to the inclusive p_T spectra for all the centralities.	207
5.12	The inverse slope parameters obtained by fitting function - II to the inclusive p_T spectra for all the centralities.	209
5.13	The inverse slope parameters obtained by fitting function - III to the inclusive p_T spectra for all the centralities.	211

Chapter 1

INTRODUCTION

1.1 Quarks and Quark-Gluon Plasma (QGP)

High-energy heavy-ion collision experiments are built to study the elementary constituents of matter or radiation. A fundamental/elementary particle is a particle which cannot be further divided into constituent particles or which has no substructure. Earlier it was believed that atoms are the fundamental particles and everything in this universe is made up of atoms. Later on, it was discovered that atoms contain protons and neutrons confined in nucleus and electrons revolving around it. As of now, it is established that the neutrons and protons are also not the fundamental particles and that these are the bound states of quarks and gluons, collectively called as *partons*. Quarks are not observed as free particles and are confined in hadrons by the inter quark potential. Baryons are made up of three quarks and mesons consist of a quark-antiquark pair. Deep-inelastic electron scattering experiments [1] showed that constituent quarks have fractional electric charges, $+2/3$ or $-1/3$, and carry effective mass (m^*) of about one third of the nucleon mass and only half of the nucleon's momentum. It was proposed that the other half of the nucleon's momentum is ascribed to the force carriers called as *gluons* which are responsible for the inter quark binding.

With the discovery of Δ^{++} (uuu), Δ^- (ddd) and Ω^- (sss), a new problem came into the picture. These particles consist of three identical quarks (fermions) having parallel spins and identical s-wave states, hence violating the Pauli exclusion principle. To account for this, a new quantum number called the color quantum number [2, 3] was proposed and

it was postulated that even if the quarks in a hadron are identical, their color charges are different and hence Pauli exclusion principle is not violated. There are three color charges (red, blue and green) and three anti-color charges (antired, antiblue and antigreen). These color charges have nothing to do with the visible colors, they are only the quantum numbers. Since baryons and mesons are color neutral, the color charge combination forming a baryon or meson must sum to zero. In this way, baryons consist of red, blue and green color charges having overall color charge zero. Similarly, anti-baryons have antired, antiblue and antigreen color charges. Mesons have red-antired or blue-antiblue or green-antigreen color charges.

The beginning of the universe is considered from the explosion known as big-bang. It is believed that after few microseconds of the big-bang, the quarks and gluons existed in free state called as Quark-Gluon Plasma (QGP) [4]. Quark-gluon plasma can be defined as deconfined state of matter or more precisely - *A (locally) thermally equilibrated state of matter in which quarks and gluons are deconfined from hadrons, so that color degrees of freedom become manifest over nuclear, rather than merely nucleonic, volumes* [5]. The term plasma suggests an ionized gas, however the results from high-energy heavy-ion collision experiments suggested that instead of behaving like a gas of free quarks and gluons, the matter created in the nucleus-nucleus collisions appears to be more like a *liquid* [6]. This matter interacts more strongly than originally expected, hence it was given another name “sQGP”. So the terms QGP and sQGP can be used interchangeably.

Deconfinement means quarks and gluons are able to move over larger distances than that of the size of a nucleon (~ 1 fm) and hence forming the quark-gluon plasma. Deconfinement can be achieved in two cases: either at very high energies where the partons effective color charge approaches zero (asymptotic freedom), or at high density where the hadronic wave functions overlap delocalising the partons (Debye screening). Relativistic Heavy Ion Collider (RHIC) at Brookhaven National Laboratory (presently running) and A Large Ion Collider Experiment (ALICE) at LHC (Large Hadron Collider) at CERN (expected to run soon) are the facilities which work on the principle of creating QGP by increasing the center of mass energy ($\sqrt{s_{NN}}$) to a higher value. Maximum center of mass energy achieved for heavy-ion collisions at RHIC is $\sqrt{s_{NN}} = 200$ GeV and that at ALICE

will be 5.5 TeV. As of now, various ions used for the collisions at RHIC are gold (Au), copper (Cu), and deuteron (d). Proposed heavy-ion for collisions at ALICE is the lead (Pb). In addition to heavy ions, nucleon-nucleon e.g. $p + p$ collisions are also performed in these experiments. The $p + p$ collisions are useful for the reference studies to compare with those of heavy ions. Compressed Baryonic Matter (CBM) at FAIR (Facility for Antiproton and Ion Research) in Germany will exploit the baryon density rich region for its physics programs [7]. The major goals of the CBM experiment include determination of the nuclear equation of state at high baryon density, search for the existence of the first order phase transition from hadronic to partonic matter and the location of the critical point in the phase diagram. The CBM experiment will be the fixed target experiment in contrast to collider experiments at RHIC and LHC. The results presented in this thesis are obtained by analyzing the data recorded by the STAR (Solenoidal Tracker At RHIC) detector at RHIC.

1.2 Lattice QCD and Phase Transition

The theory which describes the interaction of color charges of quarks and gluons is called Quantum Chromodynamics (QCD) [8]. The theory is useful to describe the strong force, which is so strong that a non-perturbative treatment is necessary to study its properties. So the lattice QCD calculations are used to predict the thermodynamic properties of hadronic matter in the non-perturbative regime. In these calculations, the quarks and gluons are assumed on a discrete space-time lattice and computational numerical methods are used to predict the temperature and energy density of the system. Main goals of lattice QCD are to calculate the masses and decay properties of the hadrons. Its another major goal is to determine the properties of QGP, which is assumed to be formed just after the collision of two high-energy heavy-ion nuclei. Lattice QCD calculations provide important input to the hydrodynamic models by looking at several important properties of strongly interacting matter, which are discussed below -

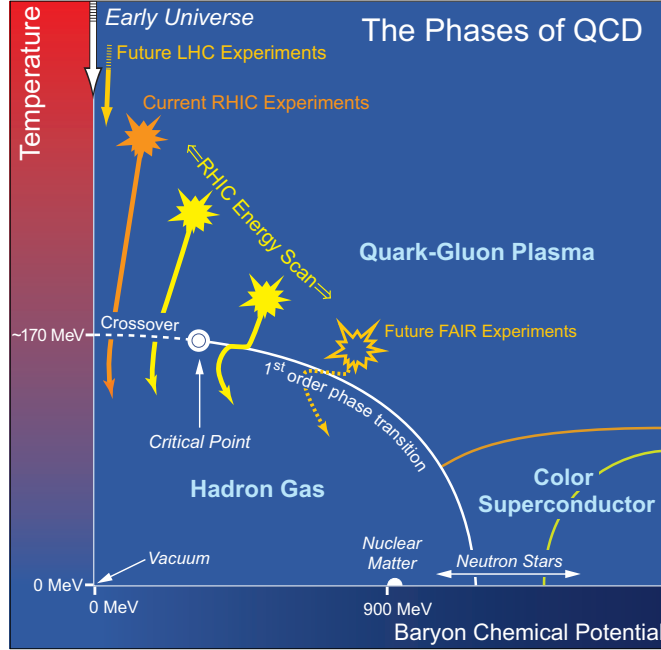


Figure 1.1: Schematic picture of the QCD phase diagram shown in $T - \mu_B$ space [9].

1.2.1 Phase Diagram

Phase diagram for hadronic matter is described by the temperature (T) and the baryon chemical potential (μ_B). When $\mu_B = 0$, the matter and the antimatter are equal in amount. When $\mu_B > 0$, the matter is favored over the antimatter. Figure 1.1 shows the schematic phase diagram of hadronic matter. Lattice QCD predicts a boundary in the phase diagram which separates the region of matter dominated by hadronic degrees of freedom from that dominated by quark-gluonic degrees of freedom. This boundary is called the “first order phase transition” line or “QCD phase boundary”. The point in the phase diagram where the first order phase transition ends is called the “critical point”. The dotted line which is close to $\mu_B \sim 0$, represents the rapid crossover, with no real transition. The only point known in this diagram is of nuclear matter, all other things are the lattice predictions. One of the main aim of high-energy heavy-ion collision experiments is to map the QCD phase diagram, to locate the position of critical point, and to determine the QCD phase boundary.

- *Critical Point Search and Energy Scan:* Search for the QCD critical point and to locate the QCD phase boundary in the phase diagram has been of great interest to the high-energy heavy-ion theorists as well as the experimentalists. On experimental side, this interest is further increased recently as there are proposals for the facilities, which will help in locating the critical point, phase boundary and exploring the QCD phase diagram. Experiments which are presently focusing on these exciting physics issues are - STAR (Solenoidal Tracker At RHIC) [10] at RHIC, SHINE (SPS Heavy Ion and Neutrino Experiment) [11] at SPS, CBM (Compressed Baryonic Matter) [7] at FAIR, and NICA (Nuclotron-based Ion Collider fAcility) at Dubna [12]. These will cover different regions of the phase diagram and hence are complementary to each other. Of these, the STAR experiment has a proposal to start a new program called “Critical Point Search”, in which the $\sqrt{s_{NN}}$ (and hence μ_B and T) will be varied in order to explore the QCD phase diagram [13]. The region of the planned RHIC beam energy scan is also indicated in the phase diagram in Fig. 1.1. As a first step of this program, a test run was conducted at RHIC in the year 2008 by colliding Au ions at $\sqrt{s_{NN}} = 9.2$ GeV. The results from these data form chapter 4 of this thesis. The successful analyses of various observables and the beautiful results demonstrate the readiness of the STAR experiment and hence the RHIC collider to perform the critical point search program in the near future.

The lattice QCD calculations predict a phase transition from a hadronic gas to a quark-gluon plasma [14, 15]. The critical values of energy density ($\epsilon^{\text{critical}}$) predicted by these calculations are at ≈ 2 GeV/fm³, at a critical temperature (T_c) ≈ 170 – 190 MeV. A lower value of T_c means it is easier to create the QGP.

1.2.2 Equation of State

The equation of state (EOS) can be expressed as the relationship between energy and temperature or pressure and temperature. For example, the ideal gas equation of state can be written as: $pV = nRT$, where p , V , and T are the pressure, volume and temperature respectively. Similarly, the equation of state (EOS) for the hadronic matter will be the relation between these quantities, but it is more complicated in this case.

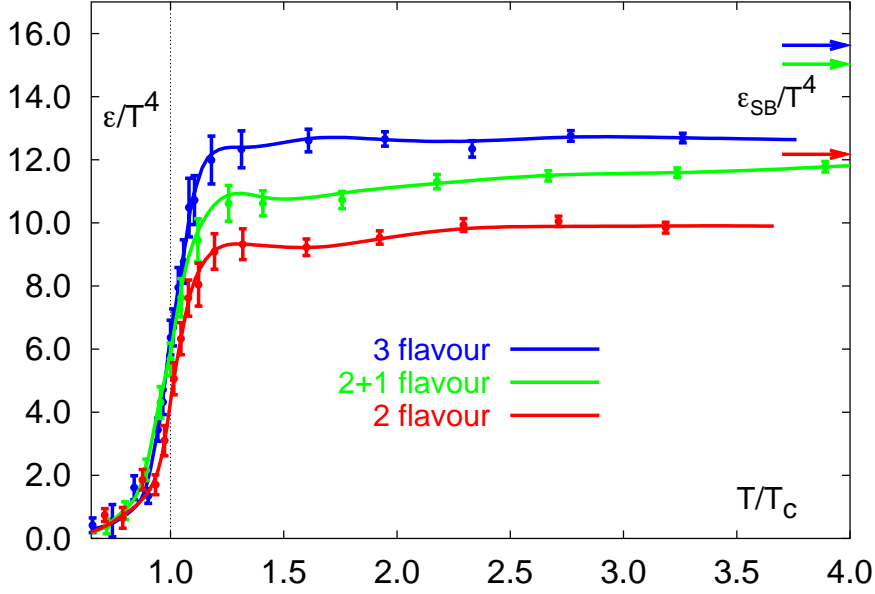


Figure 1.2: Energy density as a function of temperature as per the lattice QCD calculations [16].

Figure 1.2 shows an example of a typical equation of state from lattice QCD calculations [16]. The energy density (ϵ) is plotted as a function of temperature (T), where T_c represents the critical temperature. These calculations are performed for non-zero temperatures and non-zero chemical potentials. The ϵ/T^4 is proportional to the number of degrees of freedom. The significant increase of ϵ/T^4 around critical temperature indicates the increase in the number of degrees of freedom, showing the quarks and gluons become the relevant degrees of freedom. The arrows indicate the Stefan-Boltzmann limit:

$$\epsilon = g \frac{\pi^2}{30} T^4, \quad (1.1)$$

where g is the number of degrees of freedom. For a hadron gas, the number of degrees of freedom are given by the three pion states (π^+ , π^- , π^0), so $g = 3$ for this case:

$$\epsilon = 3 \frac{\pi^2}{30} T^4, \quad (1.2)$$

In the QGP phase, the relative number of degrees of freedom are the quarks and gluons. This number is much larger in case of QGP as compared to hadron gas phase:

$$\epsilon_{\text{QGP}} = \left(16 + \frac{21}{2} n_{\text{flavor}} \right) \frac{\pi^2}{30} T^4. \quad (1.3)$$

The critical temperature depends on the number of flavors and the mass of quarks. The blue curve in the Fig. 1.2 shows the expectation for the three light quark flavors, the red curve shows the two light quarks calculation. The green curve shows the more realistic calculation with two light quarks (u , d) and a heavy quark (s).

1.3 Nucleus-Nucleus Collisions

Nucleus-nucleus collisions can be considered as the interaction between the nucleons. In high-energy heavy-ion collision experiments, two nuclei are accelerated to a very high energy. They approach each other with velocities close to the speed of light. As a result, these nuclei, which are spherical in shape are Lorentz contracted along the direction of motion (beam direction or z -axis by convention). Due to this, their shape changes and they look like a pancake. When the two nuclei collide, there is an overlap region depending upon the impact parameter. The nucleons which come into this overlap region are called *participants* and those which do not participate are called *spectators*. These are shown in the Fig. 1.3. The collisions in which the impact parameter values are close to zero are termed as *central collisions*, and those with large impact parameter values are termed as *peripheral collisions*.

The dynamics of nucleus-nucleus collisions can be understood from the space-time diagram with the longitudinal coordinate z and the time coordinate t , as shown in the Fig. 1.4. Let us consider the head-on collision of two Lorentz contracted nuclei along the beam direction or z -axis. Soon after the collision of two nuclei at $(z, t) = (0, 0)$, the nucleons inside the overlap regions of the two nuclei start interacting to produce a dense matter with densities much higher than normal nuclear matter density. The energy density and the temperatures reached can be so high that it may melt down the constituents of the colliding nucleons into a soup of quarks and gluons. After a certain time, the system will reach equilibrium and the deconfined quarks and gluons again will start to hadronize. If this phase transition from quarks and gluons to hadrons is of first order then it will go through a mixed phase at a certain critical temperature. In the mixed phase, the temperature of the system is expected to be constant with the increase

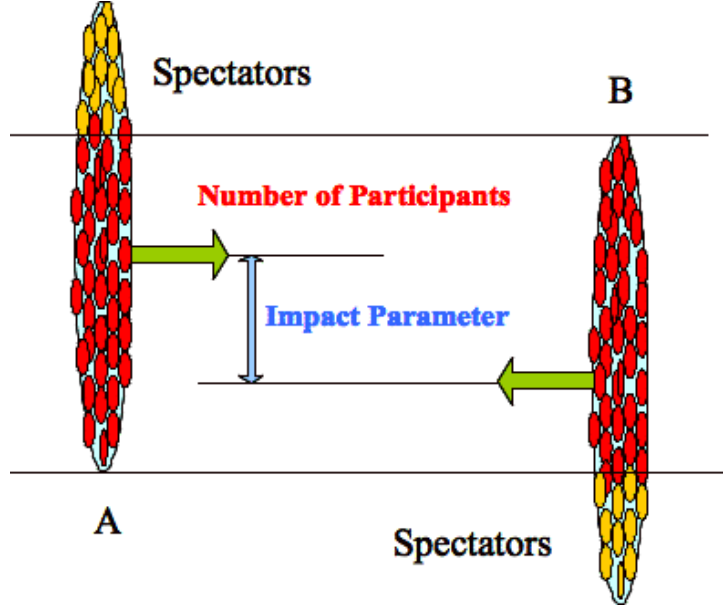


Figure 1.3: Collision of two nuclei A and B, with a non-zero impact parameter. Number of participants and the spectators are also shown.

in the entropy and there will be co-existence of hadrons, quarks and gluons. Also, the latent heat is used up to convert the quarks and gluons to hadrons. When all the quark and gluon degrees of freedom are converted into hadronic degrees of freedom, the mixed phase ends. The interactions, however, persist and the system expands and cools down. When the inelastic interactions stop, resulting in no more new particles being produced, we say the system has reached the chemical equilibrium. This time/temperature, at which the inelastic interactions stop, is called the chemical freeze out time/temperature. After this time, the particle ratios are fixed. However, the system keeps on expanding with elastic collisions still going on and as a result, it keeps on further cooling. A time and temperature is reached when the distance between any two particles in the medium is larger than the average mean free path. At this point of time the elastic collisions also stop. We call this time/temperature as kinetic freeze out time/temperature. The particles at this point come out of the system and gets detected in the detectors.

Since we can only detect the final products of the collisions, which are the particles after the freeze out, most of the information about the early stage of the collision, the QGP, its properties and hadronization could have been washed out by final state interactions.

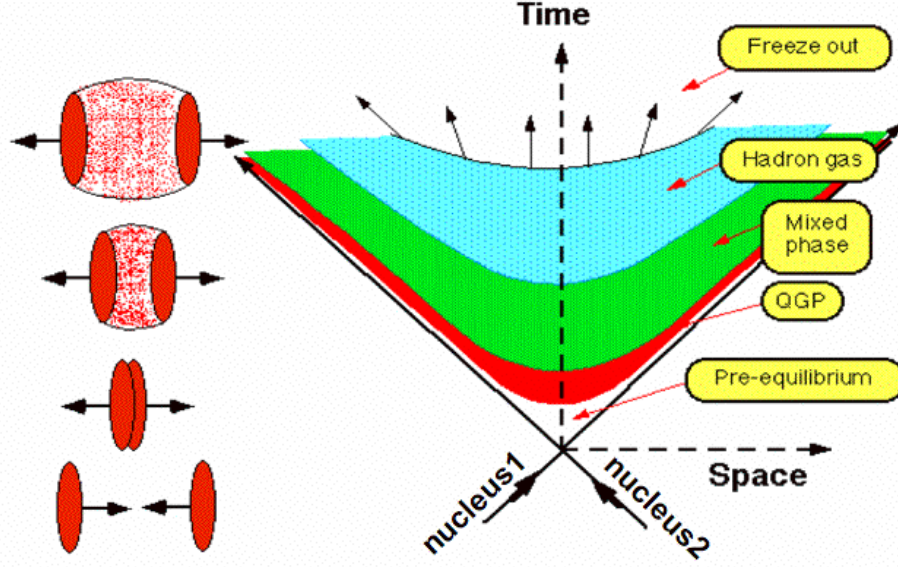


Figure 1.4: Space-time diagram and different evolution stages of a relativistic heavy-ion collision.

Yet, there are several signatures [17–21] which provide the information about the QGP and early stage of the collision.

1.4 Probes of Quark-Gluon Plasma Formation

The size and duration of quark-gluon plasma are expected to be very small, at most a few fm in diameter and perhaps 5 to 10 fm/c in duration. Furthermore, it is also important to distinguish the signals of QGP from the background emitted from the hot hadronic gas phase that follows the hadronization of the plasma. The QGP signals are also modified by the final state interactions in the hadronic phase. Some of these signatures of the quark-gluon plasma production are discussed in the following subsections.

1.4.1 Strangeness Enhancement

The strangeness content in hadronic matter and quark-gluon plasma are different. The s and \bar{s} quarks are enhanced in quark-gluon plasma in chemical and thermal equilibrium [22]. As, in QGP scenario, quarks and gluons are produced in abundance. The two possible main production channels for $s\bar{s}$ pairs are $q\bar{q} \rightarrow s\bar{s}$ and $gg \rightarrow s\bar{s}$. If we

consider the $s\bar{s}$ production from the $q\bar{q}$ interaction, it would take about 8 times the natural lifespan of a QGP fireball, to attain chemical equilibrium in strangeness. So it was proposed by Rafelski and others that many quark-antiquark pairs are created dominantly via the gluon-gluon fusion. In the QGP region, the energy available is so large that the temperature attained is of the same order as the mass of strange quark. In such a case, the coupling of gluons to the strange quarks will be similar to that with light quarks and as a result, strange quark-antiquark would be produced more frequently as compared to nucleon-nucleon collisions. The strangeness enhancement in a baryon rich matter can also be a result of Pauli exclusion principle. Since initially the u and d quarks are in abundance as compared to the s quarks, the $u\bar{u}$ and $d\bar{d}$ pair production is prohibited by Pauli exclusion principle, whereas for $s\bar{s}$ production it can be neglected. Furthermore, the u and d quarks annihilate respectively with the \bar{u} and \bar{d} antiquarks, while $s\bar{s}$ annihilation occurs less frequently until the saturation of s and \bar{s} abundances.

When we say the strangeness is enhanced, a question comes in mind that relative to what it is enhanced. We observe the strangeness enhancement in terms of strangeness enhancement factor. It is defined as the yield per participating nucleon of a given type of strange particle in the heavy-ion collisions (e.g. Au+Au at RHIC) relative to strange particle yield in a light reference system collisions (e.g. $p+p$ at RHIC). Figure 1.5 shows the strangeness enhancement as a function of average number of participating nucleons ($\langle N_{\text{part}} \rangle$) for K , ϕ , $\bar{\Lambda}$ and $\Xi+\bar{\Xi}$ for Au+Au and Cu+Cu collisions relative to $p+p$ collisions at 200 and 62.4 GeV in STAR experiment [23].

1.4.2 J/Ψ Suppression

In a quark-gluon plasma, the color charge of a quark is subject to screening due to the presence of quarks and gluons in the plasma. This is called the *Debye screening*. The J/Ψ particle is a bound state of charm quark c and charm antiquark \bar{c} . Let us consider the J/Ψ particle as a two-body system of a charm quark interacting with a charm antiquark, without the quark-gluon plasma. Consider the c quark with a color charge $q > 0$ at the origin and the \bar{c} antiquark with a color charge $(-q)$ at r . The color potential from the c quark as seen by the antiquark \bar{c} can be represented phenomenologically by the Coulomb

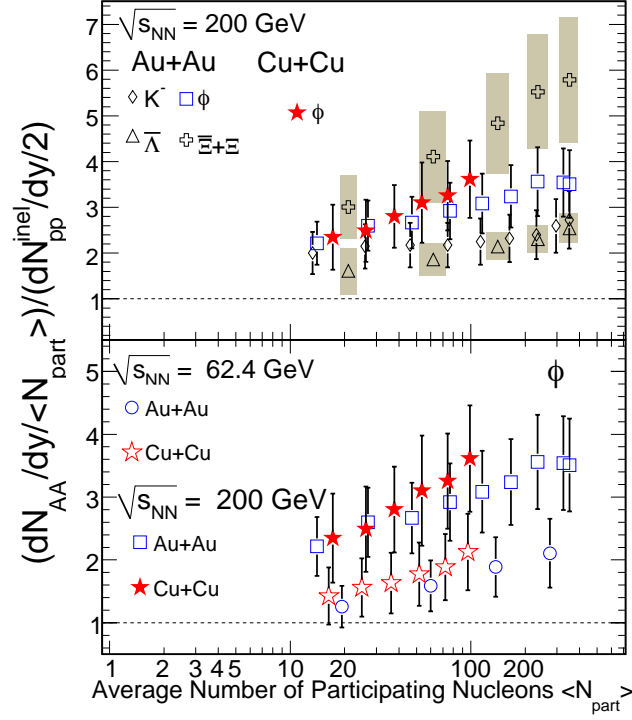


Figure 1.5: Upper panel: The ratio of the yields of K , ϕ , $\bar{\Lambda}$ and $\Xi + \bar{\Xi}$ normalized to $\langle N_{\text{part}} \rangle$ in Au+Au and Cu+Cu collisions to corresponding yields in inelastic $p+p$ collisions at 200 GeV. Lower panel: Same as above for only ϕ mesons at 200 and 62.4 GeV. The error bars shown represent the statistical and systematic errors added in quadrature.

potential

$$V_0(r) = \frac{q}{4\pi r} \quad (1.4)$$

There is also the confining linear potential between c and \bar{c} which increases with their separation,

$$V_{\text{linear}}(r) = kr, \quad (1.5)$$

where k is the string tension coefficient. The potential energy for the $c\bar{c}$ system is [24]

$$H_I = (-q)\frac{q}{4\pi r} + kr, \quad (1.6)$$

which can be written as

$$H_I = -\frac{\alpha_{eff}}{r} + kr, \quad (1.7)$$

where, $\alpha_{eff} = q^2/4\pi$. In a quark-gluon plasma, where quarks and gluons are deconfined, the string tension is zero. Also in the QGP, the interaction between $c\bar{c}$ is modified from

Coulomb-type long-range interaction to the Yukawa-type short-range interaction

$$V(r) = \frac{q}{4\pi} \frac{e^{-r/\lambda_D}}{r} \quad (1.8)$$

here, λ_D is the Debye screening length.

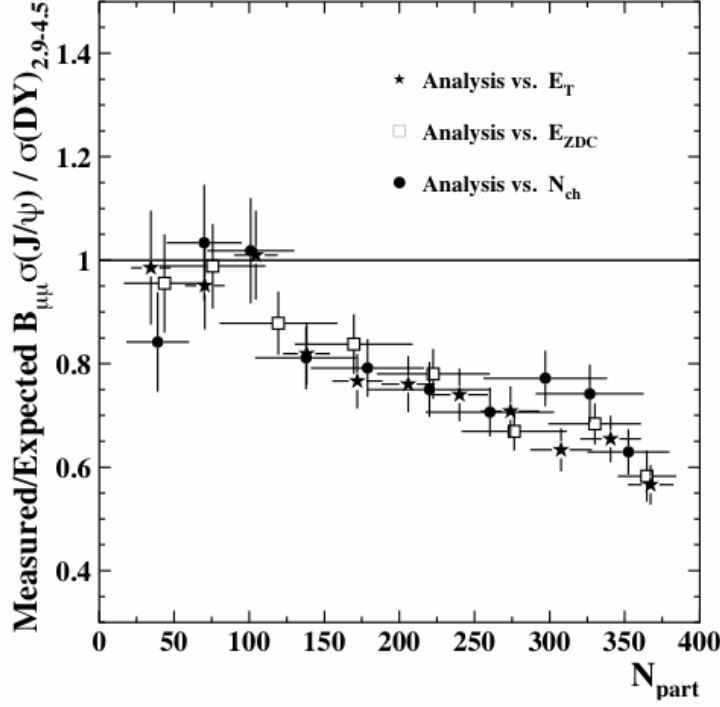


Figure 1.6: The $(J/\Psi)/\text{Drell-Yan}$ cross-sections ratio as a function of N_{part} for three analyses of the Pb+Pb collisions at $\sqrt{s_{NN}} = 17.3$ GeV, divided by the normal nuclear absorption values. The data are from NA50 experiment at SPS.

If we place a J/Ψ particle in the plasma, the Debye screening will weaken the interaction between c and \bar{c} . This will modify the long-range Coulomb-type color interaction between c and \bar{c} to turn it into a short-range Yukawa-type interaction, with the range given by the Debye screening length λ_D . Within this distance λ_D , the attractive interaction between c and \bar{c} is effective but beyond this range, the attractive interaction is ineffective, as the magnitude of the interaction diminishes exponentially with the distance. The Debye screening length λ_D is inversely proportional to the temperature. At high temperatures, the range of the attractive interaction becomes so small as to make

it impossible for the $c\bar{c}$ pair to form a bound state. When this happens, the $c\bar{c}$ system dissociates into a separate c quark and \bar{c} antiquark in the plasma. The c quark and \bar{c} antiquark subsequently hadronize by combining with the light quarks or light antiquarks to give “open charm” mesons as $D(c\bar{u}, \text{ and } c\bar{d})$, $\bar{D}(\bar{c}u, \text{ and } \bar{c}d)$, $D_s(c\bar{s})$ and $\bar{D}_s(\bar{c}s)$.

In nucleus-nucleus collisions, J/Ψ particles are produced in the initial stage of the collision process. If the quark-gluon plasma is formed in the region of J/Ψ production, it will unbind the J/Ψ and hence final yield of the J/Ψ particles will be less. This is called J/Ψ suppression. Therefore, the suppression of J/Ψ may be used as signature of the quark-gluon plasma formation [25].

Fig. 1.6 shows the $(J/\Psi)/\text{Drell-Yan}$ cross-sections ratio as a function of N_{part} for three analyses of the Pb+Pb collisions at $\sqrt{s_{NN}} = 17.3$ GeV, divided by the normal nuclear absorption values. The data are from NA50 experiment at SPS [26]. This ratio is less than unity for central collisions and around unity for peripheral collisions indicating a clear suppression in central Pb+Pb collisions at $\sqrt{s_{NN}} = 17.3$ GeV at SPS. However, some theoretical developments revealed that the suppression can be explained by other nuclear effects as well [27].

1.4.3 Direct Photons

Direct photons refer to those photons which carry information about the early stages of the relativistic heavy-ion collisions. Direct photons are created in the thermally equilibrated quark-gluon plasma through gluonic channels: $q\bar{q} \rightarrow \gamma g$, $gq \rightarrow \gamma q$ and $g\bar{q} \rightarrow \gamma\bar{q}$.

We know the photons interact with the particles through the electromagnetic interaction. When photons are produced in the quark-gluon plasma region, they do not participate much in the strong interactions with the quarks and gluons. Consequently, their mean-free path is quite large and they may not suffer a collision after they are produced. As a result, they would keep the memory of the temperature at which they were produced. In this way, they may provide the information about the quark-gluon plasma created in the early stages of collisions and hence can serve as a signal of the QGP [28].

Unfortunately, the direct photon production is very small in a collision, and in addition to that, there are other significantly contributing photon sources through the

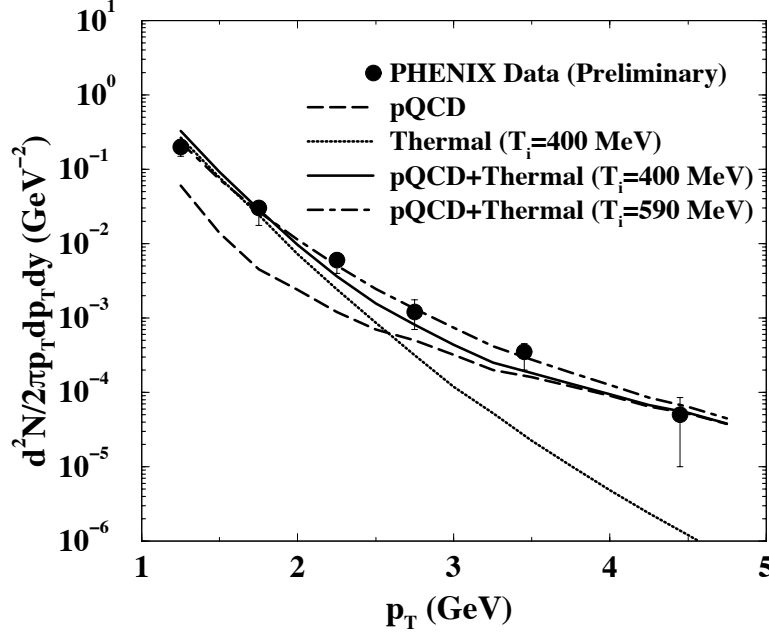


Figure 1.7: Direct photon spectra at RHIC energies measured by PHENIX.

evolution of the collision, especially photons from the hard scatterings in the QGP phase or the photons from electromagnetic hadronic decay. If the direct photon yields are separated from the backgrounds, they could reflect the dynamics of the quarks and gluons in the system before hadronization. Direct photon yields have been obtained in the PHENIX experiment at RHIC in Au+Au collisions at $\sqrt{s_{NN}} = 200$ GeV. Figure 1.7 shows the transverse momentum spectra of the direct photon as measured in the PHENIX experiment. The lines represent the theoretical calculations for different cases described in [29]. Dashed line in the figure indicate hard photons from NLO pQCD calculations and solid (dot-dashed) line represent the total (pQCD + thermal) photon yield obtained from QGP initial state with $T_i = 400$ MeV, $\tau_i = 0.2$ fm/c (or $T_i = 590$ MeV, $\tau_i = 0.15$ fm/c). The results for which the in-medium effects are included (ignored), are shown by the solid (dot-dashed) line. The data can be reproduced by assuming a deconfined state of quarks and gluons with initial temperature ~ 400 MeV and thermalization time scale ~ 0.2 fm/c. The extracted average temperature (T_{av}) from photon spectra is found to be ~ 265 MeV for the p_T range 1.25–2.25 GeV corresponding to the thermal contributions. This indicates that the temperature of the system formed after the collisions is higher

than the temperature for deconfinement.

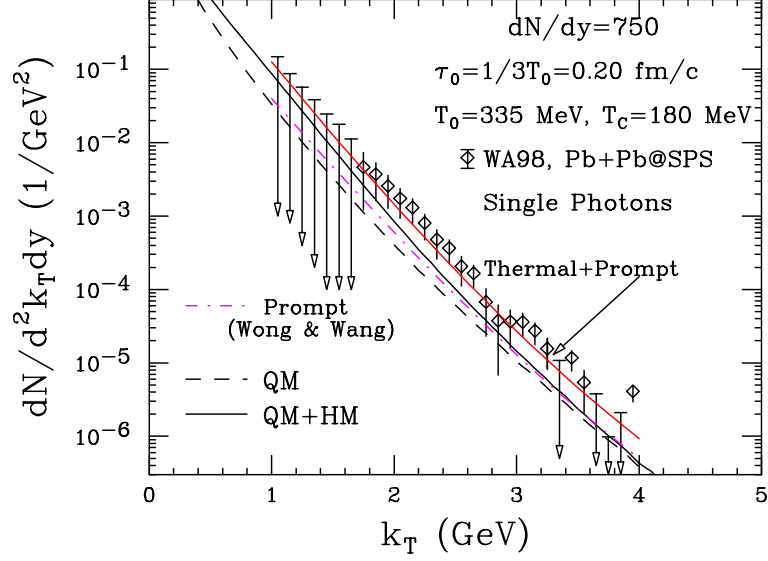


Figure 1.8: The invariant direct photon multiplicity for central Pb+Pb collisions at $\sqrt{s_{NN}} = 17.3$ GeV [30]. The model calculations [31] are shown in the form of lines.

Direct photon measurements have also been made in the WA98 experiment at SPS at $\sqrt{s_{NN}} = 17.3$ GeV [30]. Figure 1.8 shows the invariant direct photon multiplicity for central Pb+Pb collisions at $\sqrt{s_{NN}} = 17.3$ GeV [30]. The figure also shows the model calculations [31] with the assumption that a chemically and thermally equilibrated quark-gluon plasma is formed at $\tau_0 = 1/3T_0$. The QGP is assumed to expand, cool, enter into a mixed phase and attain freeze-out from a hadronic phase. QM represents the radiations from quark matter in the QGP and mixed phase. HM represents the radiations from the hadronic matter in the mixed and hadronic phase. T_0 is the initial temperature of the system and τ_0 is the initial time.

1.4.4 Azimuthal Anisotropy or Flow

In the relativistic heavy-ion collisions, when there is a non-central collision, the particles in the overlap region are subjected to the spatial anisotropy. This is because of the almond-shape of the overlap region formed after the collision (see Fig. 1.9). The particles which are along the short axis are subject to the more pressure gradient as compared to those along the long axis. As a result, the initial spatial anisotropy is converted

into the anisotropy in the momentum space. This momentum anisotropy will reflect the time evolution of pressure gradients generated in the system at very early time [32, 33]. Thus, the collective transverse expansion or *flow* of the produced particles can provide

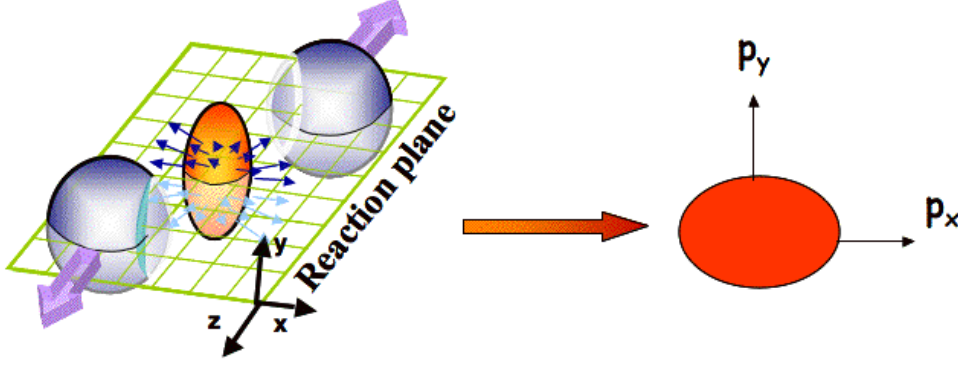


Figure 1.9: Schematic diagram showing the initial spatial anisotropy created after the non-central heavy-ion collision, converted into the anisotropy in momentum space.

information of the creation of a hot and dense system or QGP, formed very early in the non-central collisions [34].

The anisotropy in the momentum space can be quantified by studying the azimuthal distribution of produced particles with respect to the *reaction plane*. The reaction plane is a plane spanned by the beam direction and the direction of the impact parameter. The azimuthal distribution of the produced particles can be decomposed into the Fourier series:

$$E \frac{d^3 N}{d^3 p} = \frac{1}{2\pi} \frac{d^3 N}{p_T dp_T dy} \left(1 + \sum_{n=1}^{\infty} 2v_n \cos(n[\phi - \Psi_r]) \right) \quad (1.9)$$

where Ψ_r is the reaction plane angle. The zeroth harmonic in the above Fourier decomposition represents the radial flow, first harmonic (v_1) is called the directed flow and the second harmonic (v_2) is called the elliptic flow.

1.4.4.1 Directed Flow

Directed flow describes collective side-ward motion of the produced particles and nuclear fragments. It carries the information of the very early stages of the collision [35]. A first order phase transition is associated with the presence of ‘softest point’ in the equation of state (EOS) and in the transition region, the tendency of matter to expand is reduced [36,

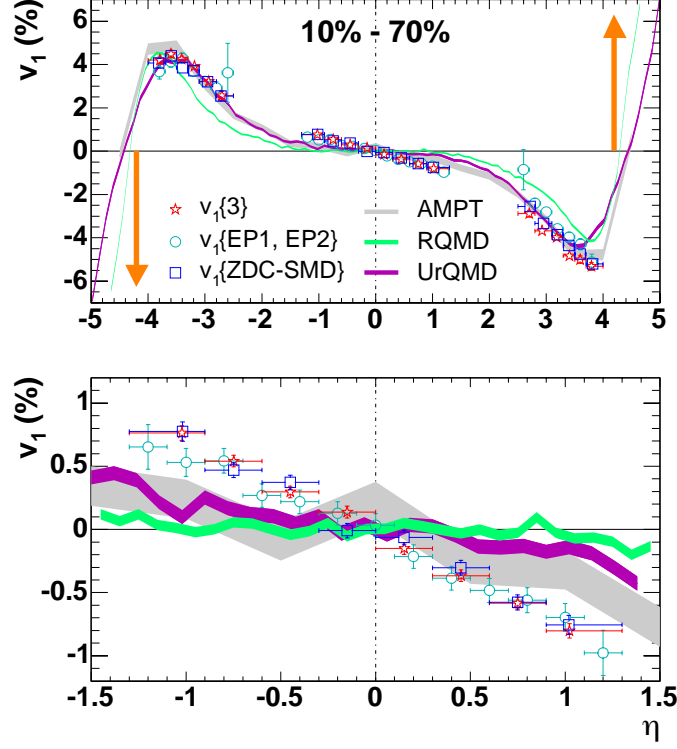


Figure 1.10: Top panel: Directed flow of charged particles as a function of pseudorapidity measured in STAR experiment [43]. Lower panel: mid-pseudorapidity region shown in more detail.

37]. It was proposed that the softening of equation of state can be deduced experimentally by observing a minimum in the directed flow as a function of beam energy [38, 39]. It was suggested that the softening of EOS, which shows a distinct flow pattern, is due to the possible formation of QGP [40]. Also the hydrodynamic calculations assuming QGP show that the directed flow when plotted as a function of rapidity, crosses zero three times around midrapidity, displaying a *wiggle* shape which is predicted to occur in the close-to-central collisions. It is shown in Ref. [41] that the wiggle in $v_1(y)$ could be produced by a tilted, ellipsoidally expanding fluid source with QGP. The magnitude of $v_1(y)$ becomes large when the source is more tilted. However, the RQMD (Relativistic Quantum Molecular Dynamics) model calculations also describe the wiggle shape [42] (see Fig. 1.10). RQMD model is a microscopic nuclear transport model which does not assume the formation of QGP. The wiggle predicted by this model appears in peripheral and mid-central collision events.

Figure 1.10 shows the charged particle v_1 as a function of pseudorapidity, η , for 10–70% collision centrality in Au+Au collisions at $\sqrt{s_{NN}} = 62.4$ GeV [43]. The results are shown for three different methods employed to calculate v_1 , which are observed to be consistent with each other. Also shown are the results from the AMPT [44], RQMD [35] and UrQMD [45] model calculations for same collision energy, system and centrality. The arrows in the upper panel indicate the direction of flow for spectator neutrons. It is found that the models under-predict the charged particles v_1 around mid-pseudorapidity (see lower panel), but are in good agreement for higher $|\eta|$. It can be seen that no apparent wiggle structure, as discussed above, is observed within the measured pseudorapidity range for this data set.

1.4.4.2 Elliptic Flow

Elliptic flow is expected to develop early in the collision and survives the hadronization, hence the hadron v_2 measurements carry the information from the partonic and hadronic level of the collision [46]. Elliptic flow is “self-quenching” [35, 47], and any flow anisotropy measured in the final state must have been generated early when the collision fireball was still spatially deformed. If the elliptic flow does not develop early, it will never develop at all. It thus reflects the pressure and stiffness of the equation of state during the earliest collision stages [35, 47–49]. The advantage in having the elliptic flow observable as a QGP signature (in contrast to many other signatures) is it can be easily measured with high statistical accuracy since it affects all the *final* state particles.

Elliptic flow results from the STAR show that the elliptic flow as a function of p_T follow distinct curves for mesons and baryons [50, 51]. STAR also reported a non-zero elliptic flow for strange baryons (Ω , Ξ , Λ) and mesons (K_S^0) [50, 51]. In this scenario, where multi-strange baryons are less affected by the hadronic stage [52] and where v_2 develops primarily at the early stage of the collision [47, 53], the large v_2 of multi-strange baryons shows that the partonic collectivity is generated at RHIC.

Figure 1.11 shows very interesting result for elliptic flow which is called the constituent quark scaling. In this figure, n_q -scaled v_2 is plotted as a function of n_q -scaled p_T for π , K_S^0 , p , Λ , Ξ , and Ω . We observe that all hadrons except for pions, fall on a

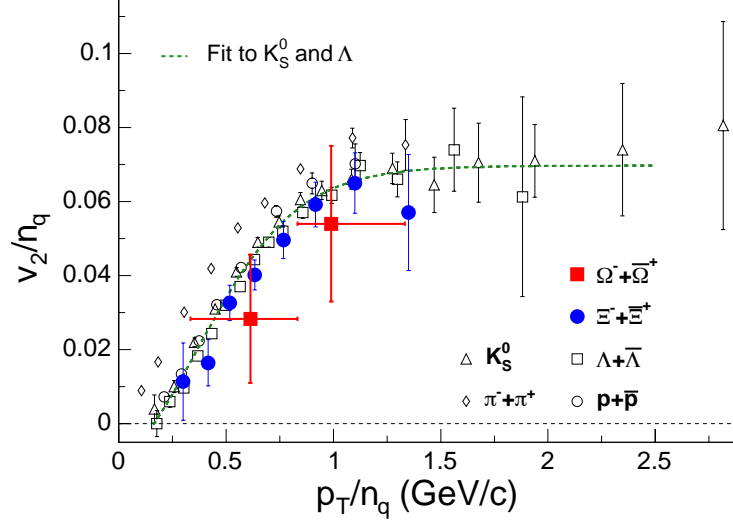


Figure 1.11: v_2 scaled by number of quarks (n_q) as a function of p_T scaled by n_q for various particles measured in the STAR experiment [50].

common curve. This suggests that partonic degrees of freedom are the constituent quarks. In addition, the good agreement for $p(ud)$, $\Lambda(uds)$, $\Xi(dss)$, and $\Omega(sss)$ suggests that s quark flows similarly to u , d quarks.

1.4.5 High p_T probes

Highly energetic partons when propagating through a dense medium lose energy via the two phenomena - collisional energy loss due to elastic scattering, and multiple scattering and induced gluon radiation [54]. It was proposed that the energy loss of partons in QGP is much higher than that in hadronic matter [55]. This phenomenon leads to the *jet quenching* [56, 57], which is defined as the suppression of high p_T hadron yields in nucleus-nucleus (e.g. Au+Au) collisions relative to that in a $p + p$ collision scaled by the number of elementary nucleon-nucleon collisions. The observable used to measure such an effect is called the Nuclear Modification Factor (R_{AA}). It can be given as -

$$R_{AA} = \frac{d^2 N^{AA}/dp_T d\eta}{T_{AA} d^2 \sigma^{NN}/dp_T d\eta} \quad (1.10)$$

where $T_{AA} = \langle N_{\text{bin}} \rangle / \sigma_{\text{inel}}^{NN}$ from a Glauber calculation accounts for the nuclear collision geometry.

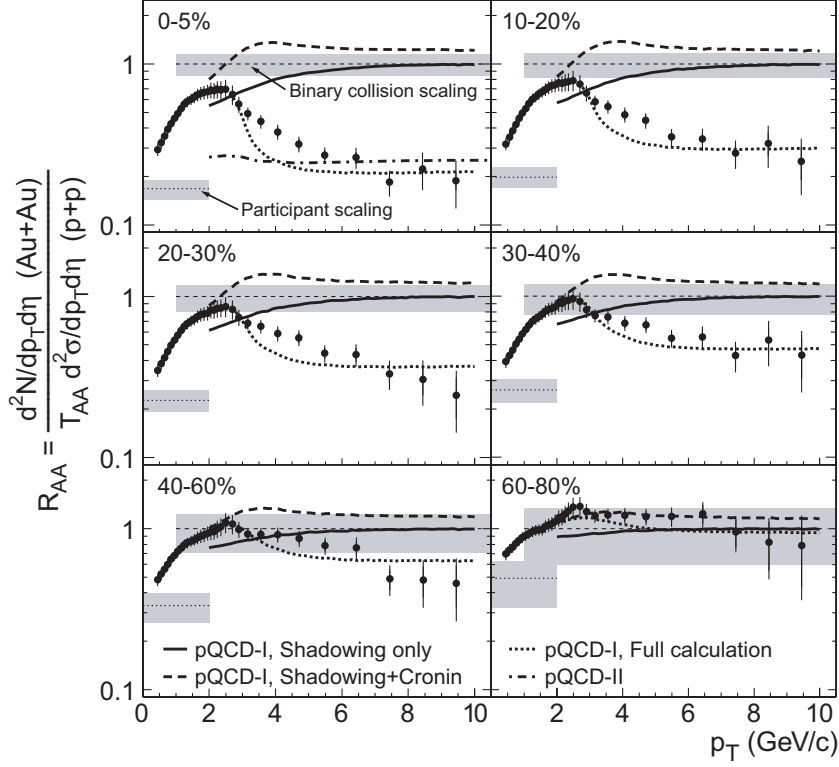


Figure 1.12: $R_{AA}(p_T)$ for charged hadrons for different centralities as measured in STAR experiment [58].

Figure 1.12 shows the measurement of $R_{AA}(p_T)$ for unidentified charged hadrons for different collision centralities in Au+Au collisions at STAR experiment [58]. We observe that for $6 < p_T < 10$ GeV/c, $R_{AA}(p_T)$ is suppressed for each collision centrality (except peripheral collisions). However, $R_{AA}(p_T)$ is much more suppressed (by a factor of 4-5) in central Au+Au relative to $p + p$ collisions. As can be seen from the figure, the Cronin enhancement and shadowing alone cannot explain the suppression, which is reproduced only if parton energy loss in dense matter is included. The suppression of $R_{AA}(p_T)$ at high p_T was predicted to be one of the signature of QGP formation [56, 59]. The peripheral $R_{AA}(p_T)$ is in agreement with $p + p$ measurement indicating that strong medium effects are only taking place in central collisions.

Partonic energy loss is also observed by using two particle azimuthal correlations. During the early stage of the collision, hard scattering of partons results in the production of jets and di-jets. *Jet* is a localized collection of hadrons which come from a fragmented

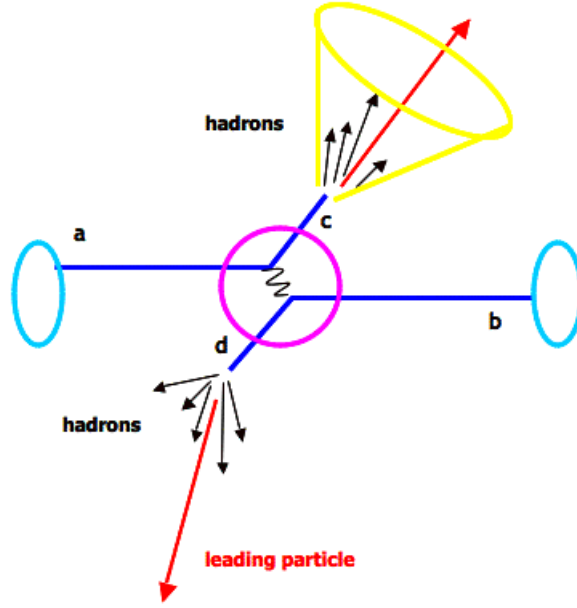


Figure 1.13: Schematic diagram showing jets produced from hard scattering.

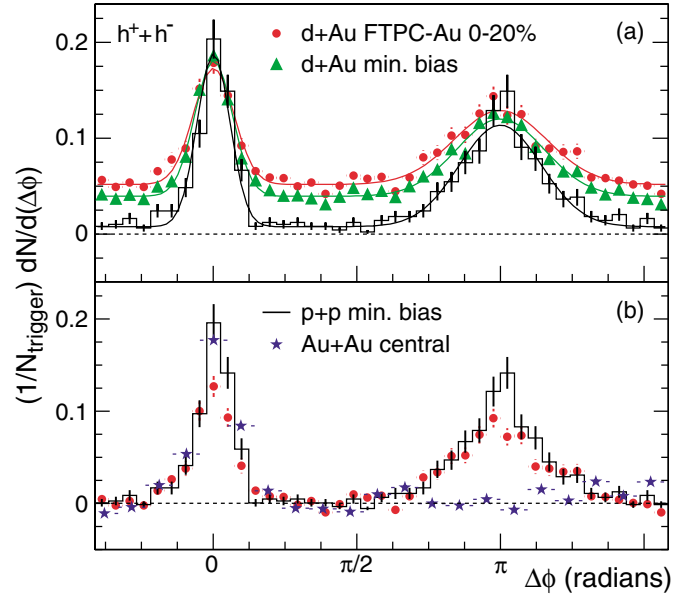


Figure 1.14: Jet azimuthal correlations for Au+Au, d+Au and $p+p$ collisions at $\sqrt{s_{NN}} = 200$ GeV measured in STAR experiment [60].

parton. Figure 1.13 shows a schematic diagram of a hard scattering process with the presence of a medium. The scattered partons will fragment into many co-moving hadrons via the processes of jet fragmentation. Ideally due to momentum conservation the total transverse momentum of all produced hadrons in the center of mass should be equal to zero. If we formed a di-hadron correlation function in $\Delta\phi$, we expect a peak at zero which represents the same side correlations (correlations within the same jet cone) and another peak at 180° which represents the away side correlations (correlation between two different jet cones).

Figure 1.14 shows the jet azimuthal correlations in Au+Au, d+Au and $p+p$ collisions at $\sqrt{s_{NN}} = 200$ GeV, as measured by STAR experiment [60]. The upper panel (a) shows the distributions for central and minimum bias d+Au collisions, and the lower panel (b) shows these distributions for the central Au+Au and minimum bias $p+p$ collisions. In central Au+Au collisions, it is found that the away side correlations are totally quenched, whereas large away side correlations exist for d+Au and $p+p$ collisions. These measurements indicate that the medium created in central Au+Au collisions causes a strong suppression effect on the away side correlation. The suppression of away side correlations is simply due to the fact that particles emitted on the away sides always need to travel a longer distance through the medium compared to the same side particles. Such a geometry effect is confirmed by measuring the difference in suppression between particles close to the reaction plane (in plane) and perpendicular to the reaction plane (out of plane) [61]. The conclusion from the high p_T probes at RHIC is that the suppression is a final state effect and is due to the medium induced energy loss. However, if both the $p_T^{\text{trig.}}$ and $p_T^{\text{assoc.}}$ thresholds [62] are increased, away-side partner fragmenting as in vacuum can be recovered.

1.4.6 Hanbury Brown-Twiss (HBT) Effect

Equation of state of nuclear matter is a key point in further understanding of the properties of QGP since it directly provides the relationship between the pressure and energy at a given net-baryon density. Phase transitions from hadronic degrees of freedom (or hadron gas) to the quark-gluonic degrees of freedom (or QGP) require changes in the underlying

equation of state [63]. The information of the QCD equation of state can be extracted from the collective dynamics studies of heavy-ion collisions. Lattice QCD simulations suggest that the speed of light (c_s) is expected to reach a minimum near the critical temperature, T_c and then increase in the hadronic gas domain. At T_c , the equation of state is expected to be softest [64]. If the matter is produced near this point, it will expand slowly due to internal pressure which results in the increased lifetime of the emission source or fireball [65]. So it is important to know about the space-time configuration of the source or fireball created in the high-energy heavy-ion collisions and system lifetime of the nuclear collisions. The technique used to extract information about the space-time configuration of the source is called the *Hanbury Brown-Twiss (HBT)* effect. This technique is based on the two-particle intensity interferometry techniques and was first applied by Robert Hanbury Brown and Richard Twiss, in astrophysics to measure sizes of stars [66]. Later on, HBT became a very useful method to understand the crucial mechanisms and equation of state of the particle emitting source [67] in relativistic heavy-ion collisions, where the QGP is expected to be formed.

The observable used to measure the prolongation of the lifetime of fireball (or as signature of QGP) is the ratio of the HBT radii R_{out} (R_O) and R_{side} (R_S). These radii are obtained from the inverse of widths of the two-particle correlation functions in the outward and the side-ward directions, respectively. It is proposed that the ratio $R_{\text{out}}/R_{\text{side}}$ will be enhanced in case of first order phase transition with respect to the ideal gas case, where there is no such transition [65]. In heavy-ion collisions, the HBT correlation functions are mainly studied with pions (most abundantly produced) and direct photons (carry the initial information of collision system).

Figure 1.15 shows the ratio R_O/R_S as function of lab frame energy (E_{lab}) for negatively charged pions [68]. The NA49 data are indicated by solid stars. UrQMD cascade calculation is shown by dotted line. Hybrid model calculations with equation of state of Hadron Gas (HG), Bag Model (BM), and Chiral + HG (CH), with Hadronic rescattering and Resonance decays (HR) are shown by lines with solid symbols. The HG equation of state (HG-EoS) is shown for various freeze-out criteria with HR and without HR by dashed lines with open symbols. The k_T bin chosen is 200–300 MeV/ c . It is clearly seen

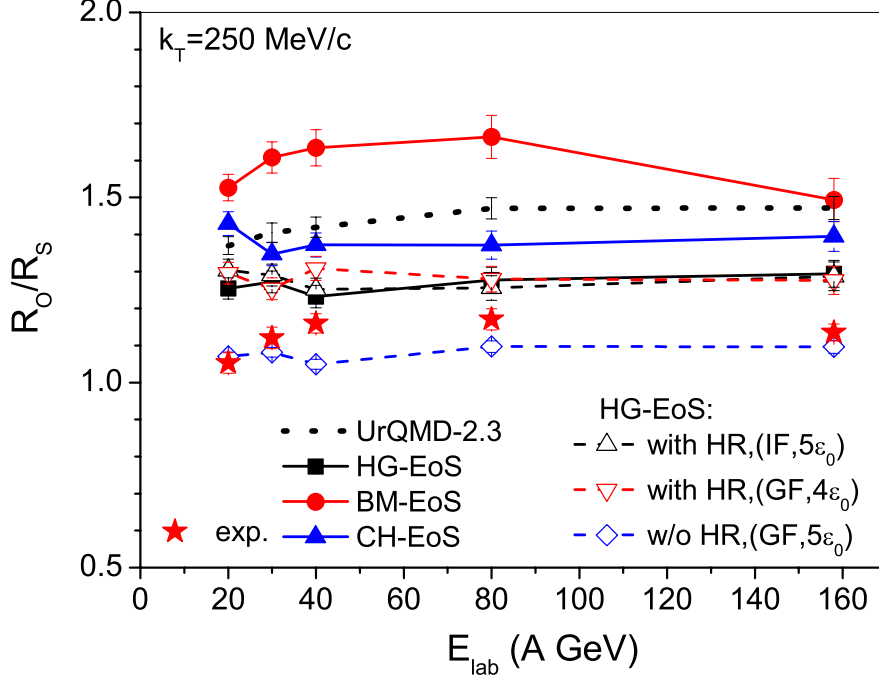


Figure 1.15: Ratio R_O/R_S as function of lab frame energy (E_{lab}) for negatively charged pions as source [68].

that the ratio R_O/R_S is sensitive to the equation of state, but not to the HG-EoS with different freeze-out prescriptions when HR is included (open triangles and open inverted triangles). With increasing latent heat which corresponds to softness of equation of state, the ratio R_O/R_S is increased. The “excessively” large latent heat in BM-EoS results in a long duration time of the pion source and hence a large R_O/R_S ratio. The chiral equation of state (CH-EoS) exhibits a lower R_O/R_S ratio because the first order phase transition is less pronounced. The calculation with HG model (line with solid squares) leads to smallest R_O/R_S ratio due to the most stiffest equation of state among the three cases. The result of the cascade calculation lies between the CH and BM models, which implies a relatively soft equation of state.

1.4.7 Event-by-Event Fluctuations and Correlations

The event-by-event fluctuations of suitably chosen observables in heavy-ion collisions can provide information about the thermodynamic properties of the hadronic system at freeze-

out [69]. As discussed earlier, the lattice QCD calculations suggest a phase transition in strongly interacting matter with the increase in number of effective degrees of freedom [70]. Fluctuations are very sensitive to the nature of the transition. For example, specific heat diverges at the second order phase transition, and the fluctuations decrease drastically if the matter freezes out at critical temperature, T_c [69, 71–73]. It has been proposed that the temperature fluctuation is related to the heat capacity [71, 72] via

$$\frac{\langle(\Delta T)^2\rangle}{T^2} = \frac{1}{C_V(T)}, \quad (1.11)$$

and can tell about *thermodynamic* properties of the matter at freeze-out. Furthermore, Mrówczyński has proposed that the event-by-event fluctuations of the particle number are related to the compressibility of hadronic matter at freeze-out [74]. The mean transverse momentum ($\langle p_T \rangle$) in an event could provide information about specific heat as explained below. One can measure the $\langle p_T \rangle$ of the charged particles in each event in an ensemble. Since the average transverse momentum of particles from an ensemble of events reflects (although does not equal) the temperature of the ensemble, one can use $\langle p_T \rangle$ of particles in a single event as a reflection of temperature of a single event and by using Eq. (1.11), can have the idea of C_V .

Fluctuations involve two components, statistical and non-statistical (or dynamic). Statistical fluctuations arise from the stochastic nature of the particle production and detection processes. The dynamic fluctuations arise due to correlations in various particle production processes. Possible observation of dynamic fluctuations associated with the phase transition would give direct information about the order of transition and the effective degrees of freedom in the earlier phase [69]. There are numerous observables which can be used to measure dynamical p_T fluctuations in high-energy heavy-ion collisions. A natural one is the distribution of the average transverse momentum of the events defined as [75]

$$\langle p_T \rangle = \frac{1}{N} \sum_{i=1}^N p_{T_i}, \quad (1.12)$$

where N is the multiplicity of accepted particles in a given event and p_{T_i} is the transverse momentum of the i^{th} particle. The distribution of $\langle p_T \rangle$ is usually compared to the

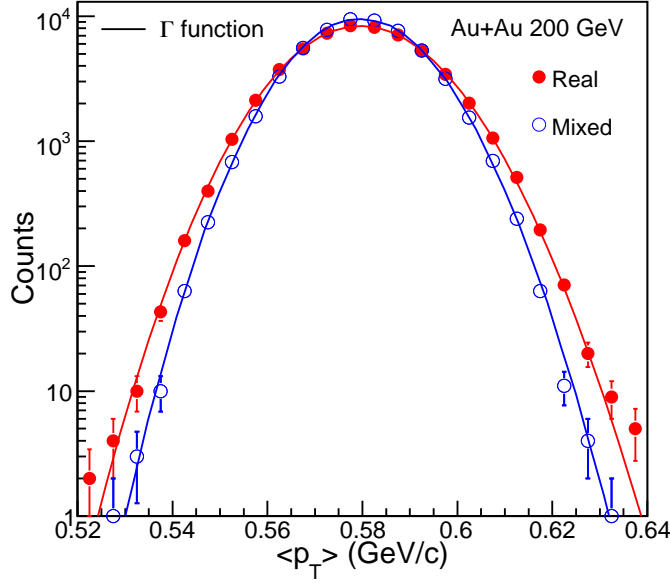


Figure 1.16: Event-wise mean p_T distribution for top central Au+Au collisions at $\sqrt{s_{NN}} = 200$ GeV measured in STAR experiment [76].

corresponding distribution obtained for “mixed events” in which the particles are independent from each other and follow the experimental inclusive spectra (the multiplicity distribution for mixed events is the same as for the data). A difference between the two distributions signals the presence of dynamical fluctuations. The STAR experiment reported finite dynamical fluctuations present in the data for Au+Au collisions at $\sqrt{s_{NN}} = 20, 62.4, 130$ and 200 GeV [76]. Figure 1.16 shows the event-by-event $\langle p_T \rangle$ distribution for Au+Au collisions at $\sqrt{s_{NN}} = 200$ GeV. The lines are the gamma distributions. It can be clearly seen that the distribution for data are broader as compared to those for mixed events, indicating the presence of dynamic fluctuations in the data. It is proposed that first increasing and then saturating trend of p_T fluctuations and $\langle p_T \rangle$, as a function of number of participating nucleons could be related to the phenomena associated with QCD transitions and onset of thermalization [77]. The dynamical fluctuations can be analyzed by using two-particle transverse momentum correlations [76]. It is proposed that the non-monotonic change in p_T correlations as a function of centrality and/or as the incident energy can be treated as a signal of QGP [78].

1.5 Photon Multiplicity Measurements

Most of the studies in high-energy heavy-ion collisions have been carried out with charged particle measurements [79]. Since it is difficult to measure precisely the photon distributions, there are very few measurements of photon multiplicity reported earlier [80, 81]. However, photon multiplicity as an additional observable will definitely provide a better understanding to the well established methods of charged hadrons measurements. Photon multiplicity is measured using the Photon Multiplicity Detector (PMD) [82]. Photon multiplicity and pseudorapidity distributions have been obtained previously in experiments at CERN at SPS. Presently, PMD is installed at STAR experiment at RHIC. In ALICE experiment at CERN, PMD is now being installed and will provide further understanding of the nucleus-nucleus collisions at such a high-energy ($\sqrt{s_{NN}} = 5.5$ TeV).

Various physics goals which can be achieved by using observables from PMD are discussed below. PMD is helpful in the determination of reaction plane and probes of thermalization via studies of azimuthal anisotropy and flow. Earlier, we have mentioned that azimuthal anisotropy could be a possible signature of the QGP. It is suggested that if flow occurs in the plasma state, then the subsequent hadronization may affect the kinematic quantities of different particle species differently. It is therefore desirable to measure the azimuthal anisotropy of different particle species in the final state. It is advantageous to study the event shapes with photons because their transverse distribution and that of the parent pions is not affected by the final-state Coulomb effects. Photon multiplicity measurements using a preshower PMD have already been used to study collective flow at the SPS [83] and RHIC energies [84] using the Fourier expansion technique.

In the QGP scenario, chiral symmetry is proposed to be restored. After the initial stage of the collision, the system cools and expands leading to normal QCD vacuum in which the chiral symmetry is spontaneously broken. During this process, a metastable state may be formed in which the chiral condensate is disoriented from the true vacuum direction. This transient state would subsequently decay by emitting coherent pions within finite sub-volumes or domains of the collision region [85]. This possibility of formation of disoriented chiral condensate (DCC) would lead to a large imbalances in the production

of charged and neutral pions. The primary signature of DCC is a large event-by-event fluctuation in photon to charged-particle multiplicity by measuring photons and charged particles in a common coverage. Some of the interesting observations of the photon multiplicity are discussed in the following subsections.

1.5.1 Photon Pseudorapidity Distribution

High-energy heavy-ion collisions lead to the production of large number of particles and measuring these produced particles is one of the major challenges of this field. One convenient way to measure the particles and to describe the heavy-ion collisions is measuring the particle density in rapidity (or pseudorapidity). Studying particle density directly reflects how much of the initial beam energy can be converted to new particles and it is therefore directly related to the stopping mechanism of the initial protons and nucleons. Thus, the particle multiplicity contains information about the entropy of the system and the gluon density in the first stage of the collision. There have been measurements of charged particle pseudorapidity distributions ($dN_{\text{ch}}/d\eta$), and this motivated people to understand the photon pseudorapidity distributions ($dN_{\gamma}/d\eta$) in heavy-ion collisions and see how these compare with charged particles.

1.5.2 Scaling with Number of Participants

The scaling of particle multiplicity with average number of participating nucleons ($\langle N_{\text{part}} \rangle$) suggests that the particle production at RHIC is dominated by soft processes, whereas scaling with average number of binary collisions ($\langle N_{\text{bin}} \rangle$) indicates the onset of hard processes (pQCD jets). It was first shown by PHENIX experiment that the charged particle production scales with a combination of $\langle N_{\text{part}} \rangle$ and $\langle N_{\text{bin}} \rangle$ [86]. The PHOBOS experiment showed that such scaling has a pseudorapidity dependence [87, 88]. Figure 1.17 (left panel) shows detailed study of the centrality dependence of the charged particle density from PHOBOS experiment. The panel (a) shows total charged particles detected within the range $|\eta| < 5.4$ for Au+Au collisions at $\sqrt{s_{NN}} = 200$ GeV. Panels (b)-(f) show the $\langle N_{\text{part}} \rangle$ dependence of $dN_{\text{ch}}/d\eta$ per participant nucleon pair ($\langle N_{\text{part}}/2 \rangle$), plotted for five pseudorapidity bins ranging from $|\eta| < 1$ to $5 < |\eta| < 5.4$. The charged particles

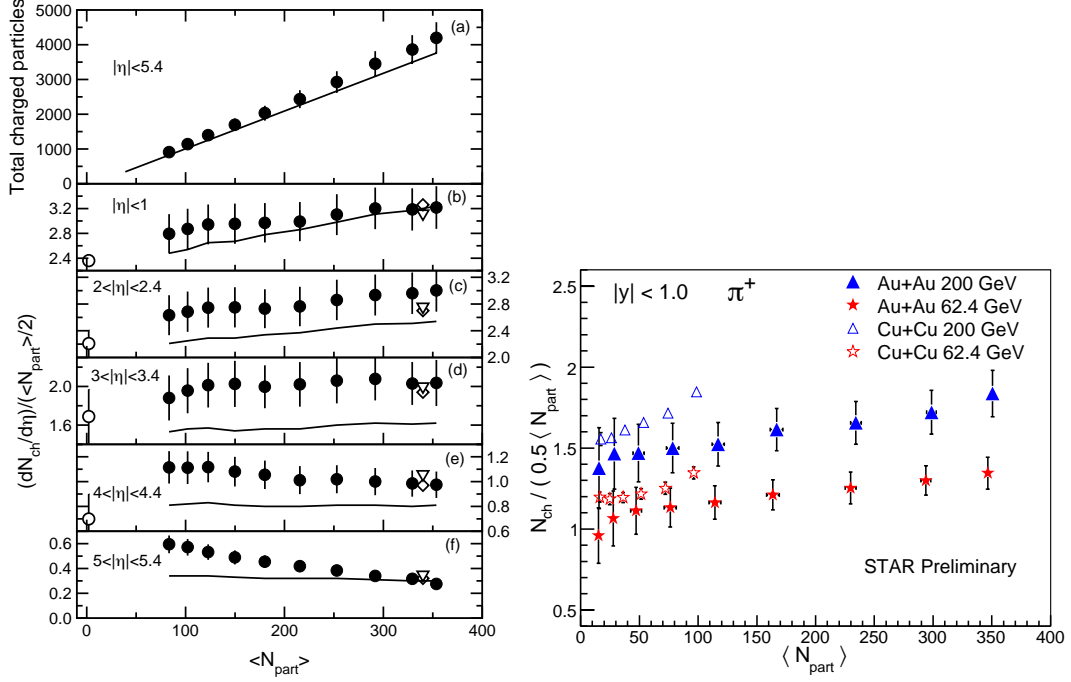


Figure 1.17: Left panel: (a) Total number of charged particles detected within the range $|\eta| < 5.4$, and (b)-(f) Centrality dependence of $dN_{ch}/d\eta$ for different ranges of $|\eta|$, for Au+Au collisions at $\sqrt{s_{NN}} = 200$ GeV [87]. Right panel: Number of produced pions scaled by $\langle N_{part}/2 \rangle$ as a function of $\langle N_{part} \rangle$ for Au+Au and Cu+Cu collisions at $\sqrt{s_{NN}} = 62.4$ and 200 GeV at midrapidity measured at RHIC.

scale with the $\langle N_{part} \rangle$ at forward rapidity. Furthermore, Fig. 1.17 (right panel) shows the number of pions divided by $\langle N_{part}/2 \rangle$ as a function of $\langle N_{part} \rangle$ for Au+Au and Cu+Cu collisions at $\sqrt{s_{NN}} = 62.4$ and 200 GeV at midrapidity. It is observed that number of pions per average number of participating nucleon pair increases with increase in $\langle N_{part} \rangle$ at midrapidity. It is also known that the photons which are measured in the PMD, come dominantly from the pion decay. In view of these observations, it will be of interest to see the $\langle N_{part} \rangle$ dependence of photons, which are measured at forward rapidity in PMD. Indeed the photons scale with the $\langle N_{part} \rangle$ at forward rapidity as reported in the Refs. [89, 90]. Clearly the particle production mechanism is different in different pseudorapidity regions.

1.5.3 Longitudinal Scaling

At RHIC, the longitudinal scaling of charged particles has been observed in heavy-ion collisions. Particles near beam and target rapidity were proposed to be governed by the

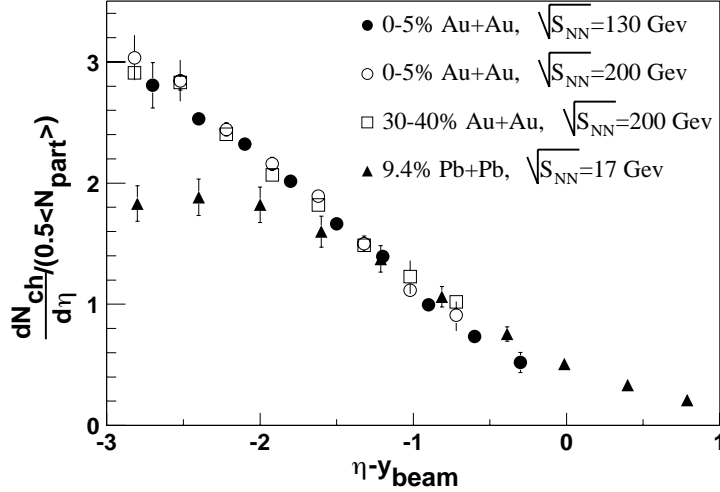


Figure 1.18: Charged particle multiplicities normalized to the number of participant nucleon pairs as a function of $\eta - y_{\text{beam}}$ for different collision centralities and different center of mass energies [94].

“limiting fragmentation hypothesis” [91]. In this model, the momentum distribution of particles of species in the rest frame of one of the original colliding hadrons (commonly denoted with a prime to distinguish it from the center-of-mass frame), Ed^3N/dp'^3 , or equivalently $d^3N/p_T dy' dp_T d\phi$, becomes energy-independent at high enough collision energy. The basic concept is that projectile hadron when seen from the target, appears to be Lorentz-contracted into a very narrow strongly-interacting pancake (as discussed earlier). When this projectile passes through the target, the interaction leaves behind a state which does not depend on the energy or even identity of the projectile. This state then fragments into a final state distribution of particles, Ed^3N/dp'^3 . The produced particles were assumed to be restricted in a rapidity window around $y' = 0$, leading to scarcity of particles at midrapidity in a very high-energy hadron-hadron collisions [92].

At RHIC, it was observed that when charged particle and photon pseudorapidity density, normalized by $\langle N_{\text{part}}/2 \rangle$, are plotted as a function of $|\eta| - y_{\text{beam}}$ (where y_{beam} is beam rapidity), the distributions are independent of beam energy. This is called “longitudinal scaling” at RHIC. The BRAHMS experiment first reported the longitudinal scaling which is independent of both collision centrality and beam energy over a limited range of rapidity [93, 94] (see Fig. 1.18). On the other hand, the PHOBOS experiment observed the

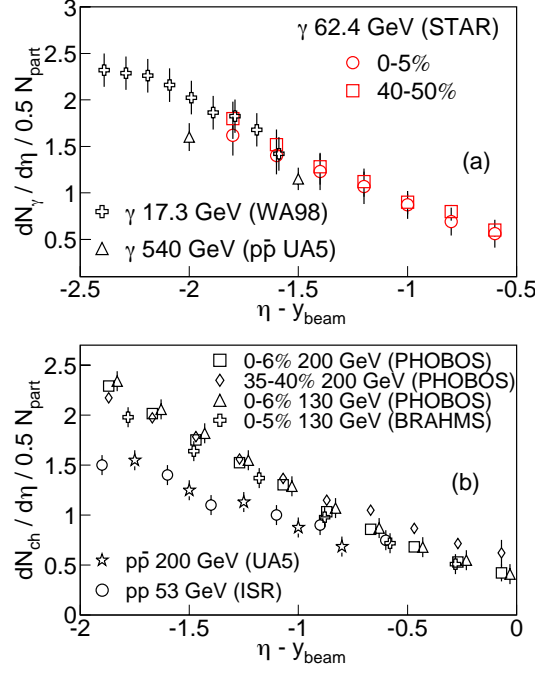


Figure 1.19: (a) Photon pseudorapidity density normalized to the number of participant nucleon pairs as a function of $\eta - y_{\text{beam}}$, for different collision energies and centralities [89]. Also shown $dN_\gamma/d\eta$ for $p + \bar{p}$ collisions. (b) Same as (a) but for charged particles.

longitudinal scaling which was found to be broken when studied as a function of collision centrality [87, 88] (see Fig. 1.19, bottom panel). The longitudinal scaling when studied for photons, was found to be independent of collision centrality and beam energy [89, 90] (see Fig. 1.19, top panel).

1.6 Transverse Momentum Spectra

Identified particle spectra in transverse momentum is very useful in extracting initial conditions like chemical and kinetic freeze-out properties of high-energy heavy-ion collisions. In hydrodynamics, a given initial condition is mapped to final spectra that depends on the equation of state. Transverse momentum (p_T) spectra are usually studied by calculating the invariant cross section given by:

$$E \frac{d^3 N}{dp^3} = \frac{1}{2\pi p_T} \frac{d^2 N}{dp_T dy}, \quad (1.13)$$

where E is the particle energy and $d^2N/dp_T dy$ represents an event-wise yield density.

The p_T spectra can be characterized by extracting yield (dN/dy), inverse slope parameter (T) and average transverse momentum ($\langle p_T \rangle$) or average transverse mass ($\langle m_T \rangle$). These quantities are discussed in the following subsections.

1.6.1 Yield and Ratios

The inclusive particle yield (dN/dy) at midrapidity for each identified particle is calculated from the available measured p_T range and extrapolating up to the unmeasured region. Yields are very useful in understanding the dynamics of collisions. For example, low energy collisions are dominated by the incoming nuclei which undergo a significant stopping in the collision zone. This will result in higher yield of nucleons (e.g. protons) at midrapidity at low energy. On the other hand, at higher energies, the nuclei become more transparent and contribution due to stopping will be less. Yields are used to obtain the particle ratios

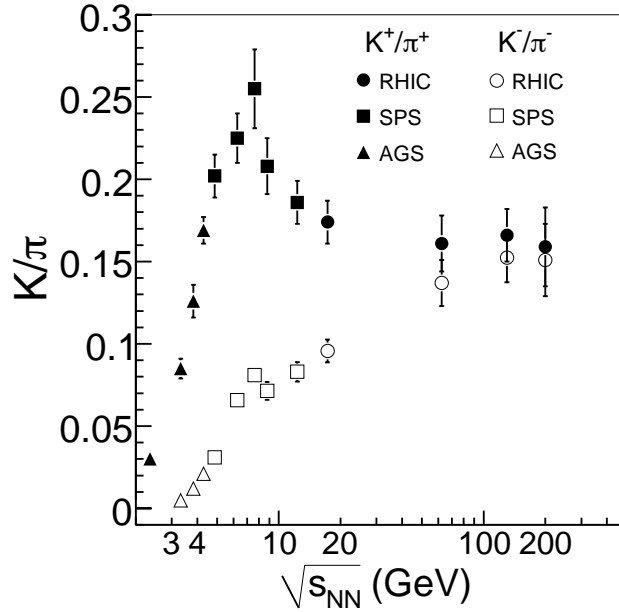


Figure 1.20: Beam energy dependence of K/π ratio at midrapidity in heavy-ion collisions. The AGS, SPS, and RHIC data points are from the Refs. [95], [96], and [97], respectively.

which are useful in understanding the mechanisms involved in the particle production in heavy-ion collisions. In heavy-ion collisions, various ratios have been studied at different

center of mass energies at AGS, SPS, and RHIC. The K/π ratio at midrapidity is of interest as it expresses the enhancement of strangeness production relative to non-strange hadrons in heavy-ion collisions compared to $p + p$ collisions. The K^+/π^+ ratio shows a very interesting behavior as function of beam energy as shown in Fig. 1.20. It increases as function of collision energy, then decreases after $\sqrt{s_{NN}} = 7.7$ GeV, and gets saturated with increasing collision energy. This is very interesting observation first observed by the NA49 experiment at SPS [96]. The region where maxima observed, is generally referred to as “horn”. It has been proposed that the beam energy dependence of K/π ratio can be explained if the relevant degrees of freedom are assumed to be quarks and gluons [98]. However, various hadron resonance gas models could also explain the beam energy dependence of K/π ratio [99].

1.6.2 Average Transverse Momentum and Mass

Changes in the measured spectral shapes by collision type, energy and centrality can be characterized by the average transverse momentum. It can be obtained as:

$$\langle p_T \rangle = \frac{\int \frac{1}{2\pi p_T} \frac{dN}{dy dp_T} \times 2\pi \times p_T^2 \times dp_T}{\int \frac{1}{2\pi p_T} \frac{dN}{dy dp_T} \times 2\pi \times p_T \times dp_T}, \quad (1.14)$$

where the numerical integration goes from 0 to 10 GeV/ c . It has been proposed that the anomalous behavior of the $\langle p_T \rangle$ as a function of measured charged particle multiplicity (N_{ch}) can indicate the phase transition from the hadronic to quark-gluon plasma phase [100]. According to Van Hove [100], charged particle multiplicity is proportional to the entropy. The entropy is created early in the collision at thermalization, and followed by hydrodynamical adiabatic expansion with conserved entropy. The shape of the transverse momentum spectrum carries the combined effect of the temperature in the collision and the expansion of the system. The average transverse momentum increases as a function of charged particle multiplicity. In the phase transition scenario, the entropy is expected to increase but the temperature is expected to remain nearly constant. Accordingly, the $\langle p_T \rangle$ is expected to reach a plateau at large charged particle multiplicities. Figure 1.21 (top panel) shows the $\langle p_T \rangle$ as a function of dN_{ch}/dy for Au+Au collisions at 62.4, 130 and 200 GeV. The minimum bias $p + p$ data and d+Au data are also shown. We observe that $\langle p_T \rangle$

for a given particle species are same within errors at all energies. This suggests similar system evolution for different energies despite different initial conditions (energy density and baryon constant of the collisions zone). It is observed that $\langle p_T \rangle$ for pions increases slightly with centrality for Au+Au collisions. For kaons, protons and anti-protons, the $\langle p_T \rangle$ increases significantly with centrality.

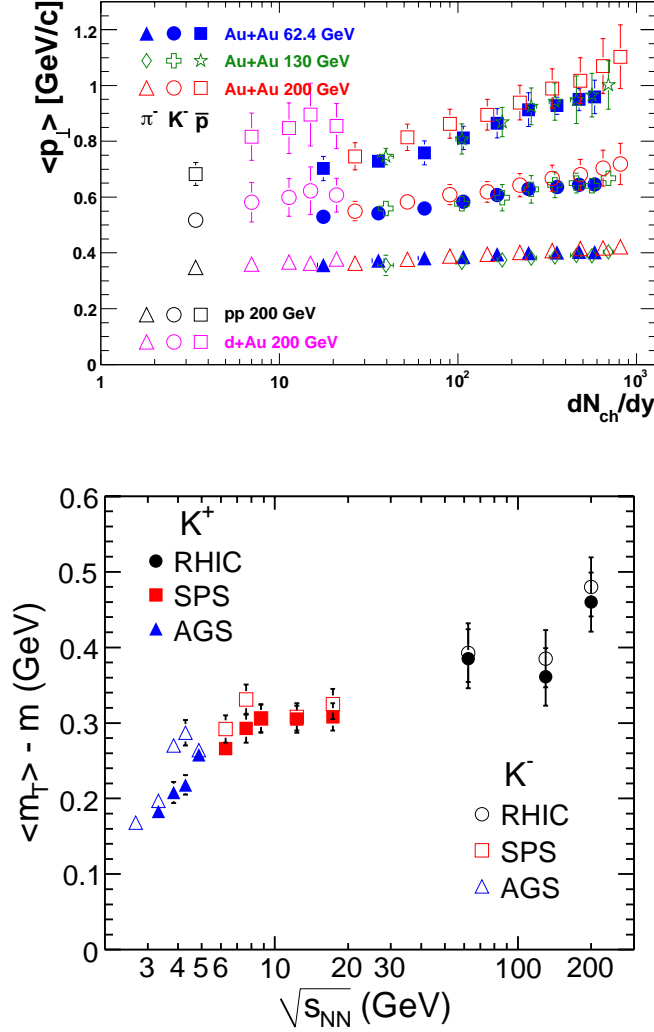


Figure 1.21: Top panel: Mean p_T as a function of dN_{ch}/dy for Au+Au collisions at $\sqrt{s_{NN}} = 62.4, 130$ and 200 GeV [97]. Results from minimum bias $p + p$ and $d+Au$ collisions are also shown. Bottom panel: $\langle m_T \rangle - m$ as a function of center of mass energy for charged kaons [95–97].

To seek a better understanding of spectral shape evolution, it is better to investigate average transverse mass ($\langle m_T \rangle$) rather than $\langle p_T \rangle$ [101]. The average transverse mass is

given by $m_T = \sqrt{p_T^2 + m^2}$, where m is the rest mass of the particle. The spectra can be fitted with the exponential m_T function as given below:

$$\frac{d^2 N}{2\pi m_T dm_T dy} \approx C \cdot e^{-m_T/T}, \quad (1.15)$$

where T is the inverse slope parameter and the average transverse mass is given by:

$$\langle m_T \rangle = T + m + \frac{T^2}{m + T}, \quad (1.16)$$

Figure 1.21 (bottom panel) shows the $\langle m_T \rangle - m$ as a function of center of mass energies for kaons. The data are taken from the Refs. [95–97]. There is a plateau region observed at around SPS energies in this figure which is similar to that observed in the $\langle p_T \rangle$ vs. dN_{ch}/dy plot (top panel). It is proposed that the plateau region occurs at the energies where the transition between confined and deconfined matter is expected to be located [101]. So the observed plateau region in Fig. 1.21 (bottom panel) might indicate the onset of the phase transition. This plateau region observed for kaons seems to increase towards the RHIC energies. For pions, this region is the flattest and for protons it is observed to be increasingly steepest as we go towards the higher energies.

1.6.3 Freeze-Out Properties

We know that the high-energy heavy-ion collisions lead to a fireball in the collision region, which undergo expansion with time. The pressure generated in the fireball during the collision process boosts the produced particle away from the center of the collision. In this process, the particles interact among themselves elastically and in-elastically. This leads to the chemical and thermal equilibrium among the produced particles. Specifically these equilibria are called as “chemical and kinetic freeze-out” in heavy-ion collisions. Chemical freeze-out describes the point where inelastic processes that convert one kind of hadronic species into a different one, cease and the hadron abundances stop changing. Thermal freeze-out defines the point where the momenta of the particles stop changing, i.e. where all types of momentum-changing collisions, elastic and inelastic cease.

The measured particle abundance ratios are fitted using the chemical equilibrium model [102–105]. The model assumes that the system is in thermal and chemical equi-

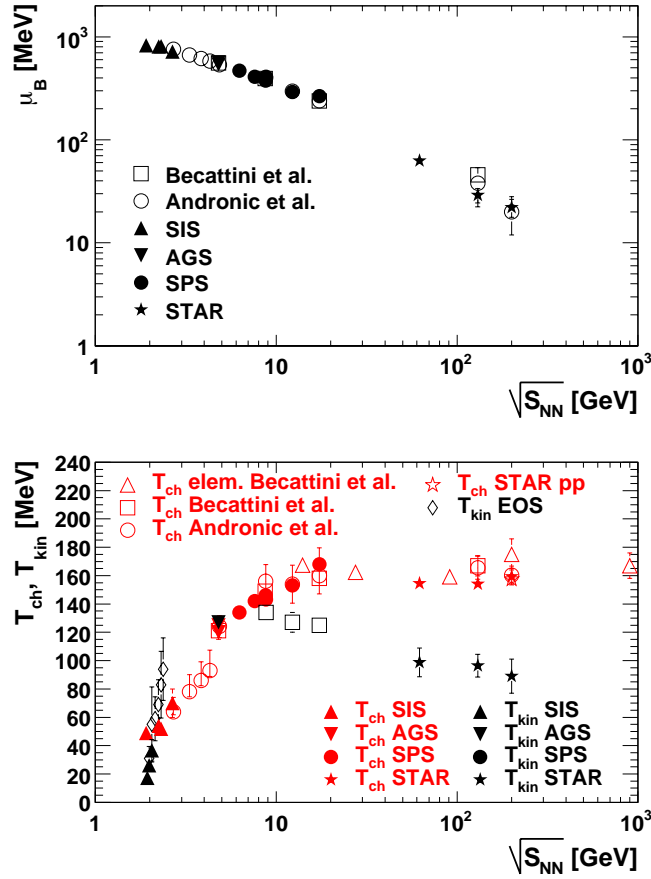


Figure 1.22: Top panel: Baryon chemical potential extracted for central heavy-ion collisions as a function of the collision energy. Bottom panel: The extracted chemical (red points) and kinetic (black points) freeze-out temperatures for central heavy-ion collisions as a function of the collision energy. The figure is taken from the Ref. [97].

librium at that stage. The model fit parameters are the chemical freeze-out temperature (T_{ch}), the baryon and strangeness chemical potentials (μ_B and μ_S), and the *ad hoc* strangeness suppression factor, γ_S .

The p_T spectra of the particles are well described by the hydrodynamics-motivated blast-wave model [33, 106–111]. The blast wave model makes the simple assumption that particles are locally thermalized at a kinetic freeze-out temperature and are moving with a common collective transverse radial flow velocity field. The common flow velocity field results in a larger transverse momentum of heavier particles, leading to the change in the observed spectral shape with increasing particle mass. The measured spectra of all the

particle species are simultaneously fitted with blast wave model. The fit parameters are the kinetic freeze-out temperature (T_{kin}), the average transverse flow velocity ($\langle\beta\rangle$) and the exponent of the assumed flow velocity profile (n).

Figure 1.22 (top panel) shows the baryon chemical potential extracted from chemical equilibrium model fits to central heavy-ion data at various energies. The extracted μ_B falls monotonically from low to high energies. The low value of μ_B at midrapidity at high energy is because fewer baryons can transport over the larger rapidity gap. Fig. 1.22 (bottom panel) shows the evolution of the extracted chemical and kinetic freeze-out temperatures as a function of the collision energy in central heavy-ion collisions. The extracted T_{ch} rapidly rises at SIS and AGS energy range, and saturates at SPS and RHIC energies. This suggests that the central heavy-ion collisions can be characterized by a unique, energy independent chemical freeze-out temperature. The value of T_{ch} at higher energies is close to the phase transition temperature predicted by Lattice QCD [112]. This suggests the collision system at high energies decouples chemically at the phase boundary. On the other hand, the extracted kinetic freeze-out temperature rises at SIS and AGS energies, and decreases at higher energies, especially at RHIC energies. At low energies, the extracted T_{kin} is similar to T_{ch} . This suggests that kinetic freeze-out happens relatively quickly after or concurrently with chemical freeze-out. As the collision energy increases, the two extracted temperatures begin to separate (around $\sqrt{s_{NN}} = 10$ GeV). The T_{ch} increases and T_{kin} decreases thereafter, suggesting that towards the higher energies, T_{kin} occurs long after the T_{ch} . This indicates that there is a longer time during which the particles scatter elastically, building up additional collective motion in the system while it undergoes further expansion and cooling.

1.7 Terminology and Kinematic Variables

High-energy heavy-ion physics is an emerging field which has a unique and new terminology. In this section, we will provide general introduction to the terms and concepts which are commonly used in heavy-ion physics and which will be used in this thesis. In high-energy heavy-ion experiments, two nuclei moving with relativistic energy are collided

with each other. Accordingly, one can define the following terms.

- **Center of Mass Energy ($\sqrt{s_{NN}}$):** This is the total energy created per nucleon in the center of mass frame, when two heavy-ions collide with each other. Suppose in a collider (e.g. RHIC), a Au beam can be accelerated to 100 GeV per nucleon. In the collision of a Au nucleus with another Au nucleus in such a collider, the energy carried by each nucleus is about 100×197 GeV, or 19.7 TeV, and the center of mass energy \sqrt{s} is about 2×197 GeV, or 39.4 TeV. This is in general can be written as $\sqrt{s_{NN}} = 200$ GeV.
- **Event:** When a collision occurs in heavy-ion experiments, it is called an *event*. Each heavy-ion experiment consists of a group of complementary detectors which are centered around the beam crossing point where events occurs.
- **Multiplicity:** The collision of heavy-ions may produce a large number of particles. The number of particles produced in a particular event is called the event's *multiplicity*. Within an experiment there are many individual detectors which are optimized to detect particular types of particles. e.g. some detectors measure charged particles, some may detect neutral particles.
- **Acceptance:** Each detector has a certain area in which it is able to detect the particles. This area is called the *acceptance* of that detector. The probability that a certain particle will reach a detector depends on its acceptance.
- **Efficiency:** *Efficiency* is basically the ratio of number of particles detected by a detector to the number of particles falling within its area.
- **Vertex:** The position of origin of an event is called the event *vertex*. All the produced particles of an event originate from a particular event vertex where the collision has occurred.
- **Momentum, Transverse Momentum, Polar Angle and Azimuthal Angle:** The most convenient coordinate system to describe a collision is often a combination of cylindrical and spherical coordinates. Let us assume an event to be occurred at the

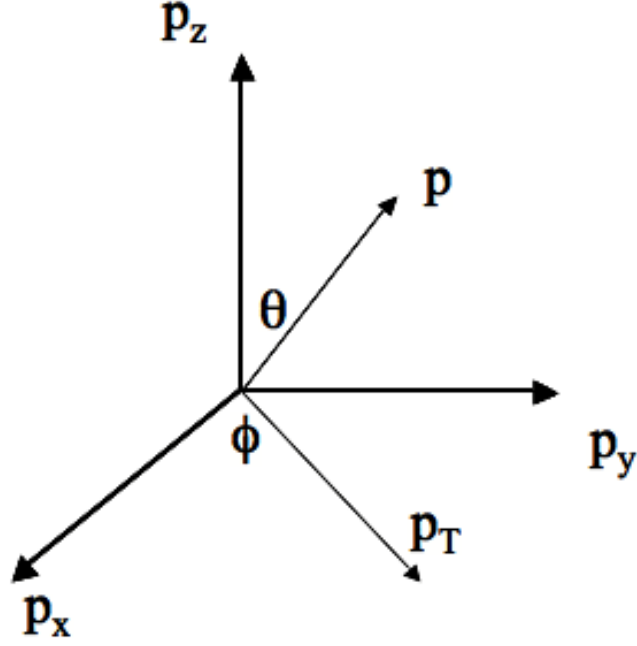


Figure 1.23: Coordinate system describing the heavy-ion collision system.

center of a Cartesian coordinate system. The beam direction is usually along the z -axis. The Fig. 1.23 represents the coordinate system describing a heavy-ion collision. The momentum vector p can be decomposed into two components, *longitudinal* component along the beam axis, and a *transverse* component perpendicular to the beam direction. The x - y plane is represented in cylindrical coordinates as a vector with magnitude p_T , called as *transverse momentum*. The angle made by total momentum vector p with the z -axis is called the *polar angle* (θ) and that made by p_T with the x -axis is called the *azimuthal angle* (ϕ). We can write following relations for these quantities:

$$p_x = p \times \sin \theta \times \cos \phi; \quad (1.17)$$

$$p_y = p \times \sin \theta \times \sin \phi; \quad (1.18)$$

$$p_z = p \times \cos \theta; \quad \text{and} \quad (1.19)$$

$$p_T = \sqrt{p_x^2 + p_y^2}. \quad (1.20)$$

- **Rapidity and Pseudorapidity:** Another useful variable commonly used to describe the kinematic condition of a particle is called the *rapidity variable* (y). The rapidity of a particle is defined in terms of its energy-momentum components:

$$y = \frac{1}{2} \ln \left[\frac{E + p_z}{E - p_z} \right]. \quad (1.21)$$

Rapidity is a dimensionless quantity related to the ratio of the forward light-cone momentum to the backward light-cone momentum. It can be either positive and negative. In the relativistic limit, the rapidity of a particle travelling in the longitudinal direction is equal to the velocity of the particle in units of speed of light. The rapidity of the particle depends on the frame of reference and is additive in nature if one goes from one frame to another.

The calculation of rapidity requires the information of energy and longitudinal momentum. However in many experiments it is only possible to measure angle of the particle relative to the beam axis. So to characterize a particle in that case, a new variable *pseudorapidity* is introduced and is defined as:

$$\eta = -\ln [\tan(\theta/2)], \quad (1.22)$$

where θ is the angle between the particle momentum p and the beam direction z (see Fig. 1.23). In terms of momentum the pseudorapidity can be defined as:

$$\eta = \frac{1}{2} \ln \left[\frac{|p| + p_z}{|p| - p_z} \right]. \quad (1.23)$$

Comparing Eqs. (1.21) and (1.23), it can be seen that $y = \eta$ when the momentum is large or when $E = p$.

1.8 Organization of Thesis

The results presented in this thesis involve the study of various observables to understand the particle production mechanism in high-energy heavy-ion collisions and to study the formation of QGP. In chapter 2, we discuss the details of STAR detector and its subsystems. Chapter 3 presents the details of Photon Multiplicity Detector (PMD) and results

obtained from it using the data from Au+Au and Cu+Cu collisions at $\sqrt{s_{NN}} = 62.4$ and 200 GeV. In chapter 4, we discuss results from the lowest collision energy ($\sqrt{s_{NN}} = 9.2$ GeV) so far at RHIC. In this chapter, we discuss results of identified hadron spectra, ratios, and freeze-out parameters. In addition, we compare these results with different lower and higher collision energies. In chapter 5, the results of transverse momentum fluctuations and correlations for Cu+Cu collisions at $\sqrt{s_{NN}} = 62.4$ and 200 GeV, are discussed. These results are compared with the published results from Au+Au collisions at similar energies. Finally, in chapter 6, we give conclusions.

Bibliography

- [1] J. D. Bjorken and E. A. Paschos, Phys. Rev. **185**, 1975 (1969).
- [2] D. H. Perkins, Introduction to High Energy Physics, Cam. Uni. Press 4th Ed., 2000.
- [3] M. Gell-Mann, Phys. Rev. **125**, 1067 (1962).
- [4] J. P. Blaizot and E. Iancu, Phys. Rept. **359**, 355 (2002).
- [5] J. Adams *et al.* (STAR Collaboration), Nucl. Phys. A **757** 102 (2005);
- [6] T. Ludlam, L. McLerran, (Brookhaven) . 2003. 7pp. Published in Phys.Today 56N10:48-54,2003.
- [7] C. Höhne, Internat. J. Mod. Phys. E **16**, 2419 (2007); Nucl. Phys. News **16**, 1 (2006).
- [8] S. Gottlieb, J. Phys. Conf. Ser. **78**, 012023 (2007).
- [9] USA-NSAC 2007, Long-range plan.
- [10] K. H. Ackermann *et al.*, Nucl. Instr. Meth. A **499**, 624 (2003).
- [11] The NA61/SHINE homepage [<http://na61.web.cern.ch>]; A. Laszlo [NA61/SHINE Collaboration], Nucl. Phys. A **830**, 559C (2009) [arXiv:0907.4493 [nucl-ex]].
- [12] A. N. Sissakian and A. S. Sorin (NICA Collaboration), J. Phys. G **36**, 064069 (2009);
A. N. Sissakian, V. D. Kekelidze and A. S. Sorin (NICA Collaboration), Nucl. Phys. A **827**, 630C (2009).
- [13] B. I. Abelev *et al.* (STAR Collaboration), STAR Internal Note - SN0493, 2009; L. Kumar (for the STAR Collaboration), SQM-2008, QM-2009; L. Kumar (for the STAR

- Collaboration), J. Phys. G: Nucl. Part. Phys. **36**, 064066 (2009); L. Kumar (for the STAR Collaboration), Nucl. Phys. A **830**, 275c (2009).
- [14] T. Biró, P. Levai and B. Müller, Phys. Rev. D **42**, 3078 (1990).
- [15] A. Peshier, B. Kämpfer, O. P. Pavlenko and G. Soff, Phys. Lett. B **337**, 235 (1994).
- [16] F. Karsch, Nucl. Phys. A **698**, 199 (2002).
- [17] J. W. Harris and B. Müller, Ann. Rev. Nucl. Part. Sci. **46**, 71 (1996).
- [18] K. Kajantie and L. McLerran, Ann. Rev. Nucl. Part. Sci. **37**, 293 (1987) and references therein.
- [19] V. Bernard, Quark-Gluon Plasma Signatures, (Editions Frontières, Paris, 1990) and references therein.
- [20] C. P. Singh, Phys. Rep. **236**, 147 (1993) and references therein.
- [21] B. Müller, Rep. Prog. Phys. **58**, 611 (1995) and references therein.
- [22] P. Koch, B. Müller and J. Rafelski, Phys. Rep. **142**, 167 (1986).
- [23] B. I. Abelev *et al.* (STAR Collaboration), Phys. Lett. B **673**, 183 (2009).
- [24] E. Eichten *et al.*, Phys. Rev. D **21**, 203 (1980); C. Quigg and J. L. Rosner, Phys. Rep. **56**, 167 (1979).
- [25] T. Matsui and H. Satz, Phys. Lett. B **178**, 416 (1986); T. Matsui, Zeit. Phys. C **38**, 245 (1988).
- [26] M. C. Abreu *et al.* (NA50 Collaboration), Phys. Lett. B **410**, 327 (1997), M. C. Abreu *et al.* (NA50 Collaboration), Phys. Lett. B **410**, 337 (1997).
- [27] A. Capella, E. G. Ferreira and A. B. Kaidalov, Phys. Rev. Lett. **85**, 2080 (2000) [arXiv:hep-ph/0002300]; N. Armesto, A. Capella and E. G. Ferreira, Phys. Rev. C **59**, 395 (1999) [arXiv:hep-ph/9807258].

- [28] J. Alam, B. Sinha and S. Raha, Phys. Rept. **273**, 243 (1996).
- [29] J. Alam, J. K. Nayak, P. Roy, A. K. Dutt-Mazumder and B. Sinha, J. Phys. G **34**, 871 (2007) [arXiv:nucl-th/0508043].
- [30] M. M. Aggarwal *et al.* (WA98 Collaboration), Phys. Rev. Lett. **85**, 3595 (2000).
- [31] D. K. Srivastava and B. Sinha, Phys. Rev. C **64**, 034902 (2001).
- [32] P. Huovinen, P. F. Kolb, U. W. Heinz, P. V. Ruuskanen and S. A. Voloshin, Phys. Lett. B **503**, 58 (2001);
- [33] D. Teaney, J. Lauret and E. V. Shuryak, arXiv:nucl-th/0110037.
- [34] C. Adler *et al.* (STAR Collaboration), Phys. Rev. Lett. **87**, 182301 (2001); *ibid.* Phys. Rev. Lett. **89**, 132301 (2002); Phys. Rev. Lett. **90**, 032301 (2003); S. S. Adler *et al.* (PHENIX Collaboration), Phys. Rev. Lett. **91**, 182301 (2001); S. Esumi (PHENIX collaboration), Nucl. Phys. A **715**, 599 (2003).
- [35] H. Sorge, Phys. Rev. Lett. **78**, 2309 (1997).
- [36] E. Shuryak and O. V. Zhirov, Phys. Lett. B **89**, 253 (1979).
- [37] L. Van Hove, Z. Phys. C **21**, 93 (1983); K. Kajantie, M. Kataja, L. McLerran and P. V. Ruuskanen, Phys. Rev. D **34**, 2746 (1986); S. Chakrabarty, J. Alam, D. K. Srivastava and B. Sinha, Phys. Rev. D **46**, 3802 (1992).
- [38] L. V. Bravina, N. S. Amelin, L. P. Csernai, P. Levai and D. Strottman, Nucl. Phys. A **566**, 461c (1994); L. V. Bravina, L. P. Csernai, P. Levai and D. Strottman, Phys. Rev. C **50**, 2161 (1994).
- [39] D. H. Rischke, Y. Pursun, J. A. Maruhn, H. Stoecker and W. Greiner, Heavy Ion Phys. **1**, 309 (1995) [arXiv:nucl-th/9505014].
- [40] L. P. Csernai and D. Rohrich, Phys. Lett. B **458**, 454 (1999).
- [41] A. Nyiri *et al.*, J. Phys. G **31**, S1045 (2005).

- [42] R. J. Snelling, H. Sorge, S. A. Voloshin, F. Q. Wang and N. Xu, Phys. Rev. Lett. **84**, 2803 (2000).
- [43] J. Adams *et al.* (STAR Collaboration), Phys. Rev. C. **73**, 34903 (2006).
- [44] Z. W. Lin and C. M. Ko, Phys. Rev. C **65**, 034904 (2002); L. W. Chen and C. M. Ko, J. Phys. G **31**, S49 (2005); L. W. Chen, private communication (2005).
- [45] S. A. Bass *et al.*, Prog. Part. Nucl. Phys. **41**, 225 (1998); M. Bleicher *et al.*, J. Phys. G **25**, 1859 (1999); X. L. Zhu, private communication (2005).
- [46] P. F. Kolb and U. W. Heinz, arXiv:nucl-th/0305084v2.
- [47] H. Sorge, Phys. Rev. Lett. **82**, 2048 (1999).
- [48] B. Zhang, M. Gyulassy, and C. M. Ko, Phys. Lett. B **455**, 45 (1999).
- [49] P. F. Kolb, J. Sollfrank, and U. Heinz, Phys. Rev. C **62**, 054909 (2000); P. F. Kolb, J. Sollfrank, and U. Heinz, Phys. Lett. B **459**, 667 (1999).
- [50] J. Adams *et al.* (STAR Collaboration), Phys. Rev. Lett. **95**, 122301 (2005) [arXiv:nucl-ex/0504022].
- [51] J. Adams *et al.* (STAR Collaboration), Phys. Rev. Lett. **92**, 052302 (2004).
- [52] J. Adams *et al.* (STAR Collaboration), Phys. Rev. Lett. **92**, 182301 (2004).
- [53] J. Y. Ollitrault, Phys. Rev. D **46**, 229 (1992).
- [54] R. Baier, D. Schi and B.G. Zakharov, Ann. Rev. Nucl. Part. Sci. **50**, 37 (2000).
- [55] M. H. Thoma and M. Gyulassy, Nucl. Phys. A **538**, 37c (1991); S. Mrowczynski Phys. Lett. B **269**, 383 (1991); Y. Koike and T. Matsui, Phys. Rev. D **45**, 3237 (1992).
- [56] M. Gyulassy and M. Plumer, Phys. Lett. B **243**, 432 (1990).
- [57] M. Gyulassy, I. Vitev, and X. N. Wang, Phys. Rev. Lett. **86**, 2537 (2001).

- [58] J. Adams *et al.* (STAR Collaboration), Phys. Rev. Lett. **91**, 172302 (2003) [arXiv:nucl-ex/0305015].
- [59] X. N. Wang, Nucl. Phys. A **715**, 775 (2003).
- [60] J. Adams *et al.* (STAR Collaboration), Phys. Rev. Lett. **91**, 072304 (2003).
- [61] J. Adams *et al.* (STAR Collaboration), Phys. Rev. Lett. **93**, 252301 (2004).
- [62] J. Adams *et al.* (STAR Collaboration), Phys. Rev. Lett. **97**, 162301 (2006).
- [63] D. H. Rischke, Y. Pürsün and J. A. Maruhn, Nucl. Phys. A **595**, 383 (1995) [Erratum-
ibid A **596**, 717 (1996)]; C. Spieles, H. Stöcker and C. Greiner, Phys. Rev. C **57**, 908
(1998); M. Bluhm, B. Kampfer, R. Schulze, D. Seipt and U. Heinz, Phys. Rev. C **76**,
034901 (2007).
- [64] C. M. Hung and E. V. Shuryak, Phys. Rev. Lett. **75**, 4003 (1995) [arXiv:hep-
ph/9412360].
- [65] D. H. Rischke and M. Gyulassy, Nucl. Phys. A **608**, 479 (1996) [arXiv:nucl-
th/9606039].
- [66] R. Hanbury Brown and R. Q. Twiss, Phil. Mag. **45**, 663 (1954).
- [67] U. A. Wiedemann, Nucl. Phys. A **661**, 65C (1999) [arXiv:nucl-th/9907048].
- [68] Q. f. Li, J. Steinheimer, H. Petersen, M. Bleicher and H. Stocker, Phys. Lett. B **674**,
111 (2009) [arXiv:0812.0375 [nucl-th]].
- [69] M. A. Stephanov, K. Rajagopal and E. V. Shuryak, Phys. Rev. D **60**, 114028 (1999).
- [70] C. Bernard *et al.*, Phys. Rev. D **55**, 6861 (1997); Y. Iwasaki, K. Kanaya, S. Kaya,
S. Sakai and T. Yoshi, Phys. Rev. D **54**, 7010 (1996); G. Boyd *et al.*, Phys. Rev.
Lett. **75**, 4169 (1995); E. Laermann, Proc. Quark Matter '96, Nucl. Phys. A **610**, 1c
(1996).
- [71] L. Stodolsky, Phys. Rev. Lett. **75**, 1044 (1995).

- [72] E. V. Shuryak, Phys. Lett. B **430**, 9 (1998).
- [73] M. Stephanov, K. Rajagopal, and E. Shuryak, Phys. Rev. Lett. **81**, 4816 (1998); K. Rajagopal, proc. of the Minnesota conference on Continuous Advances in QCD 1998 (hep-th/9808348). B. Berdnikov and K. Rajagopal, Phys. Rev. D **61**, 105017 (2000); K. Rajagopal, Nucl. Phys. A **680**, 211 (2000) [arXiv:hep-ph/0005101].
- [74] St. Mrówczyński, Phys. Lett. B **430**, 9 (1998).
- [75] T. Anticic *et al.* (NA49 Collaboration), Phys. Rev. C **70**, 034902 (2004) [arXiv:hep-ex/0311009].
- [76] J. Adams *et al.* (STAR Collaboration), Phys. Rev. C **72**, 044902 (2005).
- [77] S. Gavin, Phys. Rev. Lett. **92**, 162301 (2004) [arXiv:nucl-th/0308067]; E. G. Ferreira, F. del Moral and C. Pajares, Phys. Rev. C **69**, 034901 (2004) [arXiv:hep-ph/0303137]; J. Dias de Deus and A. Rodrigues, arXiv:hep-ph/0308011; M. Rybczynski, Z. Włodarczyk and G. Wilk, Acta Phys. Polon. B **35**, 819 (2004) [arXiv:hep-ph/0305329].
- [78] H. Heiselberg, Phys. Rep. **351**, 161 (2001).
- [79] J. Stachel and G. R. Young, Ann. Rev. Nucl. Part. Sc. **44**, 537 (1994).
- [80] M. M. Aggarwal *et al.* (WA93 Collaboration), Phys. Rev. C **58**, 1146 (1998).
- [81] M. M. Aggarwal *et al.* (WA98 Collaboration), Phys. Lett. B **458**, 422 (1999).
- [82] <http://www.vecal.ernet.in/~pmd/>
- [83] M. M. Aggarwal *et al.* (WA93 Collaboration), Phys. Lett. B **403**, 390 (1997); G. C. Mishra, Ph. D. Thesis, Utkal University (1999).
- [84] R. Raniwala (for the STAR Collaboration), J. Phys. G **35**, 104104 (2008).
- [85] B. Mohanty and J. Serreau, Phys. Rep. **414**, 263 (2005) and references therein.
- [86] K. Adcox *et al.* (PHENIX Collaboration), Phys. Rev. Lett. **86**, 3500 (2001).

- [87] B. B. Back *et al.* (PHOBOS Collaboration), Phys. Rev. Lett. **87**, 102303 (2001).
- [88] B. B. Back *et al.* (PHOBOS Collaboration), Phys. Rev. Lett. **91**, 052303 (2003).
- [89] J. Adams *et al.* (STAR Collaboration), Phys. Rev. Lett. **95**, 62301 (2005).
- [90] J. Adams *et al.* (STAR Collaboration), Phys. Rev. C **73**, 34906 (2006).
- [91] J. Benecke *et al.*, Phys. Rev. **188**, 2159 (1969).
- [92] T. T. Chou and C. N. Yang, Phys. Rev. Lett. **25**, 1072 (1970).
- [93] I. G. Bearden *et al.* (BRAHMS Collaboration), Phys. Lett. B **523**, 227 (2001).
- [94] I. G. Bearden *et al.* (BRAHMS Collaboration), Phys. Rev. Lett. **88**, 202301 (2002).
- [95] L. Ahle *et al.* (E866 Collaboration and E917 Collaboration), Phys. Lett. B **490**, 53 (2000); L. Ahle *et al.* (E866 Collaboration and E917 Collaboration) Phys. Lett. B **476**, 1 (2000); J. L. Klay *et al.* (E895 Collaboration), Phys. Rev. Lett. **88**, 102301 (2002); J. Barrette *et al.* (E877 Collaboration), Phys. Rev. C **62**, 024901 (2000); Y. Akiba *et al.* (E802 Collaboration), Nucl. Phys. A **610**, 139c (1996); L. Ahle *et al.* (E802 Collaboration), Phys. Rev. C **60**, 064901 (1999); L. Ahle *et al.* (E802 Collaboration and E866 Collaboration), Phys. Rev. C **60**, 044904 (1999); L. Ahle *et al.* (E802 Collaboration), Phys. Rev. C **57**, 466 (1998).
- [96] S. V. Afanasiev *et al.* (NA49 Collaboration), Phys. Rev. C **66**, 054902 (2002); C. Alt *et al.* (NA49 Collaboration), Phys. Rev. C **77**, 024903 (2008); Phys. Rev. C **73**, 044910 (2006); T. Anticic *et al.* (NA49 Collaboration), Phys. Rev. C **69**, 024902 (2004).
- [97] B. I. Abelev *et al.* (STAR Collaboration), Phys. Rev. C **79**, 034909 (2009).
- [98] M. Gazdzicki and D. Rohrich, Z. Phys. C **71**, 55 (1996) [arXiv:hep-ex/9607004].
- [99] S. Chatterjee, R. M. Godbole and S. Gupta, arXiv:0906.2523v1 [hep-ph]; A. Andronic, P. Braun-Munzinger and J. Stachel, Phys. Lett. B **673**, 142 (2009); J. K. Nayak, J. Alam, P. Roy, A. K. Dutt-Mazumder and B. Mohanty, Acta Phys. Slov.

- 56**, 27 (2006); B. Tomasik and E. E. Kolomeitsev, Eur. Phys. J. C **49**, 115 (2007); J. Cleymans, H. Oeschler, K. Redlich and S. Wheaton, Eur. Phys. J. A **29**, 119 (2006); J. Rafelski, I. Kuznetsova and J. Letessier, J. Phys. G **35**, 044011 (2008).
- [100] L. Van Hove, Phys. Lett. B **118**, 138 (1981).
- [101] M. I. Gorenstein, M. Gazdzicki and K. A. Bugaev, Phys. Lett. B **567**, 175 (2003) [arXiv:hep-ph/0303041].
- [102] P. Braun-Munzinger, J. Stachel, J. P. Wessels, and N. Xu, Phys. Lett. B **344**, 43 (1995).
- [103] P. Braun-Munzinger, J. Stachel, J. P. Wessels, and N. Xu, Phys. Lett. B **365**, 1 (1996).
- [104] P. Braun-Munzinger, I. Heppe and J. Stachel, Phys. Lett. B **465**, 15 (1999).
- [105] N. Xu and M. Kaneta, Nucl. Phys. A **698**, 306 (2002).
- [106] E. Schnedermann, J. Sollfrank, and U. Heinz, Phys. Rev. C **48**, 2462 (1993).
- [107] D. Teaney, J. Lauret, and E. V. Shuryak, Phys. Rev. Lett. **86**, 4783 (2002).
- [108] P. Kolb *et al.*, Nucl. Phys. A **696**, 197 (2001).
- [109] P. Huovinen *et al.*, Phys. Lett. B **503** (2001).
- [110] U. Heinz and P. Kolb, Nucl. Phys. A **702**, 269 (2002).
- [111] F. Retiere and M. A. Lisa, Phys. Rev. C **70**, 044907 (2004).
- [112] F. Karsch, Lecture Notes in Physics **583**, 209 (2002).

Chapter 2

THE STAR EXPERIMENT

2.1 Relativistic Heavy Ion Collider (RHIC)

The main aim of high-energy heavy-ion collision experiments is to discover and study the new phase of the matter called QGP. This can be achieved by depositing a large amount of energy in a small volume in a very short time. It can be accomplished by colliding heavy-ions by accelerating them to the relativistic speed. As a result the temperature of the colliding region may reach very high values. Relativistic Heavy Ion Collider (RHIC) is built at Brookhaven National Laboratory (BNL) [1] which gives unique opportunity to accelerate the heavy ions and polarized protons. The RHIC machine can be operated at wide range of energies. It can accelerate heavy-ions up to $\sqrt{s_{NN}} = 200$ GeV, and polarized protons upto $\sqrt{s_{NN}} = 500$ GeV. RHIC consists of two concentric quasi-circular superconducting storage accelerator rings that are arbitrarily called as “blue” and “yellow” rings, thus allowing a virtually free choice of colliding projectiles. The rings share a common horizontal plane inside the tunnel, with each ring having an independent set of bending and focusing magnets as well as radio frequency acceleration cavities.

Figure 2.1 shows the layout of the RHIC collider. RHIC has a circumference of about 3.8 km. The counter-rotating particle beams can cross at six interactions around the RHIC ring. The four main experiments located at the four intersection points currently in use at RHIC are - Solenoidal Tracker At RHIC (STAR) [2], Pioneering High Energy Nuclear Interaction eXperiment (PHENIX) [3], Broad RAnge Hadron Magnetic Spectrometers (BRAHMS) [4] and PHOBOS (not an acronym, but named after moon of Mars) [5]. If

the RHIC is considered as a clock, the positions of four experiments can be enumerated by clock positions. The BRAHMS, STAR, PHENIX, and PHOBOS experiments are located at 2 o'clock, 6 o'clock, 8 o'clock, and 10 o'clock positions, respectively as shown in Fig. 2.1.

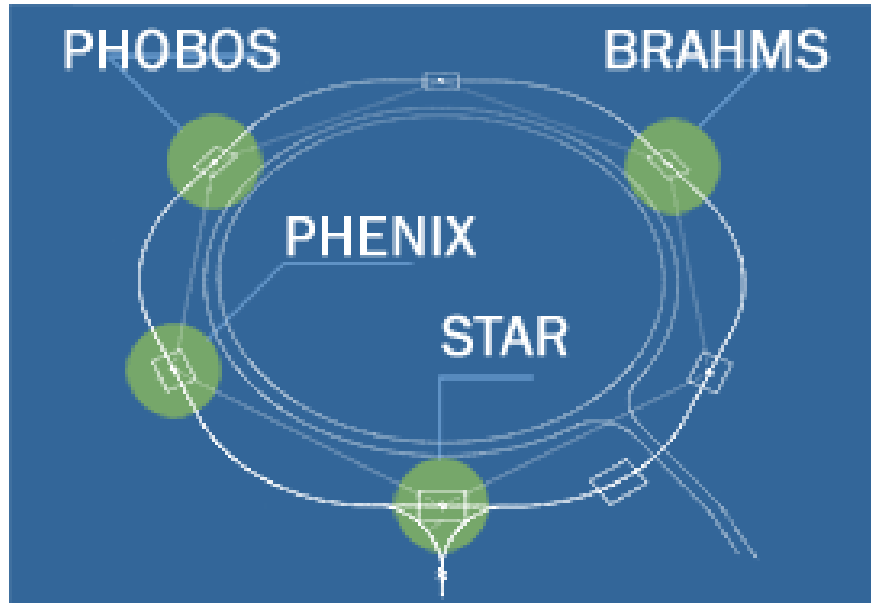


Figure 2.1: Layout picture of the RHIC collider shown along with four main experiments positions.

Figure 2.2 shows the schematic picture of RHIC collider along with the main experiments. The acceleration steps of heavy-ions and polarized protons are also shown in this figure. The multi-steps of acceleration are described below:

1. **Tandem Van de Graff:** The Tandem provides billions of ions, gives them an energy boost and send them towards the Booster.
2. **Tandem-to-Booster line (TTB):** The bunches of ions from the Tandem are passed through the Tandem-to-Booster beam line, which carries them through a vacuum via a magnetic field to the Booster. At this time, the ions are moving at about 5% the speed of light.
3. **Linear Accelerator (Linac):** For collision of protons beams at RHIC, the energetic protons are supplied by the 200 MeV Linac. Protons are transfered from the Linac to Booster.

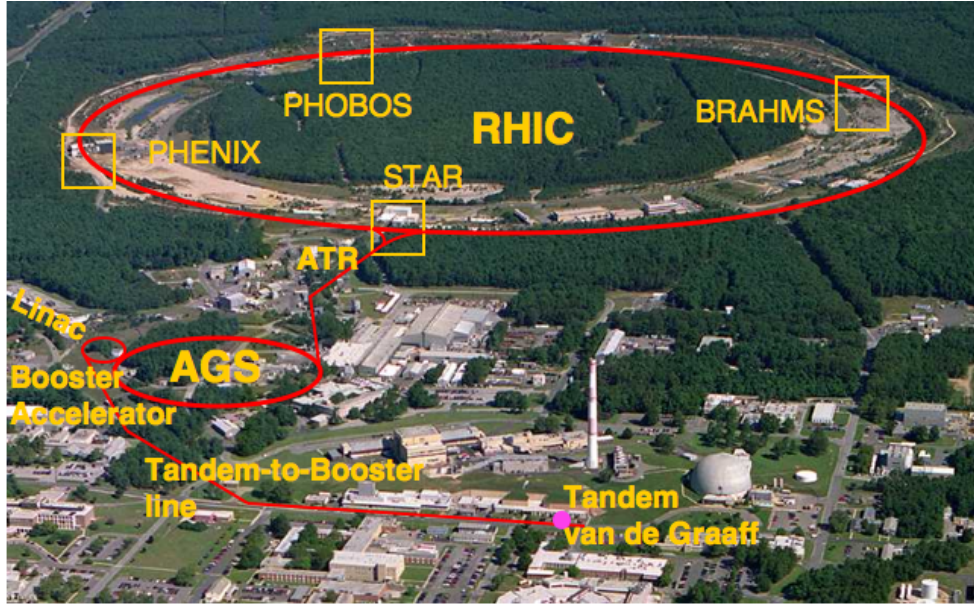


Figure 2.2: Diagram shows the RHIC complex. The various stages of acceleration of ions and the locations of four experiments at RHIC are also shown.

4. **Booster Synchrotron:** The Booster synchrotron is a powerful circular accelerator that provides the ions more energy, by having them “surf ride” on the downhill slope of radio frequency electromagnetic waves. The ions are propelled forward at higher and higher speeds, getting closer and closer to the speed of light. The Booster then feeds the beam into the Alternating Gradient Synchrotron.
5. **Alternating Gradient Synchrotron:** When the ions enter the Alternating Gradient Synchrotron (AGS) they are travelling at about 37% the speed of light. In AGS, the ions are rotated in a circle and are accelerated. On account of this, the energy of ions increases and in a short time they reach the speed of about 99.7% speed of light.
6. **AGS-to-RHIC Line:** When the ion beam is travelling at top speed in the AGS, it is passed through the another beam line called the AGS-To-RHIC (ATR) transfer line. At the end of this line, there is a “fork in the road” where a switching magnet sends the ion bunches down one of two beam lines. Bunches are directed either left to travel clockwise in the RHIC ring or right to travel anti-clockwise in the

Table 2.1: Nominal RHIC parameters for Au+Au collisions

Au+Au collisions	$\sqrt{s_{NN}} = 200 \text{ GeV}$
Avg. luminosity \mathcal{L} (10 hour storage)	$2 \times 10^{26} \text{cm}^{-2} \text{s}^{-1}$
Bundles per ring	60
Gold ions per bunch	10^9
Crossing points	6
Beam lifetime (storage length)	10 hours
RHIC circumference	3833.845 m

second RHIC ring. So there are counter-rotating beams in the RHIC rings, which are accelerated and circulated in the RHIC where they can be collided into one another at as many as six interaction points.

Another important aspect of RHIC is to provide beams of very high luminosities, which makes possible of measurements of rare processes having small cross sections. For a process with the cross section σ_i , the event rate (R_i) is given by $R_i = \sigma_i \cdot \mathcal{L}$. The luminosity \mathcal{L} is given by $\mathcal{L} = fn \frac{N_1 N_2}{A}$, where N_1 and N_2 are the number of particles contained in each bunch, A is the cross-sectional area of the overlap between the two colliding beams of particles, f is the frequency of revolution, and n is the number of bunches per beam. High luminosities can therefore be achieved by maximizing f , n and decreasing the beam profile. For an example, the Table 2.1 lists the nominal RHIC parameters for Au+Au collisions.

2.2 The STAR Detector

The STAR detector [2] is the largest detecting system at RHIC. The main motivation to build the STAR detector was to investigate the behavior of strongly interacting matter at high energy density and to search for signatures of QGP. The STAR is designed to measure many observables simultaneously to study signatures of a possible QGP phase

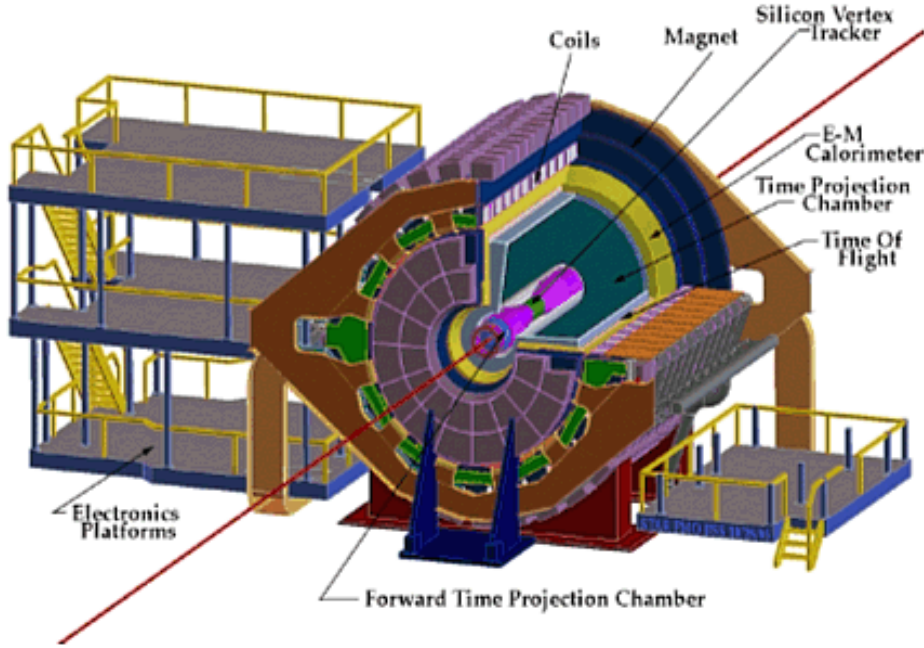


Figure 2.3: Perspective view of the STAR detector, with a cutaway for viewing inner detector systems [2].

transition and to understand the space-time evolution of the collision process in ultra-relativistic heavy ion collisions. The goal is to obtain a fundamental understanding of the microscopic structure of these hadronic interactions at high energy densities. In order to accomplish this, STAR was primarily designed for measurements of hadron production over a large solid angle. STAR is also very effective in high precision tracking, momentum analysis, and particle identification at the central rapidity region. The large acceptance of STAR detector makes it well suited for event-by-event characterizations of heavy ion collisions and for the detection of hadron jets [2].

Figure 2.3 shows the layout of the STAR detector along with the subsystems, and Fig. 2.4 shows the cross-sectional side view of the STAR detector [2]. The whole detector is enclosed in a solenoidal magnet that provides a uniform magnetic field (0.5 T) parallel to the beam direction as shown in Fig. 2.4. All the detectors are kept at the room temperature. The uniform magnetic field provides ability to perform momentum measurements of charged particles. The charged particle tracking near the interaction region is accomplished by a *Silicon Vertex Tracker* (SVT) [6]. Inner tracking is also accomplished

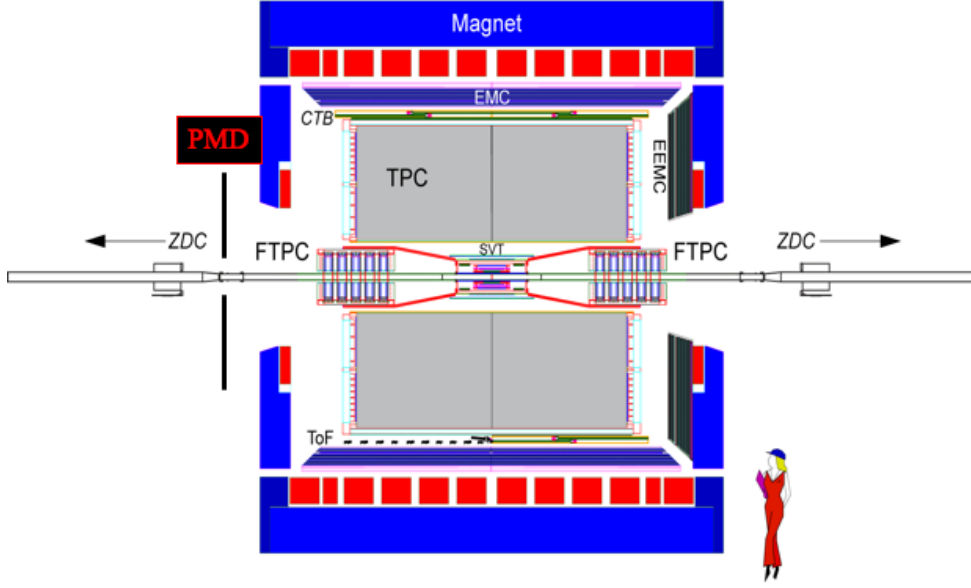


Figure 2.4: Cross-sectional side view of the STAR detector [2].

by employing *Silicon Strip Detectors* (SSD) [7]. The heart of the STAR detector is the *Time Projection Chamber* (TPC) [8] which is used for the charged particle tracking and particle identification. The TPC is 4 meters long and it covers a pseudorapidity range $|\eta| \leq 1.8$ for tracking with complete azimuthal symmetry ($\Delta\phi = 2\pi$). Both the SVT and TPC contribute to particle identification using the ionization energy loss, with an anticipated combined energy loss resolution (dE/dx) of 7% (σ). The tracking is extended to the forward region by installation of two radial-drift TPCs or *Forward Time Projection Chambers* (FTPC) [9]. The FTPCs cover the pseudorapidity region $2.5 < |\eta| < 4$, on either side of the TPC in forward and backward rapidity with complete azimuthal coverage. To extend the particle identification in STAR to larger momenta over a small solid angle for identified single-particle spectra at mid-rapidity, a *Ring Imaging CHerenkov* (RICH) detector [10] covering $|\eta| < 0.3$ and $\Delta\phi = 0.11\pi$, and a *Time-Of-Flight patch* (TOFp) [11] covering $1 < \eta < 0$ and $\Delta\phi = 0.04\pi$ (as shown in Fig. 2.3) were installed at STAR in 2001 [11]. In 2003, a *Time-Of-Flight tray* (TOFr) based on Multi-gap Resistive Plate Chamber (MRPC) technology [12] was installed in STAR detector, covering $1 < \eta < 0$ and $\Delta\phi = \pi/30$. For the time-of-flight system, the *pseudo-Vertex Position Detectors* (pVPD) was installed as the start-timing detector, which was 5.4 m away from TPC center and

covered $4.43 < |\eta| < 4.94$ with the 19% azimuthal coverage [11] in 2003.

For detection of electromagnetic particles STAR has a set of calorimeters. The full *Barrel ElectroMagnetic Calorimeter* (BEMC) [13] covers $|\eta| < 1$ and *Endcap ElectroMagnetic Calorimeter* (EEMC) [14] covers $1 < \eta \leq 2$. Both these detectors are azimuthally symmetric. These calorimeters include shower-maximum detectors to distinguish high momentum single photons from pairs resulting from π and η meson decays. The EMC can also be employed to provide prompt charged particle signals essential to discriminate against pileup tracks in TPC. The STAR detector is also capable of detecting photons at forward rapidity using the *Photon Multiplicity Detector* (PMD) [15, 16].

In the following subsections, we first describe the trigger detectors. Then the DAQ (Data AcQuisition) and triggering, the STAR magnet, and the main detectors of the STAR are discussed. The data collected by the TPC and PMD are used for the results presented in this thesis. These detectors are discussed in detail in the later part of this chapter.

2.3 Trigger Detectors

The detectors (except EMC) discussed in the previous section are called the slow detectors because they can only operate at rates of ~ 100 Hz. But the interaction rates at RHIC for the highest luminosity beams can even approach ~ 10 MHz. So in order to reduce the rate by almost 5 orders in magnitude, we need some fast detectors. Interactions are selected based on the distributions of particles and energy obtained from the fast trigger detectors. STAR detector consists of some fast detectors, basically employed to provide trigger for the slow detectors in order for them to record data. The main triggering detectors for STAR are: *Central Trigger Barrel* (CTB), *Zero Degree Calorimeter* (ZDC), *Beam Beam Counter* (BBC), and Electro Magnetic Calorimeters (BEMC - *Barrel ElectroMagnetic Calorimeter* and EEMC - *Endcap Electromagnetic Calorimeter*). These are discussed below.

2.3.1 Central Trigger Barrel

As shown in Fig. 2.4, the CTB [17] surrounds the outer cylinder of the TPC. The CTB consists of 240 scintillator slats of plastic scintillator with $0 \leq \phi \leq 2\pi$ and $|\eta| \leq 1$ coverage. Each slat consists of a scintillator, light guide, and mesh dynode photomultiplier tube (PMT). As the charged particles travel through the tiles, the generated scintillation photons are collected by PMTs, digitized and converted into electric signals. The amplitude of the signal is proportional to the multiplicity of the charged particles. The response time of the CTB is fast (260 ns), therefore in combination with the ZDC signal (which detect the neutrons), it can provide a powerful charged particle multiplicity trigger. Figure 2.5 shows a CTB segment with two slats which are mounted in aluminium trays (two slats per tray). The CTB calibration yields an average 5 ADC counts for one minimum ionizing charged particles. For central Au+Au collisions the average occupancy per CTB tile is about 10 hits per slat, however in $p + p$ collisions it is about 0.05 per event.

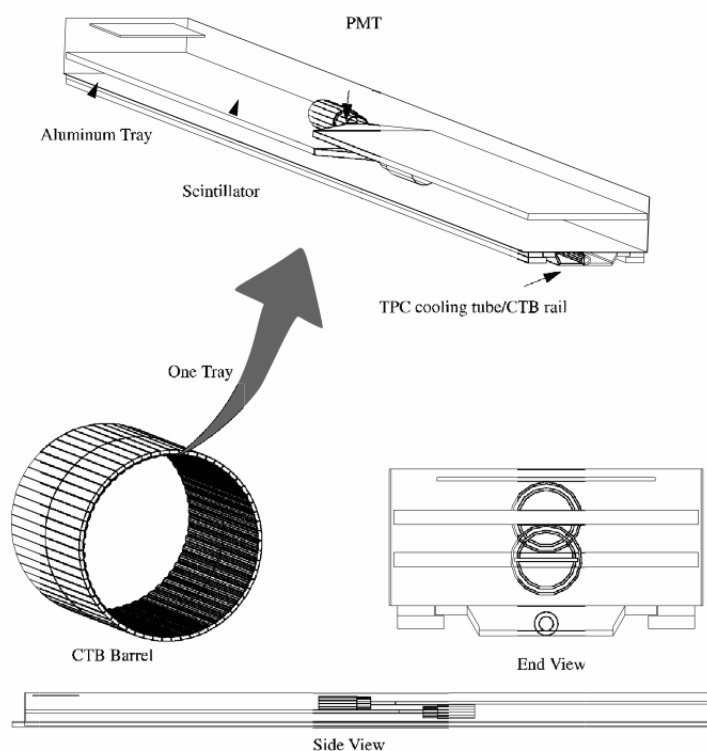


Figure 2.5: CTB cylinder and detail of tray and slat.

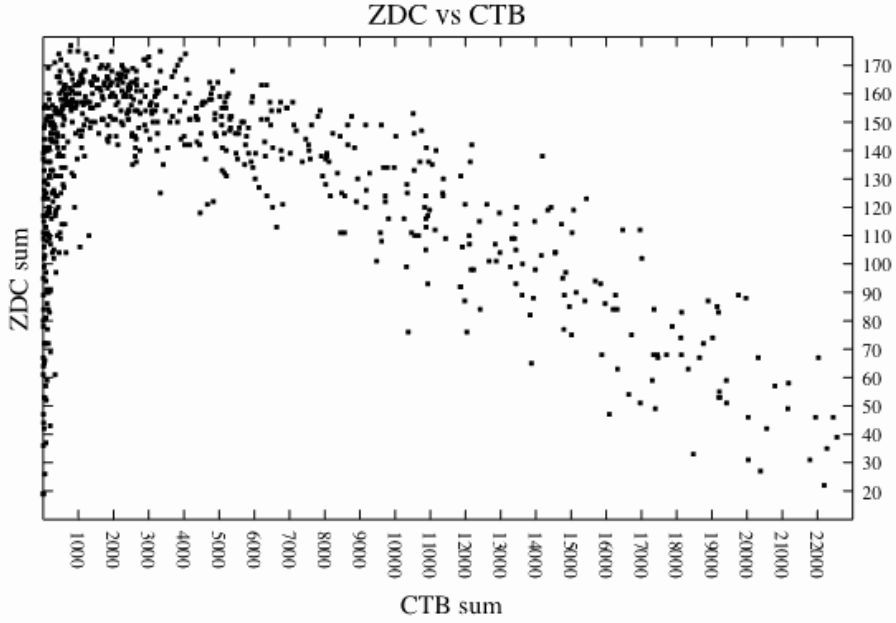


Figure 2.6: Correlation of ZDC and CTB signals.

2.3.2 Zero Degree Calorimeter

The ZDCs [18] are situated ± 18 m from the center of the STAR detector and are at zero degrees with respect to the beam direction (within $\theta < 2$ mrad). The ZDCs measure the energy of spectator neutrons, since the charged fragments are bent away by the steering dipoles situated between the STAR and the ZDCs. In the zero degree region, the produced particles and other secondary particles deposit negligible energy as compared to that of beam fragmentation neutrons. The real collisions can be distinguished from the background events by selecting events with ZDC coincidence from the two beam directions. This makes ZDC a useful event trigger and a luminosity monitor and for this reason all four experiments at RHIC are using identical ZDC detectors. The neutron multiplicity is also known to be correlated with the event geometry and can be used to measure collision centrality.

Each ZDC consists of three modules. Each module consists of a series of tungsten plates alternating with layers of wavelength shifting fibres which are connected to a PMT. The ZDCs are basically used for the beam monitoring, triggering, and locating interaction

vertices. The Fig. 2.6 shows the correlation between the signals from ZDC and CTB. In terms of impact parameter, the figure shows that there is a region of strong forward neutron production during which there are few charged tracks produced in the CTB (region I, characterized by $\sum \text{CTB} \leq 1500$), followed by an anti-correlation between ZDC and CTB signals (region II, $1500 \leq \sum \text{CTB} \leq \sim 20,000$), and ending in a region (III, $\sum \text{CTB} \geq \sim 20,000$) of high charged particle multiplicity with low neutron signal. The behavior of the correlation is as expected, since in more central collisions (very small impact parameters) we expect large number of charged particles to hit the CTB while less number of spectator neutrons to fall on ZDC. In peripheral collisions (large impact parameters), we expect comparatively less number of charged particles falling on CTB and larger number of spectator neutrons giving signal in ZDC.

2.3.3 Beam-Beam Counter

The ZDC and CTB were specifically designed for triggering in Au+Au collisions. The multiplicity of $p + p$ collisions is much less and therefore requires a different trigger subsystem. The BBC was implemented to mainly work as the trigger subsystem for $p + p$ collisions.

The BBCs are the scintillator annuli mounted around the beam pipe beyond the east and west pole-tips of the STAR magnet at about 375 cm from the center of nominal interaction region (IR). BBC consists of small and large scintillator tiles as shown in the Fig. 2.7. The 2×18 array of small hexagonal tiles cover a full ring of 9.6 cm inner and 48 cm outer diameter, corresponding to the pseudorapidity region of $3.4 < |\eta| < 5.0$. The small hexagon in the center of the BBC (marked “B” in Fig. 2.7) is reserved for the beam pipe. The 2×18 array of large hexagonal tiles span a ring of 38 cm to 193 cm in diameter, corresponding to the pseudorapidity region of $2.1 < |\eta| < 3.6$. Each scintillator tile has four wavelength shifting (WLS) optical fibres inserted into circular grooves inscribed within the hexagonal scintillator to collect scintillation light. The charged particles traversing through the BBCs produce light in their scintillator tiles. Both BBCs were required to fire to trigger minimum bias $p + p$ collisions.

Apart from providing the minimum bias trigger for $p + p$ collisions, BBCs have

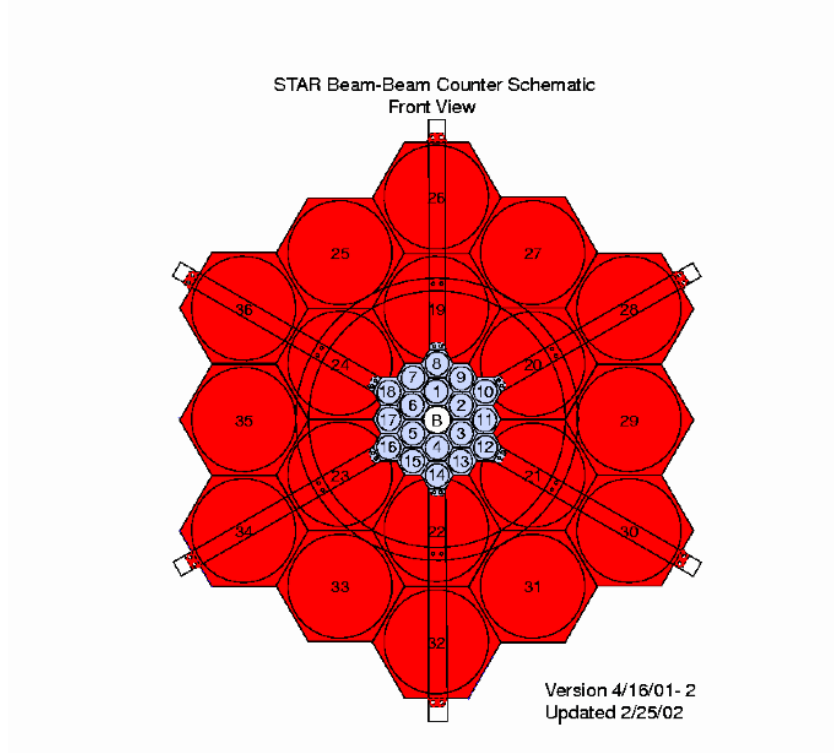


Figure 2.7: Schematic view of BBC, shown along with small (blue) and large (red) tiles. The beam pipe crosses BBC from the location designated by “B” at the center.

applications for other purposes also, as described below. BBC coincidences were used to reject beam gas events, to measure the absolute luminosity \mathcal{L} with 15% precision, and to measure the relative luminosities R for different proton spin orientations with high precisions. In another application, the small tiles of BBC are used to reconstruct the first-order event plane for the directed flow analysis. The timing difference between the two counters (east BBC and west BBC) is used to get information of the primary vertex position.

2.3.4 Electromagnetic Calorimeters

The Electromagnetic Calorimeters can be used to select events with rare probes such as high energy γ and π^0 particles, or electrons from J/Ψ and Υ decays. Other applications include general event characterization in heavy ion collisions including ultra peripheral collisions. In order to achieve these goals, STAR employs two electromagnetic calorimeters

- Barrel Electro-Magnetic Calorimeter and Endcap Electro-Magnetic Calorimeter. Figure 2.8 shows the schematic end view and side view of the STAR EMC showing the EMC Barrel and EMC Endcap. We will discuss these calorimeters in the following subsections.

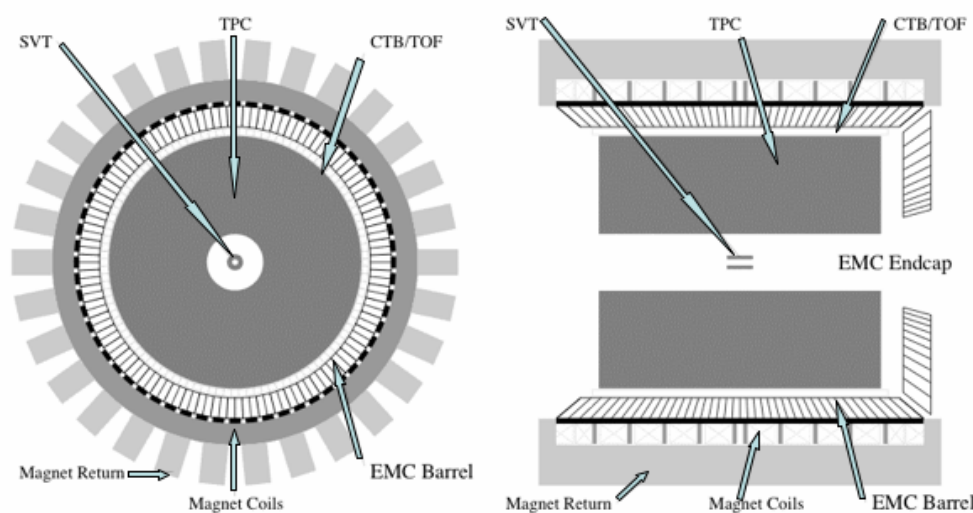


Figure 2.8: Schematic end view and side view of the STAR EMC showing the EMC Barrel and EMC Endcap [13].

2.3.4.1 Barrel Electro-Magnetic Calorimeter

BEMC [13] covers the pseudorapidity region $|\eta| < 1$ with full azimuthal angle. It is basically a sampling calorimeter which consists of alternate layers of lead and scintillator planes, having 20 layers of lead plates and 21 layers of scintillator. BEMC is used to trigger and study rare and high p_T processes like jets, leading hadrons, direct photons and heavy quarks. It also provides large acceptance for photons, electrons along with neutral pions and eta mesons in both polarized $p + p$ and heavy ion systems like Au+Au and Cu+Cu collisions. With BEMC, it is possible to reconstruct neutral pions at relatively high $p_T \approx 25\text{--}30 \text{ GeV}/c$ and also to identify single electrons and pairs in dense hadron backgrounds from the heavy vector mesons, W and Z bosons decays. All these measurements require precise electromagnetic shower reconstruction along with high spatial resolution. For this, two layers of shower maximum detectors which are essentially the gas wire pad chambers

are placed within the BEMC lead/scintillator stack to provide the high spatial resolution measurements of shower distributions in two mutually orthogonal dimensions.

2.3.4.2 Endcap Electro-Magnetic Calorimeter

The EEMC [14] is situated on the west pole-tip of the STAR detector and covers the pseudorapidity region $1 \leq \eta \leq 2$ with full azimuthal angle. In this way, EEMC enhances the rapidity region covered by BEMC, described in the previous subsection. The construction of EEMC also includes a shower maximum detector optimized to discriminate between photons and π^0 or η mesons over the energy region 10–40 GeV. It also consists of preshower and postshower layers used to discriminate between electrons and hadrons. In addition, it also enhances the acceptance and triggering capabilities for jets in STAR detector.

2.4 Trigger Levels and Data Acquisition

It is very important for an experiment to be able to store or abort events. This is accomplished by triggering the interactions by means of some trigger detectors and then storing or aborting them depending upon whether they are good or bad. The STAR trigger is a pipelined system in which digitized signals from the fast trigger detectors are examined at the RHIC beam crossing rate (~ 10 MHz). There are four successive trigger Levels in STAR namely Level 0, Level 1, Level 2 and Level 3. The interactions that pass the selection criteria in four successive trigger levels are sent at a rate of ~ 5 MHz (~ 50 MB/s), to a storage, universally called the Data AcQuisition (DAQ) [19] system. The final trigger decision is made in Level 3 based on tracking in the slow detectors. The Level 3 trigger performs complete online reconstruction of the events in a dedicated CPU farm. The Level 3 trigger system includes an online display so that individual events can be visually inspected in run time.

The data flow through the trigger (TRG) is shown in Fig. 2.9. The first block represents the fast detectors or trigger detectors, which are described in the previous subsections. The DSM-based decision tree constitutes Level 0 of the trigger and is constrained to issue a decision within $1.5 \mu\text{s}$ from the time of the interaction. When an interaction

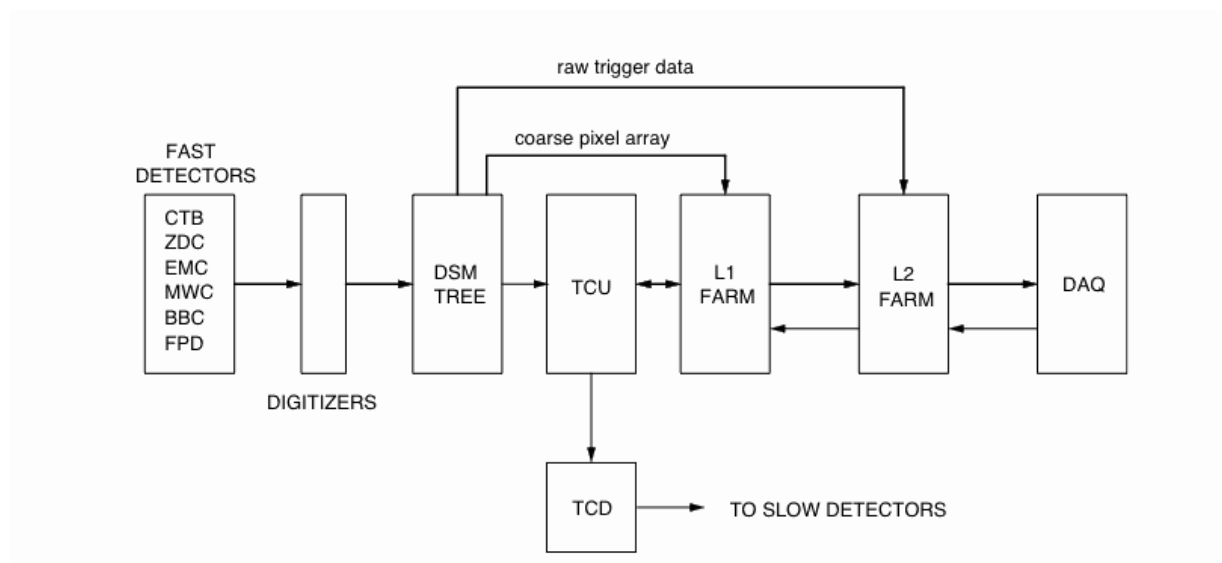


Figure 2.9: Data flow through the trigger. See text for definition of acronyms.

is selected at Level 0, each STAR detector designated to participate in this type of event is notified using a 4-bit Trigger Command and told to identify this event with a 12-bit token [20]. This 12-bit token is issued for each interaction and accepted at Level 0. Based on this token information, Level 2 decides to abort or hand off the event to DAQ within 5 ms of the occurrence of the interaction. All the raw trigger detector data and the results from Levels 1 and 2 analyses are packaged and sent to DAQ with the token. The token stays with the event and is used as an identifier to organize collection of all the fragments from each STAR detector. Once DAQ either accepts and stores the events or aborts it, the token is returned to the trigger and recycled.

2.5 STAR Magnet

The STAR magnet [21] is roughly cylindrical in geometry and consists of 30 flux return bars (backlegs), four end rings and two poletips. The flux return bars are 6.85 m long forming the outer wall of the cylinder which encloses the main and space trim coils and are attached to an inner and outer end ring pair at each end of the magnet. The inner and outer end rings have diameters of 5.27 m and 7.32 m, respectively. The magnet is shown in blue and the coils are shown in the red colour in Fig. 2.4. The magnet generates

a field along the length of the cylinder having a maximum strength of 0.5 T. Due to the uniform field the charged particles move in a helical trajectory in the lowest order of the approximation. This enables a fast pattern recognition and track reconstruction. The magnetic field is reversible, and in each run, the data are taken at both polarities to account for systematic effects. A thorough mapping of the magnetic field shows that uniformity is achieved on the level of ± 50 Gauss (25 Gauss) in radial direction and less than ± 3 Gauss (± 1.5 Gauss) in azimuthal direction for full (half) field setup. The STAR magnet has been run in full, reversed full field and half field configurations.

2.6 Time Of Flight Detector

The main goal of the STAR TOF [12] system was to provide information that extends the hadronic particle identification capabilities of the experiment. The TOFp detector (a prototype based on scintillator technology) was installed in Run II [11]. It replaced one of the CTB trays, covering a region $-1 < \eta < 0$ and $\pi/30$ in azimuth. It contained 41 scintillator slats with the signal read out by PMTs. The resolution of TOFp was ~ 85 ps in Au+Au collisions. Since, the cost of the PMTs are high, it was decided not to use TOFp in the full TOF upgrade.

A new prototype of TOF detector based on Multi-gap Resistive Plate Chamber [12] was proposed for the Run III and Run IV, called the TOFr. This covered the same pseudorapidity and azimuth coverage as was covered by TOFp. It extended the particle identification up to $p_T \sim 3$ GeV/ c for p and \bar{p} . The MRPC technology was first developed by the CERN ALICE group [23] to provide a cost-effective solution for large area time-of-flight coverage. Figure 2.10 shows the side and end views of the MRPC modules developed for STAR. In Run III, 28 MRPC modules were installed in the tray and 12 of them were equipped with electronics, corresponding to $\sim 0.3\%$ of the TPC acceptance [24]. Similar acceptance of TOFr was achieved in Run IV also. Full TOF detector in STAR will be having 120 TOFr trays, with 60 on east side and 60 on west side. For each tray, there will be 33 MRPCs and for each MRPC, there will be 6 read-out channels.

To provide a starting time for TOF detectors, two pVPDs were also installed since

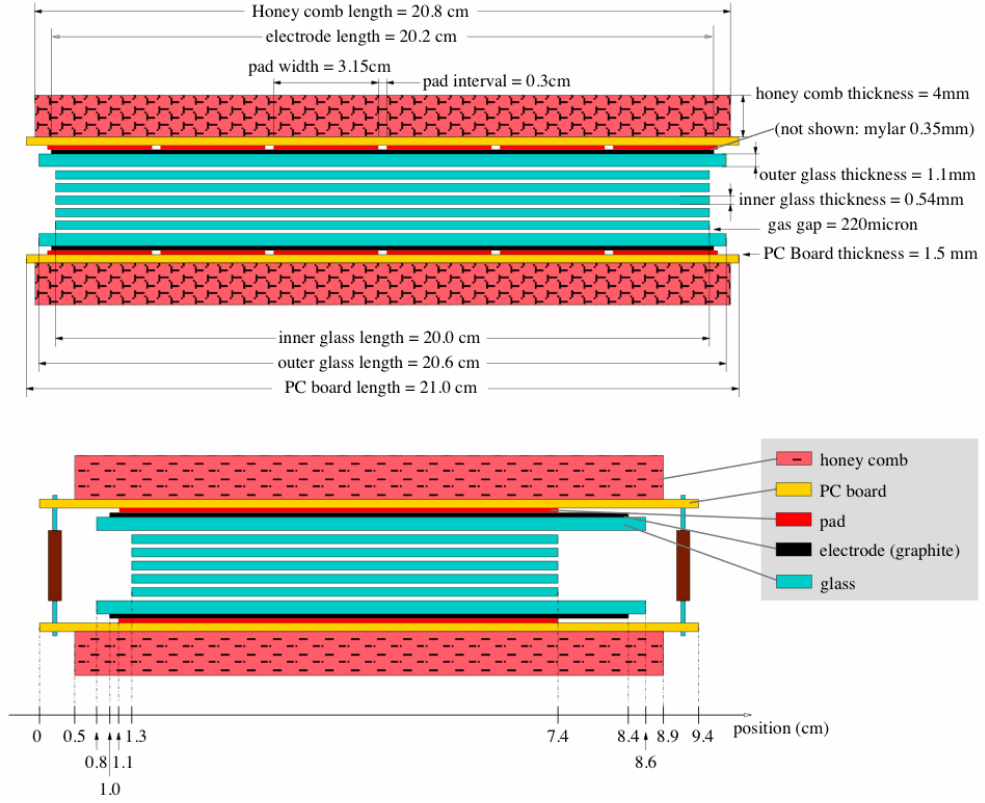


Figure 2.10: Two side views of MRPC [22]. The upper (lower) is for long (short) side view. The two plots are not at the same scale.

Run II. Each pVPD are at distance of 5.4 m from the center of the TPC along the beam direction [11]. Each pVPD consists of three detecting element tubes covering $\sim 19\%$ of the total solid angle in $4.43 < |\eta| < 4.94$. The timing resolution of total starting time depends on the multiplicity. For example, the effective timing resolution of total starting time is 25 ps, 85 ps, and 140 ps for 200 GeV Au+Au, d+Au and $p + p$ collisions, respectively.

2.7 Time Projection Chamber

The Time Projection Chamber [8, 25, 26] is the main tracking detector in the STAR experiment [27, 28]. The TPC is capable of reconstructing tracks of produced particles, measuring their momenta, and identifying the particles by measuring their ionization energy loss (dE/dx). The TPC covers a pseudorapidity region $|\eta| < 1.8$ with full azimuthal angle. The particle momenta measured in the TPC are over a range of 100 MeV/ c to 30

GeV/ c . The particle identification achieved in the TPC covers a momentum range of 100 MeV/ c to greater than 1 GeV/ c . Since the data from the TPC form major part of this thesis, we will discuss it in detail in the following subsections.

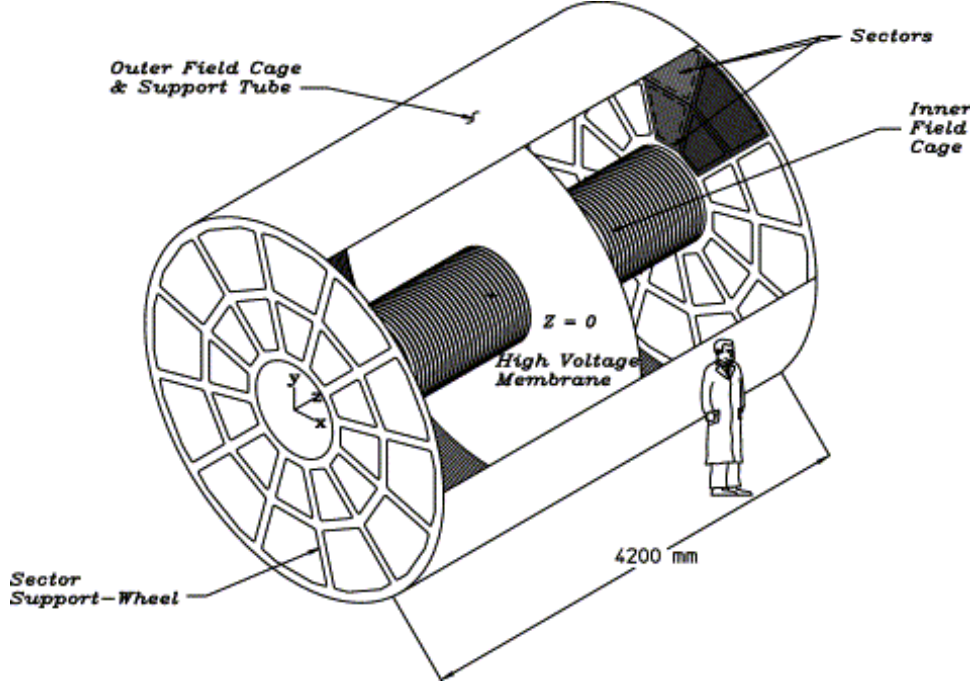


Figure 2.11: The STAR TPC surrounds a beam-beam interaction region at RHIC. The collisions take place near the center of the TPC. Figure is taken from the Ref. [8].

2.7.1 Technical Design

Figure 2.11 shows the schematic diagram of STAR TPC. The TPC is placed inside a large solenoidal magnet which provides a uniform magnetic field of 0.5 T along the length of the TPC [21]. Shape of the TPC is cylindrical with a length of 4.2 m and diameter 4 m. It is an empty volume of gas. The cylinder is concentric with beam line. It consists of one *outer field cage (OFC)*, one *inner field cage (IFC)*, and two *end caps* as shown in the figure. The inner and outer radii of the active volume are 0.5 m and 2.0 m, respectively. A large diaphragm, made of carbon coated kapton with a thickness of $70\ \mu\text{m}$ is stretched between the inner and outer field cages at the center of the TPC, called the *central membrane (CM)*. The central membrane is maintained at a voltage of $-28\ \text{kV}$ with respect to the detection planes and acts as *cathode*. The end caps providing the readout system

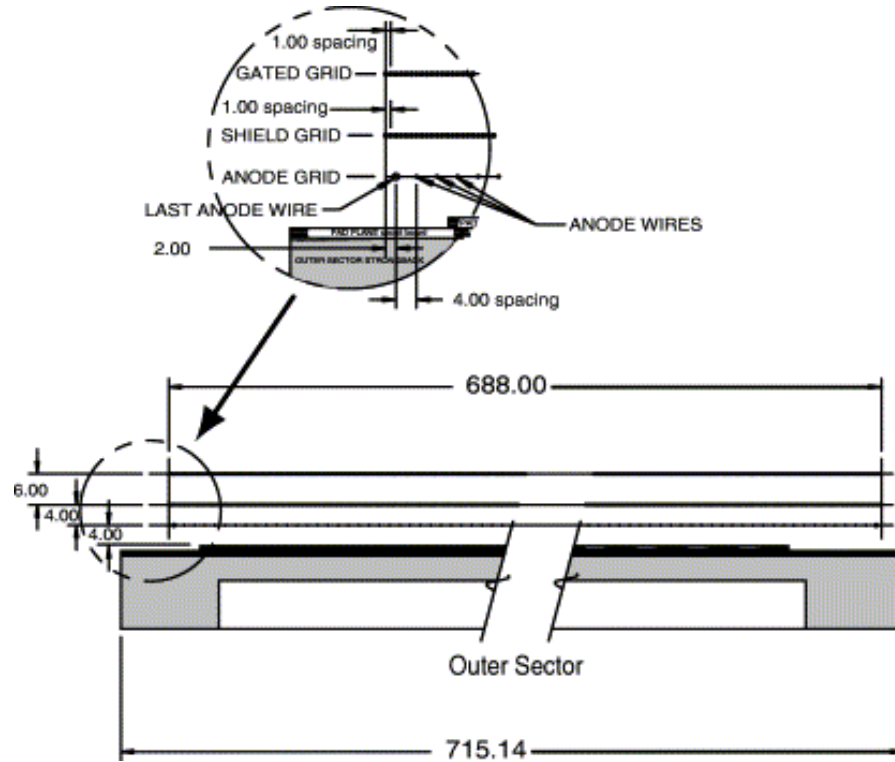


Figure 2.12: A cut-away view of an outer subsector pad plane. The cut is taken along a radial line from the center of the TPC to the outer field cage so the center of the detector is to the right. The figure shows the spacing of the anode wires relative to the pad plane, the ground shield grid, and the gated grid. The bubble diagram shows additional detail about the wire spacing.

are at ground potential and act as *anodes*. The field cage cylinders provide a series of equipotential rings that divide the space between the central membrane and the anode planes into 182 equally spaced segments. One ring at the center is common to both ends. The central membrane is attached to this ring. The TPC is provided a uniform electric field of ≈ 135 V/cm, which is required to drift the electrons within the gas volume.

TPC Readout System:

The readout system is based on MWPC with readout pads. The readout planes, MWPC chambers with pad readout, are modular units mounted on aluminium support wheels. These readout modules or sectors, are arranged as on a clock with 12 sectors around the

circle in the ϕ plane. The chambers consist of four components; a pad plane and three wire planes (see figure 2.12). The readout or amplification layer is composed of the *anode wire plane* with the *pad plane* on one side and the *ground wire plane* on the other. Anode wire plane consists of small $20\ \mu\text{m}$ wires called the anode wires. The direction of anode wires is set perpendicular to the straight radial tracks of highest transverse momentum particles because the resolution is best along the direction of the anode wire. In the other direction, the resolution is limited, because of the quantized spacing of the wires ($4\ \text{mm}$ between anode wires). The dimensions of the rectangular pads are likewise optimized to give the best position resolution perpendicular to the stiff tracks. The width of the pad along the wire is chosen such that the induced charge from an avalanche point shares most of its signal with only three pads. This gives the best centroid resolution using either a 3-point Gaussian fit or a weighted mean. The third plane of the chamber is a *gating grid* which is the outermost wire plane on the sector structure. This grid is a shutter to control entry of electrons from the TPC drift volume into the MWPC. It also blocks positive ions produced in the MWPC, keeping them from entering the drift volume where they would distort the drift field. It can have different voltages on every other wire. The grid is “open” to the drift of electrons while the event is being recorded, with all of the wires on the same potential ($\sim 110\ \text{V}$). It is “closed” when the voltages alternate $\pm 75\ \text{V}$ from the nominal value. The ground grid plane of $75\ \mu\text{m}$ wires completes the sector MWPC. The primary purpose of the ground grid is to terminate the field in the avalanche region and provide additional rf shielding for the pads.

TPC Sector:

Figure 2.13 shows the design of one full sector. Each sector is subdivided into inner and outer subsectors characterized by a change in the readout padrow geometry. Each subsector consists of straight rows of pads that act as cathodes. The subsectors were designed in order to enhance the event reconstruction capabilities of TPC as explained below. The inner subsectors are in the region of highest track density and thus optimized for good two-hit resolution. This design uses a smaller pads of dimension $2.85\ \text{mm}^2 \times$

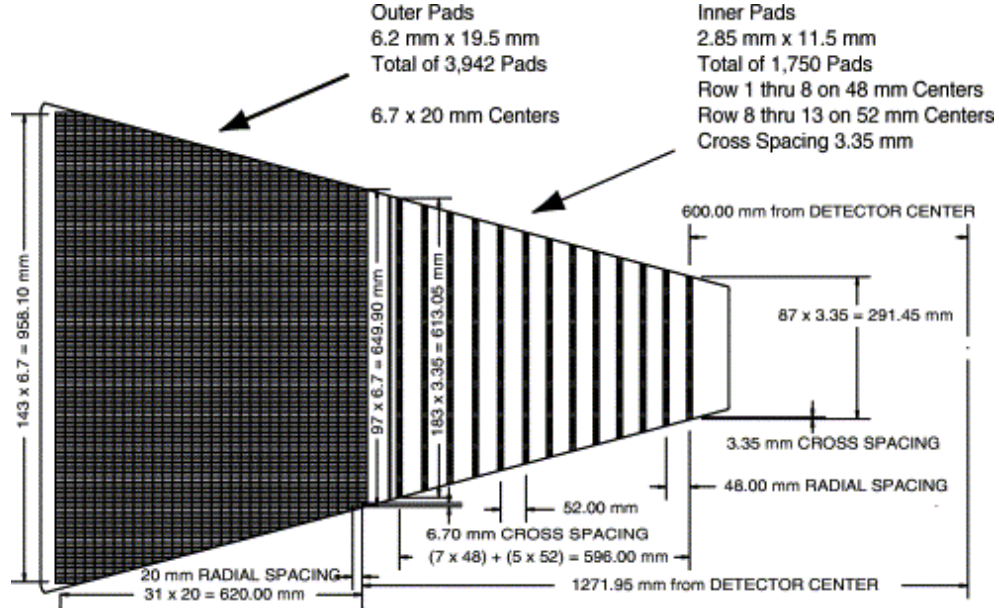


Figure 2.13: The anode pad plane with one full sector shown [8]. The inner subsector is on the right and it has small pads arranged in widely spaced rows. The outer subsector is on the left and it is densely packed with larger pads.

11.5 mm² in 13 rows (1 – 13) to improve the hit resolution. This improves the tracking by reducing the occurrence of split tracks. The advantages of inner sector are to extend the position measurements along the track to small radii thus improving the momentum resolution and the matching to inner tracking detectors. An additional benefit is detection of particles with lower momentum. The outer radius subsectors have continuous pad coverage to optimize the dE/dx resolution (i.e. no spacing between the pad rows). This is optimal because the full track ionization electrons improve statistics on the dE/dx measurement and hence improve the particle identification. Another modest advantage of full pad coverage is an improvement in tracking resolution due to anti-correlation of errors between pad row. The outer sector consists of 32 pad rows (14 – 45) with pad dimension 6.2 mm² × 19.5 mm².

Drift Gas:

The TPC volume is filled with P10 gas (90% Ar, 10% CH₄) at 2 mbar above the at-

mospheric pressure [29]. The gas system circulates the gas in the TPC and maintains purity, reducing electro-negative impurities such as oxygen and water which could capture drifting electrons. The choice of the drift gas is based on several features necessary for optimal TPC performance. The P10 gas has an advantage of fast drift velocity which peaks at a low electric field. Operating on the peak of the velocity curve makes the drift velocity stable and insensitive to small variations in temperature and pressure. Low voltage greatly simplifies the field cage design. The drift velocity of P10 gas is $5.45 \text{ cm}/\mu\text{s}$. The transverse diffusion in P10 gas is about $\sigma_T = 3.3 \text{ mm}$ after drifting 210 cm. The longitudinal diffusion of a cluster of electrons that drifts the full length of the TPC is $\sigma_L = 3.3 \text{ mm}$. The longitudinal diffusion width sets the scale for the resolution of the tracking system in the drift direction. The shaping time and electronic sampling rate are chosen accordingly, having values 180 ns FWHM and 9.4 MHz, respectively.

2.7.2 Event Reconstruction in the TPC

The TPC provides a complete, 3-dimensional picture of the ionization deposited in the gas volume. If an event happens to be inside the TPC active volume, the produced charged particles traverse the gas volume and liberate electrons due to the ionization energy loss (dE/dx). These electrons are drifted towards end cap planes of the TPC and provide signals on the readout pad. The signal on the readout pad is amplified and integrated by preamplifier and shaper, and after digitization, transmitted to the STAR DAQ. Figure 2.14 shows the event display reconstructed in the TPC. The figure shows the beam's eye (left) and side (right) views of a central event in Au+Au collisions at $\sqrt{s_{NN}} = 9.2 \text{ GeV}$. The full event reconstruction in the TPC is explained in the following subsections.

2.7.2.1 Hit and Cluster Finding

The track of a primary particle passing through the TPC is reconstructed by finding ionization clusters along the track. The clusters are found separately in x , y and in z space. The local x -axis is along the direction of the pad row, while the local y -axis extends from the beam line outward through the middle of, and perpendicular to, the pad rows. The z -axis lies along the beam line. The x and y coordinates of a cluster

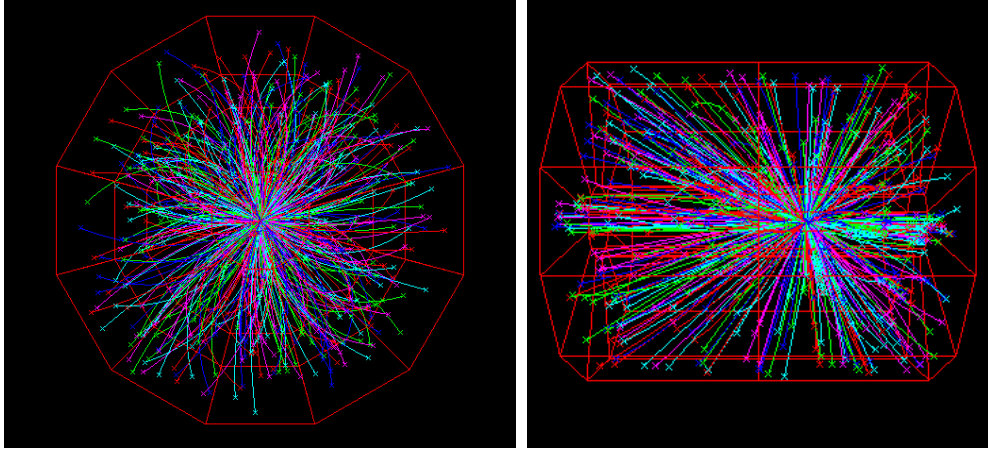


Figure 2.14: Beam's eye (left) and side (right) views of a central event in Au+Au collisions at $\sqrt{s_{NN}} = 9.2$ GeV [30].

are determined by the charge measured on adjacent pads in a single pad row. The z coordinate of a point inside the TPC is determined by measuring the time of drift of a cluster of secondary electrons from the point of origin to the anodes on the endcap and dividing by the average drift velocity. The arrival time of the cluster is calculated by measuring the time of arrival of the electrons in “time buckets” and weighting the average by the amount of charge collected in each bucket (each time bucket is approximately 100 ns long). The length of the signal reaching a pad depends on the *dip angle* (θ)¹. The ionization electrons are spread over a distance d along the beam axis, with $d = L/\tan(\theta)$ and L is the length of the pad.

The drift velocity for the electrons in the gas must be known with a precision of 0.1% in order to convert the measured time into a position with sufficient accuracy. Drift velocity may change with atmospheric pressure, and with small changes in gas composition. These effects can be minimized in two ways. First, the cathode voltage is so set that the electric field in the TPC corresponds to the peak in the drift velocity curve (velocity vs. electric field/pressure). The peak is broad and flat, and small pressure changes do not have a large effect on the drift velocity at the peak. Secondly, the drift velocity is measured independently every few hours during data taking, using the artificial

¹Dip angle: The angle between the particle momentum and the z -direction. Crossing angle: The angle between the particle momentum and the TPC pad row direction.

tracks created by laser beams [8, 31].

2.7.2.2 Track Finding

Once the information of hits or clusters are there in the TPC, the tracks can be reconstructed using track finder. In the first iteration, many track segments (track-lets) are created as candidates for a track. Then, these track segments are fitted by an algorithm that keeps or rejects hits, depending on their position with respect to the fitted track. At this stage, the effect of Coulomb scattering and energy loss assuming pion mass are taken into account. At the end of the algorithm, the collection of the tracks is produced with information of their space coordinates and their 3-momenta.

2.7.2.3 Global and Primary Tracks

In the final step of the event reconstruction, *global* and *primary* tracks are created. The tracks are reconstructed in the local coordinate system of the TPC, as mentioned in the previous subsection. For data analysis, the global information of the tracks is required. The global track finder re-fits the tracks in the TPC, based on a 3D helix model. After re-fitting and with the knowledge of the alignment of different subsystems, the global track finder reconstructs the global tracks from the “local” tracks in the sub detectors. The primary collision vertex is then reconstructed from these global tracks. The global tracks with a distance to the primary vertex smaller than 3 cm (*distance of closest approach or DCA*), are re-fitted including the primary vertex as an additional point in the fit. The refit results are stored as primary tracks collection in the container. The primary tracks are used in the data analysis, and are largely produced in the primary interaction. Global tracks include large number of particles from background or pile-up processes.

2.7.3 Tracking Efficiency

Although the wire chambers are sensitive to almost 100% of the secondary electrons arriving at the end cap, the overall tracking efficiency is lower (80–90%). The tracking efficiency depends on the acceptance of the detector, the electronics detection efficiency, as well as the two hit separation capability of the system. Tracking efficiency of the TPC

is reduced because of the factors as described below:

- The TPC sectors have spaces between them in order to mount the wires on the sectors. This leads to $\sim 4\%$ loss of TPC acceptance. Thus, the acceptance of the TPC is reduced to 96%.
- There is a fiducial cut applied in the software to ignore any space points falling on the last two pads of a pad row. It avoids position errors due to non-symmetric pad coverage on both sides of the track. It also avoids possible local distortions in the drift field. This fiducial cut reduces the total acceptance to 94%.
- Detection efficiency of the electronics is essentially 100% except for the dead channels. Usually, the dead channel count is below 1% of the total.
- The system cannot always separate one hit from two hits on adjacent pads and this merging of hits reduces the tracking efficiency.
- The software also applies cuts to the data which also reduces tracking efficiency. For example, a track is required to have hits on at least 10 pad rows because shorter tracks are too likely to be broken track fragments. But this cut can also remove tracks travelling at a small angle with respect to the beam line and low momentum particles that curl up in the magnetic field.

The tracking efficiency is estimated by embedding the simulated tracks inside the real events and counting the number of simulated tracks that are in the data after the track reconstruction software has done its job. This technique takes care of the detector effects and especially the losses related to high density of tracks. The simulated tracks are very similar to the real tracks and the simulator tries to take into account all the processes that lead to the detection of particles including: ionization, electron drift, gas gain, signal collection, electronic amplification, electronic noise, and dead channels.

Figure 2.15 shows the pion reconstruction efficiency in Au+Au collisions as a function of the transverse momentum of the primary particle, for different centralities. In high multiplicity events, efficiency reaches a plateau of 80% for high p_T particles. Below

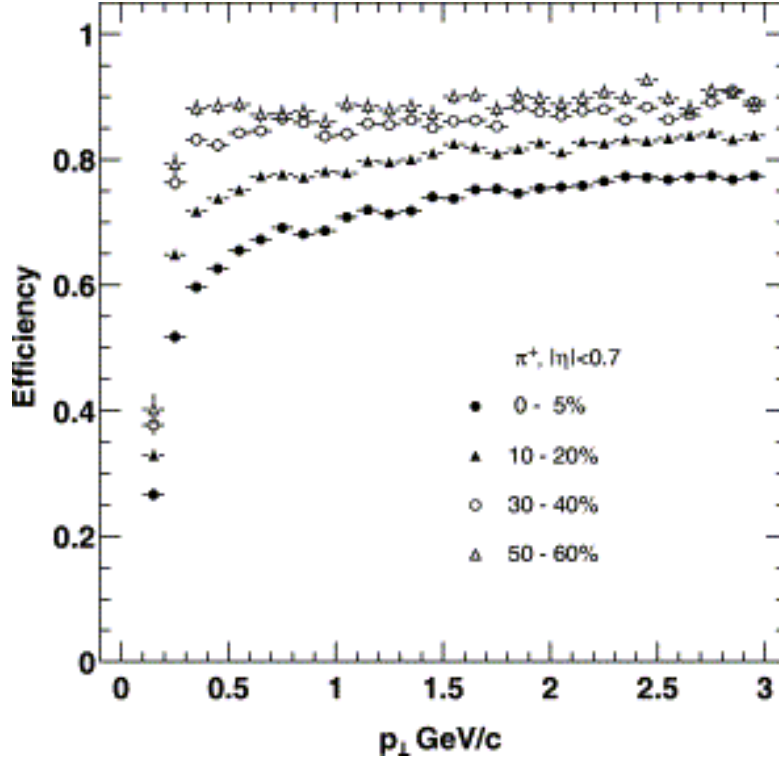


Figure 2.15: The pion tracking efficiency in STAR for central Au+Au events at RHIC [8]. The most central collisions are the highest multiplicity data, they are shown as black dots. The lowest multiplicity data are shown as open triangles.

300 MeV/c, it drops rapidly because the primary particles spiral up inside the TPC and do not reach the outer field cage. In addition, the low momentum particles interact with the beam pipe and inner cage before entering the TPC volume.

2.7.4 Particle Identification

Particle species can be identified in the TPC by measuring the amount of energy they lose while traversing the gas volume. The energy loss of a charged particle in the TPC gas volume is transferred to the liberated electrons. These electrons drift towards the two ends of the TPC, and deposit charge on the pad rows. Thus, the charge produced on a pad row in each hit is proportional to the energy loss of the particle traversing through the TPC volume. For a given charge cluster, the energy loss per unit length (dE/dx) is measured by dividing the charge collected in the pad rows by the track path length across the sensitive path length. The ionization energy loss (or dE/dx) is mass dependent and

hence useful in particle identification. The particle identification in STAR works well for the low momentum particles but the energy loss becomes less mass dependent when the particle energy rises and it becomes hard to separate particles with velocities $v > 0.7c$ [8]. The STAR was designed to be able to separate pions and protons up to 1.2 GeV/ c . This requires a relative dE/dx resolution of 7%.

If a particle travels through the entire TPC volume, it will provide 45 dE/dx points on the 45 pad rows. Energy loss of a charged particle for a given track length can be described by the Bichsel function [32]. However, the mean of the distribution is sensitive to the fluctuations in the tail of the distribution. Therefore, the highest 30% of the measured charge clusters is discarded for each track. The truncated mean is calculated from the remaining 70% and defines the average ionization energy loss ($\langle dE/dx \rangle$) used in the data analysis. For a given track momentum and particle mass, the ionization energy loss can be given by the most probable Bichsel values which is an extension of the Bethe-Bloch formula [33]:

$$-\frac{dE}{dx} = Kz^2 \frac{Z}{A} \frac{1}{\beta^2} \left[\frac{1}{2} \ln \left(\frac{2m_e c^2 \beta^2 \gamma^2 T_{\max}}{I} \right) - \beta^2 - \frac{\delta^2}{2} \right], \quad (2.1)$$

where z is the integral charge of the particle, K is a constant, Z is the atomic number of the absorber, A is the atomic mass of the absorber, m_e is the electron mass, c is the speed of light in vacuum, I is the average ionization energy of the material, T_{\max} is the maximum kinetic energy that can be given to a free electron in an interaction, δ is a correction based on the electron density, and $\beta\gamma = p/mc$, where p is the momentum and m is the mass of the charged particle. Equation (2.1) shows that different charged particles (electron, muon, pion, kaon, proton, and deuteron) with the same momentum p can result in different energy loss while traversing the TPC volume.

Figure 2.16 shows energy loss for primary and secondary particles in the TPC as a function of particle momentum. The red lines are the theoretical predictions and the bands represent the measured values of dE/dx . The prominent proton, deuteron, and muon bands come from secondary interactions in the beam pipe and IFC, and from pion and kaon decays. Pions and protons can be separated from each other up to 1 GeV/ c . The particle identification is quantified by the variable N_σ , which has a Gaussian distribution,

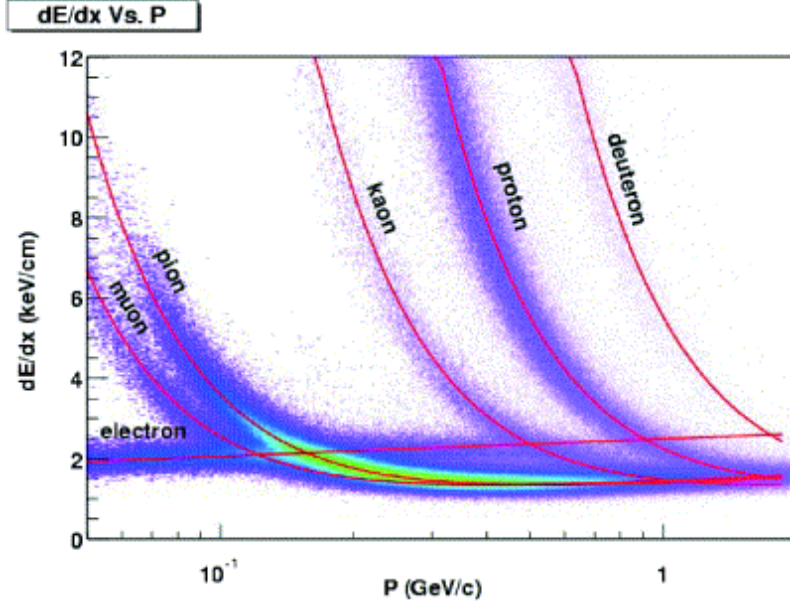


Figure 2.16: The energy loss distribution for primary and secondary particles in the STAR TPC as a function of the p_T of the primary particle.

and hence useful to extract yields of various particle species. For example, for charged pion identification, it is defined as:

$$N_{\sigma\pi} = \left[\left(\frac{dE}{dx} \right)_{\text{meas.}} - \left\langle \frac{dE}{dx} \right\rangle_{\pi} \right] / \left[\frac{0.55}{\sqrt{N}} \left(\frac{dE}{dx} \right)_{\text{meas.}} \right] \quad (2.2)$$

Here N is the number of hits for a track in the TPC, $\left(\frac{dE}{dx} \right)_{\text{meas.}}$ is the measured energy loss of a track and $\left\langle \frac{dE}{dx} \right\rangle_{\pi}$ is the mean energy loss for charged pions. The charged kaons and protons also have similar variables, $N_{\sigma K}$ and $N_{\sigma p}$, respectively. Various particles like pions, kaons, and protons can be identified by applying cuts on $N_{\sigma\pi}$, $N_{\sigma K}$, and $N_{\sigma p}$, respectively.

2.8 Forward Time Projection Chamber

The FTPCs [9] were constructed to extend the phase space coverage of the STAR experiment to the region $2.5 < |\eta| < 4.0$. Figure 2.17 shows the schematic diagram of the FTPC. The FTPCs are situated on both sides from center of the TPC along the beam pipe. Both FTPCs have cylindrical shape with a 75 cm diameter and 120 cm length. Due to the limited space, gas used in the FTPC is a mixture of equal parts Ar and CO₂ by

weight to account for the short drift length of only 23 cm. The gas mixture has a low diffusion coefficient for electrons and a small Lorentz angle [34], and shows no or little ageing. The short drift length is not sufficient to extract the dE/dx information to identify particles, but charged particle momentum can be measured between 2.5 and 4.5 GeV/ c in full azimuth. The FTPC has a radial drift field and readout chambers located in 5 rings on the outer cylinder surface. The radial drift configuration was chosen to improve the two-track separation in the region close to the beam pipe where the particle density is highest. The FTPCs are used to measure momenta and production rates of positively and negatively charged particles as well as neutral strange particles. In high multiplicities, event-by-event observables like $\langle p_T \rangle$, fluctuations of charged particle multiplicity, and collective flow anisotropies can be studied in FTPC.

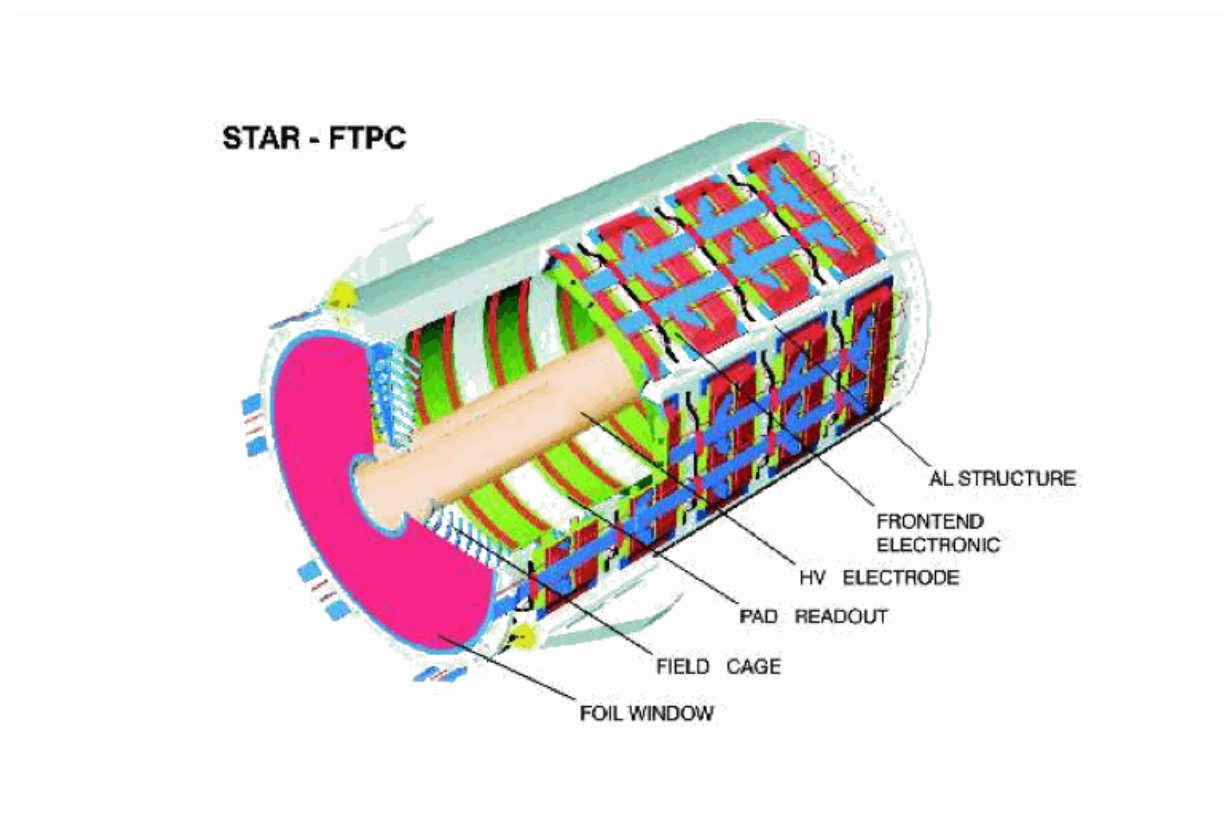


Figure 2.17: Schematic diagram of an FTPC for the STAR experiment.

2.9 Photon Multiplicity Detector

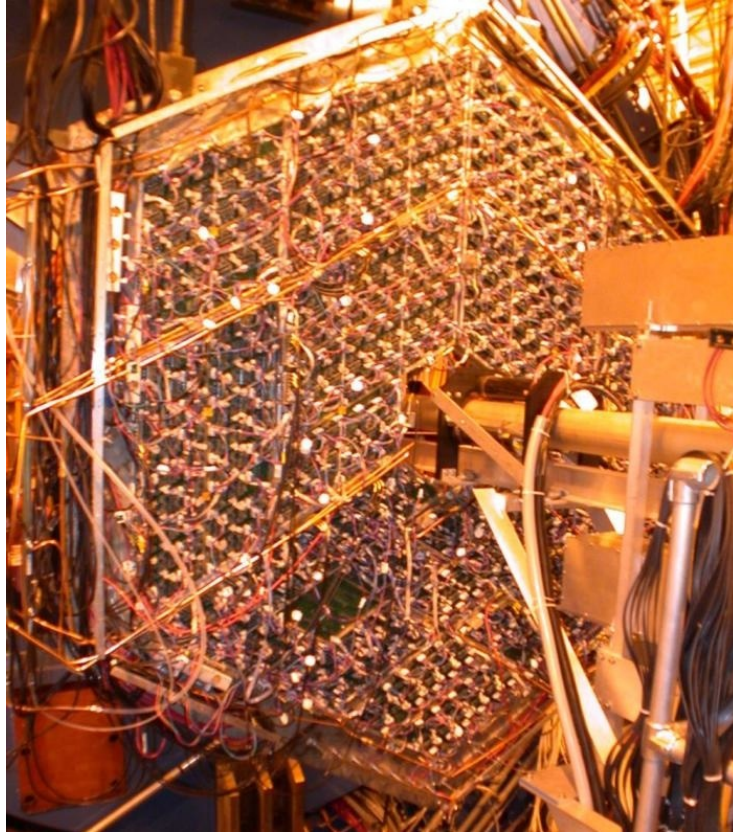


Figure 2.18: Picture of the PMD after complete installation of electronics at the STAR experiment.

We have discussed the motivations for the photon multiplicity measurements using the PMD in section 5 of the previous chapter. In this section and its subsections, we will discuss the principle of Photon Multiplicity Detector, its technical details and other characteristics. The results from the data collected by the PMD will be discussed in next chapter.

The Photon Multiplicity Detector (PMD) is installed on east wall of the wide angle hall in the STAR experiment. The PMD is designed to measure photon multiplicity in the forward region, where the calorimeters are not efficient due to high particle density. The PMD in the STAR experiment covers a pseudorapidity range $-2.3 < \eta < -3.7$ with full azimuthal angle. It can measure photons with p_T as low as 20 MeV/ c [35, 36].

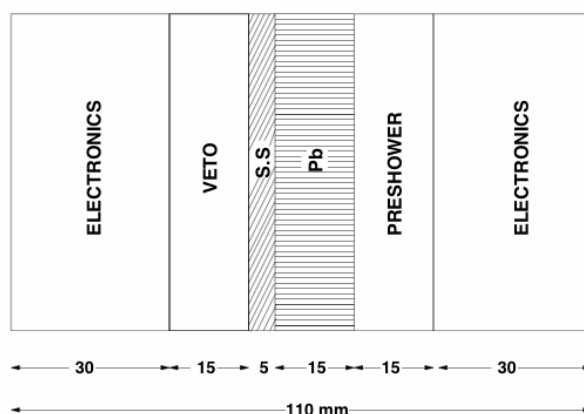


Figure 2.19: Cross-sectional schematic of the PMD [37] showing the veto plane, lead converter and preshower plane. SS is the support plane on which the lead plates and gas chambers are mounted.

Figure 2.18 shows the picture of the PMD installed at the STAR experiment after the complete installation in Brookhaven National Laboratory. Figure 2.4 shows the position of the PMD relative to other STAR detectors. It is installed at -539 cm from the center of the vertex and is kept outside the STAR magnet.

The basic principle of the PMD is discussed below. Figure 2.19 shows the schematic design of the PMD. The PMD consists of highly segmented detector called as preshower detector, placed behind a lead converter of thickness three radiation length. A photon produces an electromagnetic shower on passing through the converter (see Fig. 2.20). These shower particles produce signals in several cells of the sensitive volume of the detector. Charged hadrons usually affect only one cell and produce a signal resembling those of Minimum Ionizing Particles (MIPs)². The thickness of converter is optimized such that the conversion probability of photons is high and transverse shower spread is small to minimize shower overlap in high multiplicity environment. In order to have better hadron rejection capability, another plane of the detector of identical dimension as of the preshower part is placed before the lead plate. This acts as a veto for charged particles, and accordingly called as Charged Particle Veto (CPV). The photon-hadron

²Minimum Ionizing Particle (MIP): The mean rate of energy loss for charged particles in a medium is given by Bethe-Bloch equation. Most of the relativistic particles have energy loss rates close to a minimum value, and are said to be minimum ionizing particles or mips [38].

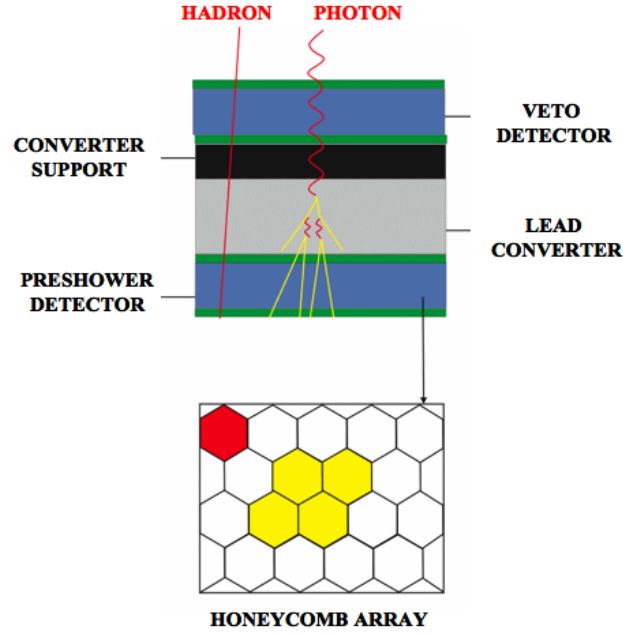


Figure 2.20: Principle of Photon Multiplicity Detector. Single cell hit is due to hadron while the signal deposited in contiguous cells is due to photon.

discrimination in the PMD is also illustrated in the Table 2.2.

The PMD is based on a proportional counter design using Ar + CO₂ gas mixture in ratio 70:30 by weight. The choice of this gas mixture is due to its insensitivity to neutrons. Since the multiplicity is very high at RHIC, the PMD is designed with considerations that (i) multi-hit probability should be less, (ii) MIP should be contained in one cell, and (iii) low energy δ -electrons should be prevented from travelling to nearby cells to avoid cross-talks. The PMD uses honeycomb cellular geometry with wire readout. The copper in

Table 2.2: Response of a photon and hadron in the PMD

Incident particle	Signal in veto	Signal in preshower	Energy deposited	Number of cells hit
Hadron	yes	yes	MIP	~ 1
Photon	no	yes	Large ($> \text{MIP}$)	> 1

Table 2.3: Basic parameters of the STAR PMD

Parameter	Value
Detectors (or planes)	2 (Veto and Preshower)
Total cells	82,944 (41,472 in one plane)
Cell area	1 cm ²
Cell depth	0.8 cm
Anode wire diameter	20 μ m
Area of the detector	4.2 m ²
Weight of detector	900 Kg
Gas used	Ar + CO ₂ (70:30)
Distance from vertex	−539 cm
η coverage	−2.3 to −3.8
ϕ coverage	0 – 360 ⁰

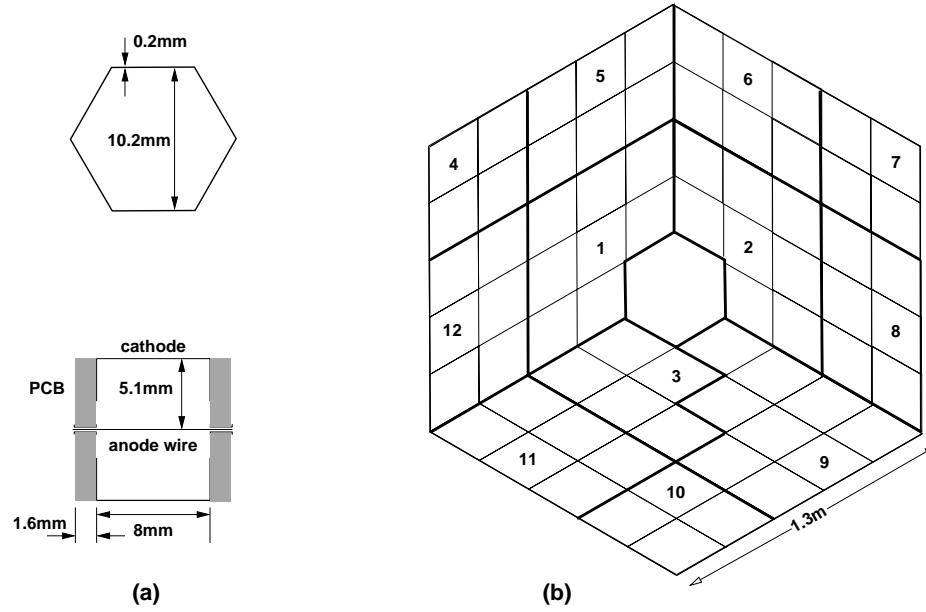


Figure 2.21: (a) Unit cell schematic with cross-section showing the dimensions and the cathode extension, (b) Layout of the STAR PMD. Thick lines indicate supermodule boundaries. There are 12 supermodules each in the preshower plane and the veto plane. Divisions within a supermodule denote unit modules.

honeycomb body forms the common cathode and is provided a large negative potential. The gold-plated tungsten wire (20 μm diameter) acts as anode and is kept at ground potential. The copper honeycomb also supports the printed circuit boards (PCBs) which are used for signal collection and for extension of cathode required for proper field shaping. Further details can be found in Refs. [37, 39]. The basic parameters of the STAR PMD are given in Table 2.3.

The PMD consists of an array of hexagonal cells. A schematic diagram of *unit cell* is shown in Fig. 2.21(a). The longitudinal section of unit cell is also shown illustrating the use of extended cathode for field shaping. This design is selected after performing several simulation studies and prototype tests to ensure uniform charged particle detection efficiency throughout the cell [16]. A *unit module* is formed by honeycomb of 24×24 cells. The shape of unit module is rhombus of side ~ 254 mm having identical boundaries on all four sides. Cell walls at the boundary are kept half as thick as those inside so that adjacent unit modules join seamlessly. A set of unit modules are enclosed in a gas-tight chamber called *supermodules*. The number of unit modules may vary from 4 to 9 within a supermodule. The STAR PMD consists of 24 supermodules arranged in the form of a hexagon as shown in Fig. 2.21(b). The choice of this geometry ensures full azimuthal coverage with minimum number of supermodules. Further technical details of cells, unit modules, supermodules, their fabrication and assembly can be found in Ref. [15].

The PMD is designed in two halves with a vertical split axis. The two halves can be independently assembled and installed. The PMD is hanged at the STAR experimental site with the help of support structure. The drawing of the support structure is shown in Fig. 2.22. It has two parts: (a) the support plates, and (b) the suspension movement mechanisms. A 5 mm thick flat stainless steel plate is used to support the lead converter plates and supermodules in each half of the PMD. The two halves of the detector are supported on the girders and hang freely in a vertical position. The support structure allows both x and z movements of the detector. Each half of the detector can be separated for access by a smooth independent movement controlled by limit switches. The services of the two halves are also independent. When fully open, the two halves provide sufficient clearance for the pole-tip support of the STAR magnet to move in. Figure 2.23 shows

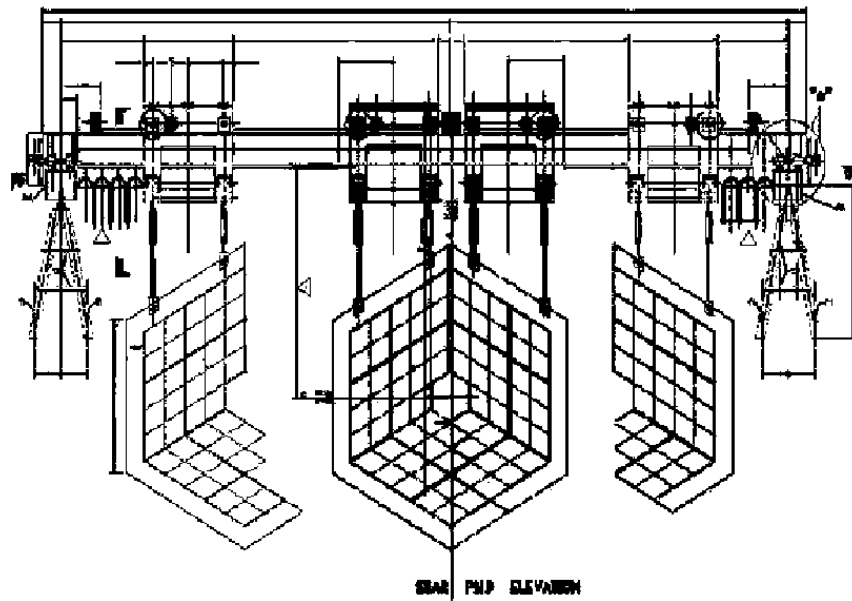


Figure 2.22: PMD support mechanism. The inner hexagonal part shows the two halves joined during data taking operation. The two halves, when separated for servicing, look as shown on the right and left.

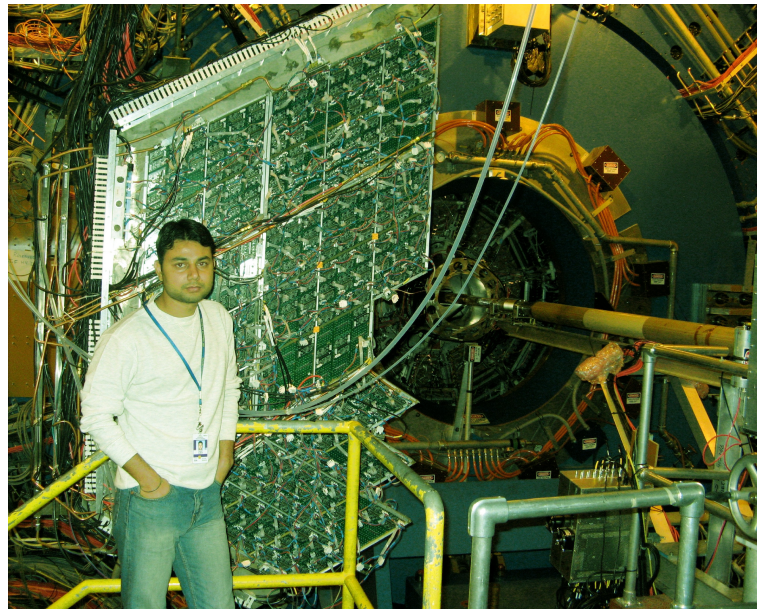


Figure 2.23: Picture of the PMD after completion of data taking at STAR experiment. The PMD is disassembled so only one half is visible in the figure. Beam pipe can also be seen in the picture.

Table 2.4: Specifications of a GASSIPLEX chip.

Parameter	Value
Linear dynamic range	-250 to -300 fC
Conversion gain	4.9 mV/fC
Range peaking time	400 – 1000 ns
Base line recovery	$\leq 0.5\%$ after $3 \mu\text{s}$
Noise at peaking time	$485 e^-$ RMS at 0 pF
Noise slope at peaking time	$15.8 e^-$ RMS/pF
Power dissipation	6 mW/ch
Analog readout speed	10 MHz max.

the picture of the PMD, disassembled after the completion of data taking. Only one half of the PMD is visible in the picture. The edges of the support plate are also used for mounting the gas feed manifolds, shoe boxes for low voltage supplies and general support for distribution of cables onto the detector.

2.9.1 Front-End Electronics and Readout

The signals from the PMD are processed through the front-end electronics which employs 16-channel GASSIPLEX chips developed at CERN [40]. These chips provide analog multiplexed signals and readout using the custom built ADC board (C-RAMS) which are obtained from CAEN, Italy. C-RAMS can handle a maximum of 2000 multiplexed signals. A GASSIPLEX chip consists of a charged sensitive amplifier (CSA), deconvoluted/switchable filter, a shaping amplifier and a Track and Hold (T/H) to store charges in a capacitor [41]. Table 2.4 lists detailed specifications of the GASSIPLEX chip. Figure 2.24 shows the block diagram of the PMD front-end electronics readout system. The readout of the entire PMD has been divided into 48 chains. Table 2.5 provides information of chains used in the STAR PMD. Each readout chain consists of the following components:

- (a) A translator board,

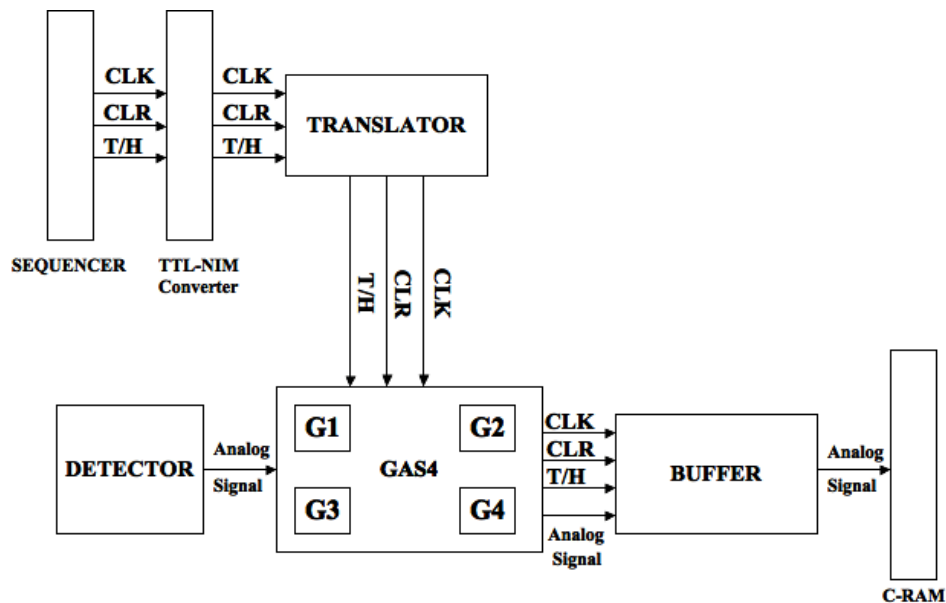


Figure 2.24: Block diagram of the front-end electronics readout system.

- (b) 27 Front-End Electronic Boards (FEE), each consisting of 4 GASSIPLEX chips, and
- (c) A buffer amplifier board.

These three components are discussed below.

- (a) Translator Board: It converts NIM levels of all control signals into the level required for the operation of GASSIPLEX chips. Operating voltage for these chips is $\pm 2.75\text{V}$ and hence all the NIM signals are to be translated to 0 to 2.75V levels.
- (b) FEE board: The cells in the unit modules are arranged in clusters consisting of 8×8 cells connected to a 70-pin connector. This cluster of 64 cells is read out by a FEE board having four GASSIPLEX chips. One such board is shown in Fig. 2.25. For geometrical considerations, the FEE board is also made in rhombus shape. When all the boards are placed on the detector, they almost fully cover the detector area. This arrangement helps to reduce the material and also provides a ground shield for the detector.

To reduce voltage drops over a long chain of 1728 channels, a bus-bar like design has been adopted to provide power to the FEE boards. To protect the input channels

Table 2.5: Electronic chain in STAR PMD.

Parameter	Value
Total chains	48 (24 chains per plane)
Unit modules per chain	3
Channels in a chain	1728
FEE boards per chain	27
Translator boards	1
Buffer boards	1

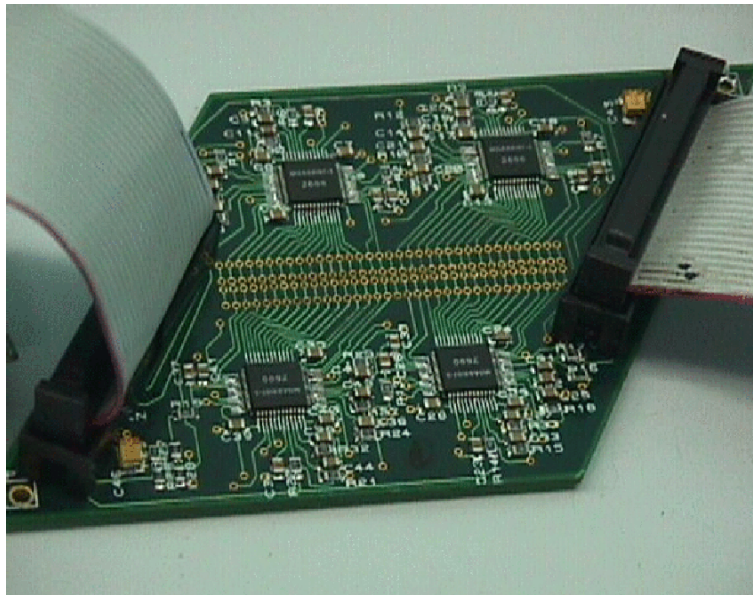


Figure 2.25: Photograph of a FEE board with four GASSIPLEX chips.

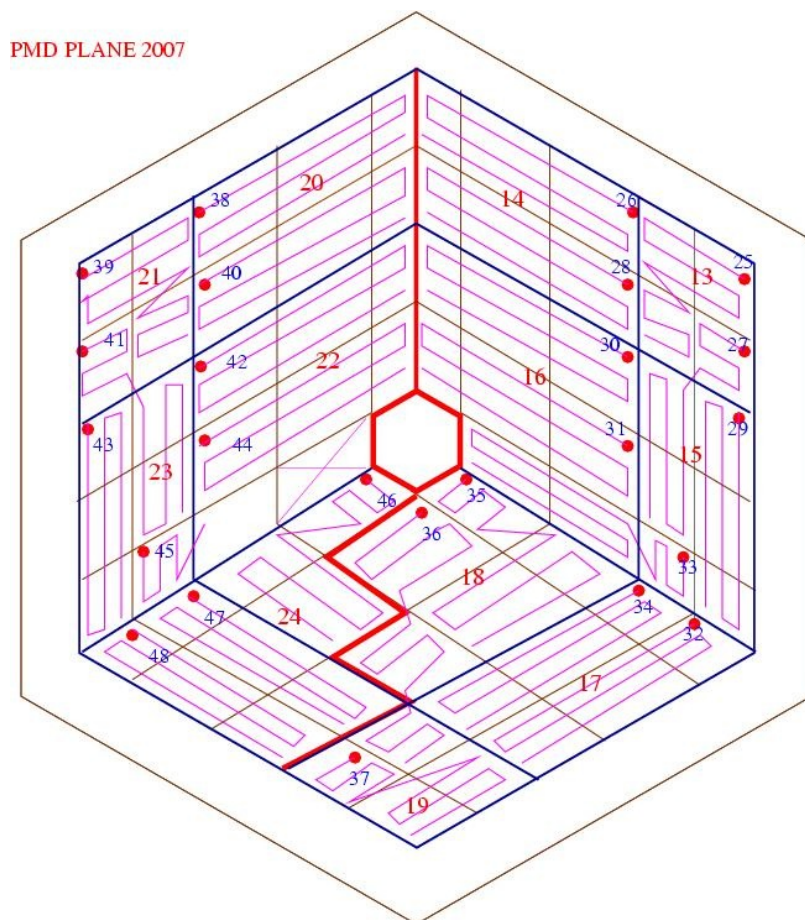


Figure 2.26: Chain configuration of the preshower plane of the PMD used during run 7 Au+Au collisions at $\sqrt{s_{NN}} = 200$ GeV. The view is from the tunnel side.

against high voltage spikes, a provision has been made on the board layout to connect a diode protection circuit.

- (c) Buffer amplifier board: The buffer amplifier is used for the transmission of a train of analog multiplexed signals to the readout module via a low impedance cable.

Figure 2.26 shows the chains and their numbering in the preshower plane spanning different supermodules. This numbering scheme is implemented for the run 7 Au+Au collisions at $\sqrt{s_{NN}} = 200$ GeV in 2007.

Digitization using C-RAMS requires that all multiplexed pulses within a chain should have the same polarity. In order to read the full chain, the pedestals in the chain need to be adjusted to the minimum of the pedestals in the chain. This shifting of

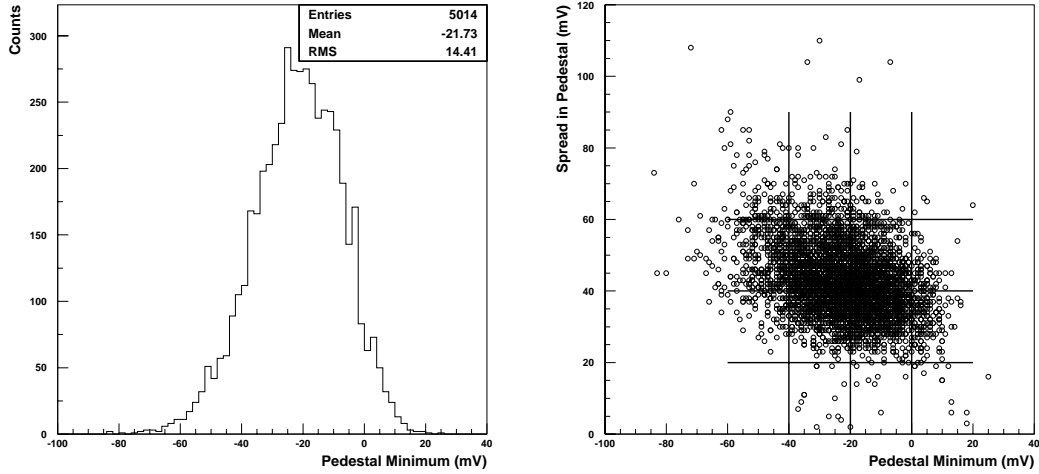


Figure 2.27: Left panel: Pedestal minimum values (in mV) for 5000 chips. Right panel: Pedestal minimum vs. pedestal spread for these chips. Lines are drawn to suggest the grouping of chips for a uniform chain.

the pedestal effectively reduces the dynamic range. To minimize the reduction in dynamic range due to pedestal adjustment, we need to select the chips for a chain having minimum pedestals in very close range. For proper quality control in the assembly of FEE boards, each GASSIPLEX chip has been tested for full functionality of each channel. In addition the pedestals of all the channels have been measured. The minimum pedestal as well as the spread in pedestal has been determined for each chip. Fig. 2.27 (left panel) shows the distribution of pedestal minima and Fig. 2.27 (right panel) shows the scatter plot of pedestal minima vs. pedestal spread for 5000 chips. It is seen that we can select chips of four categories having close ranges of pedestal minima and pedestal spreads. The narrow width of the distribution shows that the usable number of chips is a large fraction of the total number of chips tested.

2.9.2 PMD Trigger and Data Acquisition

The Level 0 (L0) in STAR issues a trigger within $1.5 \mu\text{s}$ of the occurrence of the interaction [17]. However, peaking time of the GASSIPLEX chips used in the FEE boards is $1.2 \mu\text{s}$. So a pre-trigger is needed for the PMD. The pre-trigger is generated for the PMD within 500 ns of the interaction from the ZDC coincidences. As soon as ZDC gets any

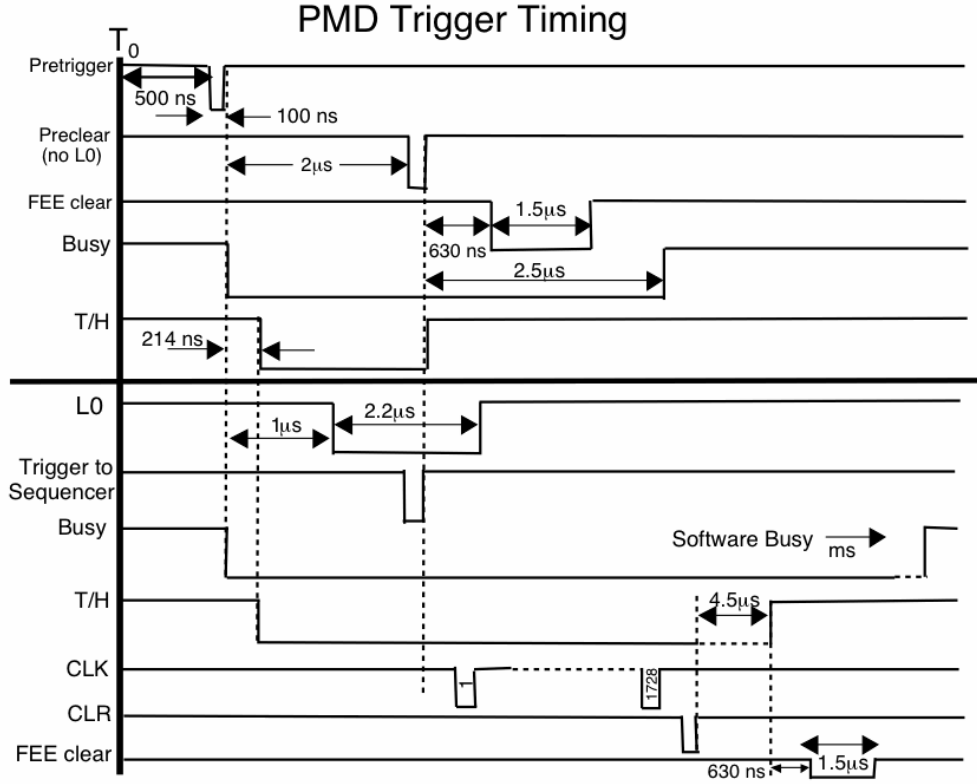


Figure 2.28: The PMD timing diagram is shown with different trigger signals arriving at the calculated times to record an event.

signal it sends a pre-trigger to the PMD and the charge accumulation in the GASSIPLEX chip. The trigger scheme for the PMD is described below. When a pre-trigger is reached, a BUSY signal is sent and after 814 ns of the RHIC collisions, Track/Hold (T/H) signals are sent to the FEE. If L0 has not arrived within the pre-defined time, T/H and BUSY are cleared. Since the baseline recovery time of the FEE is 4.5 μ s, BUSY is cleared after 4.5 μ s of its start. If L0 has arrived within the pre-defined time, T/H and BUSY signals are sent. A check is made to see if for the present L0, a corresponding pre-trigger exists. If it exists, trigger signal is sent to sequencer which generates the signals Clocks (CLK), T/H, CLR, BUSY, and CONV. The CLK signals are sent to FAN IN and FAN OUT modules and distributed to various chains. Similar distributions are done for T/H and CLR signals. The CONV is passed through a delay module and fed to CRAMS. CRAMS digitize the analog signal and send the ready signal to the sequencer and the readout of this digitized signal starts. After the readout, the FEE clear signal is sent and also the

Software BUSY (VME_{BUSY}) signal is withdrawn. If the corresponding pre-trigger does not exist for the present L0, then BUSY is cleared. Figure 2.28 shows the schematic timing diagram of the logic described above.

Bibliography

- [1] <http://www.bnl.gov/rhic/>.
- [2] K. H. Ackermann *et al.*, Nucl. Instr. Meth. A **499**, 624 (2003).
- [3] K. Adcox *et al.*, Nucl. Instr. Meth. A **499**, 469 (2003).
- [4] M. Adamczyk *et al.*, Nucl. Instr. Meth. A **499**, 437 (2003).
- [5] B. B. Back *et al.*, Nucl. Instr. Meth. A **499**, 603 (2003).
- [6] R. Bellwied *et al.*, Nucl. Instr. Meth. A **499**, 640 (2003).
- [7] L. Arnold *et al.*, Nucl. Instr. Meth. A **499**, 652 (2003).
- [8] M. Anderson *et al.*, Nucl. Instr. Meth. A **499**, 659 (2003).
- [9] K. H. Ackermann *et al.*, Nucl. Instr. Meth. A **499**, 713 (2003).
- [10] A Ring Imaging Cherenkov Detector for STAR, STAR note 349, STAR/ALICE RICH Collaboration (1998); ALICE Collaboration, Technical Design and Report, Detector for High Momentum PID, CERN/LHCC 98-19; A. Braem *et al.*, Nucl. Instr. Meth. A **499**, 720 (2003).
- [11] W. J. Llope *et al.*, Nucl. Instr. Meth. A **522**, 252 (2004).
- [12] B. Bonner *et al.*, Nucl. Instr. Meth. A **508**, 181 (2003); M. Shao *et al.*, Nucl. Instr. Meth. A **492**, 344 (2002).
- [13] M. Beddo *et al.*, Nucl. Instr. Meth. A **499**, 725 (2003).
- [14] C. E. Allgower *et al.*, Nucl. Instr. Meth. A **499**, 740 (2003).

- [15] M. M. Aggarwal *et al.*, Nucl. Instr. Meth. A **499**, 751 (2003).
- [16] M. M. Aggarwal *et al.*, Nucl. Instr. Meth. A **488**, 131 (2002), nucl-ex/0112016.
- [17] F. S. Bieser *et al.*, Nucl. Instr. Meth. A **499**, 766 (2003).
- [18] C. Adler *et al.*, Nucl. Instr. Meth. A **470**, 488 (2001).
- [19] J. M. Landgraf *et al.*, Nucl. Instr. Meth. A **499**, 762 (2003).
- [20] H. J. Crawford and V. Lindenstruth, Apparatus and method for managing digital resources by passing digital resource tokens between queues, US Patent 5, 918, 055, 1999.
- [21] F. Bergsma *et al.*, Nucl. Instr. Meth. A **499**, 633 (2003).
- [22] STAR Collaboration, Proposal for a large area time of flight system for STAR, (2004).
- [23] E. Cerron Zeballos *et al.*, Nucl. Instr. Meth. A **374**, 132 (1996); M. C. S. Williams *et al.*, Nucl. Instr. Meth. A **478**, 183 (2002).
- [24] J. Adams *et al.* (STAR Collaboration), Phys. Lett. B **616**, 8 (2005).
- [25] H. Wieman *et al.*, IEEE Trans. Nuc. Sci. **44**, 671 (1997).
- [26] J. Thomas *et al.*, Nucl. Instrum Meth. A **478**, 166 (2002).
- [27] STAR Collaboration, *The STAR Conceptual Design Report*, June 15, 1992 LBL-PUB-5347.
- [28] STAR Collaboration, *STAR Project CDR Update*, Jan. 1993 LBL-PUB-5347 Rev.
- [29] L. Kotchenda *et al.*, Nucl. Instr. Meth. A **499**, 703 (2003).
- [30] L. Kumar (for the STAR Collaboration), SQM-2008, QM-2009; L. Kumar (for the STAR Collaboration), J. Phys. G: Nucl. Part. Phys. **36**, 064066 (2009); L. Kumar (for the STAR Collaboration), Nucl. Phys. A **830**, 275c (2009).

- [31] W. Blum and L. Rolandi, Particle Detection with Drift Chambers, Springer-Verlag, (1993).
- [32] H. Bichsel, “Energy loss in thin layers of argon”, STAR Note 418, <http://www.star.bnl.gov/star/starlib/doc/www/sno/ice/sn0418.html>; H. Bichsel, “Comparison of Bethe-Bloch and Bichsel Functions”, STAR Note 439, <http://www.star.bnl.gov/star/starlib/doc/www/sno/ice/sn0439.html>.
- [33] W M Yao et al., J. Phys. G: Nucl. Part. Phys. **33**, 1 (2006).
- [34] X. Bittl *et al.*, Nucl. Instr. Meth. **A 398**, 249 (1997).
- [35] “A Preshower PMD for STAR Experiment”, STAR Note 310 (1997).
- [36] “Photon Multiplicity Detector for STAR : Technical Proposal”, VECC Internal Report VECC/EQG/00-04, May 2000, revised : Jan. 2001.
- [37] “Photon Multiplicity Detector for STAR : Technical Proposal”, VECC Internal Report VECC/EQG/00-04, May 2000, revised: Jan. 2001.
- [38] Particle Data Group, C. Caso *et al.*, Eur. J. Phys. C **3**, 1 (1998).
- [39] ALICE PMD Technical Design Report, CERN/LHCC 99-32 (1999).
- [40] ALICE HMPID Technical Design Report, CERN/LHCC 98-19 (1998).
- [41] ALICE Dimuon Forward Spectrometer Technical Design Report, CERN/LHCC 99-22.

Chapter 3

PHOTON MULTIPLICITY MEASUREMENTS

The Photon Multiplicity Detector (PMD) has two planes, the Charged Particle Veto (CPV) plane and preshower plane, separated by a lead converter plate of three radiation length ($3X_0$). A photon passing through the lead converter in front of the preshower plane of the PMD, gives electromagnetic showers. The electrons and positrons coming out of the shower hit a group of cells on the preshower plane. A clustering algorithm is used to obtain photon clusters in each event. Each photon cluster is characterized by its total ADC (E_{dep}) and (η, ϕ) position of its center. The photon clusters are distinguished from the charged particle clusters by using the following criteria:

- (a) Number of cells affected in the preshower plane. The charged particles mostly hit one cell in the preshower plane and photons usually give signal in more than one cell.
- (b) Energy deposited in the sensitive medium. The charged particles deposit less energy compared to photons in the preshower plane.

Following these two criteria, photon-like clusters can be obtained from the total detected clusters. The steps followed in the photon reconstruction are shown in the flow chart in Fig. 3.1. Various features of photon clusters, photon counting efficiency and purity, obtained using the GEANT simulation and the HIJING event generator for the PMD have been discussed in this chapter.

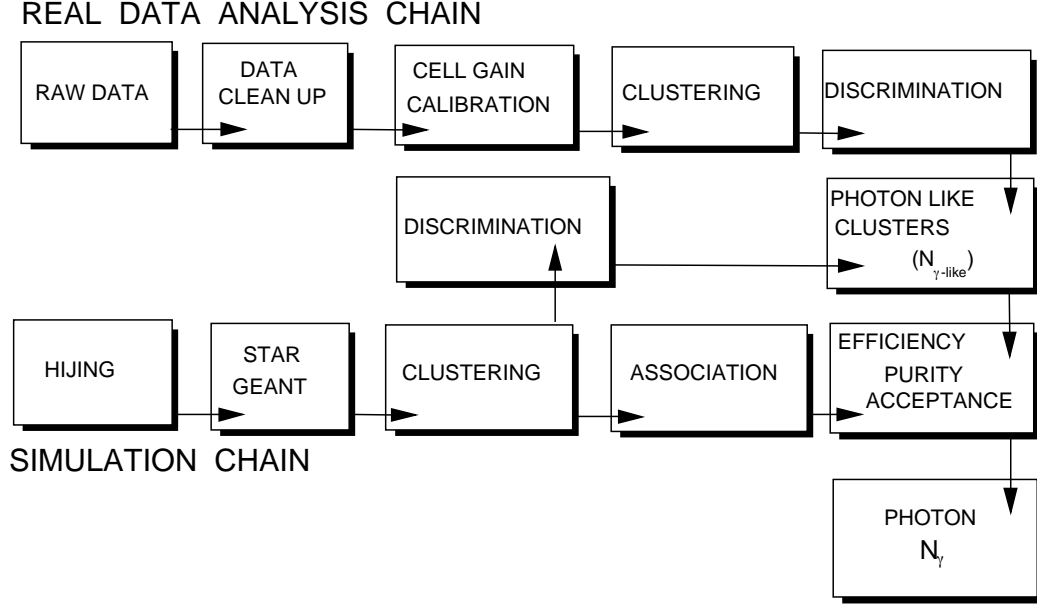


Figure 3.1: Flow chart for the photon reconstruction from PMD in real data and simulation.

The event generator used for the simulation study is a Monte Carlo model, HIJING (Heavy Ion Jet INteraction Generator) [1] with default settings. The simulation study also uses the detector simulation package GEANT (GEometry AND Tracking) [2], which incorporates the full STAR detector framework.

3.1 Data Selection

The new work presented in this thesis are the photon multiplicity results from Au+Au collisions at $\sqrt{s_{NN}} = 200$ GeV. The results are compared with previous measurements from Cu+Cu collisions at $\sqrt{s_{NN}} = 62.4$ and 200 GeV, and Au+Au collisions at $\sqrt{s_{NN}} = 62.4$ GeV [3]. All the analyses are done following the similar procedure. The steps involved in the data selection are described below.

- (a) **Trigger Selection:** The data acquisition is through minimum bias triggers. Minimum bias triggers are defined by the coincidence of two zero-degree calorimeters (ZDCs) [4] located at ± 18 m from the center of the interaction region along the

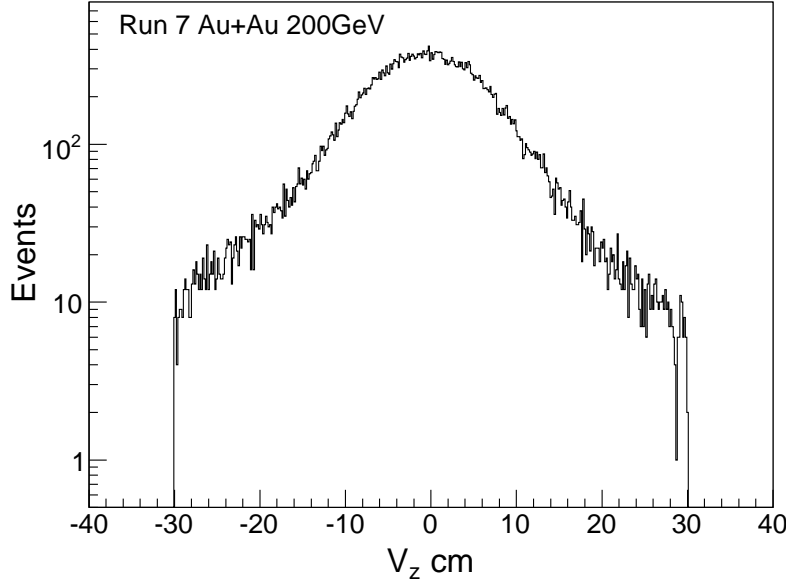


Figure 3.2: Vertex- z range selected for the Au+Au 200 GeV analysis.

beam line, using charged particle hits from an array of scintillator slats arranged in a barrel, called the Central Trigger Barrel (surrounding the TPC) and two Beam-Beam Counters [5]. The detailed description of triggers in the STAR experiment are given in Chapter 2.

- (b) **Vertex Selection:** Those events are selected for the analysis whose collision vertex position lie within ± 30 cm from the center of the TPC along the beam axis. Figure 3.2 shows the z -position of the vertex range selected for data analysis in Au+Au 200 GeV.
- (c) **Data Set Selection and Acceptance of PMD:** The present analysis is done by using the preshower plane of the PMD. The supermodule numbering for CPV plane goes from 1–12 and that for preshower plane goes from 13–24. Only those run numbers are used for the analysis for which the voltage applied to preshower plane is -1400 V. As will be discussed in section 3.2, the data showed abnormal behavior due to some supermodules not working properly in the preshower plane. These supermodules are declared “bad” and are not used for the analysis. These are

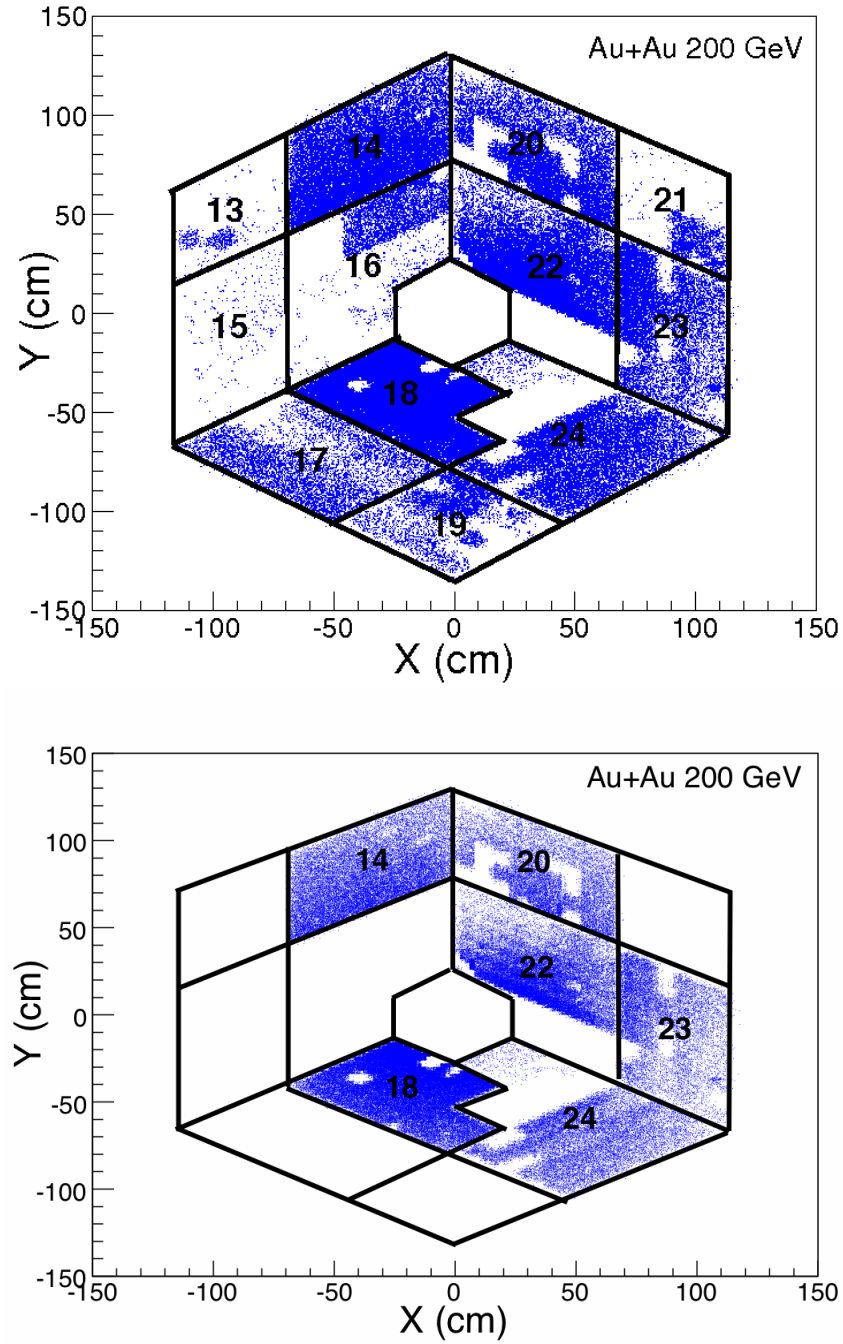


Figure 3.3: Top : XY display of hits on PMD (preshower plane) shown along with the supermodules which were working during the run time. The blank spaces are the dead areas during the run time. Bottom : XY display of PMD after the dead cell implementation and data clean-up. The supermodules shown here are used for data analysis.

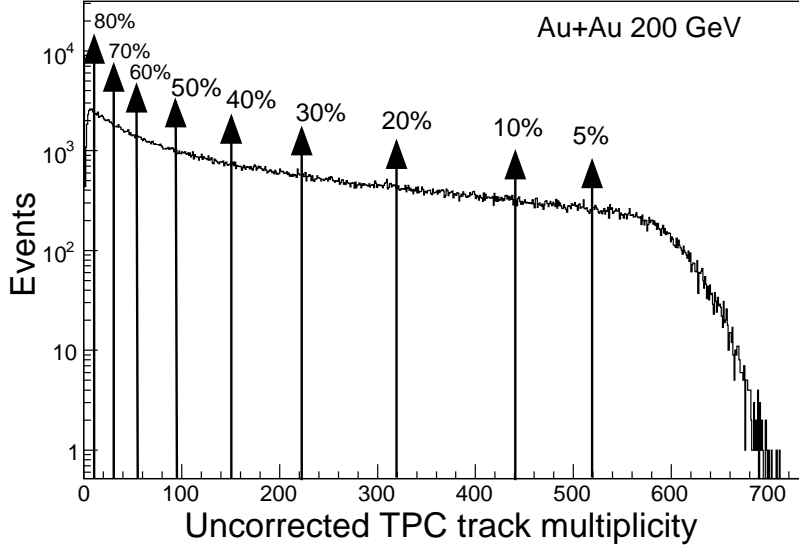


Figure 3.4: Centrality selection for Au+Au collisions at $\sqrt{s_{NN}} = 200$ GeV. The uncorrected TPC track multiplicity measured within $|\eta| < 0.5$, is shown. Vertical lines show the reference multiplicity cuts and the corresponding fraction of interaction cross-section. These multiplicity cuts decide the various centrality classes used in the analysis.

SM - 13, SM - 15, SM - 16, SM - 17, SM - 19 and SM - 21. The cells belonging to these supermodules are called as *dead cells*. In addition, there were cells belonging to particular chain or board, which caused problems in the data. Those are also called dead cells. These dead cells which are lost due to bad supermodules or otherwise, are accounted in the analysis by using the acceptance correction factor. This correction factor is then used to correct the photon multiplicity results. The acceptance correction factor is estimated by implementing the dead cells in the simulation. Figure 3.3 (top) shows the XY display of the preshower plane of PMD with supermodules working during the data taking period. The bottom figure shows the acceptance of the preshower plane after the dead cell implementation and data clean-up. The supermodules listed here are used for the Au+Au 200 GeV analysis.

- (d) **Centrality Selection:** The centrality selection is done by using the standard definition of the centrality determination adopted in STAR. This uses the uncorrected charged particle multiplicity (N_{ch}^{TPC}) measured event-wise in the TPC [6] within the

Table 3.1: Average number of participating nucleons ($\langle N_{\text{part}} \rangle$) for various collision centrality in Au+Au and Cu+Cu collisions at $\sqrt{s_{NN}} = 62.4$ and 200 GeV.

% cross section	$\langle N_{\text{part}}^{\text{AuAu}} \rangle$ 200 GeV	$\langle N_{\text{part}}^{\text{AuAu}} \rangle$ 62.4 GeV	$\langle N_{\text{part}}^{\text{CuCu}} \rangle$ 200 GeV	$\langle N_{\text{part}}^{\text{CuCu}} \rangle$ 62.4 GeV
0-5	$352.4^{+3.4}_{-4.0}$	$347.3^{+4.3}_{-3.7}$	—	—
0-10	$325.9^{+5.5}_{-4.3}$	—	$99.0^{+1.5}_{-1.2}$	$96.4^{+1.1}_{-2.6}$
5-10	$299.3^{+6.6}_{-6.7}$	$293.3^{+7.3}_{-5.6}$	—	—
10-20	$234.5^{+9.1}_{-7.8}$	$229.0^{+9.2}_{-7.7}$	$74.6^{+1.3}_{-1.0}$	$72.2^{+0.6}_{-1.9}$
20-30	$166.6^{+10.1}_{-9.6}$	$162.0^{+10.0}_{-9.5}$	$53.7^{+1.0}_{-0.7}$	$51.8^{+0.5}_{-1.2}$
30-40	$115.5^{+9.6}_{-9.6}$	$112.0^{+9.6}_{-9.1}$	$37.6^{+0.7}_{-0.5}$	$36.2^{+0.4}_{-0.8}$
40-50	$76.7^{+9.0}_{-9.1}$	$74.2^{+9.0}_{-8.5}$	$26.2^{+0.5}_{-0.4}$	$24.9^{+0.4}_{-0.6}$
50-60	$47.3^{+7.6}_{-8.1}$	$45.8^{+7.0}_{-7.1}$	$17.2^{+0.4}_{-0.2}$	$16.3^{+0.4}_{-0.3}$
60-70	$26.9^{+5.5}_{-6.5}$	$25.9^{+5.6}_{-5.6}$	—	—
70-80	$14.1^{+3.6}_{-4.0}$	$13.0^{+3.4}_{-4.6}$	—	—

pseudorapidity region $|\eta| < 0.5$. The reason for using the pseudorapidity region $|\eta| < 0.5$ instead of $|\eta| < 1.0$ for the centrality determination is to reduce the effects such as detector acceptance and efficiency on the centrality. The centrality bins are calculated as fraction of the uncorrected charged track multiplicity starting at the highest multiplicities. Figure 4.4 shows the centrality selection from the $N_{\text{ch}}^{\text{TPC}}$ in Au+Au collisions at $\sqrt{s_{NN}} = 200$ GeV. Table 3.1 lists the percentage cross sections, the average number of participating nucleons ($\langle N_{\text{part}} \rangle$) and the average number of binary collisions ($\langle N_{\text{coll}} \rangle$) for various collision systems at different collision energies. The $\langle N_{\text{part}} \rangle$ and the $\langle N_{\text{coll}} \rangle$ numbers have been obtained from Monte Carlo Glauber calculations [6] using Woods-Saxon distribution for the nucleons inside the nucleus. The systematic uncertainties on N_{part} and N_{coll} are determined by varying the Woods-Saxon parameters. The final systematic uncertainties associated in calculation of N_{part} and N_{coll} are presented in the Table 3.1 as upper and lower

errors.

3.2 Data Clean-up

The PMD data is cleaned by identifying and removing hot and noisy channels. Hot channels are those which fire abnormally high (~ 10 times more) in a chain than the average frequency of firing during the run time. The data clean-up is also necessary to look for some unexpected effects happened during data taking (e.g. some supermodules, chains and boards not working properly). These effects are taken into account during data analysis. The following steps are employed in data cleaning -

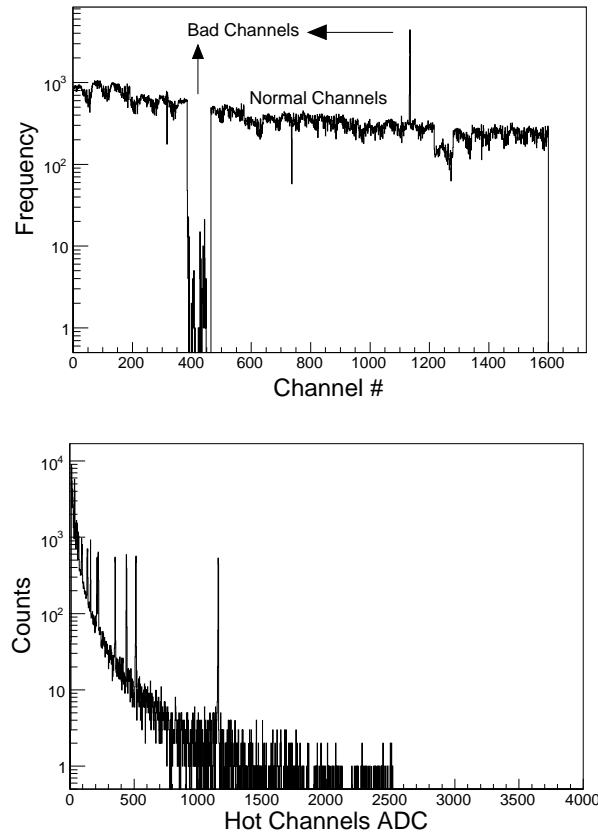


Figure 3.5: Top: Channel hit frequency of a typical chain over a large number of events. The peak reflects the hot channels for which the hit frequency is very high compared to rest of the channels in the chain for the same set of events. The channels not showing any hit frequency represent the dead or bad channels. Bottom: The cell ADC spectra for channels in a chain. The ADC spectra due to hot channels shows spikes.

(i) **Identification of hot channels:**

During data taking it was observed in some chains that few channels were giving abnormally large signal (~ 10 to 100 times) as compared to other channels in the chain for a similar multiplicity events. This can be easily seen from the hit frequency distribution of channels in a chain as shown in Fig. 3.5 (top). The bottom panel in this figure shows the cell ADC spectra for channels in a chain. It can be seen that the distribution has many spikes and has low ADC value due to presence of hot channels.

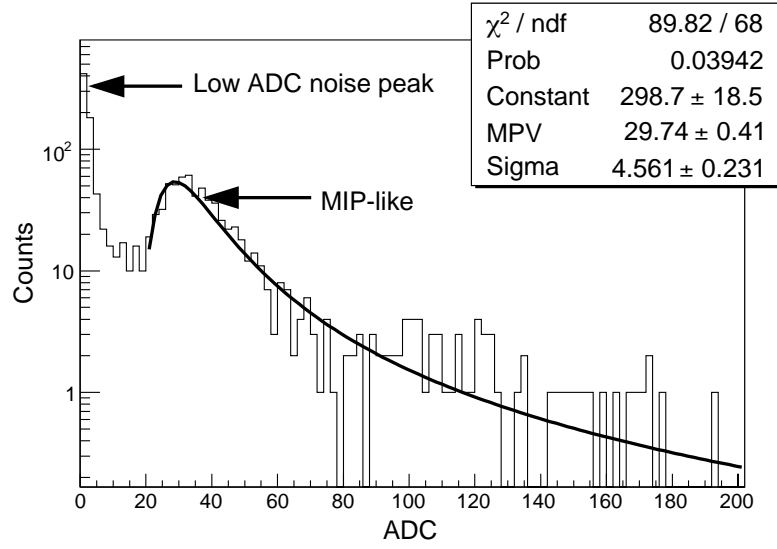


Figure 3.6: The cell ADC spectra of isolated cells for a typical chain in PMD. The low ADC peak observed are due to noisy channels.

(ii) **Removal of random noise with low ADC value:**

This effect is removed by looking at the ADC spectra of isolated cells for a chain. Isolated cells are those cells which have non-zero ADC value and are surrounded by six neighboring cells having zero ADC values. It was observed that a random low ADC value in some chains was present over large number of events. Figure 3.6 also shows the ADC distribution of low ADC noisy channels in a chain. These noisy channels were associated with the lower ADC values ($< 7\text{ADC}$). These low ADC noisy channels were removed by applying a uniform cut of 10 ADC on the cell level.

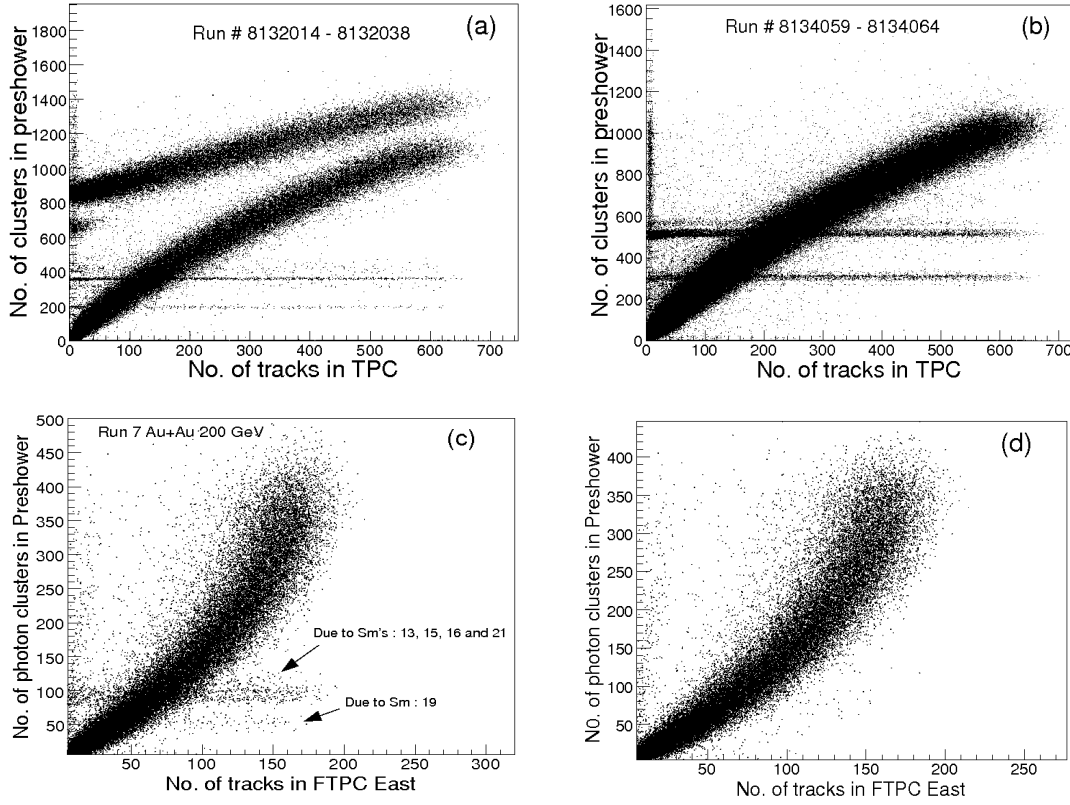


Figure 3.7: Problems in data due to bad run numbers and SMs before clean-up. (a) Correlation between the TPC track multiplicity and photon-like clusters in PMD. (b) Similar plot but after excluding bad runs from the analysis. (c) Correlation between the FTTPC tracks and the PMD clusters. (d) Similar plot but after removing bad supermodules. See text for details.

(iii) **Miscellaneous problems:**

Due to above problems in data, the distributions for various other global features also got affected and showed abnormal distributions. Figure 3.7 (a) shows the correlation plot between number of photon-like clusters in preshower plane and number of charged tracks in the TPC. We observe two correlation bands in this plot. After some investigations, it was found that these bands were due to the data corresponding to few bad run numbers. These run numbers are listed in the figure, run numbers 8132014 to 8132038. We removed these bad run numbers from the analysis and found the single correlation band as seen in Fig. 3.7 (b). But as seen in this figure, there were two horizontal bands suggesting further problem in

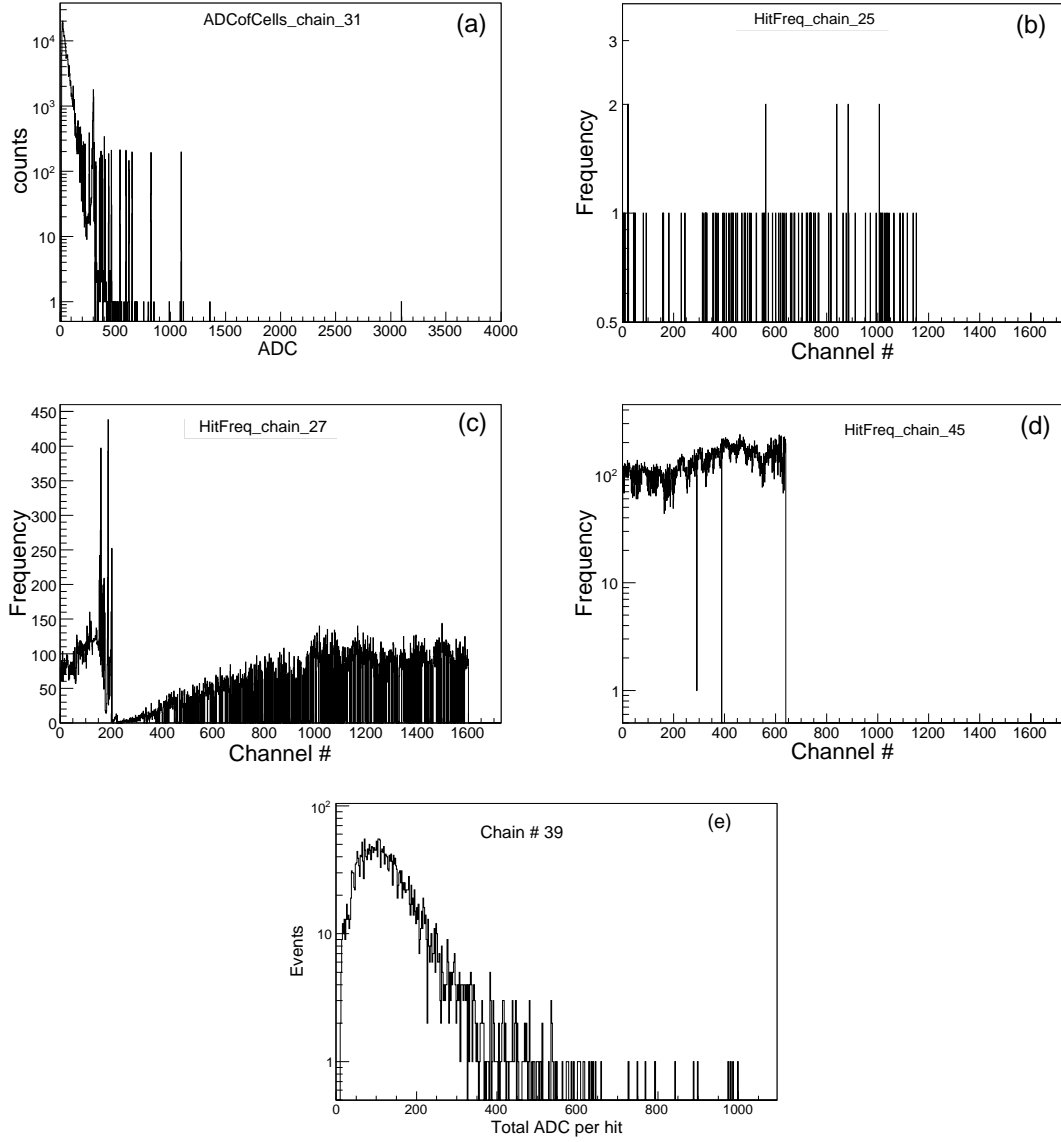


Figure 3.8: Examples of problems in data before clean-up: (a) ADC distribution of cells in chain - 31, (b) Hit frequency distribution of channels in chain - 25 (c) Hit frequency distribution of channels in chain - 27, (d) Hit frequency distribution of channels in chain - 45, and (e) Total ADC per hits for chain - 39.

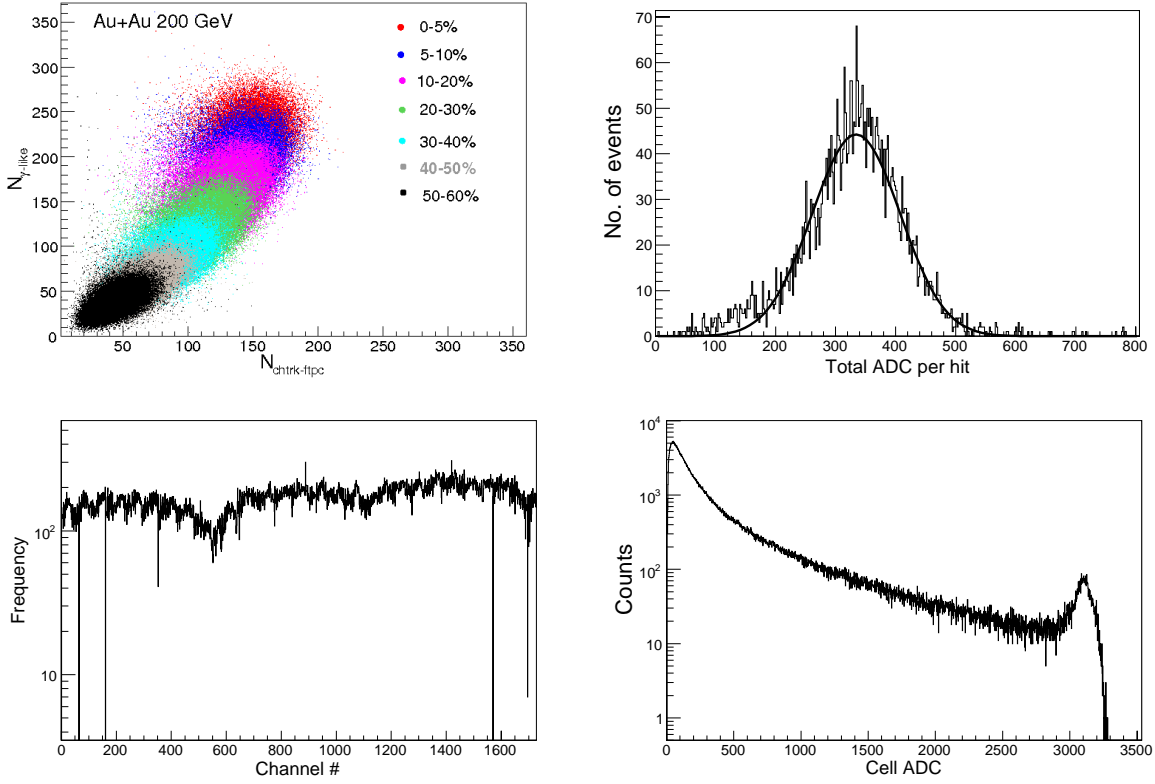


Figure 3.9: Global features of data after clean-up in Au+Au collisions at $\sqrt{s_{NN}} = 200$ GeV. Left-top plot shows the nice correlation between FTPC east track multiplicity and PMD photon-like clusters. Right-top plot shows a nice total ADC per hit distribution of a good chain. Left-bottom plot shows the hit frequency distribution of a good chain, and right-bottom plot shows the cleaned cell ADC spectra of a good chain.

data. After investigation, it was found that these problems arose because of some bad supermodules, viz. SM - 13, SM - 15, SM - 16, SM - 19 and SM - 21. The lower horizontal band was due to SM - 19, while the upper horizontal band was due to other supermodules (see Fig. 3.7 (c)). Figure 3.7 (d) shows a nice correlation between the number of photon-like clusters and number of charged tracks, after removing the bad supermodules.

Figure 3.8 depicts some more examples suggesting requirement of data cleaning. Figure 3.8 (a) Shows ADC distribution of cells in chain - 31. These represent bad channels and have the low ADC values which is basically a noise. Figure 3.8 (b) Shows the hit frequency distribution of all channels in chain - 25, called as bad

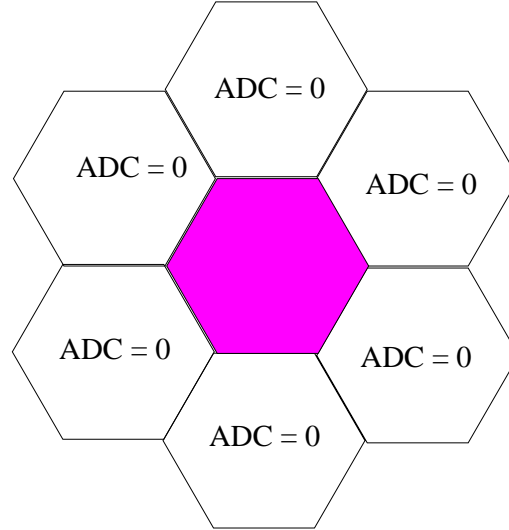


Figure 3.10: Schematic diagram of an isolated cell in PMD. A cell is said to be isolated (shaded) if it has a non zero ADC content and its six neighboring cells (non shaded) have zero ADC content.

chain since all channels in this chain are bad. Figure 3.8 (c) Shows hit frequency distribution of chain - 27 going partially bad, Fig. 3.8 (d) shows the hit frequency distribution of channels in a chain in which half of the channels are dead, and Fig. 3.8 (e) shows the bad distribution for the total ADC per hit of chain - 39. In view of the above, we identified the bad channels, bad chains, bad supermodules and bad run numbers which were not used in the present data analysis.

The global features after clean-up of PMD data can be seen in the Fig. 3.9.

3.3 Cell-to-Cell Gain Calibration

In the data analysis, it is essential to understand the response of each cell of the detector. This is because of the following reasons:

- (a) Response of each cell reflects the gain of a cell.
- (b) It is important that this response should be stable and does not vary much with η and ϕ .

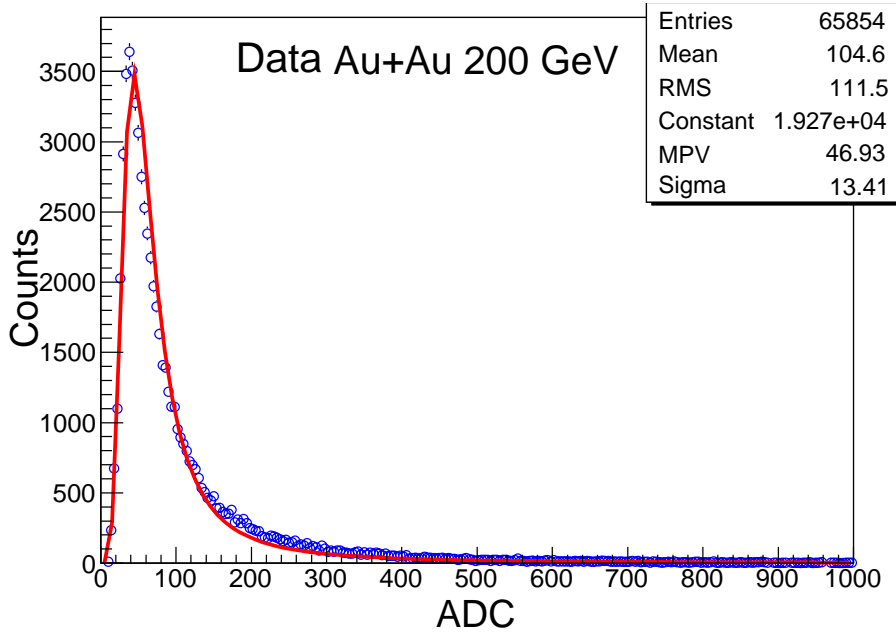


Figure 3.11: Typical isolated cell ADC spectra, along with fit to Landau distribution.

- (c) Test beam results [7] indicate that the response of charged particles and photons in the PMD is different. This difference in responses can be utilized to discriminate the photons from charged hadrons.

The response of each cell in the PMD is obtained by studying the isolated cell ADC spectra. A hexagonal cell is defined as isolated when it has a non zero ADC and its six neighbors have zero ADC. This is schematically shown in Fig. 3.10. The shaded cell represents the isolated cell. From the test beam data, we know that charged hadron hits are confined mostly to a single cell. The pulse height spectra obtained from the hit cell should follow Landau distribution since the typical energy deposited for a minimum ionizing charged particle [8] (MIP) in a thin detector follows a Landau distribution [9]. Figure 3.11 shows the isolated cell ADC distribution obtained from 200 GeV Au+Au data set with detector operating at -1400 V. As expected, the pulse height spectrum follows the Landau distribution. The isolated cell spectra are obtained with same procedure in simulation, as described above for data. In simulation the MPV and mean for the isolated cell energy deposited spectra is 1.1 keV and 2.5 keV respectively.

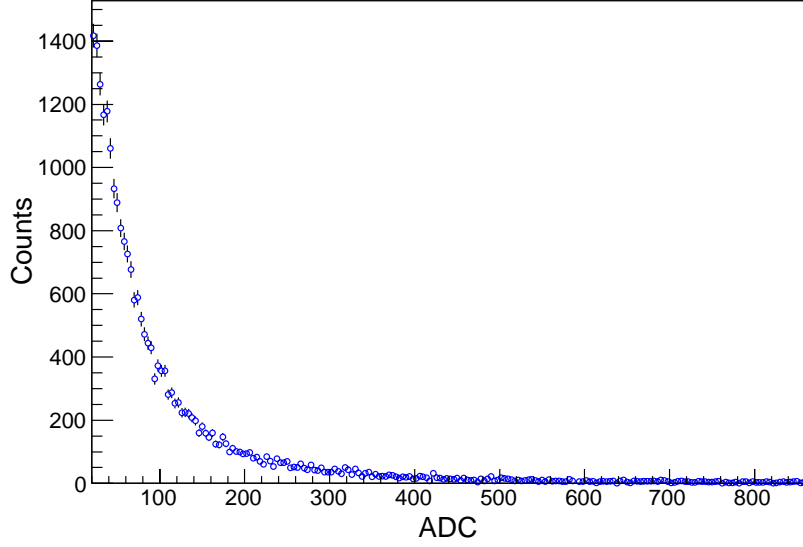


Figure 3.12: Typical isolated cell ADC spectra for a cell with low gain in data.

It is observed that for some of the cells the peak of the distribution is not developed properly in real data. This results in isolated cell ADC spectra for many cases not having a well defined peak as expected from the Landau distribution. One such typical example is shown in Fig. 3.12. Such cells might have low gain resulting in underdeveloped distribution. So we do not record good Landau distributions in some of the cells with relatively lower gains than other cells. Hence the peak of the distribution in data cannot be used for checking the uniformity of the gain for all cells in PMD or for finding out the cell-to-cell gain normalization factor. We further observe, for those cells which have well defined peak, the peak ADC (MPV) and mean ADC (MEAN) are linearly proportional. This is shown in Fig. 3.13. So we have decided to use the mean ADC of the isolated cell ADC distribution for calibration and studying the uniformity of response of the cells in the detector. From Fig. 3.13, it is evident that the gain varies by a factor two over the entire detector in real data. To study the cell-to-cell response in more detail, we look into the variation of mean of isolated cell ADC spectra in each SM-chain combination of PMD. The variation of the mean for few SM-chains are shown in the Fig. 3.14. From this figure, we observe that the gain or response of the cells within a SM varies within $\sim 10\%$. It may be mentioned that each SM is a separate gas tight and high voltage entity.

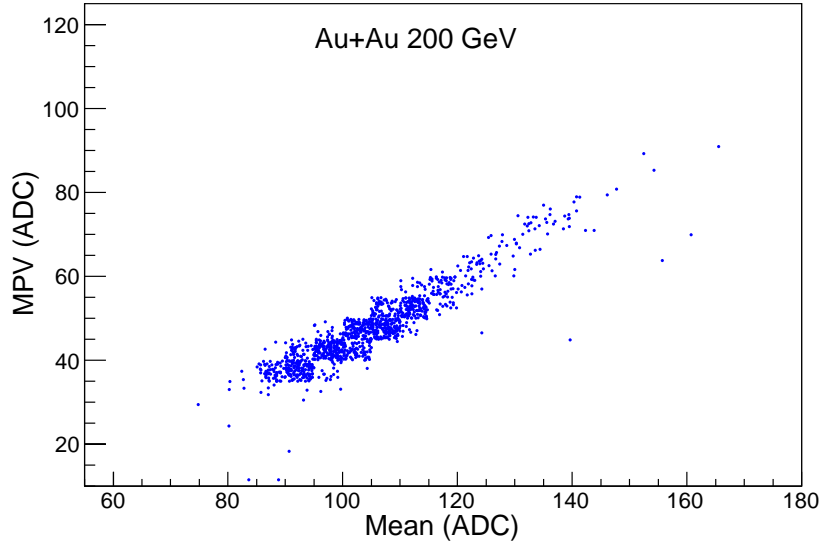


Figure 3.13: Variation of most probable value and the mean of the isolated cell ADC spectra from real data. The correlation is linear.

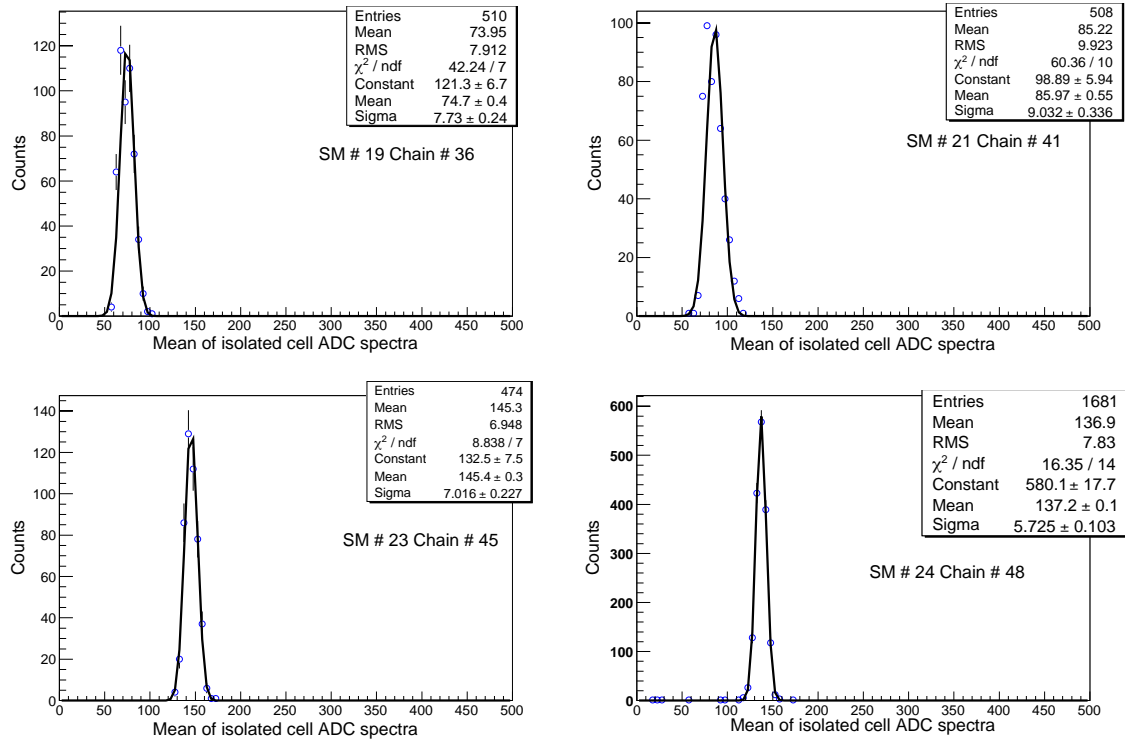


Figure 3.14: Variation of mean of isolated cell ADC spectra for various SM-chains of PMD.

Table 3.2: Global means of the isolated cell ADC distribution of cells for working SMs of PMD in Au+Au collisions at $\sqrt{s_{NN}} = 200$ GeV.

SM No.	Mean in ADC units
14	135
18	128
20	96
22	60
23	88
24	140

The reconstruction of the PMD data is carried out SM-wise. So it is important to have uniformity of response over a SM, before reconstruction is carried out. This study suggests the necessity of cell-to-cell gain calibration for PMD before further analysis of the data. The calibration is also done SM-wise. The cell-to-cell gain calibration in a supermodule is done by the following procedure. First, mean of the ADC distribution of each isolated cell in a supermodule is obtained. Then, mean of all isolated cell ADC distributions is obtained for a supermodule. This is called *global mean* for that supermodule. The ratio of this global mean to the mean of each isolated cell ADC distribution is obtained for each cell in that SM. This is called the *calibration factor* of that isolated cell. Each cell belonging to a particular SM, for all events, is then calibrated by the calibration factor to have uniform response. The global means are later on used as a discrimination threshold. The global mean values obtained for the working supermodules in the preshower plane are given in Table 3.2.

3.4 Occupancy

The occupancy for the STAR-PMD is defined as the ratio of total number of cells hit to the total number of cells in the PMD. The detector configuration is designed to keep the

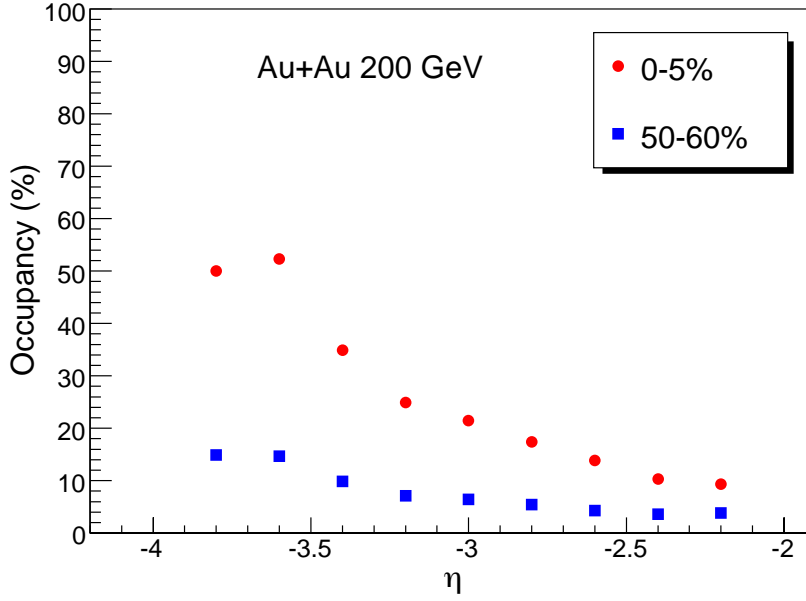


Figure 3.15: Occupancy of the STAR PMD as a function of η from real data for 0–5% central and 50–60% peripheral Au+Au collisions at $\sqrt{s_{NN}} = 200$ GeV.

occupancy to a lower level to have better efficiency of particle detection. Figure 3.15 shows the occupancy of the STAR PMD as a function of η from real data in Au+Au collisions at $\sqrt{s_{NN}} = 200$ GeV. The 0–5% centrality corresponds to low impact parameter collisions or central collisions and the 50–60% centrality corresponds to higher impact parameter collisions or peripheral collisions. As the particle density is higher for central collisions, the occupancy is higher compared to peripheral collisions. The increase in occupancy as we go from -2.4 to -3.8 in η reflects the increase in particle multiplicity per unit area. It means the ratio of the number of particles falling on the detector to the number of cells in the $\eta \sim -3.6$ region is higher compared to corresponding number at $\eta \sim -2.4$. The maximum occupancy in data is less than 54% for Au+Au collisions at $\sqrt{s_{NN}} = 200$ GeV.

3.5 Clustering Algorithm

A photon passing through the lead converter in front of the preshower plane produces electromagnetic showers. The electrons and positrons coming out of the shower hit a group of cells on the preshower plane. These group of cells are called clusters [10]. Each

cluster is then characterized by its total ADC (or E_{dep}) and (η, ϕ) position of its center. The clustering is done SM-wise. The first step in the analysis is to collect all the contagious

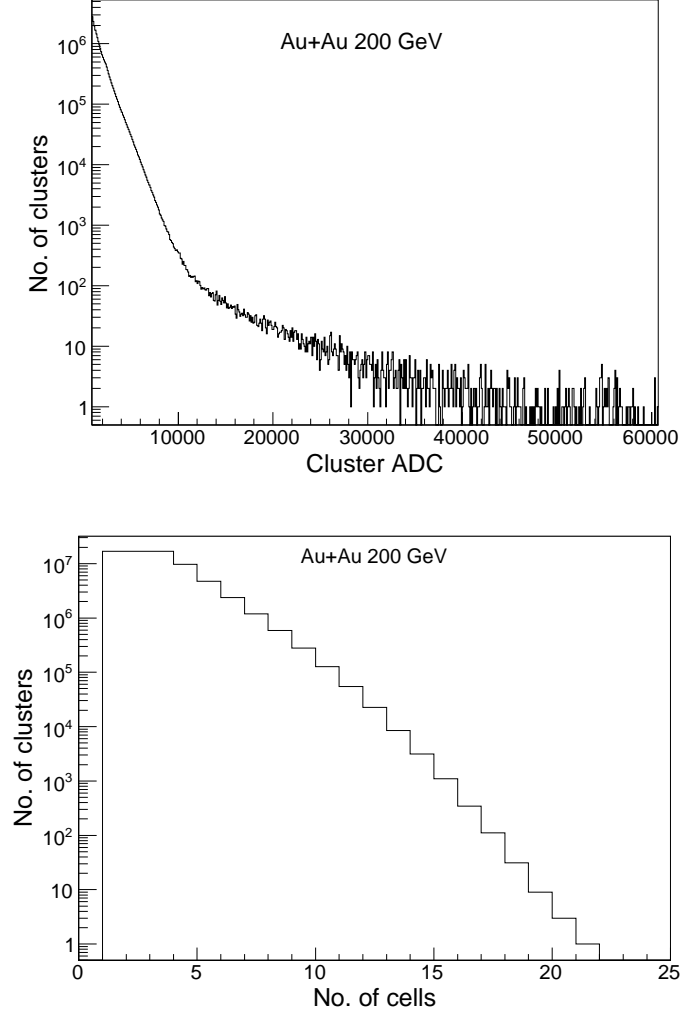


Figure 3.16: Top panel: Cluster ADC distribution. Bottom panel: Number of cells in a cluster. Results are shown for Au+Au collisions at $\sqrt{s_{NN}} = 200$ GeV.

cells having non-zero ADC (or energy deposition (E_{dep})). This group of cells is referred to as a supercluster. Thus the superclusters are separated by cells having zero ADC (E_{dep}), or part of their boundary coincides with the SM boundary. Superclusters are made starting from the cell with largest ADC (E_{dep}) and forming a cluster with contagious non-zero ADC (E_{dep}) cells. For making the subsequent superclusters we search for the next largest ADC (E_{dep}) cell and follow the same procedure of collecting contagious non-zero ADC

(E_{dep}) cells. This process is repeated till all the non-zero ADC (E_{dep}) cells in a SM are exhausted. If the number of cells having non-zero ADC (E_{dep}) is not very large, each supercluster would consist of few cells. In that case, these superclusters themselves can be identified with the particles (photons or charged particles) falling on the detector. The superclusters constructed having large number of cells may have arisen due to overlap of electromagnetic showers of different particles as a result of large particle density. In such a case, there is a need of breaking the superclusters further. If the supercluster has more than two cells then it is broken into a number of clusters. This is called refined clustering. The maxima in ADC (E_{dep}) are identified with the centers of the clusters. The proposed

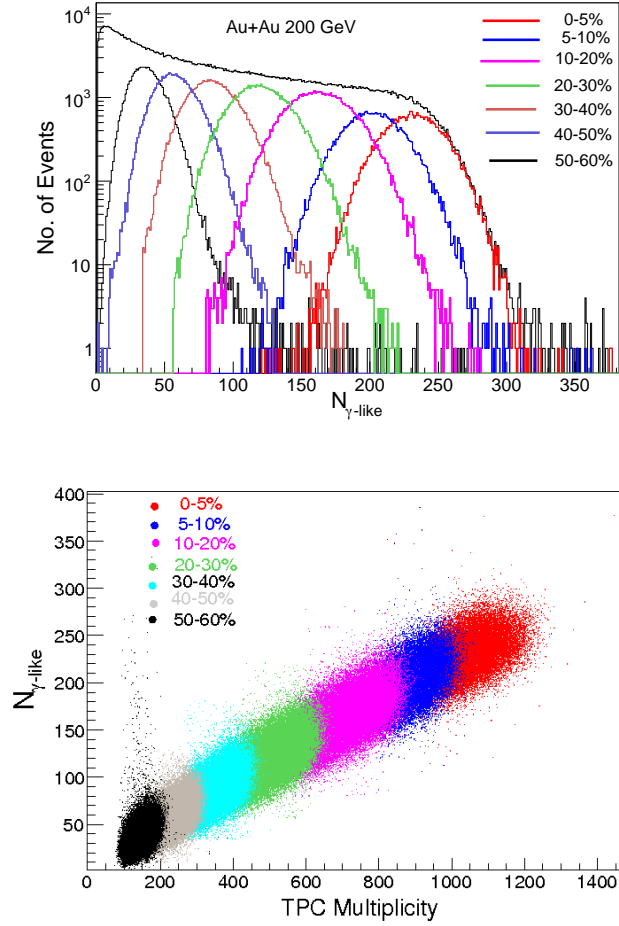


Figure 3.17: Top panel: Total number of clusters on PMD event-by-event. Bottom panel: Correlation between total clusters on the PMD and the TPC track multiplicity from experimental data at $\sqrt{s_{NN}} = 200$ GeV.

center should be at least one cell unit away from previously determined cluster centers. That is, neighboring cells cannot be cluster centers. It is also assumed that if the distance between the proposed center and the previously accepted center is between 1 and 2 cell units, the strength of the (new) cell should be larger than 25% of the previously accepted center cell. This is to ensure that fluctuations do not give rise to clusters. The number 25% is *ad hoc* and is tuned depending on the particle density. Note that this distance condition implies the two cells are next nearest neighbors. If the distance between the proposed center and the previously accepted center is 2 cell units (next-to-next nearest neighbor), the cell strength should be larger than 10% of the strength of the previously accepted cell. If the distance is larger than 2 cell units, it is accepted as new cell center.

Figures 3.16 and 3.17 show typical features of the clusters in the PMD. Top panel in Fig. 3.16 shows a typical cluster ADC distribution, bottom panel shows the distribution of number of cells in a cluster. Figure 3.17 (top panel) shows the event-by-event photon-like clusters in the PMD. The photon-like ($N_{\gamma\text{-like}}$) clusters are the clusters above hadron rejection threshold, discussed in next section. The distributions are shown for various collision centrality classes for Au+Au collisions at $\sqrt{s_{NN}} = 200$ GeV. The most central collisions are represented by the centrality class 0–5% and the most peripheral by 50–60% centrality class. Figure 3.17 (bottom panel) shows the correlation between total photon-like clusters on the PMD and the TPC track multiplicity from data for different collision centralities.

We checked for Au+Au collisions at $\sqrt{s_{NN}} = 200$ GeV, and found that it is sufficient to use algorithm up to supercluster formation for obtaining photon counting and determination of photon spatial positions, as was used in Ref. [12].

3.5.1 Physics Performance Criteria for PMD

The physics performance of the preshower PMD is characterized by two quantities:

- (i) photon counting efficiency (ϵ_γ) and
- (ii) purity (f_p) of the detected photon sample.

These are defined by the following relations [3].

$$\epsilon_\gamma = N_{\text{cls}}^{\gamma,\text{th}} / N_{\text{inc}}^\gamma, \quad (3.1)$$

$$f_p = N_{\text{cls}}^{\gamma,\text{th}} / N_{\gamma\text{-like}}. \quad (3.2)$$

where N_{inc}^γ is the number of incident photons from the HIJING event generator, $N_{\text{cls}}^{\gamma,\text{th}}$ is the number of photon clusters above the photon-hadron discrimination threshold and $N_{\gamma\text{-like}}$ is the total number of clusters above the hadron rejection threshold. The fractional contamination in the $N_{\gamma\text{-like}}$ sample is given by $(1-f_p)$.

3.5.2 Photon Conversion Efficiency

The PMD has a 3 radiation length (X_0) of lead converter material in front of the preshower plane. Photon being an electromagnetic particle is converted into electromagnetic shower (electrons and positrons), and these being charged get detected in the preshower plane of the PMD. Low energy photons may get absorbed in the converter and hence will not be detected in the preshower plane of the PMD.

Photon conversion efficiency is defined as the ratio of number of photons which give signal in the preshower plane of the PMD above the noise threshold ($\sim 0.2 \times E_{\text{dep}}^{\text{MIP}}$ in simulation) to the number of photons incident on the converter material ($3X_0$ of lead). The conversion efficiency (shown in Fig. 3.18) is calculated by using single incident photons of various transverse momenta in simulation. This conversion efficiency puts an upper limit on photon counting efficiency (ϵ_γ). Figure 3.18 shows the conversion efficiency for photons as a function of transverse momentum of incident photon. It can be seen that above an incident transverse momentum of 0.5 GeV/ c , the photon conversion efficiency is higher than 90%.

In an event, photons are produced in all energy ranges following a distribution in p_T . So it is important to know what is the average photon conversion efficiency in an event and how it varies with collision centralities. Figure 3.19 (top panel) shows the photon conversion efficiency which is around 77% in Au+Au collisions at $\sqrt{s_{NN}} = 200$ GeV. This is the upper limit for the photon counting efficiency at this energy. Middle panel shows

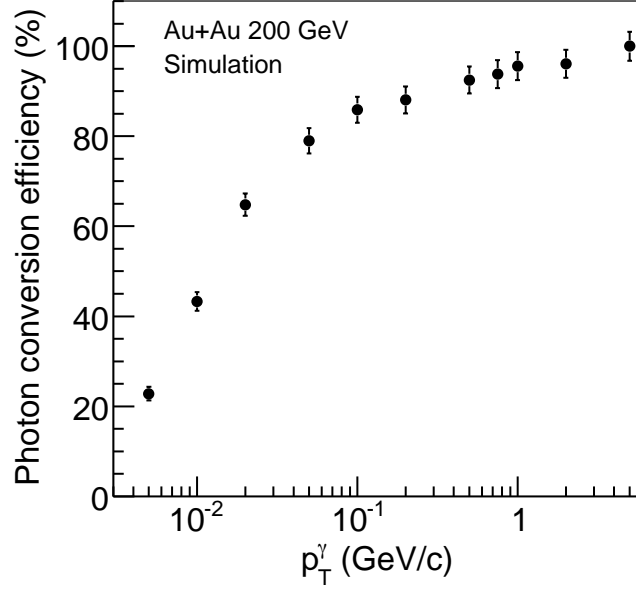


Figure 3.18: Typical conversion efficiency for photons as a function of transverse momentum of incident photons in simulation.

the correlation between the number of incident photons and the detected photons, where a photon is considered to be detected if it gives signal in any of the cells on the preshower plane of the PMD. The correlation is linear which suggests that most of the times the incident photon gets detected in the PMD. Bottom panel shows the dependence of photon conversion efficiency on photon multiplicity in PMD acceptance in Au+Au collisions at $\sqrt{s_{NN}} = 200$ GeV. The figure suggests that the photon conversion efficiency is almost constant (for $N_\gamma > \sim 100$) as function of number of incident photons within the PMD acceptance.

3.5.3 Clustering Efficiency

The photon after getting converted into electromagnetic shower particles, hits a group of cells in the preshower detector. A clustering algorithm is used to detect these clusters and associate them with photons. Clustering efficiency is defined as the ratio of number of photons (tracks) that has converted and given a signal on the preshower

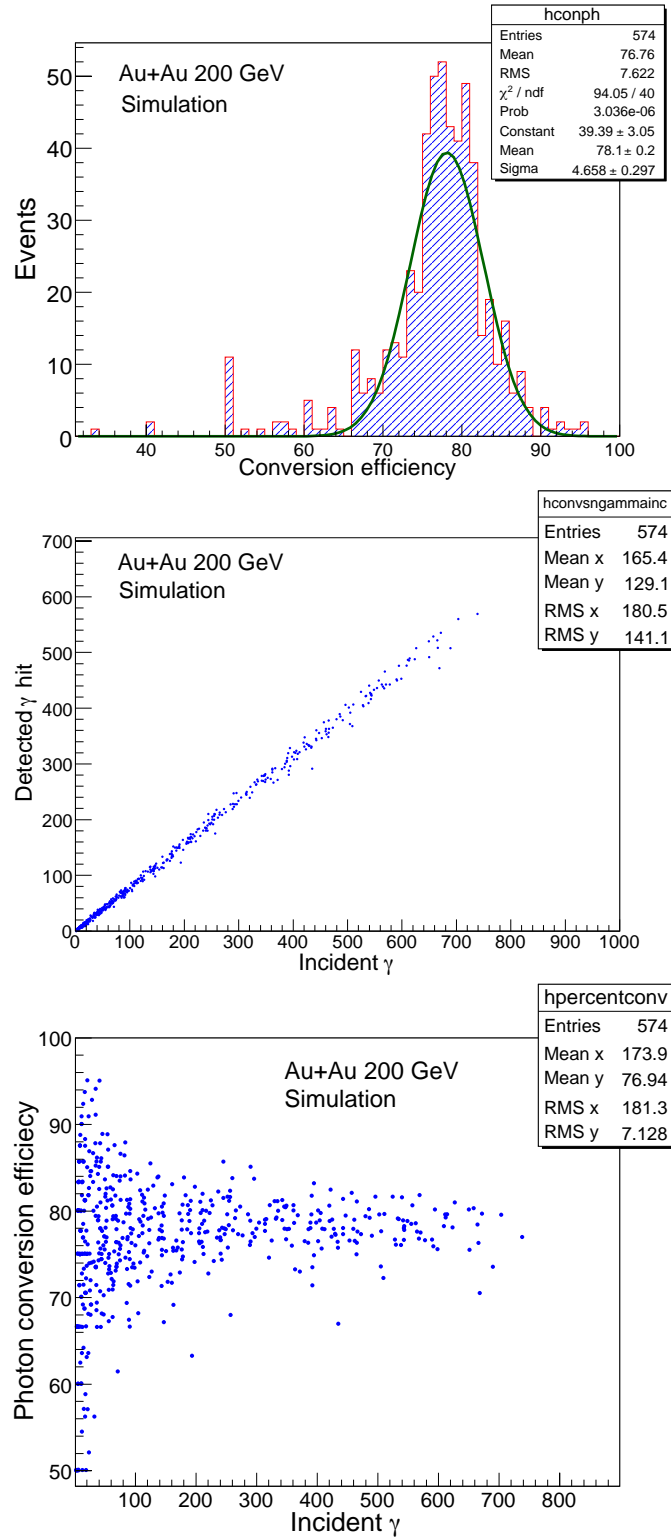


Figure 3.19: Top panel: The photon conversion efficiency for many events in Au+Au collisions at $\sqrt{s_{NN}} = 200$ GeV. Middle panel: Correlation between number of incident photons on the PMD and number of photons detected within the PMD. Bottom panel: Variation of average photon conversion efficiency over a set of events as a function of photon multiplicity in the PMD acceptance.

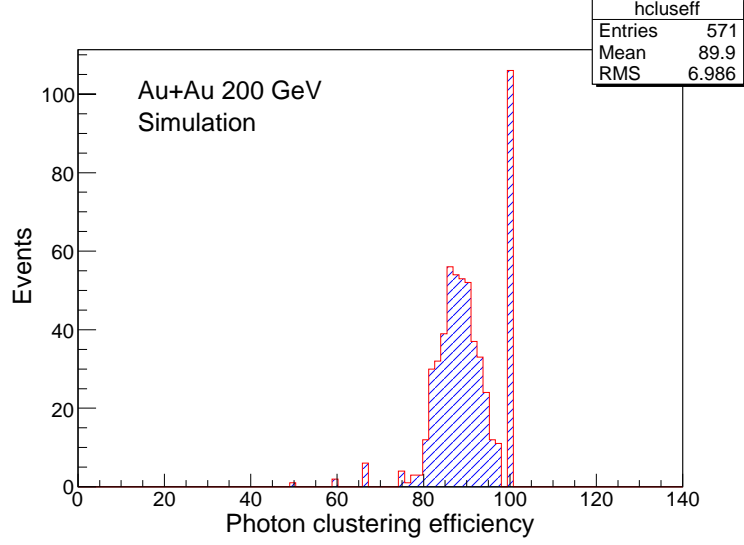


Figure 3.20: Event-wise photon clustering efficiency.

plane of the PMD to the number of photon clusters (associated with converted photon tracks) obtained through the clustering algorithm in the detector. Figure 3.20 shows the clustering efficiency for large number of minimum bias events. We find that the clustering efficiency is $\sim 90\%$ for Au+Au collisions at $\sqrt{s_{NN}} = 200$ GeV. So the upper limit on photon counting efficiency can be 0.77 (photon conversion efficiency) $\times 0.90$ (clustering efficiency) ~ 0.70 (70%) for Au+Au collisions at $\sqrt{s_{NN}} = 200$ GeV.

3.5.4 Cluster Properties and Optimization of Clustering Algorithm

3.5.4.1 Spilt Clusters

In order to estimate the photon counting efficiency and the background in the detected photon sample, it is essential to associate an incident track to a cluster. The background to the detected photon sample is not only from the hadron tracks but also from photon tracks (which should ideally give one cluster on the detector) that give more than one cluster on the preshower plane of the PMD. These extra clusters are called as split clusters. These may arise due to the following reasons:

- (a) upstream materials in front of PMD,

- (b) limitations of the clustering algorithm, and
- (c) the process of shower formation of photons may lead to large angle emission of particles, thus giving rise to two good clusters.

They have serious consequences as far as photon counting efficiency is concerned. The photon counting efficiency may go beyond 100% if split clusters are not properly accounted. The above quantities for the PMD are estimated from simulation studies, by passing HIJING generated events through the GEANT incorporating full STAR detectors during that period of data taking. An algorithm was previously developed to associate every incident track to detected clusters on PMD. The quantities mentioned above can be optimized by applying cuts on:

- (i) Number of cells in a cluster (N_{cell}) and
- (ii) Energy deposited by a particle in a cluster (E_{dep}).

3.5.4.2 Track and Cluster position

The fraction of photon split clusters is defined as the ratio of total number of photon split clusters in the event to the total number of photon clusters. Figure 3.21 shows the percentage split clusters (a) as a function of number of incident photons in the PMD coverage for PMD only case (top panel), (b) as a function of number of incident photons in the PMD coverage for PMD with all (PMD+All) detectors (middle panel), and (c) as a function of η for PMD+All detectors with refined clustering ON and OFF (bottom panel). All results are obtained for cluster E_{dep} greater than $3 \times E_{\text{dep}}^{\text{MIP}}$ and $N_{\text{cell}} > 1$. Percentage split clusters with the PMD only (GEANT simulations with only PMD detector) is less than the PMD+All detector condition (GEANT simulations with full STAR framework). There is no significant eta dependence of percentage split clusters. A weak centrality dependence is observed with central collisions having higher percentage split clusters. Percentage split clusters decrease if we switch OFF the refined clustering. Ideally the cluster should have the same η and ϕ or x and y position as its incident track. If we take the difference between incident track η and its cluster η or incident track ϕ and its cluster ϕ , it should be zero. This may not happen due to the following reasons:

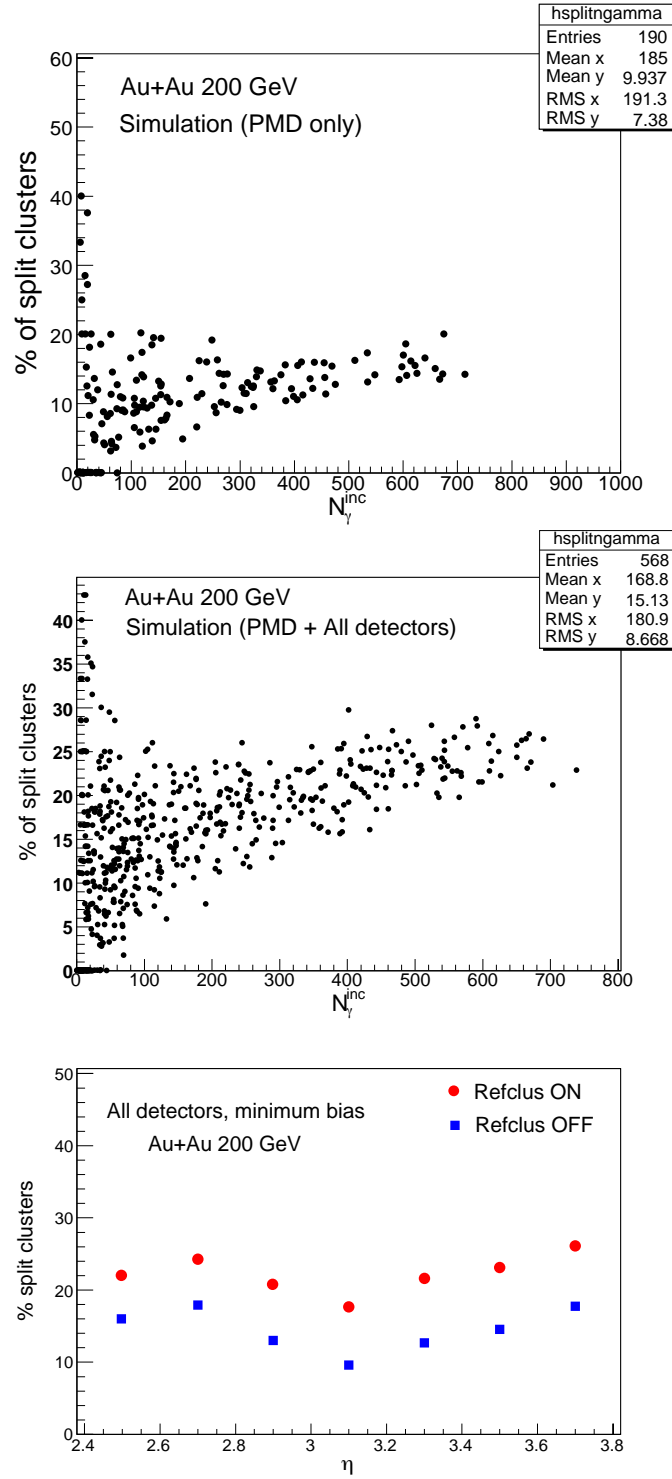


Figure 3.21: Percentage of split clusters as a function of (a) photons incident in the PMD coverage for PMD only case (top panel), (b) photons incident in the PMD coverage for PMD+All detectors (middle panel), and (c) η for PMD+All detectors with refined clustering ON and OFF (bottom panel).

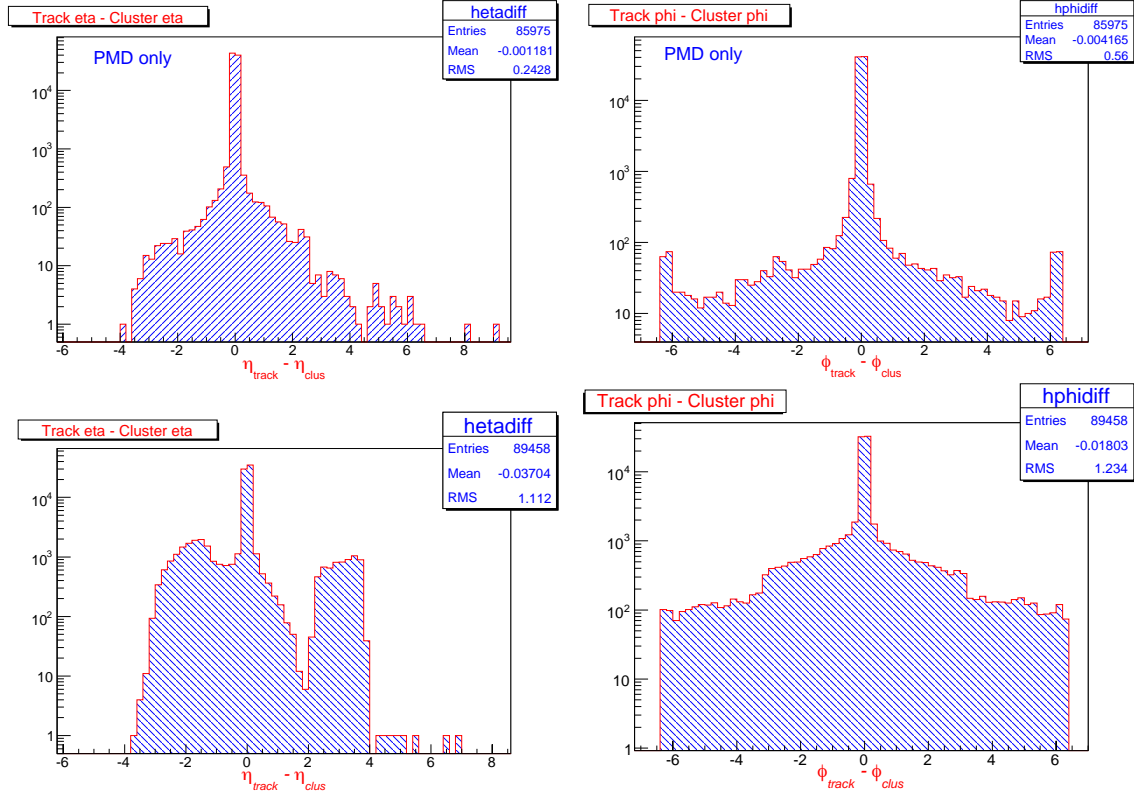


Figure 3.22: The difference between the incident track (η, ϕ) and its cluster (η, ϕ) positions for the PMD only (top) and for the PMD with all detectors case (bottom) for photons.

- (i) Upstream materials in front of the PMD,
- (ii) Limitations of the clustering algorithm, and
- (iii) Shower centroid shift due to transmission through the converter.

Since one of the main observables in the PMD is the spatial distribution of photons, it is crucial to see if we have most of photon clusters at the same position as its incident track. For knowing the best possible results expected from the PMD, we compare the results from simulation for the PMD only case with those from PMD+All detectors case. The comparison will reflect the effect of material in front of the PMD. Due to the material effect, the cluster position (η, ϕ) on the PMD from incident photon track position (η, ϕ) will be different.

Figure 3.22 shows the difference between incident track η and corresponding cluster η as well as incident track ϕ and corresponding cluster ϕ . The results are shown for PMD

only (top panels) and PMD with all detectors (bottom panels). The deviation of the clusters from the incident track position is very less for the PMD only case as compared to PMD with all detector case. A high value of difference between cluster η and incident track η suggests that it is due to upstream material in front of PMD. More important is the sign of the difference. The positive sign means that η_{track} is high, which in turn means that these tracks are coming from close to the beam pipe. Since the difference is as high as 4, it is most likely due to scattering of the incident tracks from beam pipe and falling on the PMD.

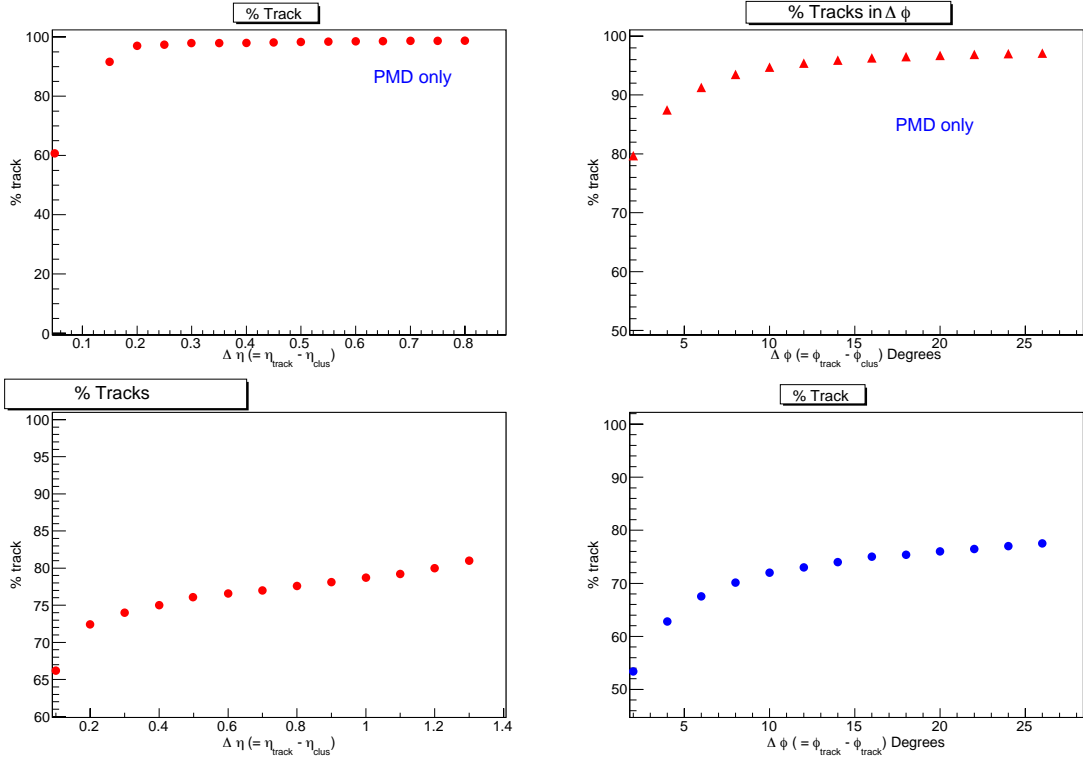


Figure 3.23: Total number of clusters (%) lying within certain $\Delta\eta$ and $\Delta\phi$ from its incident track for the PMD only case (top panels) and for PMD with all detectors case (bottom panels).

In Fig. 3.23, we show the percentage of tracks within certain $\Delta\eta$ and $\Delta\phi$. We find that $\sim 90\%$ of the clusters have their positions within $\Delta\eta < 0.2$ for PMD only case (top panels) and $\sim 70\%$ of the clusters have their positions within $\Delta\eta < 0.2$ of their incident

tracks for PMD with all detectors (bottom panels). Further, about 80% of the clusters have their position within $\Delta\phi < 2^\circ$ for PMD only case and about $\sim 70\%$ for $\Delta\phi < 8^\circ$ of their incident tracks for PMD with all detectors. For a combined condition on both $\Delta\eta$ and $\Delta\phi$, we have the following percentage of incident tracks for the PMD with all detectors case.

- (a) For $\Delta\eta < 0.1$ and $\Delta\phi < 2^\circ$: $\sim 50\%$ of the clusters;
- (b) For $\Delta\eta < 0.2$ and $\Delta\phi < 4^\circ$: $\sim 62\%$ of the clusters; and
- (c) For $\Delta\eta < 0.3$ and $\Delta\phi < 6^\circ$: $\sim 66\%$ of the clusters are recovered on preshower plane.

All these are evaluated for minimum bias Au+Au collisions at $\sqrt{s_{NN}} = 200$ GeV.

3.5.4.3 Optimization of Photon-Hadron Discrimination

In order to discriminate clusters due to photon track and clusters due to charged hadron track, we need to know the properties of photon clusters and charged hadron clusters. Some of these features are discussed below -

- (a) Photon cluster will deposit more energy in the sensitive medium of the detector as compared to the cluster formed due to charged hadron.
- (b) Photon cluster will have more number of cells hit in the preshower plane due to the electromagnetic shower of e^+, e^- coming from photon conversion in the $3X_0$ of lead converter. The charged hadrons, which essentially hit single cell, will form cluster with single isolated cell in the preshower plane.

These features can be used to discriminate a photon cluster from a charged hadron cluster. One expects a hadron to be a MIP and deposit some minimum energy (~ 2.5 keV from simulation studies) and give signal in only one cell in both pre-shower and veto plane, as seen in test beam studies [7]. But the following points are needed to be considered, which may lead to contrary results.

- (a) A low energy photon may have most of its shower particles (e^+, e^-) get absorbed in the $3X_0$ converter material. This may lead to less number of cells hit in preshower

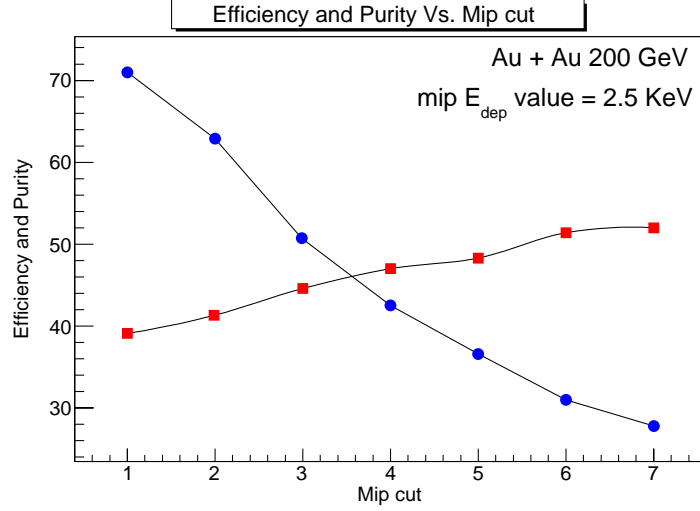


Figure 3.24: Efficiency (solid circles) and purity (solid squares) of photon counting as a function of MIP E_{dep} cut for Au+Au collisions at 200 GeV. One MIP E_{dep} value is ~ 2.5 keV.

plane and hence depleting a photon cluster with less number of cells as well as less energy deposition in the preshower plane.

- (b) A charged particle may interact with the converter material (for $3X_0$ the interaction probability is about 10%). It may give signal in larger number of cells in preshower plane and can form a cluster with $N_{\text{cell}} > 1$, and hence deposit more energy ($> E_{\text{dep}}^{\text{MIP}}$).
- (c) The clustering algorithm in its attempt to separate overlapping clusters (expected in high particle density at forward rapidity in nucleus-nucleus collisions) may split a photon cluster into many small clusters. This results in the formation of clusters having smaller energy deposition and less number of cells.

The variation of photon counting efficiency and purity for various threshold cuts decides the photon-hadron discrimination criteria. Figure 3.24 shows the efficiency of photon counting and purity of photon sample as a function of MIP E_{dep} cut. One MIP E_{dep} is equivalent to 2.5 keV as obtained from simulation studies. We observe that efficiency of photon counting varies from greater than 70% to less than 30% with MIP E_{dep} cut. Purity of photon sample varies from 40% to 50% with MIP E_{dep} cut. Since we do not

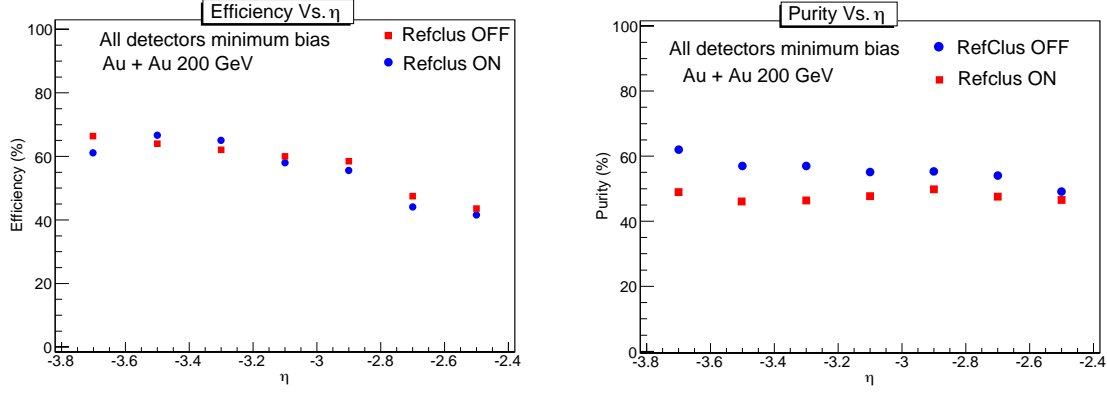


Figure 3.25: Efficiency of photon counting (left panel) and purity of photon sample (right) as a function of pseudorapidity for PMD+All detectors in Au+Au 200 GeV collisions for refined clustering OFF and ON case.

want the cases of low efficiency and purity, it is appropriate to use the threshold values for photon-hadron discrimination to be close to $3 \times E_{\text{dep}}^{\text{MIP}}$. Similar studies for efficiency and purity as a function of N_{cell} cut, suggest the second condition for photon-hadron discrimination to be $N_{\text{cell}} > 1$.

Figure 3.25 shows the efficiency of photon counting (left panel) and purity of photon sample (right panel) as a function of pseudorapidity in Au+Au collisions at 200 GeV for PMD with all detectors for refined clustering OFF and ON case. We observe that efficiency of photon counting varies from 60% to 40% from pseudorapidity region -3.8 to -2.4 , respectively for the two cases of refined clustering OFF and ON. Purity of photon sample is around 50% for the PMD range of pseudorapidity for refined clustering ON case, whereas it varies from 60% to 50% with pseudorapidity for refined clustering OFF case. Since the purity is better in case of refined clustering OFF, we take the efficiency and purity values with refined clustering OFF for the subsequent analysis. All subsequent analysis results presented will be based on refined clustering OFF scheme.

3.6 Efficiency and Purity

To estimate the number of photons (N_γ) from the detected $N_{\gamma\text{-like}}$ clusters, we use the photon reconstruction efficiency (ϵ_γ) and purity (f_p) of the γ -like sample, defined by

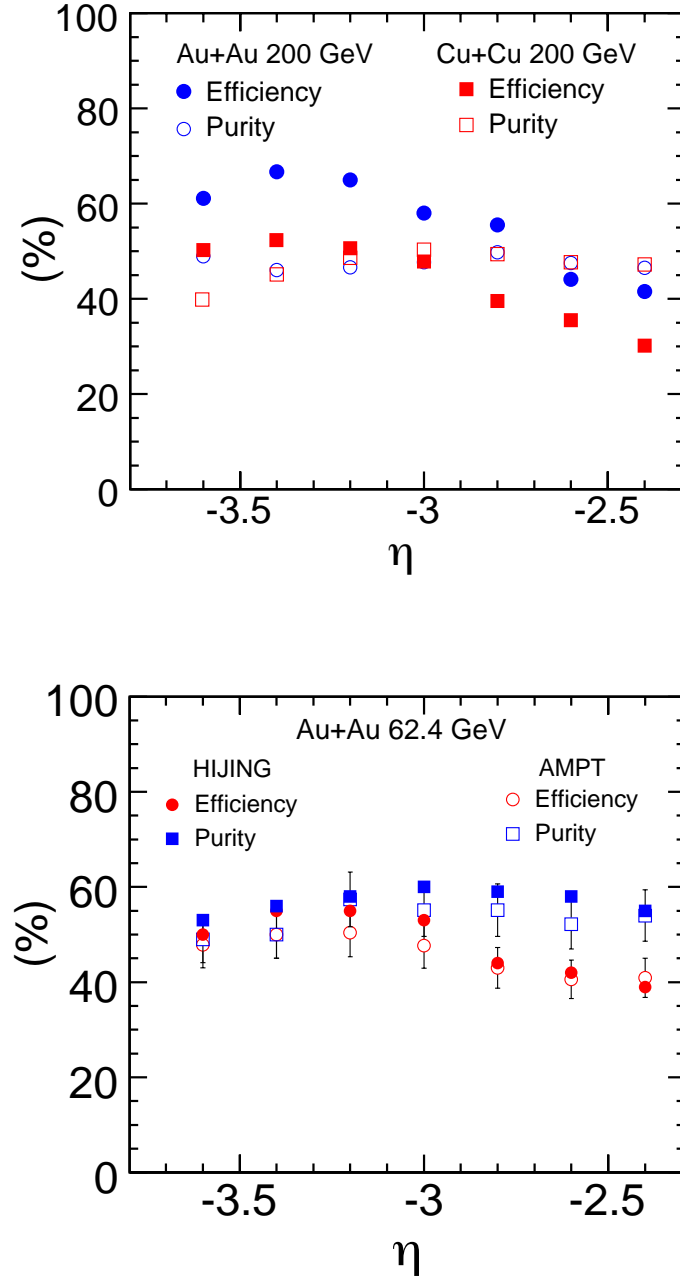


Figure 3.26: Top panel: Photon reconstruction efficiency (ϵ_γ) (solid symbols) and purity of photon sample (f_p) (open symbols) for PMD as a function of pseudorapidity (η) for minimum bias Au+Au and Cu+Cu at $\sqrt{s_{NN}} = 200$ GeV. Bottom panel: Comparison between estimated ϵ_γ and f_p for PMD as a function of η for minimum bias Au+Au at $\sqrt{s_{NN}} = 62.4$ GeV using HIJING and AMPT models. The error bars on the AMPT data are statistical and those for HIJING are within the symbol size.

Eqs. (3.1) and (3.2), respectively. The photon multiplicity in data is then obtained as $N_\gamma = (f_p/\epsilon_\gamma)N_{\gamma\text{-like}}$ [3, 7, 11], where the ratio f_p/ϵ_γ is estimated from simulations as described below. Both ϵ_γ and f_p are obtained from a detailed Monte Carlo simulation using HIJING version 1.382 [1] with default parameter settings and the detector simulation package GEANT [2], which incorporates the full STAR detector framework. In our previous work [12], it has been shown that HIJING reproduces the N_{ch}/N_γ ratio in Au+Au collisions at $\sqrt{s_{NN}} = 62.4$ GeV. For estimation of ϵ_γ in simulations, it may be important to know the inclusive photon p_T distribution. Due to lack of experimental measurement of the inclusive photon p_T distribution at forward rapidity, it is assumed that they are similar to those from HIJING model. In order to investigate the possible differences, ϵ_γ and f_p are also obtained from a detailed Monte Carlo simulation using AMPT model [13] with default parameter settings. The AMPT model is a multiphase transport model which includes both initial partonic and final hadronic interactions. The differences between the ϵ_γ and f_p values estimated using the two models are less than 5%. This difference is attributed to systematic errors on N_γ . Both ϵ_γ and f_p can vary with pseudorapidity and centrality. The ϵ_γ and f_p for minimum bias Au+Au and Cu+Cu at 200 GeV are shown in top panel of Fig. 3.26. The photon reconstruction efficiency (which includes the detector acceptance corrections) varies from 30% at $\eta = -2.3$ to 60% at $\eta = -3.7$ for all collision centralities obtained from simulations for Au+Au and Cu+Cu collisions at 62.4 [3, 12] and 200 GeV. The purity of the photon sample is nearly constant as a function of η and varies between 40% and 60% for Au+Au and Cu+Cu collisions at 62.4 [3, 12] and 200 GeV. Both ϵ_γ and f_p show slight variation with system-size. The η dependence of the ϵ_γ reflects mainly the varying detector acceptance between $\eta = -2.0$ and $\eta = -3.0$. There is also a small effect of η -dependence on ϵ_γ due to varying particle density as a function of η . This effect is already reflected in the comparison of ϵ_γ values between Au+Au and Cu+Cu. The f_p values by definition are not affected by detector acceptance. The bottom panel of Fig. 3.26 shows a typical comparison of estimated ϵ_γ and f_p using HIJING and AMPT models for Au+Au minimum bias collisions at 62.4 GeV. The differences are within 5% level. The lower limit of photon p_T acceptance in the PMD is estimated from detector simulations to be 20 MeV/ c .

3.7 Photon Production

For high-energy heavy-ion collisions, measurements of particle multiplicity provide information on particle production mechanisms [14]. Event-by-event fluctuations in the multiplicity of produced particles within a thermodynamic picture could be related to matter compressibility [15]. The event-by-event correlation between photon and charged particle multiplicities can be used to test the predictions of formation of disoriented chiral condensates [16]. The variation of particle density in pseudorapidity (η) with collision centrality can shed light on the relative contribution of soft and hard (perturbative QCD jets) processes in particle production [17]. Multiplicity measurements can provide tests of ideas on initial conditions in heavy-ion collisions based on parton saturation [18] and color glass condensates [19]. Under certain model assumptions, the particle density in pseudorapidity can provide information on the initial temperature and velocity of sound in the medium [20]. The pseudorapidity distributions are found to be sensitive to the effects of re-scattering, hadronic final-state interactions, and longitudinal flow [21].

Several interesting features of the dependence of particle density in pseudorapidity have been observed in collisions from the experiments at the Relativistic Heavy-Ion Collider (RHIC). Particle production is found to follow a unique, collision energy independent, longitudinal scaling [22] in $p+p$ and $d+Au$, as well as in heavy-ion collisions [23, 24]. Such longitudinal scaling is also found to be independent of collision centrality for photons [3, 12]. The total charged particle multiplicity (integrated over the full pseudorapidity range) per average number of participating nucleon ($\langle N_{\text{part}} \rangle$) pair is found to be independent of collision centrality [23]. However, at midrapidity ($|\eta| < 1$), charged particle multiplicity per $\langle N_{\text{part}} \rangle$ is observed to increase from peripheral to central collisions [23]. This clearly indicates that the mechanism of particle production could be different in different pseudorapidity regions. In light of the earlier results of photon multiplicity scaling with $\langle N_{\text{part}} \rangle$ [3, 12] at forward rapidity, it is good to make direct comparison of the observables (N_γ and $dN_\gamma/d\eta$) for Cu+Cu and Au+Au collisions for systems having similar values of $\langle N_{\text{part}} \rangle$.

In following sections, we discuss results from the photon multiplicity measurements

at forward rapidities in Cu+Cu collisions at $\sqrt{s_{NN}} = 62.4$ and 200 GeV and Au+Au collisions at $\sqrt{s_{NN}} = 200$ GeV from the STAR experiment [25] at RHIC. The results from Au+Au collisions at $\sqrt{s_{NN}} = 62.4$ GeV were reported in Refs. [3, 12]. The photon multiplicity measurements are presented for various collision centrality classes and are compared to corresponding results for charged particles. The photon production is dominated by those from the decay of π^0 s [3]. HIJING [1] calculations indicate that about 93–96% of photons are from inclusive π^0 decays for the $\sqrt{s_{NN}}$ and η range studied.

3.7.1 Systematic Errors

The systematic errors for photon multiplicity (N_γ) are due to [3, 12]:

- (a) Uncertainty in estimates of ϵ_γ and f_p values arising from splitting of clusters, the choice of photon-hadron discriminator threshold and choice of different event generators for their estimation. It is estimated from Monte Carlo simulations and found to be $\leq 16\%$ for all systems and beam energies studied. It is fairly independent of collision centrality.
- (b) Uncertainty in N_γ arising from the non-uniformity of the detector response (primarily due to cell-to-cell gain variation). It is estimated using average gains for normalization and by studying the azimuthal dependence of the photon density, in an η window in the detector, and is found to be $\sim 10\%$.

The total systematic error on N_γ is $\sim 19\%$ for both central and peripheral collisions and is similar for Au+Au and Cu+Cu at 62.4 and 200 GeV. The statistical errors are small and within the symbol size for the results shown in the figures.

3.7.2 Multiplicity Distributions

Figure 3.27 shows the photon multiplicity distributions for minimum bias Au+Au and Cu+Cu collisions at 62.4 and 200 GeV. The distributions for both energies and colliding ion species show a characteristic shape with a rise at small multiplicity owing to peripheral events. This indicates the probability of occurrence of peripheral collisions is higher. This rise is followed by a near plateau region with increasing photon multiplicity. This region

is more prominent for Au+Au than Cu+Cu. It corresponds to mid-central collisions. There is a fall-off region in the distributions for the most central collisions. Also shown in Fig. 3.27 are event-by-event photon multiplicity distributions for central Au+Au (0–5%) and Cu+Cu (0–10%) at $\sqrt{s_{NN}} = 62.4$ and 200 GeV. The solid lines are Gaussian fits to the data. The fit parameters are given in Table 4.1.

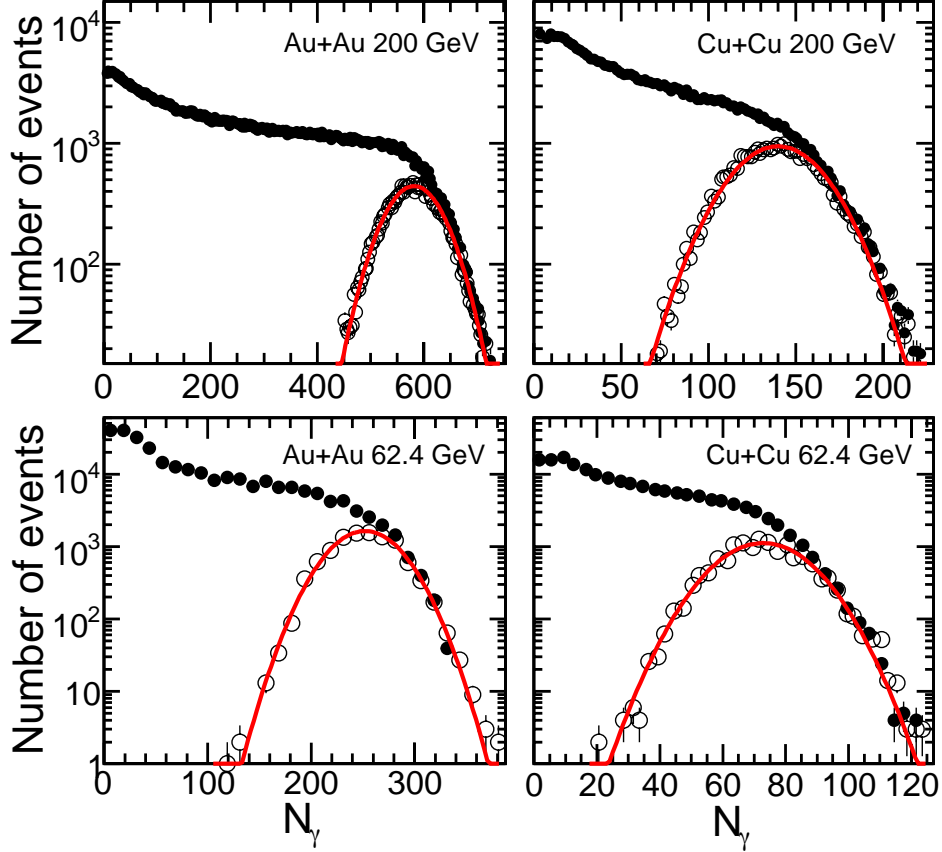


Figure 3.27: Event-by-event photon multiplicity distributions (solid circles) for Au+Au and Cu+Cu at $\sqrt{s_{NN}} = 62.4$ and 200 GeV. The distributions for top 0–5% central Au+Au collisions and top 0–10% central Cu+Cu collisions are also shown (open circles). The photon multiplicity distributions for central collisions are observed to be Gaussian (solid line). Only statistical errors are shown.

Figure 3.28 shows the pseudorapidity distributions of photons measured in the PMD for various collision centralities in Au+Au and Cu+Cu at $\sqrt{s_{NN}} = 62.4$ and 200 GeV. As expected, the photon yield increases with decreasing $|\eta|$. The photon multiplicity is found to increase from peripheral to central collisions. Comparisons to HIJING calculations for

Table 3.3: Gaussian fit parameters for photon multiplicity distributions for $-3.7 < \eta < -2.3$ for central Au+Au (0–5%) and Cu+Cu (0–10%) at $\sqrt{s_{NN}} = 62.4$ and 200 GeV.

Collision Type	$\langle N_{\text{part}} \rangle$	$\langle N_{\gamma} \rangle$	σ_{γ}
Au+Au 62.4 GeV	347.3	252	30
Au+Au 200 GeV	352.4	582	52
Cu+Cu 62.4 GeV	96.4	73	13
Cu+Cu 200 GeV	99.0	140	26

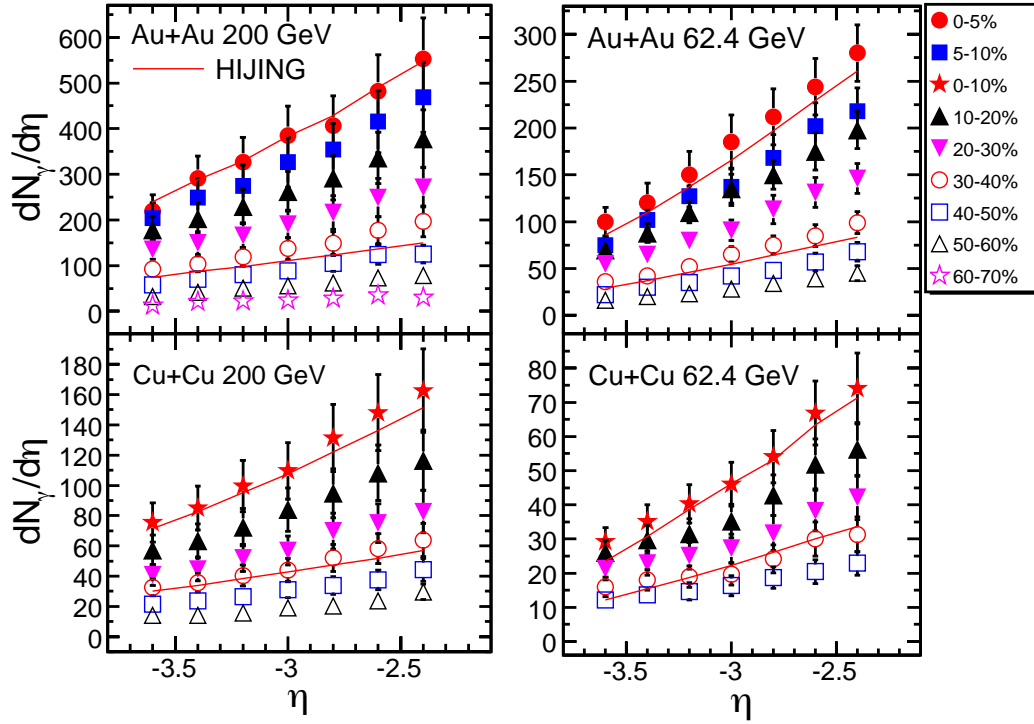


Figure 3.28: Photon pseudorapidity distributions for Au+Au and Cu+Cu at $\sqrt{s_{NN}} = 62.4$ and 200 GeV. The results for several centrality classes are shown. The solid curves are results of HIJING simulations for central (0–5% for Au+Au and 0–10% for Cu+Cu) and 30–40% mid-central collisions. The errors shown are systematic, statistical errors are negligible in comparison.

central (0–5% for Au+Au and 0–10% for Cu+Cu) and 30–40% mid-central collisions are also shown in the figure (solid curves). The HIJING results are in reasonable agreement with the data for both beam energies and colliding ion species. Similar conclusions are drawn for other centrality classes as well.

3.7.3 Scaling of Photon Production

3.7.3.1 Scaling with $\langle N_{\text{part}} \rangle$

The scaling of particle multiplicity with $\langle N_{\text{part}} \rangle$ indicates the dominance of soft processes in particle production at RHIC, whereas scaling with average number of binary collisions ($\langle N_{\text{bin}} \rangle$) indicates the onset of hard processes (pQCD jets). The PHENIX experiment first showed that at midrapidity, the charged particle production scales with a combination of $\langle N_{\text{part}} \rangle$ and $\langle N_{\text{bin}} \rangle$ [17], indicating significant contribution of hard processes in particle production. The PHOBOS experiment showed that such scaling has a pseudorapidity dependence [23]. At midrapidity ($|\eta| < 1$), the particle production scales with a combination of $\langle N_{\text{part}} \rangle$ and $\langle N_{\text{bin}} \rangle$; for the range $3 < |\eta| < 3.4$, it scales with $\langle N_{\text{part}} \rangle$; and for the region $5 < |\eta| < 5.4$, the particle production per average number of participating nucleon pair decreases with increasing $\langle N_{\text{part}} \rangle$.

Figure 3.29 (top panel) shows the variation of photon multiplicity per average number of participating nucleon pair with $\langle N_{\text{part}} \rangle$ for Au+Au and Cu+Cu at 62.4 and 200 GeV within the range $-3.7 < \eta < -2.3$. We observe that within the systematic errors, the photon multiplicity scales with $\langle N_{\text{part}} \rangle$ at forward rapidities. This indicates that the photon production at forward rapidities is due to soft processes. For collisions with similar $\langle N_{\text{part}} \rangle$, the photon multiplicity is similar for Au+Au and Cu+Cu at a given beam energy. Also shown in the figure are results from HIJING (solid lines for Au+Au and dashed lines for Cu+Cu). Considering the systematic errors shown, the HIJING results compare well with the data for most of the collision centralities studied.

Figure 3.29 (bottom panel) shows the comparison of photon multiplicity per average number of participating nucleon pair vs. $\langle N_{\text{part}} \rangle$ and the corresponding data for charged particles from the PHOBOS for the range $-3.7 < \eta < -2.3$. Like photon production, the charged particle multiplicity at forward rapidities is found to scale with $\langle N_{\text{part}} \rangle$. For

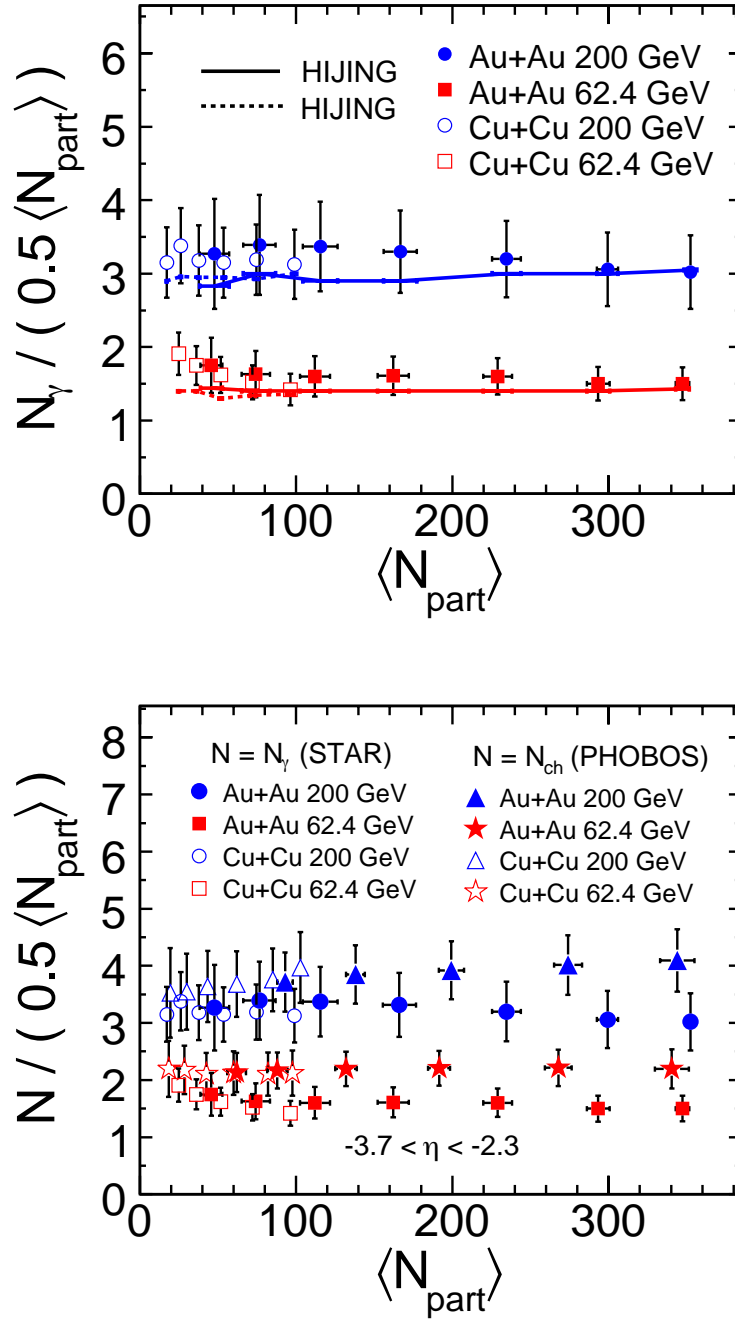


Figure 3.29: Top panel: The number of photons divided by $\langle N_{\text{part}} \rangle / 2$ as a function of average number of participating nucleons for Au+Au and Cu+Cu at $\sqrt{s_{NN}} = 62.4$ and 200 GeV for $-3.7 < \eta < -2.3$. Errors shown are systematic only and include those for $\langle N_{\text{part}} \rangle$. Results from HIJING are shown as lines (solid for Au+Au and dashed for Cu+Cu). Bottom panel: Same as above, for both photons and charged particles from PHOBOS [23].

similar $\langle N_{\text{part}} \rangle$, the charged particle production in the region $-3.7 < \eta < -2.3$ is also found to be similar for Au+Au and Cu+Cu at a given beam energy. The photon production per average number of participating nucleon pair is slightly lower compared to that for charged particles. A constant straight line combined fit to the charged particle results for Au+Au and Cu+Cu in Fig. 3.29 at $\sqrt{s_{NN}} = 200$ GeV gives 3.8 ± 0.2 , while that for photons yields 3.2 ± 0.1 . For $\sqrt{s_{NN}} = 62.4$ GeV, the values are 2.2 ± 0.1 and 1.6 ± 0.05 for charged particles and photons, respectively. The difference may be due to the contribution of protons to charged particles at forward rapidity. The measurements ($-3.7 < \eta < -2.3$) are carried out close to the fragmentation region, where protons play an increasingly larger role [12, 26]. The ratio of the number of charged particles to photons in the range $-3.7 < \eta < -2.3$ is found to be 1.4 ± 0.1 and 1.2 ± 0.1 for $\sqrt{s_{NN}} = 62.4$ GeV and 200 GeV, respectively.

3.7.3.2 Longitudinal Scaling

Previously, it was reported that both charged particle [23, 24] and photon pseudorapidity density [3, 12], normalized by the average number of participating nucleon pairs as a function of $\eta - y_{\text{beam}}$, where y_{beam} is the beam rapidity, is independent of beam energy. Further, it was observed that such longitudinal scaling was centrality dependent for charged particles, but was centrality independent for photons [3, 12]. Figure 3.30 shows the photon pseudorapidity density normalized by the average number of participating nucleon pairs as a function of $\eta - y_{\text{beam}}$, for selected centralities (for the sake of clarity) for Au+Au and Cu+Cu at $\sqrt{s_{NN}} = 62.4$ and 200 GeV. The y_{beam} values for 62.4 and 200 GeV are -4.19 and -5.36 , respectively. The Cu+Cu results are shifted by 0.1 units in η for sake of clarity. The solid line is a second order polynomial of the form $0.54 + 0.22(\eta - y_{\text{beam}}) + 0.23(\eta - y_{\text{beam}})^2$, fitted to all the data of Fig. 3.30. A fit to the ratio of data to this function for the results in the upper panel yields a value of 0.96 ± 0.01 and those on the lower panel yields 1.03 ± 0.01 . The results demonstrate that the longitudinal scaling for produced photons is independent of colliding ion species. In addition we re-confirm that such scaling for photons is independent of beam energy and collision centrality as reported earlier [3, 12].

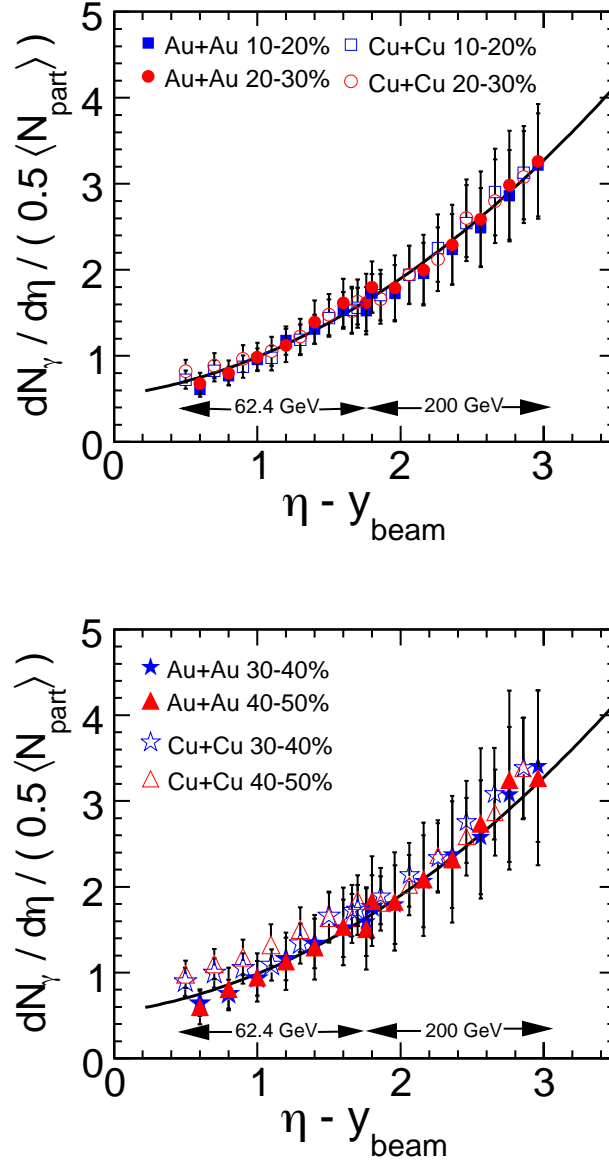


Figure 3.30: Photon pseudorapidity distributions normalized by the average number of participating nucleon pairs for different collision centralities are plotted as a function of pseudorapidity shifted by the beam rapidity (-5.36 for 200 GeV and -4.19 for 62.4 GeV) for Au+Au and Cu+Cu collisions at $\sqrt{s_{NN}} = 62.4$ and 200 GeV. Errors are systematic only, statistical errors are negligible in comparison. For clarity of presentation, results for only four centralities are shown. The Cu+Cu data are shifted by 0.1 unit in $\eta - y_{\text{beam}}$. The solid line is a second order polynomial fit to the data (see text for details).

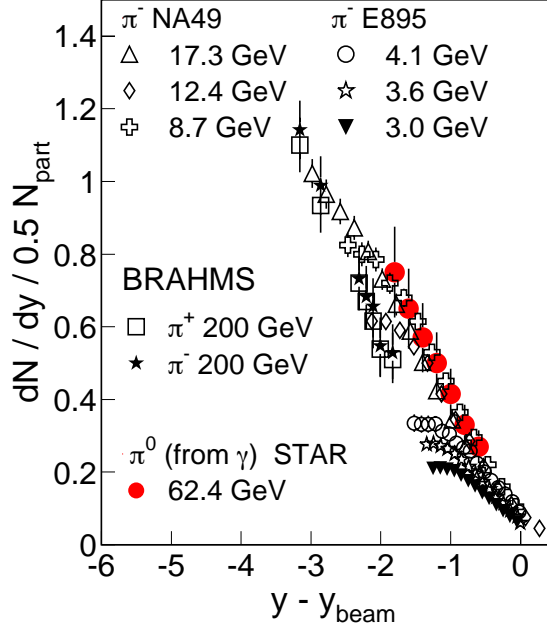


Figure 3.31: Estimated $\frac{dN_{\pi^0}}{dy}$ from $\frac{dN_\gamma}{dy}$ normalized to N_{part} , as compared to $\frac{dN_{\pi^\pm}}{dy}$ normalized to N_{part} , as a function of $y - y_{\text{beam}}$ for central collisions at various collision energies.

Figure 3.31 shows the charged pion rapidity density in Au+Au collisions at RHIC [27], Pb+Pb collisions at the SPS [28], Au+Au collisions at AGS [29], and estimated π^0 rapidity density from the photon measurement (photon rapidity density) at $\sqrt{s_{NN}} = 62.4$ GeV, all as a function of $y - y_{\text{beam}}$. HIJING calculations indicate that about 93-96% of photons are from π^0 decays. From HIJING, the ratio of photons to π^0 yields are obtained. This ratio is used to estimate the π^0 yield from the measured photon yield. The BRAHMS results at forward rapidities are slightly lower compared to the results from SPS energies. However, in general, the results show that pion production in heavy ion collisions in the fragmentation region agrees with the longitudinal scaling picture.

Bibliography

- [1] X-N. Wang and M. Gyulassy, Phys. Rev. D **44**, 3501 (1991).
- [2] V. Fine and P. Nevski, *Proceedings of CHEP-2000*, Padova, Italy.
- [3] J. Adams *et al.* (STAR Collaboration), Phys. Rev. Lett. **95** (2005) 062301; P. K. Netrakanti, Ph. D. Thesis, Jadavpur University (2008); M. Sharma, Ph. D. Thesis, Panjab University (2008); N. Gupta, Ph. D. Thesis, Jammu University (2008); D. Das, Ph. D. Thesis, Jadavpur University (2008); and S. M. Dogra, Ph. D. Thesis, Jammu University (2009); <http://drupal.star.bnl.gov/STAR/theses>.
- [4] C. Adler *et al.*, Nucl. Instr. Meth. A **470**, 488 (2001).
- [5] F. S. Bieser *et al.*, Nucl. Instr. Meth. A **499**, 766 (2003).
- [6] B. I. Abelev *et al.* (STAR Collaboration), Phys. Rev. C **79**, 034909 (2009); D. Kharzeev and M. Nardi, Phys. Lett. B **507**, 121 (2001).
- [7] M. M. Aggarwal *et al.*, Nucl. Instr. Meth. A **499**, 751 (2003); M. M. Aggarwal *et al.*, Nucl. Instr. Meth. A **488**, 131 (2002).
- [8] Particle Data Group, C. Caso *et al.*, Eur. J. Phys. C **3**, 1 (1998).
- [9] L. Landau, J. Phys. (USSR) **8**, 201 (1944); W. R. Leo, Techniques for Nuclear and Particle Physics Experiments, Narosa Publishing house.
- [10] S. C. Phatak, Clustering Algorithm for PMD,
<http://www.iopb.res.in/phatak/cluster/>.
- [11] M. M. Aggarwal *et al.* (WA98 Collaboration), Phys. Lett. B **458**, 422 (1999).

- [12] J. Adams (STAR Collaboration) *et al.*, Phys. Rev. C **73** 034906 (2006).
- [13] B. Zhang, C. M. Ko, B. A. Li and Z. Lin, Phys. Rev. C **61**, 067901 (2000).
- [14] I. Arsene *et al.* (BRAHMS Collaboration), Nucl. Phys. A **757** 1 (2005); B.B. Back *et al.* (PHOBOS Collaboration), Nucl. Phys. A **757** 28 (2005); J. Adams *et al.* (STAR Collaboration), Nucl. Phys. A **757** 102 (2005); K. Adcox *et al.* (PHENIX Collaboration), Nucl. Phys. A **757** 184 (2005).
- [15] H. Heiselberg, Phys. Rep. **351** (2001) 161; M. M. Aggarwal *et al.* (WA98 Collaboration), Phys. Rev. C **65** 054912 (2002).
- [16] B. Mohanty and J. Serreau, Phys. Rep. **414**, 263 (2005); M. M. Aggarwal *et al.* (WA98 Collaboration), Phys. Rev. C **64**, 011901(R) (2001).
- [17] K. Adcox *et al.* (PHENIX Collaboration), Phys. Rev. Lett. **86**, 3500 (2001).
- [18] L. V. Gribov, E. M. Levin and M. G. Ryskin, Phys. Rep. **100**, 1 (1983); J. P. Blaizot and A. H. Mueller, Nucl. Phys. B **289**, 847 (1987).
- [19] L. McLerran and R. Venugopalan, Phys. Rev. D **49**, 2233 (1994); L. McLerran and R. Venugopalan, Phys. Rev. D **50**, 2225 (1994); Y. V. Kovchegov, Phys. Rev. D **54**, 5463 (1996); E. Iancu and L. McLerran, Phys. Lett. B **510**, 145 (2001); A. Krasnitz and R. Venugopalan, Phys. Rev. Lett. **84**, 4309 (2000).
- [20] J. D. Bjorken, Phys. Rev. D **27**, 140 (1983); L. D. Landau, Izv. Akad. Nauk Ser. Fiz. **17**, 51 (1953); S. Belenkij and L. D. Landau, Usp. Fiz. Nauk. **56**, 309 (1955); Nuovo Cim. Suppl. 3S10 (1956) 15; R. C. Hwa and K. Kajantie, Phys. Rev. D **32**, 1109 (1985); J. Alam *et al.*, Annals of Phys. **286**, 159 (2000); B. Mohanty and J. Alam, Phys. Rev. C **68**, 064903 (2003).
- [21] P. K. Netrakanti and B. Mohanty, Phys. Rev. C **71**, 047901 (2005); J. Aichelin and K. Werner, Phys. Lett. B **300**, 158 (1993).
- [22] J. Benecke *et al.*, Phys. Rev. **188**, 2159 (1969).

- [23] B. B. Back *et al.* (PHOBOS Collaboration), Phys. Rev. Lett. **87**, 102303 (2001); B. B. Back *et al.* (PHOBOS Collaboration), Phys. Rev. Lett. **91**, 052303 (2003).
- [24] I. G. Bearden *et al.* (BRAHMS Collaboration), Phys. Lett. B **523**, 227 (2001); I. G. Bearden *et al.* (BRAHMS Collaboration), Phys. Rev. Lett. **88**, 202301 (2002).
- [25] K. H. Ackermann *et al.*, Nucl. Instr. Meth. A **499**, 624 (2003).
- [26] I. G. Bearden *et al.* (BRAHMS Collaboration), Phys. Rev. Lett. **93**, 102301 (2004); I. C. Arsene *et al.* (BRAHMS Collaboration), Phys. Lett. B **677**, 267 (2009) [arXiv:0901.0872 [nucl-ex]].
- [27] I. G. Bearden *et al.* (BRAHMS Collaboration), Phys. Rev. Lett. **94**, 162301 (2005) [arXiv:nucl-ex/0403050].
- [28] S. V. Afanasiev *et al.*, (NA49 Collaboration), Phys. Rev. C **66**, 054902 (2002).
- [29] J. L. Klay *et al.* (E895 Collaboration), Phys. Rev. Lett. **88**, 102301 (2002); J. L. Klay *et al.* (E895 Collaboration), Phys. Rev. C **68**, 054905 (2003).

Chapter 4

PARTICLE PRODUCTION AT $\sqrt{s_{NN}} = 9.2 \text{ GeV}$

4.1 Introduction

Exploring the Quantum Chromodynamics (QCD) phase diagram is one of the goals of high-energy heavy-ion collision experiments [1]. The QCD phase diagram is usually plotted as temperature (T) versus baryon chemical potential (μ_B). Assuming a thermalized system is reached in heavy-ion collisions, both of these quantities can be varied by changing the collision energy [2]. The phase diagram shows a possible transition from a high energy density and high temperature phase dominated by partonic degrees of freedom, to a phase where the relevant degrees of freedom are hadronic [3]. Several observations at the top RHIC energy, such as the suppression of high transverse momentum (p_T) hadron production in Au+Au collisions relative to $p+p$ collisions [4], large elliptic flow (v_2) for hadrons with light, as well as heavier strange valence quarks, and differences between baryon and meson v_2 at intermediate p_T for Au+Au collisions, have been associated with the existence of a phase with partonic degrees of freedom in the initial stages of heavy-ion collisions [1, 4, 5]. Lowering the collision energy and studying the energy dependence of these observables will allow us to search as a function of center of mass energy ($\sqrt{s_{NN}}$) or (T, μ_B) for the onset of the transition to a phase with partonic degrees of freedom at the early stage of the collision.

Lattice QCD calculations indicate that the system produced at $\mu_B = 0$ evolves through a rapid crossover in the quark-hadron phase transition [6]. Calculations from

lattice QCD [7] and those from several QCD-based models [8] suggest that for collisions corresponding to large μ_B , the transition is first order. The point in the (T, μ_B) plane where the first order phase transition ends, is the QCD critical point [9]. Theoretical predictions of the location of this point on the phase diagram are subject to various ambiguities [10]. An experimental program for locating the QCD critical point through its signatures [10, 11] (e.g., long range fluctuations in event-by-event observables) is one of the exciting possibilities at the RHIC facility. These motivations form the basis of the proposal [12] by the collaborations (mainly STAR and PHENIX) at RHIC to carry out a detailed program of exploring the phase diagram by varying the collision energy in high-energy heavy-ion collisions.

As an initial step to test the capabilities of the collider and experiments, a short run was conducted in the year 2008 at RHIC. The Au ions were collided at $\sqrt{s_{NN}} = 9.2$ GeV, which is below the injection energy at RHIC. The data taking period lasted for less than five hours at the Solenoidal Tracker at RHIC (STAR) experiment. This chapter presents the results based on the analysis of this small data set and demonstrates the success of the test run in achieving its objectives. The measurements shown here are the first step towards a detailed exploration of the QCD phase diagram at RHIC.

The presentation of results in this chapter are along the following lines: The next section briefly presents the detectors used and details of 9.2 GeV data analysis. After that we present the results including p_T spectra, dN/dy , $\langle p_T \rangle$ and particle ratios as a function of collision centrality and $\sqrt{s_{NN}}$. In last section, we discuss the freeze-out conditions.

4.2 STAR Detector for 9.2 GeV Run

The results presented here are based on data taken at STAR [13] in Au+Au collisions at $\sqrt{s_{NN}} = 9.2$ GeV. This data set is taken with a minimum bias trigger. The trigger detectors used are the Beam-Beam Counter (BBC) and Vertex Position Detector (VPD) [14]. The BBCs are scintillator annuli mounted around the beam pipe beyond the east and west pole-tips of the STAR magnet at about 375 cm from the center of the nominal interaction region (IR). The VPDs are based on the conventional technology of plastic scintillator

read-out by photomultiplier tubes. The VPD consists of two identical detector assemblies very close to the beam pipe, one on each side at a distance of $|V_z| = 5.6$ m from the center of the IR. The main detector used to obtain the results on p_T spectra, yields, and particle ratios for charged hadrons is the Time Projection Chamber (TPC) [15]. The TPC is the primary tracking device at STAR. The TPC data are used to determine particle trajectories, momenta, and particle-type through ionization energy loss (dE/dx). The solenoidal magnet field of the STAR used for this low energy Au+Au test run was 0.5 T. The details of the design and other characteristics of the STAR detectors can be found in Ref. [13] and are also given in chapter 2 of the present thesis.

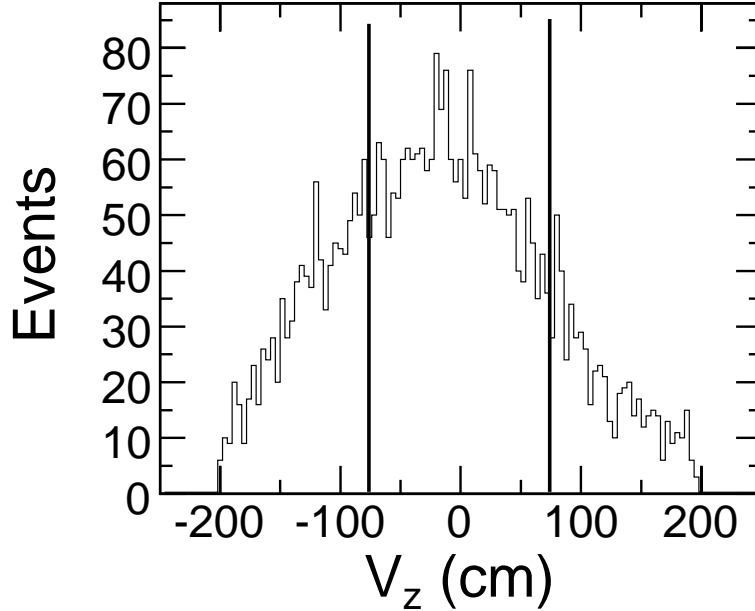


Figure 4.1: Event-by-event distribution of the z -position of the primary vertex (V_z) in Au+Au collisions at $\sqrt{s_{NN}} = 9.2$ GeV. The vertical solid lines show the condition of $|V_z| < 75$ cm for selected events.

4.3 Data Set Selection

In following subsections, we discuss the criteria used for data set selection in Au+Au collisions at $\sqrt{s_{NN}} = 9.2$ GeV.

4.3.1 Event Selection

The primary vertex for each minimum bias event is determined by finding the best point of common origin of the tracks measured in the TPC. The distribution of the primary vertex position along the longitudinal beam direction (V_z) is shown in Fig. 4.1. The distribution is a broad Gaussian varying between -200 and 200 cm, with a root mean square deviation of 89 cm. Only those events which have a V_z within 75 cm of the nominal collision point (center of the detector) are selected for the analysis, corresponding to 57% of the total events recorded. This value is chosen by the trade-off between uniform

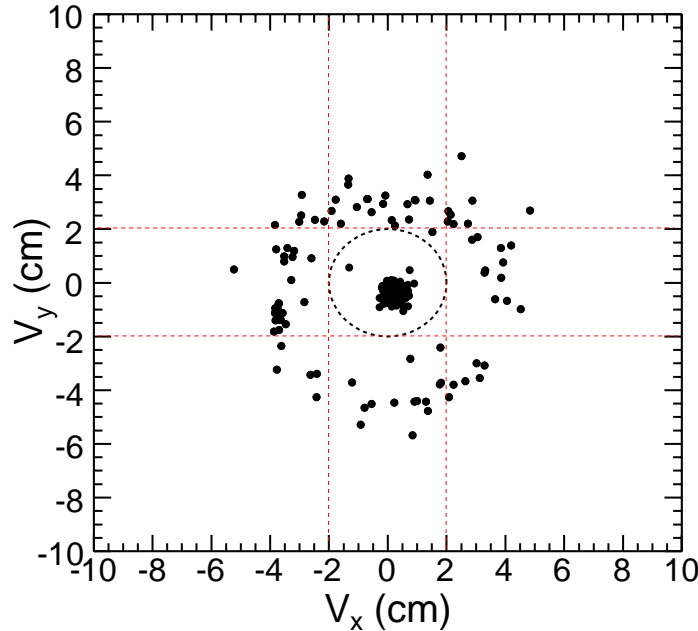


Figure 4.2: The variation of x and y positions of event vertex. The events involving beam-gas and beam-pipe interactions are rejected by applying a cut of 2 cm on the event vertex radius for the present analysis. See text for details.

detector performance within $|\eta| < 1.0$ and sufficient statistical significance of the measured observables. In order to reject events which involve interactions with the beam pipe and beam-gas interactions, the event vertex radius (defined as $\sqrt{V_x^2 + V_y^2}$ where V_x and V_y are the vertex positions along the x and y directions) is required to be less than 2 cm as shown in Fig. 4.2. A total of about 3000 events pass the selection criteria described

above. Figure 4.3 shows typical collisions recorded in STAR TPC. These are considered as good events. Upper plots show the view along z -axis (beam direction) and the lower plots show the view from the x -direction, perpendicular to the beam direction. Left plots in the two panel show a typical collision with low multiplicity, and right plots show a typical collision with high multiplicity.

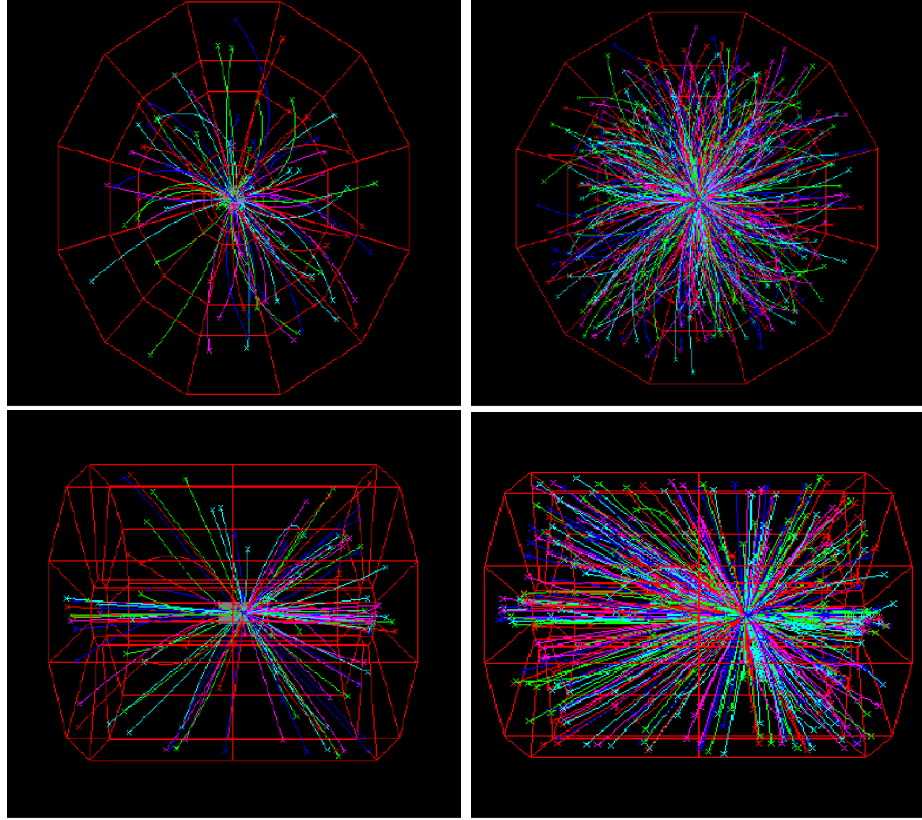


Figure 4.3: Typical event displays observed in TPC of STAR detector for Au+Au collisions at $\sqrt{s_{NN}} = 9.2$ GeV [16]. Upper plots show the view along z -axis (beam direction) and the lower plots show the view from the x -direction, perpendicular to the beam direction. Left plots in the two panel show a typical collision with low multiplicity, and right plots show a typical collision with high multiplicity.

4.3.2 Centrality Selection

Centrality classes in Au+Au collisions at $\sqrt{s_{NN}} = 9.2$ GeV are defined using the number of charged particle tracks reconstructed in the main TPC over the full azimuth, pseudo-rapidity $|\eta| < 0.5$ and $|V_z| < 75$ cm.

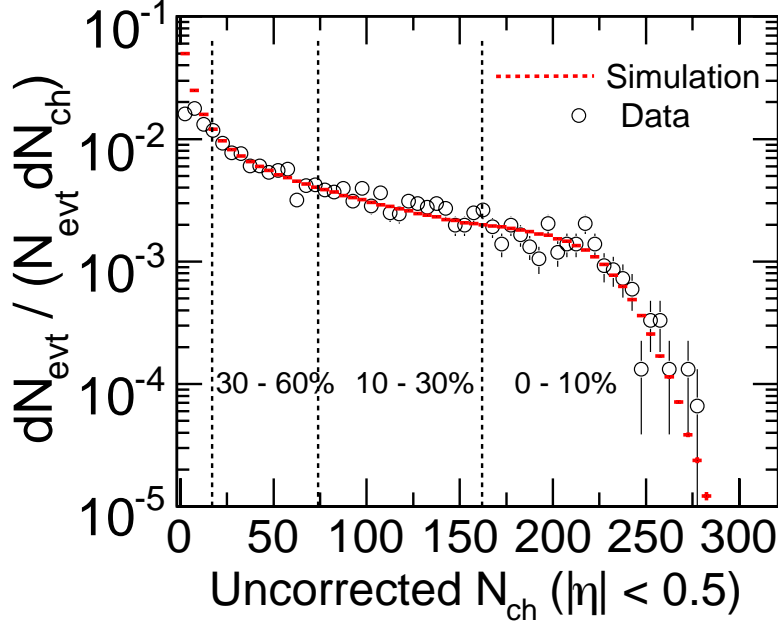


Figure 4.4: Uncorrected charged particle multiplicity distribution (open circles) measured in the TPC within $|\eta| < 0.5$ in Au + Au collisions at $\sqrt{s_{NN}} = 9.2$ GeV. The red-dashed line represents the simulated multiplicity distribution. Errors are statistical only.

Figure 4.4 shows the uncorrected multiplicity distribution for charged tracks from the real data ($N_{\text{ch}}^{\text{TPC}}$, open circles) and for those obtained from simulation (red-dashed line). Simulated multiplicity density is calculated using the two-component model [17] with the number of participants (N_{part}) and number of collisions (N_{coll}) extracted from the Glauber Monte Carlo simulation as

$$\frac{dN_{\text{ch}}}{d\eta} = n_{pp} \left[(1-x) \frac{N_{\text{part}}}{2} + x N_{\text{coll}} \right]. \quad (4.1)$$

Here n_{pp} is the average multiplicity in minimum bias $p+p$ collisions and x is the fraction of the hard component. The inelastic cross-section for $p+p$ collisions used in the Glauber Model simulations is 31.5 mb [18]. In order to introduce event-by-event variation in multiplicity, we have convoluted the Negative Binomial Distributions (NBD) for multiplicities in $p+p$ collisions with those of N_{part} and N_{coll} . The NBD distribution in multiplicity n has two parameters, n_{pp} and k , and is defined as,

$$P_{\text{NBD}}(n_{pp}, k; n) = \frac{\Gamma(n+k)}{\Gamma(n+1)\Gamma(k)} \cdot \frac{(n_{pp}/k)^n}{(n_{pp}/k + 1)^{n+k}}, \quad (4.2)$$

Table 4.1: Centrality selection, average number of participating nucleons ($\langle N_{\text{part}} \rangle$) and average number of binary collisions ($\langle N_{\text{coll}} \rangle$).

% cross section	$N_{\text{chtrk}}^{\text{TPC}}$	$\langle N_{\text{part}} \rangle$	$\langle N_{\text{coll}} \rangle$
0–10	> 162	317 ± 4	716 ± 83
10–30	74–162	202 ± 11	395 ± 34
30–60	17–74	88 ± 10	133 ± 20

where Γ is the Gamma function. The values $k = 2.1$ and $n_{pp} = 1.12$ are obtained by fitting the measured multiplicities with those from the simulation. The simulated multiplicity distribution is not sensitive to the k parameter. The distributions are found to be similar for varying k values such as $k = 1.0$, 1.6 , and 3.0 . The fitting is performed for $N_{\text{ch}} > 17$ in order to avoid the trigger inefficiency in peripheral collisions. The x value is fixed at 0.11 ± 0.03 , obtained by extrapolating data from the PHOBOS collaboration [19]. The centrality is defined by calculating the fraction of the total cross-section obtained from the simulated multiplicity.

Table 4.1 lists the centrality selection criteria for Au+Au collisions at $\sqrt{s_{NN}} = 9.2$ GeV. We have divided the events into three centrality classes, 0–10%, 10–30%, and 30–60% of the total cross-section. The mean values of N_{part} and N_{coll} have been evaluated for these centrality bins and are given in Table 4.1. Systematic uncertainties on $\langle N_{\text{part}} \rangle$ and $\langle N_{\text{coll}} \rangle$ have been estimated by varying n_{pp} and x in the two-component model as well as varying the input parameters in the Glauber Monte Carlo simulation. The final errors on $\langle N_{\text{part}} \rangle$ and $\langle N_{\text{coll}} \rangle$ are the quadrature sum of these individual systematic errors. The results presented in this chapter cover the collision centrality range of 0–60%. The results from more peripheral collisions are not presented due to large trigger inefficiencies in this test run.

Table 4.2: Track selection criteria for the analysis presented in this chapter.

Analysis	DCA	N_{fit}	η or y	p_T (GeV/ c)
p_T spectra	$< 3\text{cm}$	> 20	$ y < 0.5$	> 0.1

4.3.3 Track Selection and Particle Identification

Track selection criteria for the present analysis is presented in Table 4.2. In order to avoid admixture of tracks from secondary vertices, a requirement is placed on the distance of closest approach (DCA) between each track and the event vertex. In order to prevent multiple counting of split tracks, a condition is placed on the number of track points (N_{fit}) used in the reconstruction of the track. Tracks can have a maximum of 45 hits in the TPC. TPC in STAR detector is well known for identifying pion, kaon and proton. Pions can be cleanly identified upto ~ 0.8 GeV/ c , kaons can be identified upto ~ 0.7 GeV/ c and protons can be identified upto ~ 1.0 GeV/ c , using TPC. Particle identification is accomplished by measuring the ionization energy loss (dE/dx). Figure 4.5 shows the dE/dx of pion, kaon, proton and electron plotted as a function of “rigidity”, which is equal to charge \times momentum of the particle. It can be seen that TPC can nicely identify pion, kaon, proton and electron. To extract the pion yield in a given p_T bin, we perform an eight-Gaussian fit to the normalized dE/dx distributions of positively charged and negatively charged hadrons, simultaneously. The normalized dE/dx in general is defined as

$$n\sigma_X = \frac{\log((dE/dx)/B_X)}{\sigma_X}, \quad (4.3)$$

where X is the particle type (e^\pm, π^\pm, K^\pm, p , or \bar{p}), B_X is the expected mean dE/dx of particle X , and σ_X is the dE/dx resolution of the TPC, which is a function of the track length in the TPC. The expected mean dE/dx of particle X is calculated using a Bichsel function for the energy loss in thin layers of P10 in the STAR TPC [15, 20]. Good agreement between the measurement and the calculation was demonstrated previously [21]. Figure 4.6 shows a typical dE/dx distribution normalized to the pion dE/dx (referred to

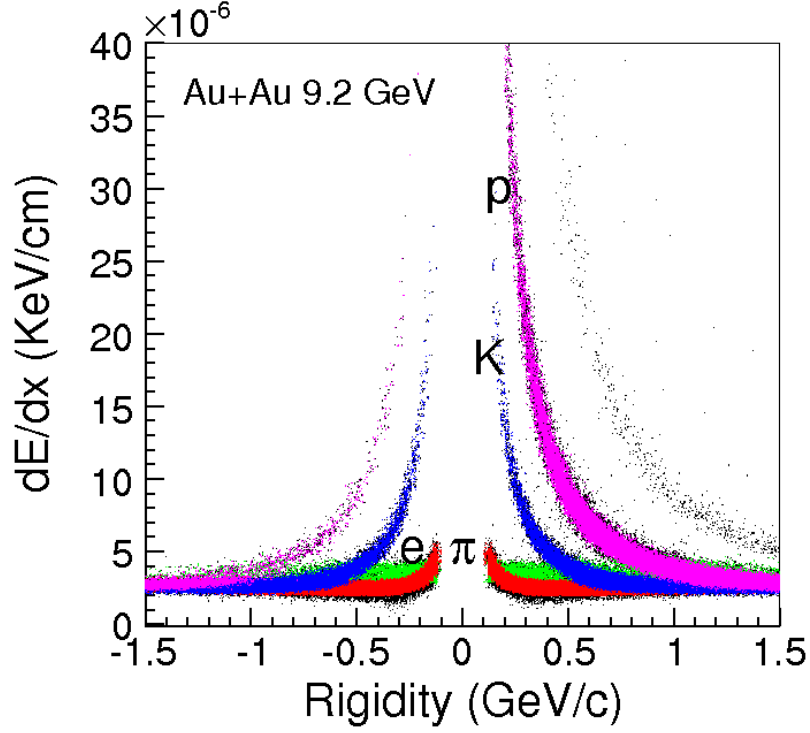


Figure 4.5: The dE/dx of pion, kaon, proton and electron plotted as function of rigidity (charge \times momentum). Red band is for pion, blue is for kaon, magenta is for proton and green is for electron.

as the $n\sigma_\pi$ distribution) for charged hadrons with $0.3 < p_T < 0.4$ GeV/ c and $|y| < 0.5$. The counts under the Gaussian about $n\sigma_\pi \sim 0$ give the yield of pions for a particular p_T range. A similar procedure is followed to obtain yields for other p_T ranges and for yields of kaons and protons. Further details of extracting raw yields of identified hadrons from normalized dE/dx distributions can be found in Ref. [22].

4.4 Correction Factors

Two major correction factors for p_T spectra account for the detector acceptance and for the efficiency of reconstructing particle tracks. These are determined together by embedding the tracks simulated using the GEANT [23] model of the STAR detector into real events at the raw data level. One important requirement is to have a match in

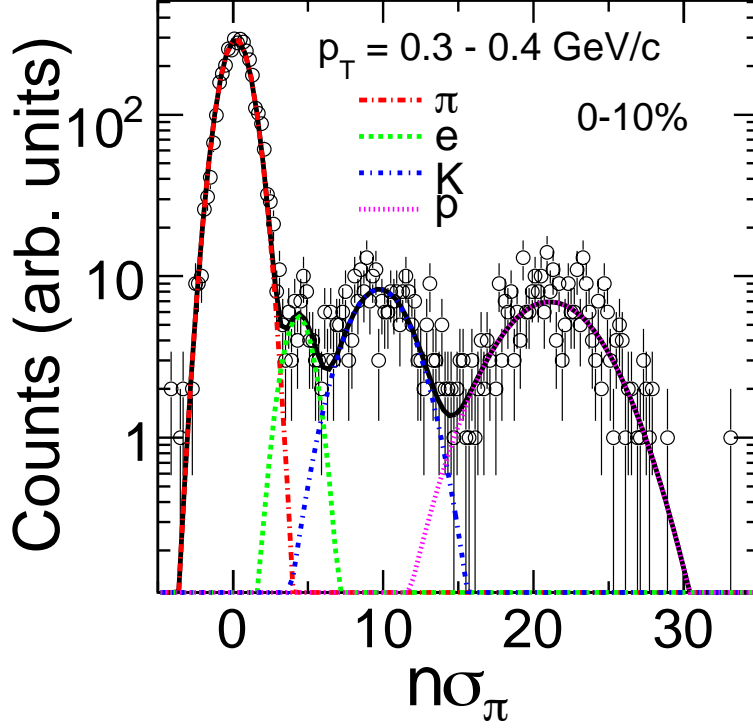


Figure 4.6: The dE/dx distribution for positively charged hadrons in the TPC, normalized by the expected pion dE/dx at $0.3 < p_T < 0.4$ GeV/c and $|y| < 0.5$ in Au+Au collisions at $\sqrt{s_{NN}} = 9.2$ GeV. The curves are Gaussian fits representing contributions from pions (dot-dashed, red), electrons (dashed, green), kaons (dot-dashed, blue), and protons (dotted, magenta). See text for details. Errors are statistical only.

the distributions of reconstructed embedded tracks and real data tracks for quantities reflecting track quality and used for track selection. Figures 4.7 (a) and (b) show the comparisons of DCA (for protons) and N_{fit} (for pions) distributions, respectively, in the range $0.4 < p_T < 0.7$ GeV/c. Similar agreement as in Fig. 4.7 is observed between embedded tracks and real data in other measured p_T ranges for all the identified hadrons presented in this chapter. The ratio of the distribution of reconstructed and original Monte Carlo tracks as a function of p_T gives the acceptance \times efficiency correction factor as a function of p_T for the rapidity interval studied. The typical efficiency \times acceptance factors in 0–60% central collisions for pions, kaons and protons at midrapidity ($|y| < 0.5$) are shown in Fig. 4.8(a). The raw yields are corrected by these factors to obtain the final

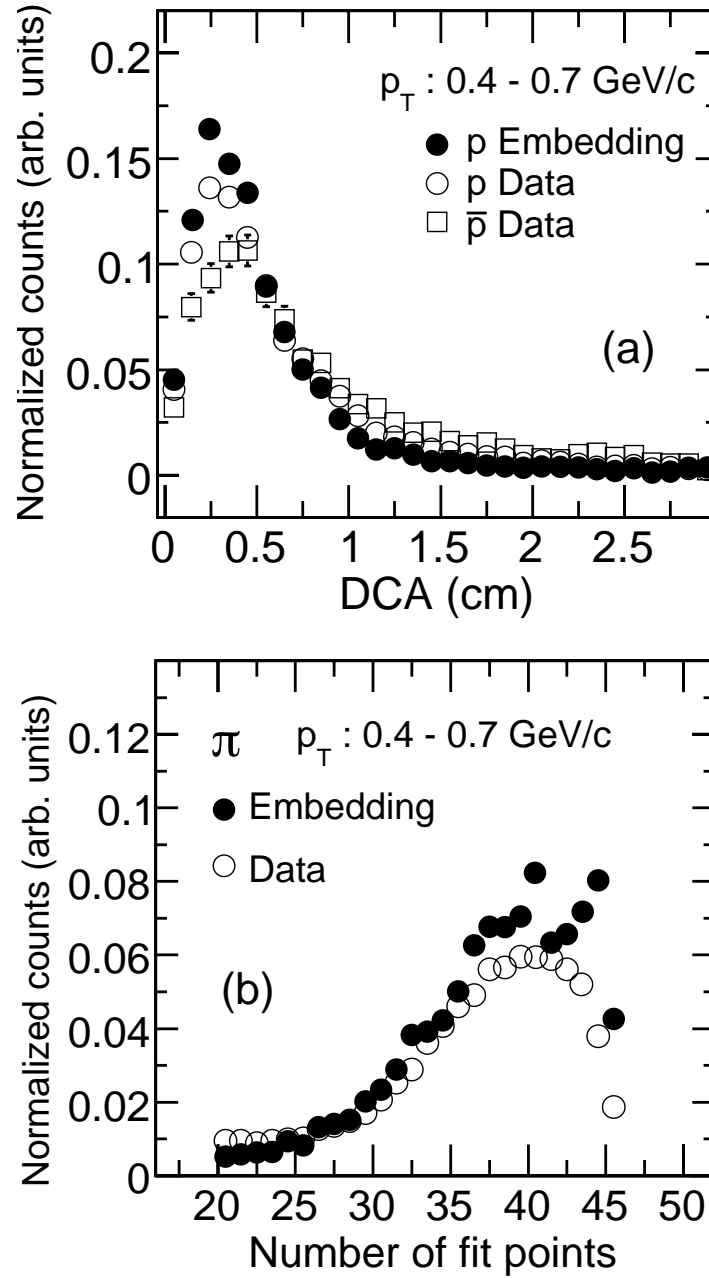


Figure 4.7: (a) Distribution of distance of closest approach of proton tracks to the primary vertex. The embedded tracks are compared to the ones in real data at $0.4 < p_T < 0.7$ GeV/c at midrapidity in Au+Au collisions at $\sqrt{s_{NN}} = 9.2$ GeV. The DCA distribution of anti-protons in a similar kinematic range is also shown for comparison. (b) Comparison between the distributions of number of fit points for pions from embedding and from real data for $0.4 < p_T < 0.7$ GeV/c at midrapidity in Au+Au collisions at $\sqrt{s_{NN}} = 9.2$ GeV.

p_T spectra.

The STAR experiment has previously observed that proton yields had significant contamination from secondary protons, due to interactions of energetic particles produced in collisions with detector materials. As these secondary protons are produced away from the primary interaction point, they appear as a long tail in the DCA distribution of protons. A comparison between shapes of DCA distributions of protons and anti-protons (which do not have such sources of background) was used in STAR to estimate the background contribution to the proton yield [22, 24]. This feature was found to be more pronounced at lower p_T . In this test run, it is observed that the DCA distribution for protons does not exhibit a long tail, and that for all the p_T ranges studied, its shape is similar to that for anti-protons (Fig. 4.7(a)). This lack of secondary protons for Au+Au collisions at $\sqrt{s_{NN}} = 9.2$ GeV could be due to the experimental configuration in the year 2008 with reduced amount of material in front of the STAR TPC, and due to the relatively small number of energetic particles produced in the interactions compared to collisions at higher energies of $\sqrt{s_{NN}} = 62.4$ and 200 GeV. No corrections for secondary proton background are applied for the present analysis at $\sqrt{s_{NN}} = 9.2$ GeV.

The charged pion spectra are corrected for feed-down from weak decays, muon contamination, and background pions produced in the detector materials. These corrections are obtained from Monte Carlo simulations of HIJING events at $\sqrt{s_{NN}} = 9.2$ GeV, with the STAR geometry for year 2008 and a realistic description of the detector response used in GEANT. The simulated events are reconstructed in the same way as the real data. The weak-decay daughter pions are mainly from K_S^0 , and are identified by the parent particle information accessible from the simulation. The muons from pion decay can be misidentified as primordial pions due to their similar masses. This contamination is obtained from Monte Carlo simulations by identifying the decay, which is accessible in the simulation. The weak-decay pion background and muon contamination obtained from the simulation are shown in Fig. 4.8(b), as a function of simulated pion p_T for 0–60% central Au+Au collisions at $\sqrt{s_{NN}} = 9.2$ GeV. The final pion spectra are corrected for this background effect.

The low momentum particles lose energy while traversing the detector material. The

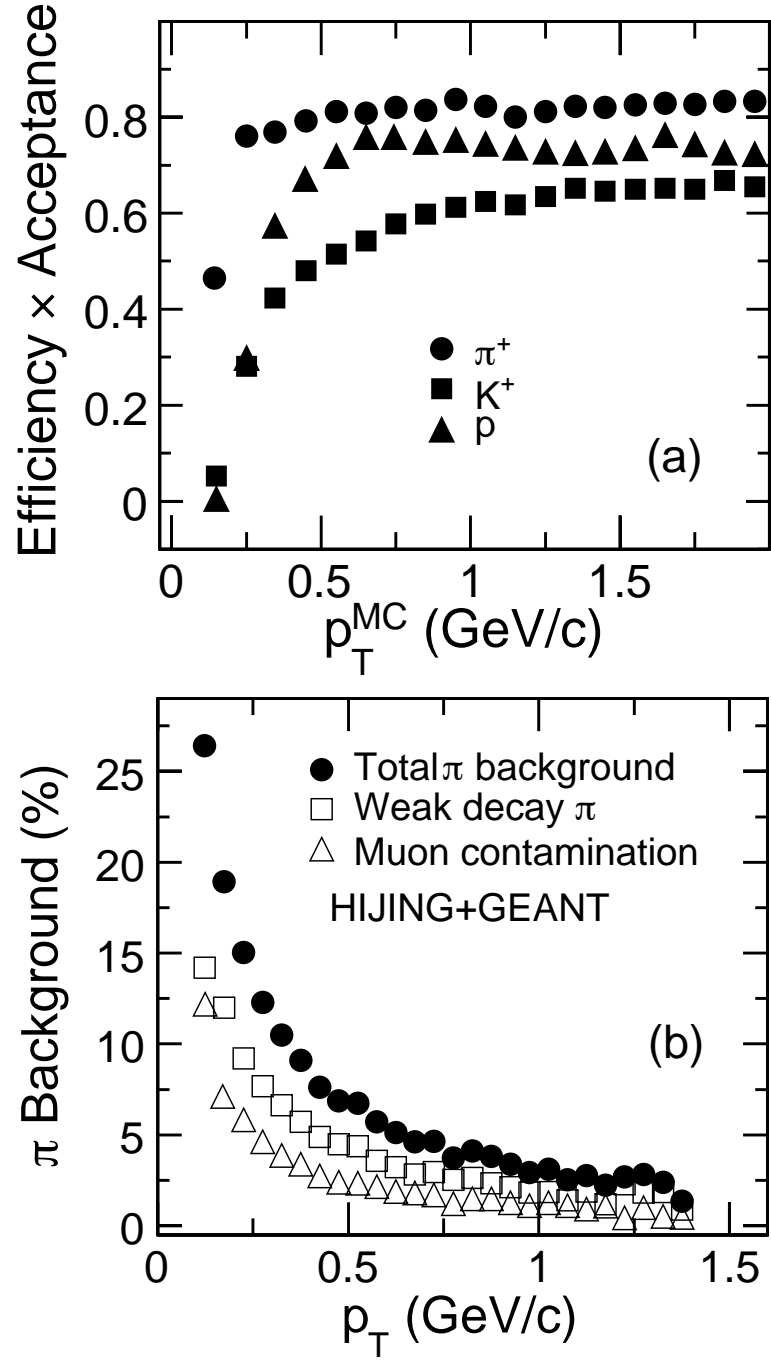


Figure 4.8: (a) Efficiency \times acceptance for reconstructed pions, kaons and protons in the TPC as a function of p_T at midrapidity in Au+Au collisions at $\sqrt{s_{NN}} = 9.2$ GeV. (b) Percentage of pion background contribution estimated from HIJING+GEANT as a function of p_T at midrapidity in Au+Au collisions at $\sqrt{s_{NN}} = 9.2$ GeV. The contributions from different sources and the total background are shown separately.

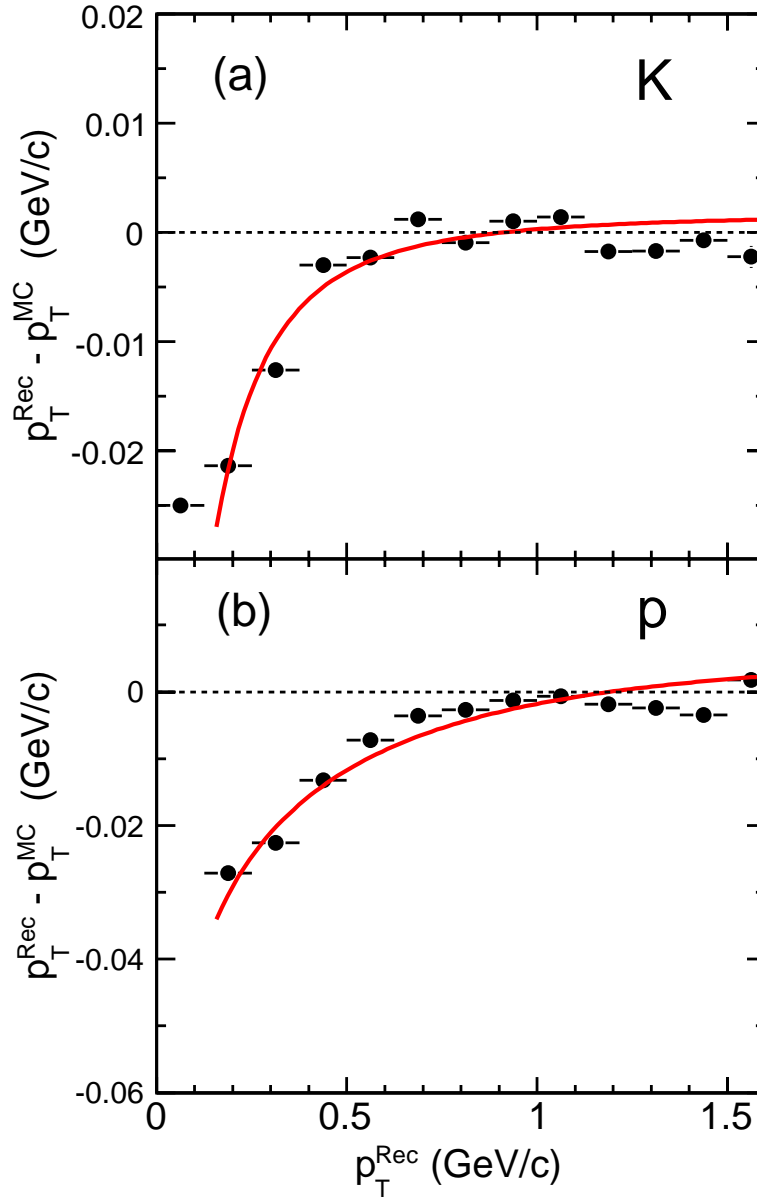


Figure 4.9: The p_T difference of reconstructed and embedded track plotted as function of p_T of embedded track for (a) kaons and (b) protons. See text for the details.

Table 4.3: Sources of systematic errors on yields of various produced hadrons.

Hadron	V_z	track cuts	y	correction	PID	extrapolation
π	3%	3.2%	2%	5%	5%	3%
K	3%	6.2%	2%	5%	10%	8%
p	3%	5.4%	10%	5%	4%	15%

track reconstruction algorithm takes into account the Coulomb scattering and energy loss, assuming the pion mass for each particle. Therefore, a correction for the energy loss by heavier particles (K^\pm , p and \bar{p}) is needed. This correction is obtained from embedding Monte Carlo simulations, in which the p_T difference of reconstructed and embedded track is plotted as function of p_T of embedded track.

Figure 4.9 (a) and (b) show the energy loss as function of p_T for kaons and protons respectively. The lines represent the function fitted to the data points, given as -

$$f(p_T) = A + B \left(1 + \frac{C}{p_T^2} \right)^D, \quad (4.4)$$

where A, B, C and D are the fit parameters. The largest change in reconstructed p_T is found to be ~ 20 MeV/ c at $p_T = 200$ MeV/ c . For all results presented in this chapter, the track p_T is corrected for this energy loss effect.

4.5 Systematic Errors

Systematic uncertainties on the spectra are estimated by varying cuts, and by assessing the purity of identified hadron sample from dE/dx measurements. In addition, the Gaussian fit ranges are varied to estimate the systematic uncertainty on the extracted raw spectra. For integrated particle yields, extrapolating yields to unmeasured regions in p_T is an additional source of systematic error. These are estimated by comparing the extrapolations using different fit functions to the p_T spectra. The detailed procedure is described in Ref. [22]. A summary of various sources of systematic errors on the identified

hadron yields for 0–60% centrality in Au+Au collisions at $\sqrt{s_{NN}} = 9.2$ GeV is given in Table 4.3. The columns in this table are explained below.

- The column titled “ V_z ” in Table 4.3 represents the systematic errors obtained by varying the V_z range in the analysis,
- “track cuts” lists systematic errors due to variation of DCA and N_{fit} cut values,
- “ y ” represents the systematic effect on yields due to a variation in rapidity range from ± 0.5 to ± 0.2 ,
- “correction” includes the contribution to systematic errors from track reconstruction efficiency and acceptance estimates,
- “PID” represents the systematic errors associated with particle identification (obtained by varying the dE/dx cuts and the range of Gaussian fits to normalized dE/dx distributions), and
- “extrapolation” refers to the contribution of systematic errors from the different fit functions used for obtaining yields in unmeasured p_T ranges.

In addition, the systematic error arising due to the pion background estimation (discussed in the previous subsection) is also calculated. It is of the order of 6%. The total systematic errors are of the order of 11%, 16%, and 20% for pion, kaon, and proton yields respectively.

4.6 Transverse Momentum Spectra

Figure 4.10 shows the transverse momentum spectra for π^\pm , K^\pm , and p (\bar{p}), in Au+Au collisions at $\sqrt{s_{NN}} = 9.2$ GeV. The results are shown for the collision centrality classes of 0–10%, 10–30%, 30–60%, and 0–60%. The \bar{p} spectrum is shown only for 0–60% centrality and the yields are multiplied by a factor of 10 for visibility. The inverse slopes of the identified hadron spectra follow the order $\pi < K < p$. The spectra can be further characterized by looking at the dN/dy and $\langle p_T \rangle$ or $\langle m_T \rangle - m$ for the produced hadrons, where m is the mass of the hadron and $m_T = \sqrt{m^2 + p_T^2}$ is its transverse mass. Those observables are discussed in the following sections.

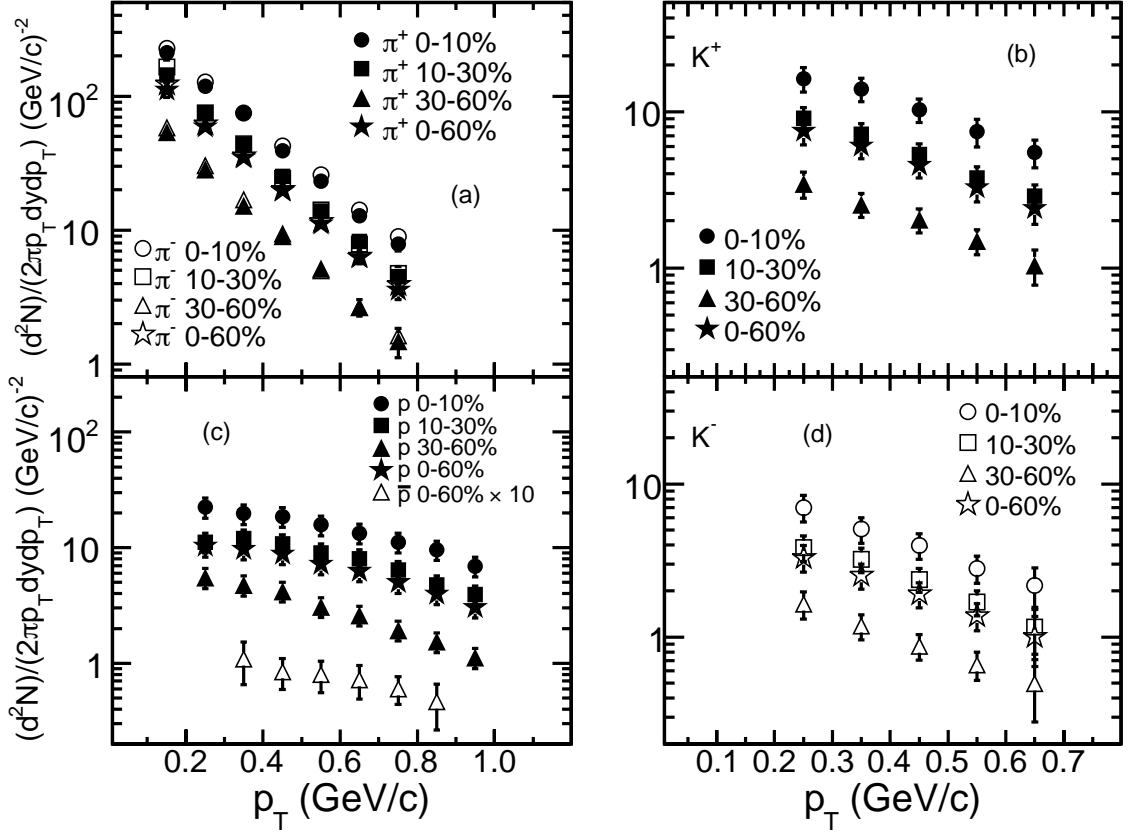


Figure 4.10: Transverse momentum spectra for (a) charged pions, (b) K^+ , (c) protons, and (d) K^- at midrapidity ($|y| < 0.5$) in Au+Au collisions at $\sqrt{s_{NN}} = 9.2$ GeV for various centralities. The distributions for anti-protons were measured in this limited statistics data only for 0–60% centrality. The anti-proton yield shown in the figure is multiplied by a factor of 10. The errors are statistical and systematic errors added in quadrature.

4.7 Centrality Dependence of Particle Production

Figure 4.11 shows the comparison of collision centrality dependence of dN/dy of π^+ , K^\pm , and p , normalized by $\langle N_{\text{part}} \rangle$, between new results at $\sqrt{s_{NN}} = 9.2$ GeV and previously published results at $\sqrt{s_{NN}} = 62.4$ and 200 GeV from the STAR experiment [4, 22, 25]. The yields of charged pions and kaons decrease with decreasing collision energy. The collision centrality dependence within the limited centrality region studied for the new results is similar to that at higher beam energies. For protons, dN/dy is larger in central Au+Au collisions at $\sqrt{s_{NN}} = 9.2$ GeV compared to corresponding results at $\sqrt{s_{NN}} =$

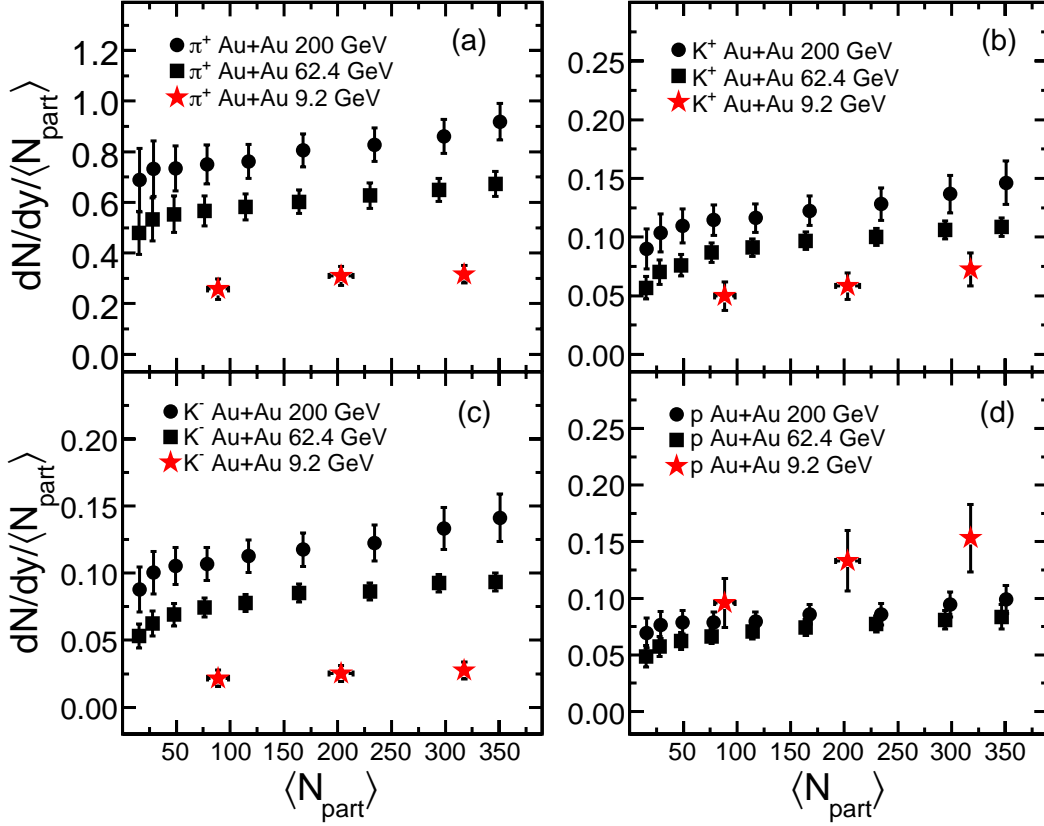


Figure 4.11: dN/dy of (a) π^+ and (b) p , normalized by $\langle N_{\text{part}} \rangle$, for Au+Au collisions at $\sqrt{s_{NN}} = 9.2$ GeV, plotted as a function of $\langle N_{\text{part}} \rangle$. The lower energy results are compared to corresponding results for Au+Au collisions at $\sqrt{s_{NN}} = 62.4$ and 200 GeV [22, 25]. Errors shown are the quadrature sum of statistical and systematic uncertainties.

62.4 and 200 GeV [4, 22, 25]. For the most peripheral collisions, the yields are comparable within errors to corresponding yields at higher beam energies. The increase in proton yield per participating nucleon with the increasing collision centrality is due to large baryon stopping in the lower energies. The inclusive $dN_{\text{ch}}/d\eta$ (sum of contributions from π^\pm , K^\pm , and p (\bar{p})) at midrapidity for various collision centralities are given in Table 4.4 along with the statistical and systematic errors for Au+Au collisions at $\sqrt{s_{NN}} = 9.2$ GeV.

Figure 4.12 shows the comparison of $\langle p_T \rangle$ as a function of $\langle N_{\text{part}} \rangle$ for π^+ , K^+ , and p from Au+Au collisions at $\sqrt{s_{NN}} = 9.2$ GeV with those from collisions at $\sqrt{s_{NN}} = 62.4$ (top panel) and 200 GeV (bottom panel) [4, 22, 25]. For the collision centralities studied,

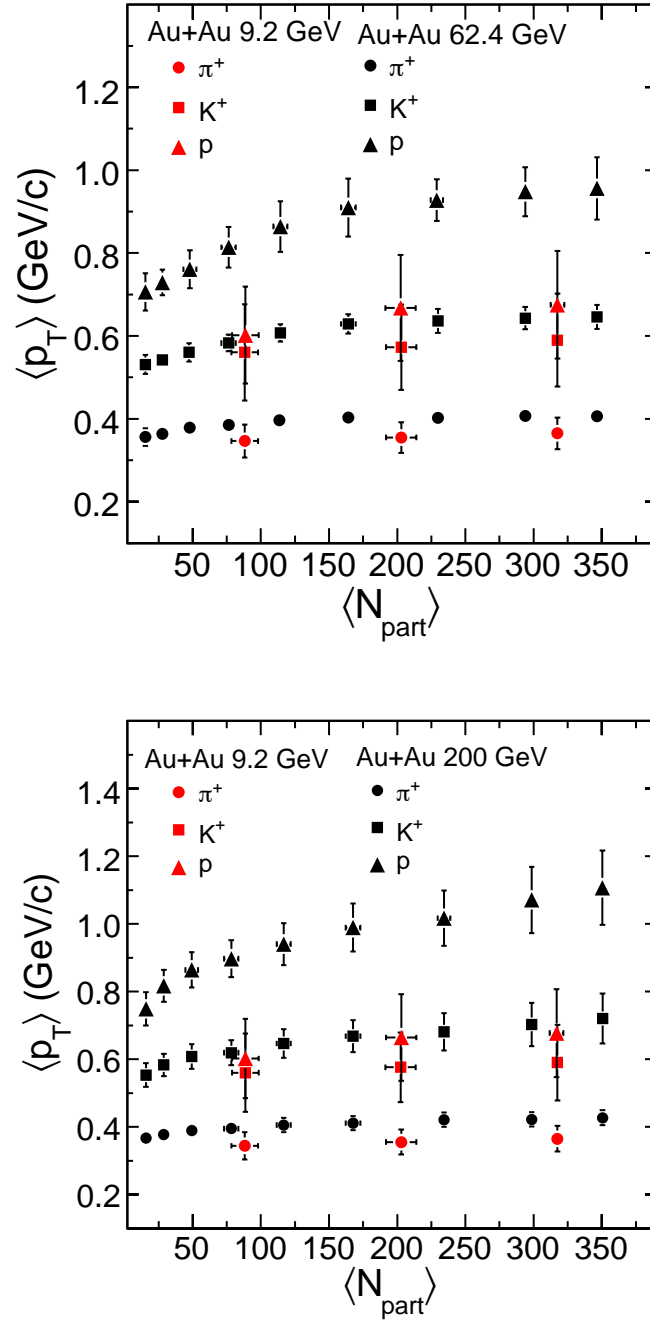


Figure 4.12: $\langle p_T \rangle$ for π^+ , K^+ , and p , plotted as a function of $\langle N_{\text{part}} \rangle$ for Au+Au collisions at $\sqrt{s_{NN}} = 9.2$ GeV and compared to corresponding results at $\sqrt{s_{NN}} = 62.4$ GeV (top panel) and $\sqrt{s_{NN}} = 200$ GeV (bottom panel). The 200 and 62.4 GeV results are from Refs. [4, 22, 25]. Errors shown are the quadrature sum of statistical and systematic uncertainties.

Table 4.4: Centrality dependence of $dN_{\text{ch}}/d\eta$ at midrapidity in Au+Au collisions at $\sqrt{s_{NN}} = 9.2$ GeV.

% cross section	$dN_{\text{ch}}/d\eta$	stat. error	sys. error
0–10	229	25	62
10–30	133	15	36
30–60	48	5	13

the dependencies of $\langle p_T \rangle$ on $\langle N_{\text{part}} \rangle$ at $\sqrt{s_{NN}} = 9.2$ GeV are similar to those at $\sqrt{s_{NN}} = 62.4$ and 200 GeV. An increase in $\langle p_T \rangle$ with increasing hadron mass is observed at $\sqrt{s_{NN}} = 9.2$ GeV. A similar dependence is also observed for $\sqrt{s_{NN}} = 62.4$ and 200 GeV. However, the differences in $\langle p_T \rangle$ between protons and kaons are much smaller compared to the observations at higher beam energies. The mass dependence of $\langle p_T \rangle$ reflects collective expansion in the radial direction. The smaller difference between $\langle p_T \rangle$ of protons and kaons at $\sqrt{s_{NN}} = 9.2$ GeV indicates that the average collective velocity in the radial direction is smaller at that energy.

Figure 4.13 shows the various particle ratios (K^-/K^+ , K^-/π^- , p/π^+ , and K^+/π^+) as a function of collision centrality expressed as $\langle N_{\text{part}} \rangle$ for Au+Au collisions at $\sqrt{s_{NN}} = 9.2$ GeV. Corresponding results from Au+Au collisions at $\sqrt{s_{NN}} = 62.4$ and 200 GeV [4, 22, 25] are also shown. The π^-/π^+ ratio is close to unity and is not shown. Due to low event statistics and the low yield of anti-protons, the centrality dependence of the \bar{p}/p ratio for $\sqrt{s_{NN}} = 9.2$ GeV collisions could not be extracted.

The K^-/K^+ and K^-/π^- ratios are lower at $\sqrt{s_{NN}} = 9.2$ GeV compared to those at $\sqrt{s_{NN}} = 62.4$ and 200 GeV. In the case of K^+/π^+ , there is less variation between 9.2 GeV and the highest RHIC energies than in case of the other particle ratios discussed above. This reflects an interplay between the decreasing importance of associated production and an increasing contribution from pair production of kaons with increasing collision energy. Associated production refers to reactions such as $NN \rightarrow KYN$ and $\pi N \rightarrow KY$, where N is a nucleon and Y a hyperon. The p/π^+ ratio is larger at $\sqrt{s_{NN}} = 9.2$ GeV than at

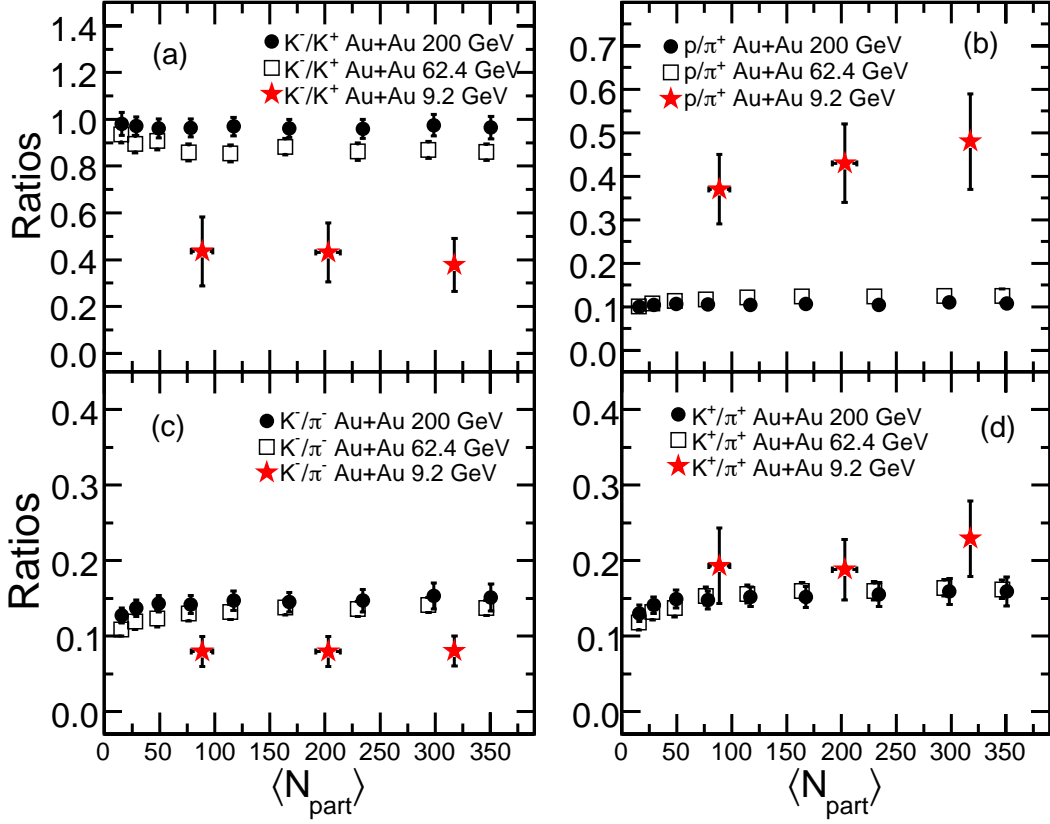


Figure 4.13: Variation of (a) K^-/K^+ , (b) p/π^+ , (c) K^-/π^- , and (d) K^+/π^+ ratios as a function of $\langle N_{\text{part}} \rangle$ for Au+Au collisions at $\sqrt{s_{NN}} = 9.2$ GeV. For comparison we also show the corresponding results from Au+Au collisions at $\sqrt{s_{NN}} = 62.4$ and 200 GeV [22, 25]. Errors shown are the quadrature sum of statistical and systematic uncertainties.

$\sqrt{s_{NN}} = 62.4$ and 200 GeV for all collision centralities studied. As discussed above, this is a consequence of the higher degree of baryon stopping for the collisions at $\sqrt{s_{NN}} = 9.2$ GeV compared to those at $\sqrt{s_{NN}} = 62.4$ and 200 GeV.

4.8 Energy Dependence of Particle Production

Figure 4.14 shows the $dN_{\text{ch}}/d\eta$ at midrapidity normalized by $\langle N_{\text{part}} \rangle/2$ as a function of $\sqrt{s_{NN}}$. The result from $\sqrt{s_{NN}} = 9.2$ GeV is in agreement with the general energy dependence trend observed at the AGS [26], SPS [27], and RHIC [22, 28]. The result at 9.2 GeV has a value close to that obtained at a similar energy ($\sqrt{s_{NN}} = 8.8$ GeV) by the

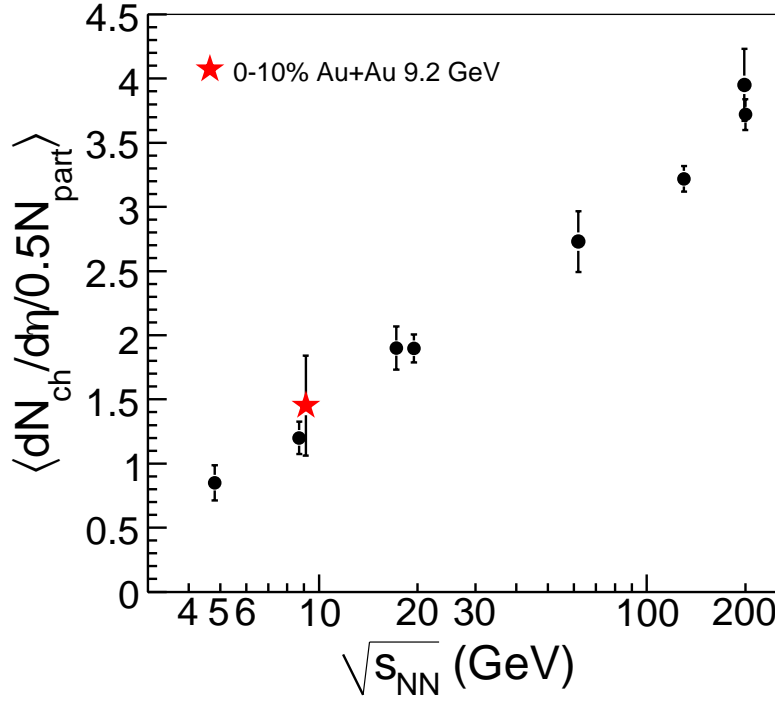


Figure 4.14: The midrapidity $dN_{ch}/d\eta$ normalized by $\langle N_{part} \rangle/2$ as a function of $\sqrt{s_{NN}}$. Au+Au collisions at $\sqrt{s_{NN}} = 9.2$ GeV are compared to previous results from AGS [26], SPS [27], and RHIC [22, 28]. Errors shown are the quadrature sum of statistical and systematic uncertainties.

NA49 experiment at SPS [27]. Figures 4.15 (a) and (b) show dN/dy normalized to $\langle N_{part} \rangle$ for π^\pm and K^\pm , respectively, in 0–10% central Au+Au collisions at $\sqrt{s_{NN}} = 9.2$ GeV, compared to previous results at AGS [26], SPS [27], and RHIC [22]. Within errors, the yields are consistent with previous results at similar $\sqrt{s_{NN}}$. Figures 4.15 (c) and (d) show the $\langle m_T \rangle - m$ for π^\pm and K^\pm , respectively, in 0–10% central Au+Au collisions at $\sqrt{s_{NN}} = 9.2$ GeV. The results are also compared to previous measurements at various energies. The results from Au+Au collisions at $\sqrt{s_{NN}} = 9.2$ GeV are consistent with corresponding measurements at SPS energies at similar $\sqrt{s_{NN}}$. Both dN/dy and $\langle m_T \rangle - m$ are obtained using data in the measured p_T ranges and extrapolations assuming certain functional forms for the unmeasured p_T ranges [22]. For the present midrapidity measurements, the percentage contribution to the yields from extrapolation are about 20% for π^\pm , 50% for

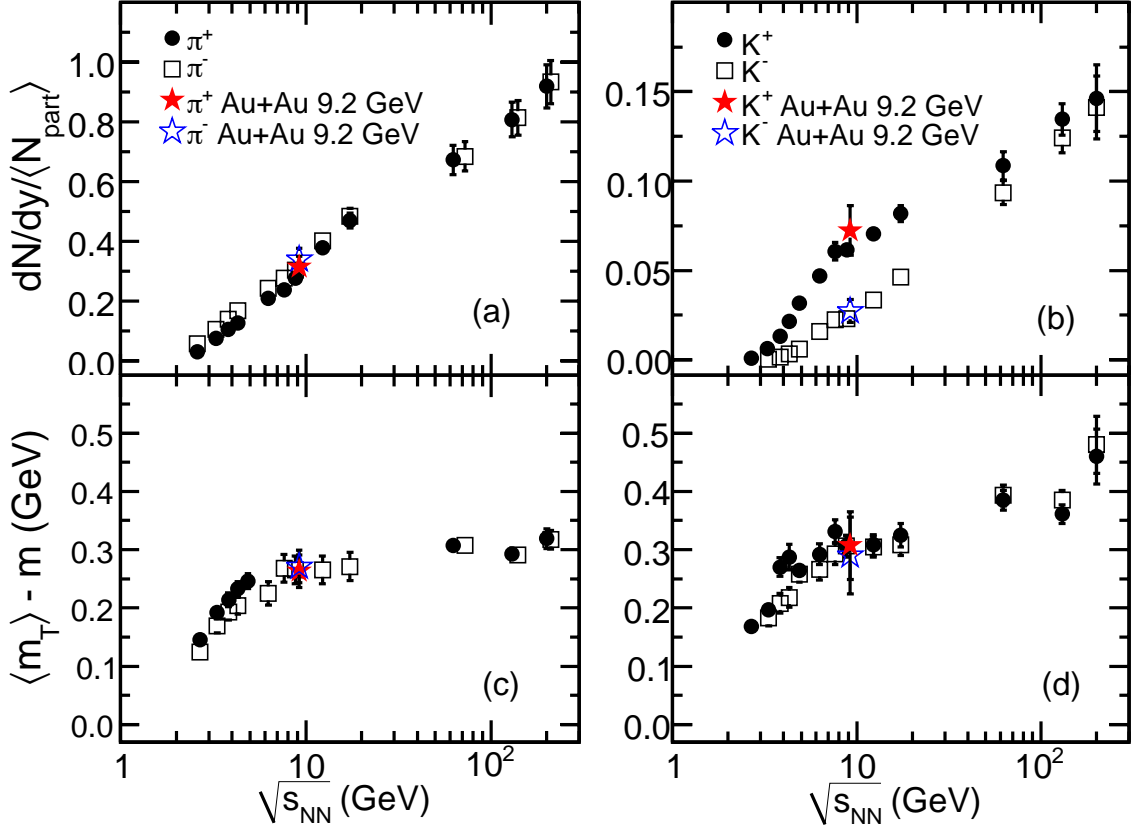


Figure 4.15: Top panels: dN/dy normalized by $\langle N_{\text{part}} \rangle$ for (a) π^\pm and (b) K^\pm . Bottom panels: $\langle m_T \rangle - m$ of (c) π^\pm and (d) K^\pm . Results are shown for 0–10% central Au+Au collisions at $\sqrt{s_{NN}} = 9.2$ GeV, and are compared to previous results from AGS [26], SPS [27], and RHIC [22]. The errors shown are the quadrature sum of statistical and systematic uncertainties.

K^\pm , and 25% for p .

The $\langle m_T \rangle - m$ values increase with $\sqrt{s_{NN}}$ at lower AGS energies, stay independent of $\sqrt{s_{NN}}$ at the SPS and RHIC 9.2 GeV collisions, then tend to rise further with increasing $\sqrt{s_{NN}}$ at the higher beam energies at RHIC. For a thermodynamic system, $\langle m_T \rangle - m$ can be an approximate representation of the temperature of the system, and $dN/dy \propto \ln(\sqrt{s_{NN}})$ may represent its entropy. In such a scenario, the observations could reflect the characteristic signature of a first order phase transition, as proposed by Van Hove [29]. Then the constant value of $\langle m_T \rangle - m$ vs. $\sqrt{s_{NN}}$ around 9.2 GeV could be interpreted as

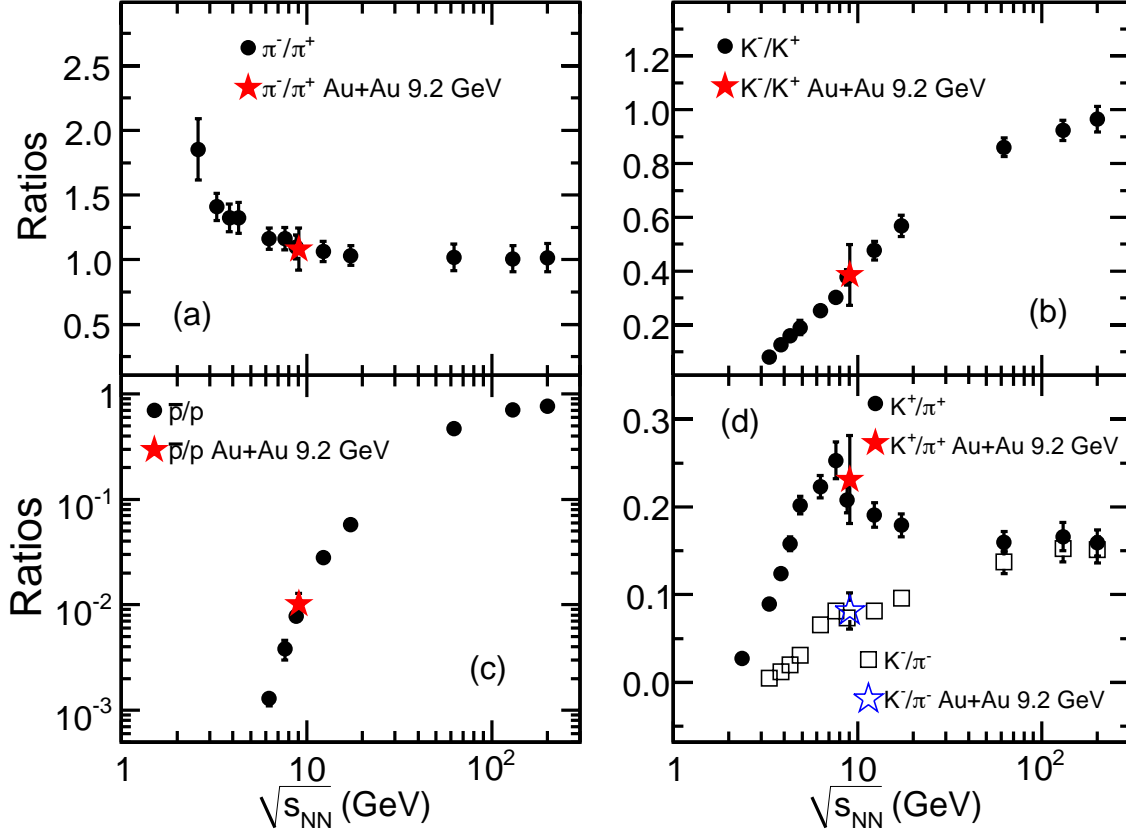


Figure 4.16: (a) π^-/π^+ , (b) K^-/K^+ , (c) \bar{p}/p , and (d) K^-/π^+ ratios at midrapidity ($|y| < 0.5$) for central 0–10% Au+Au collisions at $\sqrt{s_{NN}} = 9.2$ GeV compared to previous results from AGS [26], SPS [27], and RHIC [22]. Errors shown are the quadrature sum of statistical and systematic uncertainties.

reflecting the formation of a mixed phase of a QGP and hadrons during the evolution of the heavy-ion system. However, there could be several other effects to which $\langle m_T \rangle - m$ is sensitive, which also need to be understood for proper interpretation of the data [30]. The energy dependencies of the proton dN/dy and $\langle m_T \rangle - m$ are not discussed in this chapter, as the STAR results are presented without correction for feed down contributions. The low event statistics in the present data does not allow us to obtain feed-down corrections from the data itself. All results presented in this chapter are from inclusive protons and anti-protons similar to that at higher RHIC energies [22].

Figure 4.16 shows the collision energy dependence of the particle ratios π^-/π^+ ,

K^-/K^+ , \bar{p}/p , and K/π , in central heavy-ion collisions. The new results from Au+Au collisions at $\sqrt{s_{NN}} = 9.2$ GeV follow the $\sqrt{s_{NN}}$ trend established by previous measurements. The p_T -integrated π^-/π^+ ratio at $\sqrt{s_{NN}} = 9.2$ GeV is 1.08 ± 0.04 (stat.) ± 0.16 (sys.). Those at lower beam energies have values much larger than unity, which could be due to significant contributions from resonance decays (such as from Δ baryons). The value of the \bar{p}/p ratio at $\sqrt{s_{NN}} = 9.2$ GeV is 0.010 ± 0.001 (stat.) ± 0.003 (sys.), indicating large values of net-protons ($p-\bar{p}$) and large baryon stopping in these collisions. The \bar{p}/p ratio increases with increasing collision energy and approaches unity for top RHIC energies. This indicates that at higher beam energies the collisions have a larger degree of transparency, and the p (\bar{p}) production at midrapidity is dominated by pair production. The K^-/K^+ ratio at $\sqrt{s_{NN}} = 9.2$ GeV is 0.38 ± 0.05 (stat.) ± 0.09 (sys.), indicating a significant contribution to kaon production from associated production at lower collision energies. With increasing $\sqrt{s_{NN}}$, the K^-/K^+ ratio approaches unity, indicating dominance of kaon pair production. The K/π ratio is of interest, as it expresses the enhancement of strangeness production relative to non-strange hadrons in heavy-ion collisions compared to $p + p$ collisions. The increase in K^+/π^+ ratio with beam energies up to $\sqrt{s_{NN}} = 7.7$ GeV at SPS and the subsequent decrease and possible saturation with increasing beam energies has been a subject of intense theoretical debate recently [27, 31]. The discussions mainly focus on the question of the relevant degrees of freedom that are necessary to explain the energy dependence of the K/π ratio. Our new results from Au+Au collisions at $\sqrt{s_{NN}} = 9.2$ GeV with only 3000 events (hence with large errors) are found to be consistent with the previously observed energy dependence. A higher statistics measurement as part of the upcoming Beam Energy Scan at RHIC, with the advantages of collider geometry and with inclusion of the Time-Of-Flight detector [32] in STAR will provide a more precise comparison with as well as a significant quantitative improvement over the SPS results.

4.9 Freeze-out Parameters and Phase Diagram

The measured hadron spectra reflect the properties of the bulk matter at kinetic freeze-out, after elastic collisions among the hadrons have ceased. More direct information on the

earlier stages can be deduced from the integrated yields of the different hadron species, which change only via inelastic collisions. The point in time at which these inelastic collisions cease is referred to as chemical freeze-out, which takes place before kinetic freeze-out. The transverse momentum distributions of the different particles contain two components, one random and one collective. The random component can be identified as the one that depends on the temperature of the system at kinetic freeze-out (T_{kin}). The collective component, which arises from the matter density gradient from the center to the boundary of the fireball created in high-energy nuclear collisions, is generated by collective flow in the transverse direction, and is characterized by its velocity β_T .

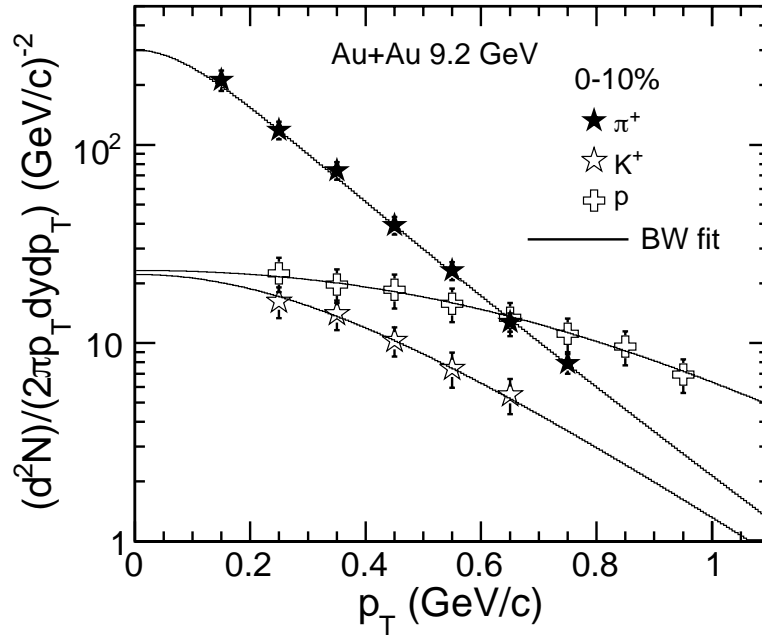


Figure 4.17: Midrapidity transverse momentum distributions of pions, kaons and protons (no feed-down correction) for 0–10% most central Au+Au collisions at $\sqrt{s_{NN}} = 9.2$ GeV, fitted to blast-wave model calculations [33]. The extracted kinetic freeze-out parameters are $T_{\text{kin}} = 105 \pm 10$ (stat.) ± 16 (sys.) MeV and $\langle\beta_T\rangle = 0.46c \pm 0.01c$ (stat.) $\pm 0.04c$ (sys.).

Assuming that the system attains thermal equilibrium, the blast-wave (BW) formulation [33] can be used to extract T_{kin} and $\langle\beta_T\rangle$. The transverse flow velocity of a particle at a distance r from the center of the emission source, as a function of the surface velocity

(β_s) of the expanding cylinder, is parameterized as $\beta_T(r) = \beta_s(r/R)^n$, where n is found by fitting the data. The transverse momentum spectrum is then

$$\frac{dN}{p_T dp_T} \propto \int_0^R r dr m_T I_0 \left(\frac{p_T \sinh \rho(r)}{T_{\text{kin}}} \right) \times K_1 \left(\frac{m_T \cosh \rho(r)}{T_{\text{kin}}} \right), \quad (4.5)$$

where I_0 and K_1 are modified Bessel functions and $\rho(r) = \tanh^{-1} \beta_T(r)$. Simultaneous fits to the p_T distributions of π , K , and p at midrapidity for central 0–10% Au+Au collisions at $\sqrt{s_{NN}} = 9.2$ GeV are shown in Fig. 4.17. The extracted parameters are $T_{\text{kin}} = 105 \pm 10$ (stat.) ± 16 (sys.) MeV, $\langle \beta_T \rangle = 0.46c \pm 0.01c$ (stat.) $\pm 0.04c$ (sys.), and $n = 0.9 \pm 6.4$ (stat.) ± 6.4 (sys.) with $\chi^2/\text{ndf} = 15/17$. The parameter n is poorly constrained by the fits in this low event statistical data set. The parameter values do not change within the quoted errors for other centrality ranges. Only statistical errors are used for obtaining the fit parameters shown in the figure. Inclusion of systematic errors gives similar values of T_{kin} and $\langle \beta_T \rangle$. Similar studies have been done for other higher energy collisions at RHIC [22].

Within a statistical model in thermodynamical equilibrium, the particle abundance in a system of volume V can be given by

$$N_i/V = \frac{g_i}{(2\pi)^3} \gamma_S^{S_i} \int \frac{1}{\exp \left(\frac{E_i - \mu_B B_i - \mu_S S_i}{T_{\text{ch}}} \right) \pm 1} d^3p, \quad (4.6)$$

where N_i is the abundance of particle species i , g_i is the spin degeneracy, B_i and S_i are the baryon number and strangeness number, respectively, E_i is the particle energy, and the integral is taken over all momentum space [22]. The model parameters are the chemical freeze-out temperature (T_{ch}), the baryon (μ_B) and strangeness (μ_S) chemical potentials, and the *ad hoc* strangeness suppression factor (γ_S). Measured particle ratios are used to constrain the values of temperature (T_{ch}) and baryon chemical potential (μ_B) at chemical freeze-out using the statistical model assumption that the system is in thermal and chemical equilibrium at that stage. Fits are performed to the various ratios for midrapidity central 0–10% Au+Au collisions at $\sqrt{s_{NN}} = 9.2$ GeV using such a model, and are shown in Fig. 4.18. The analysis is done within the framework of a statistical model as discussed in Ref. [34]. This model has been used to extract chemical freeze-out parameters at higher RHIC energies [22]. The extracted parameter values are $T_{\text{ch}} = 151$

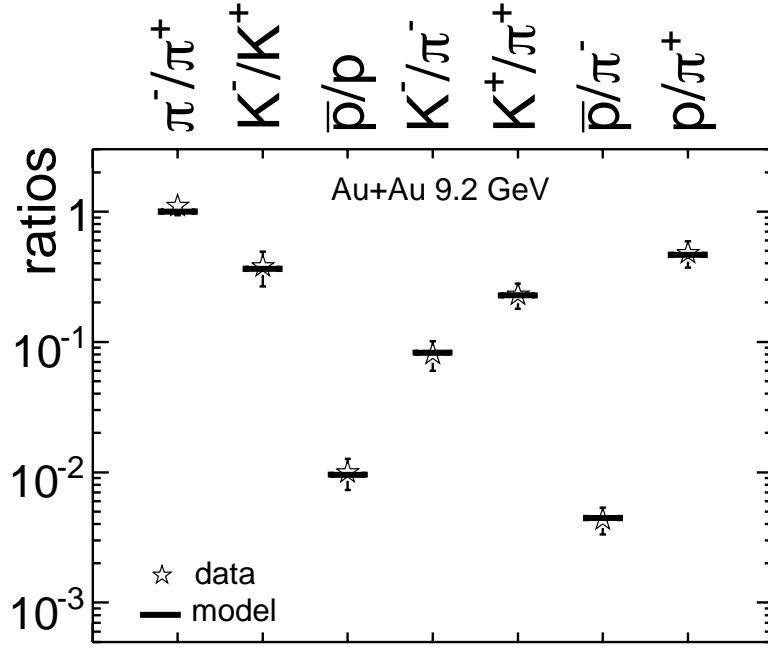


Figure 4.18: Midrapidity particle ratios for 0–10% most central Au+Au collisions at $\sqrt{s_{NN}} = 9.2$ GeV, fitted to thermal model calculations. See text for details. The extracted chemical freeze-out temperature is $T_{\text{ch}} = 151 \pm 2$ (stat.) ± 7 (sys.) MeV and baryon chemical potential is $\mu_B = 354 \pm 7$ (stat.) ± 30 (sys.) MeV.

± 2 (stat.) ± 7 (sys.) MeV, $\mu_B = 354 \pm 7$ (stat.) ± 30 (sys.) MeV, $\mu_S = 25 \pm 9$ (stat.) ± 14 (sys.) MeV, and $\gamma_S = 0.9 \pm 0.7$ (stat.) ± 0.1 (sys.) for 9.2 GeV data. These values are very close to those extracted from the measurements at SPS for similar $\sqrt{s_{NN}}$ [35]. Only statistical errors on the particle production ratios are used for obtaining the fit parameters. Inclusion of systematic errors gives similar values of T_{ch} and μ_B .

Figure 4.19 shows the temperatures at various stages in heavy-ion collisions as a function of μ_B (at different $\sqrt{s_{NN}}$). The μ_B values shown are estimated at chemical freeze-out. The initial temperatures (T_{initial}) achieved at top RHIC and SPS energies are obtained from models [36] that explain the direct photon measurements from the PHENIX experiment at RHIC [37] and from the WA98 experiment at SPS [38]. From these models, which assume that thermalization is achieved in the collisions within a time between 0.1–1.2 fm/c, the T_{initial} extracted is greater than 300 MeV at RHIC and greater than 200

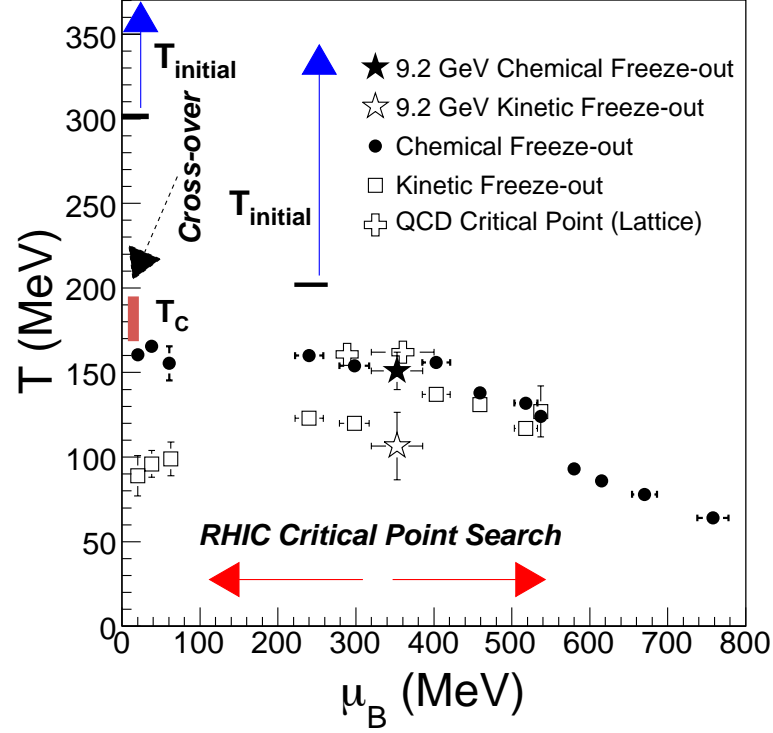


Figure 4.19: Temperature vs. baryon chemical potential (μ_B) from heavy-ion collisions at various $\sqrt{s_{NN}}$ [22]. The μ_B values shown are estimated at chemical freeze-out. The kinetic and chemical freeze-out parameters, extracted using models assuming thermal and chemical equilibrium from midrapidity measurement in central 0–10% Au+Au collisions at $\sqrt{s_{NN}} = 9.2$ GeV, are shown as star symbols. The range of critical temperatures (T_c) [39] of the cross-over quark-hadron phase transition at $\mu_B = 0$ [6] and the QCD critical point from two different calculations [9] from lattice QCD are also indicated. Model-based estimates of the range of initial temperature (T_{initial}) achieved in heavy-ion collisions based in part on direct photon data at top RHIC [37] and SPS [38] energies are also shown. The range of μ_B to be scanned in the upcoming RHIC critical point search and Beam Energy Scan program corresponding to $\sqrt{s_{NN}} = 5.5$ to 39 GeV is indicated by horizontal arrows near the μ_B axis [12].

MeV at SPS. The T_{ch} and T_{kin} values extracted from particle ratios and p_T spectra of various hadrons, respectively, from models assuming thermodynamical equilibrium are also shown. The values for $\sqrt{s_{NN}} = 9.2$ GeV are from the data presented in this thesis. The values at other $\sqrt{s_{NN}}$ are from Ref. [22] and references therein. It is interesting to observe that T_{ch} and T_{kin} values approach each other in the high μ_B regime. A few recent predictions from lattice QCD calculations [10] are also shown in Fig. 4.19. Several lattice QCD calculations indicate that the partonic to hadronic phase transition occurs around $T_c \sim 170\text{--}190$ MeV [39]. These calculations also suggest that the phase transition at $\mu_B = 0$ is a cross-over [6]. Most QCD-based model calculations [3, 7] suggest that the phase transition at large μ_B is of first-order. Two estimates of the QCD critical point [9] in the $T - \mu_B$ plane taking $T_c = 176$ MeV are shown in Fig. 4.19. A detailed plan has been proposed at RHIC to locate the QCD critical point experimentally and to explore the QCD phase boundary by varying $\sqrt{s_{NN}}$ (hence μ_B) [12]. The region planned to be explored in the critical point search program at RHIC is shown in Fig. 4.19.

These results from the lowest energy collisions studied up to now at RHIC demonstrate the capabilities of the STAR detector to pursue the proposed Beam Energy Scan. Large and uniform acceptance for all beam energies in a collider set up, excellent particle identification (augmented by the inclusion of a full barrel Time-Of-Flight in addition to the large acceptance TPC), and higher statistics will offer significant quantitative and qualitative improvement over existing data. The QCD critical point program at RHIC will allow us to extensively explore the QCD phase diagram. It will also allow us to search for the onset of various observations related to partonic matter that have already been uncovered at the highest RHIC energies.

Bibliography

- [1] J. Adams *et al.* (STAR Collaboration), Nucl. Phys. A **757**, 102 (2005).
- [2] A. Andronic, P. Braun-Munzinger and J. Stachel, Nucl. Phys. A **772**, 167 (2006); J. Cleymans and K. Redlich, Phys. Rev. C **60**, 054908 (1999); F. Becattini, J. Manninen and M. Gazdzicki, Phys. Rev. C **73**, 044905 (2006).
- [3] E. Laerman and O. Philipsen, Ann. Rev. Nucl. Part. Sci. **53**, 163 (2003); K. Rajagopal and F. Wilczek, arXiv: hep-ph/0011333; M. A. Stephanov, PoS LAT2006, 024 (2006).
- [4] J. Adams *et al.* (STAR Collaboration), Phys. Rev. Lett. **91**, 072304 (2003); Phys. Rev. Lett. **91**, 172302 (2003); B. I. Abelev *et al.* (STAR Collaboration), Phys. Rev. Lett. **97**, 152301 (2006); Phys. Lett. B **655**, 104 (2007).
- [5] B. I. Abelev *et al.* (STAR Collaboration), Phys. Rev. Lett. **99**, 112301 (2007); Phys. Rev. C **77**, 054901 (2008).
- [6] Y. Aoki *et al.*, Nature **443**, 675 (2006); M. Cheng *et al.*, Phys. Rev. D **77**, 014511 (2008).
- [7] S. Ejiri, Phys. Rev. D **78**, 074507 (2008).
- [8] M. Asakawa and K. Yazaki, Nucl. Phys. A **504**, 668 (1989); A. Barducci *et al.*, Phys. Lett. B **231**, 463 (1989); A. Barducci *et al.*, Phys. Rev. D **41**, 1610 (1990); M. A. Stephanov, Int. J. Mod. Phys. A **20**, 4387 (2005).
- [9] R. Gavai and S. Gupta, Phys. Rev. D **78**, 114503 (2008); Z. Fodor and S. D. Katz, JHEP **0404**, 050 (2004).
- [10] B. Mohanty, e-Print: arXiv:0907.4476 [nucl-ex].

- [11] M. A. Stephanov, K. Rajagopal, E. V. Shuryak, Phys. Rev. Lett. **81**, 4816 (1998); Y. Hatta and M. A. Stephanov, Phys. Rev. Lett. **91**, 102003 (2003); M. A. Stephanov, Phys. Rev. Lett. **102**, 032301 (2009); F. Karsch, D. Kharzeev and K. Tuchin, Phys. Lett. B **663**, 217 (2008) [arXiv:0711.0914 [hep-ph]].
- [12] B. I. Abelev *et al.* (STAR Collaboration), STAR Internal Note - SN0493, 2009.
- [13] K. H. Ackermann *et al.*, Nucl. Instr. Meth. A **499**, 624 (2003).
- [14] W. J. Llope *et al.*, Nucl. Instr. Meth. A **522**, 252 (2004).
- [15] M. Anderson *et al.*, Nucl. Instr. Meth. A **499**, 659 (2003).
- [16] L. Kumar (for the STAR Collaboration), SQM-2008, QM-2009; L. Kumar (for the STAR Collaboration), J. Phys. G: Nucl. Part. Phys. **36**, 064066 (2009); L. Kumar (for the STAR Collaboration), Nucl. Phys. A **830**, 275c (2009).
- [17] D. Kharzeev and M. Nardi, Phys. Lett. B **507**, 121 (2001).
- [18] C. Amsler *et al.*, Phys. Lett. B **667**, 1 (2008).
- [19] B. B. Back *et al.* (PHOBOS collaboration), Phys. Rev. C **70**, 021902 (2004).
- [20] H. Bichsel, Nucl. Instr. Meth. A **562**, 154 (2006); S. Eidelman *et al.* (Particle Data Group), Phys. Lett. B **592**, 1 (2004); Proceedings of 8th International Conference on Advance Technology and Particle Physics, ICATPP 2003, p. 448.
- [21] M. Shao *et al.*, Nucl. Instr. Meth. A **558**, 419 (2006); Y. Xu *et al.*, arXiv: 0807.4303 [physics. ins-det].
- [22] B. I. Abelev *et al.* (STAR Collaboration), Phys. Rev. C **79**, 034909 (2009).
- [23] V. Fine and P. Nevski, in *Proceedings of CHEP-2000*, Padova, Italy, p. 143.
- [24] J. Adams *et al.* (STAR Collaboration), Phys. Rev. C **70**, 041901 (2004).
- [25] J. Adams *et al.* (STAR Collaboration), Phys. Rev. Lett. **92**, 112301 (2004).

- [26] L. Ahle *et al.* (E866 Collaboration and E917 Collaboration), Phys. Lett. B **490**, 53 (2000); L. Ahle *et al.* (E866 Collaboration and E917 Collaboration), Phys. Lett. B **476**, 1 (2000); J. L. Klay *et al.* (E895 Collaboration), Phys. Rev. Lett. **88**, 102301 (2002); J. Barrette *et al.* (E877 Collaboration), Phys. Rev. C **62**, 024901 (2000); Y. Akiba *et al.* (E802 Collaboration), Nucl. Phys. A **610**, 139c (1996); L. Ahle *et al.* (E802 Collaboration), Phys. Rev. C **60**, 064901 (1999); L. Ahle *et al.* (E802 Collaboration and E866 Collaboration), Phys. Rev. C **60**, 044904 (1999); L. Ahle *et al.* (E802 Collaboration), Phys. Rev. C **57**, 466 (1998).
- [27] S. V. Afanasiev *et al.* (NA49 Collaboration), Phys. Rev. C **66**, 054902 (2002); C. Alt *et al.* (NA49 Collaboration), Phys. Rev. C **77**, 024903 (2008); Phys. Rev. C **73**, 044910 (2006); T. Anticic *et al.* (NA49 Collaboration), Phys. Rev. C **69**, 024902 (2004).
- [28] S. S. Adler *et al.* (PHENIX Collaboration), Phys. Rev. C **71**, 034908 (2005).
- [29] L. Van Hove, Phys. Lett. B **118**, 138 (1982).
- [30] B. Mohanty *et al.*, Phys. Rev. C **68**, 021901 (2008) and references therein.
- [31] S. Chatterjee, R. M. Godbole and S. Gupta, arXiv:0906.2523v1 [hep-ph]; A. Andronic, P. Braun-Munzinger and J. Stachel, Phys. Lett. B **673**, 142 (2009); J. K. Nayak, J. Alam, P. Roy, A. K. Dutt-Mazumder and B. Mohanty, Acta Phys. Slov. **56**, 27 (2006); B. Tomasik and E. E. Kolomeitsev, Eur. Phys. J. C **49**, 115 (2007); J. Cleymans, H. Oeschler, K. Redlich and S. Wheaton, Eur. Phys. J. A **29**, 119 (2006); J. Rafelski, I. Kuznetsova and J. Letessier, J. Phys. G **35**, 044011 (2008).
- [32] B. Bonner *et al.*, Nucl. Instr. Meth. A **508**, 181 (2003); M. Shao *et al.*, Nucl. Instr. Meth. A **492**, 344 (2002); J. Wu *et al.*, Nucl. Instr. Meth. A **538**, 243 (2005); J. Adams *et al.*, Phys. Lett. B **616**, 8 (2005).
- [33] E. Schnedermann, J. Sollfrank, and U. Heinz, Phys. Rev. C **48**, 2462 (1993).
- [34] P. Braun-Munzinger, I. Heppe and J. Stachel, Phys. Lett. B **465**, 15 (1999).

- [35] J. Cleymans *et al.*, Phys. Rev. C **73**, 034905 (2006); F. Becattini, J. Manninen and M. Gazdzicki, Phys. Rev. C **73**, 044905 (2006); A. Andronic, P. Braun-Munzinger and J. Stachel, Nucl. Phys. A **772**, 167 (2006).
- [36] R. Chatterjee, D. K. Srivastava and S. Jeon, Phys. Rev. C **79**, 034906 (2009); P. Huovinen, P.V. Ruuskanen and S. S. Rasanen, Phys. Lett. B **535**, 109 (2002); A. K. Chaudhuri, J. Phys. G **29**, 235 (2003); J. Alam *et al.*, Phys. Rev. C **63**, 021901 (2001); D. d’Enterria and D. Peressounko, Eur. Phys. J. C **46**, 451 (2006); J. Alam *et al.*, J. Phys. G **34**, 871 (2007).
- [37] A. Adare *et al.* (PHENIX Collaboration), arXiv: 0804.4168 [nucl-ex].
- [38] M. M. Aggarwal *et al.* (WA98 Collaboration), Phys. Rev. Lett. **85**, 3595 (2000).
- [39] Y. Aoki *et al.*, Phys. Lett. B **643**, 46 (2006); M. Cheng *et al.*, Phys. Rev. D **74**, 054507 (2006).

Chapter 5

FLUCTUATIONS AND CORRELATIONS

5.1 Introduction

The main aim of nucleus-nucleus collisions at relativistic energies is to understand the properties of strongly interacting matter under extreme conditions of high-energy and baryon densities where the creation of Quark-Gluon Plasma (QGP) formation is expected [1, 2]. QGP is believed to be formed at the early stage of collision when the system is hot and dense. As the time passes, the system dilutes, cools down and hadronizes. Fluctuations are supposed to be sensitive to the dynamics of the system, especially at the phase transition. Event-by-event analysis of fluctuations has been proposed as an important tool in understanding the nucleus-nucleus collisions [3–10]. The fluctuations have been studied extensively in several experiments [11–17]. The NA49 being the first to investigate the fluctuations of the average transverse momentum ($\langle p_T \rangle$) [12] and the fluctuations in K/π [18] ratio in central Pb+Pb collisions at the CERN SPS. Study of fluctuations in strangeness is also interesting. The K/π ratio reflects the strangeness enhancement in heavy-ion collisions and fluctuations in K/π ratio as function of centrality can be used to test the association of strangeness enhancement with thermalization [3].

The study of event-by-event fluctuations of various quantities in relativistic heavy-ion collisions like average transverse momentum ($\langle p_T \rangle$), multiplicity, and conserved quantities such as net charge, is considered as one of the main probes for Quark-Gluon Plasma (QGP) formation [19–28]. Non-statistical or dynamical fluctuations, which are produced

due to correlations arising in the particle production processes, have been of great interest in heavy-ion collision experiments. Fluctuations in temperature and thus event-by-event $\langle p_T \rangle$ are studied [29–32] in connection with critical phenomena, which are relevant if the transition is close to a critical point. It has also been observed that the multiplicity and transverse momentum are strongly correlated [33, 34].

The total transverse momentum per event is given as

$$p_T = \sum_{i=1}^N p_{T,i}, \quad (5.1)$$

where N is the event multiplicity and $p_{T,i}$ is the transverse momentum of i^{th} particle. The p_T is very similar to the transverse energy, for which fluctuations have been studied extensively [35, 36]. The mean transverse momentum and inverse slopes of the p_T distributions generally increase with centrality or multiplicity. The average transverse momentum per particle for given multiplicity N to the leading order is given as

$$\langle p_T \rangle_N = \langle \langle p_T \rangle \rangle (1 + \alpha(N - \langle N \rangle) / \langle N \rangle), \quad (5.2)$$

where $\alpha \equiv d \log(\langle p_T \rangle_N) / d \log N$, is small, $\langle \langle p_T \rangle \rangle$ is the average over all events of the single particle transverse momentum and it is given as $\langle \langle p_T \rangle \rangle = \langle p_T / N \rangle$. If the transverse momentum is approximately exponentially distributed with inverse slope T in a given event, $\langle p_{T,i} \rangle = 2T$, and $\sigma(p_{T,i}) = 2T^2 = \langle p_{T,i}^2 \rangle / 2$.

The total transverse momentum per particle in an event has fluctuations given by the following equation [3]

$$\langle N \rangle \sigma(p_T / N) = \sigma(p_{T,i}) + \alpha^2 \langle \langle p_T \rangle \rangle^2 \omega_N + \left\langle \frac{1}{N} \sum_{i \neq j} (p_{T,i} p_{T,j} - \langle \langle p_T \rangle \rangle^2) \right\rangle. \quad (5.3)$$

The three terms on the right in above equation are respectively described below:

- i) First main term represents the individual fluctuations $\sigma(p_{T,i}) = \langle p_{T,i}^2 \rangle - \langle \langle p_T \rangle \rangle^2$.
- ii) The second term gives the effects of correlations between p_T and N . These are suppressed with respect to the first term by a factor $\sim \alpha^2$. The ω_N in this term represents the number fluctuations.

- iii) The third term represents the correlations between transverse momenta of different particles in the same event. In the Wounded Nucleon Model (WNM) [37], the momenta of particles originating from the same participant are correlated. For example, quark-antiquark are produced with the same p_T but in opposite direction. The average number of pairs of hadrons from the same participants is $\langle n(n-1) \rangle$, where n is the number of particles emitted from the same participant nucleon. In this case, the third term in Eq. (5.3) becomes $(\langle n(n-1) \rangle / \langle n \rangle) (\langle p_{T,i} p_{T,j \neq i} \rangle - \langle p_T \rangle^2)$. The momentum correlation between two particles from the same participant is expected to be a small fraction of $\sigma(p_{T,i})$.

5.2 Data Selection

The results presented in this chapter are from Cu+Cu collisions at $\sqrt{s_{NN}} = 62.4$ and 200 GeV using the STAR TPC [38] detector at RHIC. The results are compared with the published results from Au+Au collisions at similar energies [39]. The data set is taken with minimum bias trigger [40]. The main physics trigger for Cu+Cu 200 GeV are based on a ZDC coincidence with vertex cut. For Cu+Cu 62.4 GeV, the ZDC is not so efficient, so a combined “minimum bias” trigger is put together from a combination of the ZDC and BBC. The details of the STAR trigger and trigger detectors are given in chapter 2.

The events with a primary vertex within ± 30 cm of the geometric center of the TPC along the beam axis are accepted for the analysis. This is done in order to remove any biasing in the data. The primary vertex for each minimum bias event is determined by finding the best point of common origin of the tracks measured in the TPC. Figure 5.1 shows the vertex distributions selected for the analysis of Cu+Cu collisions at $\sqrt{s_{NN}} = 62.4$ (top) and 200 GeV (bottom). These cuts yielded about 7.5 M and 15 M minimum bias events for Cu+Cu collisions at 62.4 and 200 GeV, respectively.

The collision centralities represent the fractions of the full cross section in a collision. In data, the collision centrality is determined by using the uncorrected charged track multiplicity ($N_{\text{ch}}^{\text{TPC}}$), measured in the TPC within $|\eta| < 0.5$. The $N_{\text{ch}}^{\text{TPC}}$ distribution is called the *reference multiplicity* distribution for charged tracks. The various centrality bins are

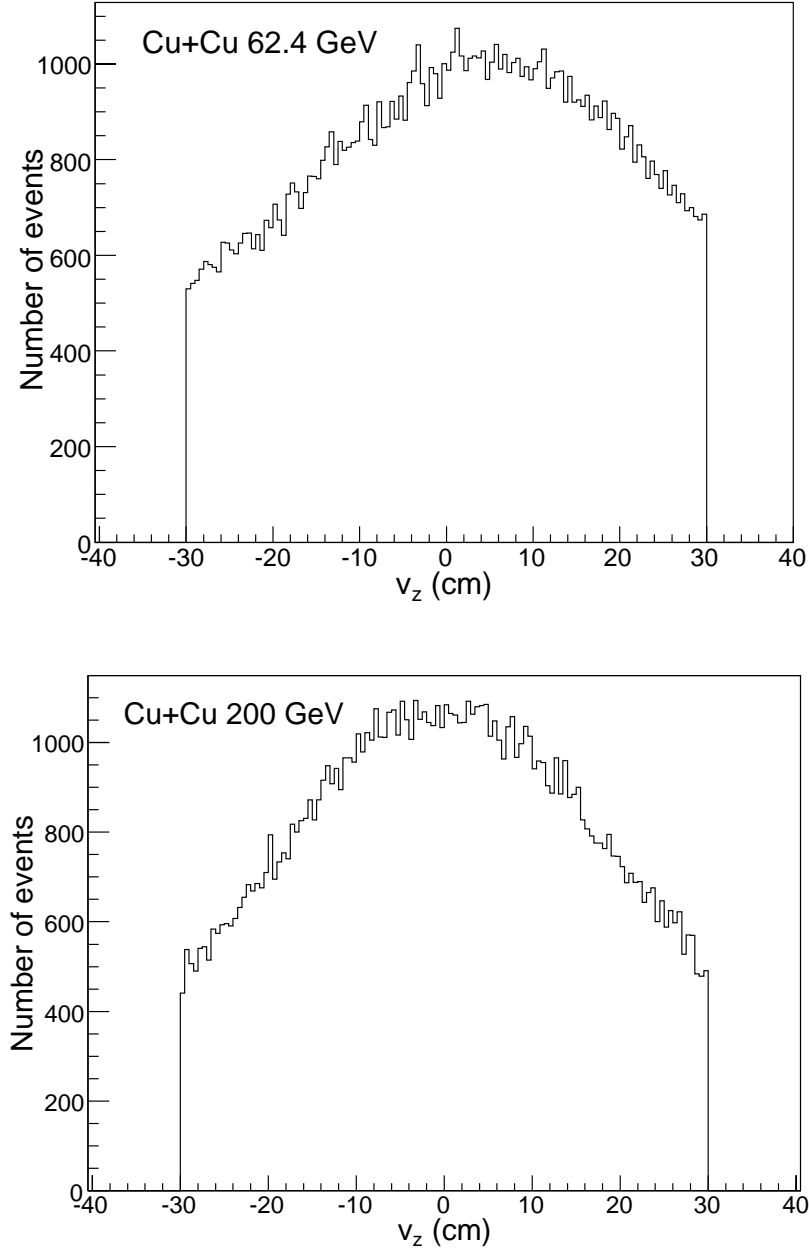


Figure 5.1: Vertex distributions for Cu+Cu collisions at $\sqrt{s_{NN}} = 62.4$ (top) and 200 GeV (bottom). The vertex range selected for the analysis is within ± 30 cm along the beam axis. The plots are STAR preliminary.

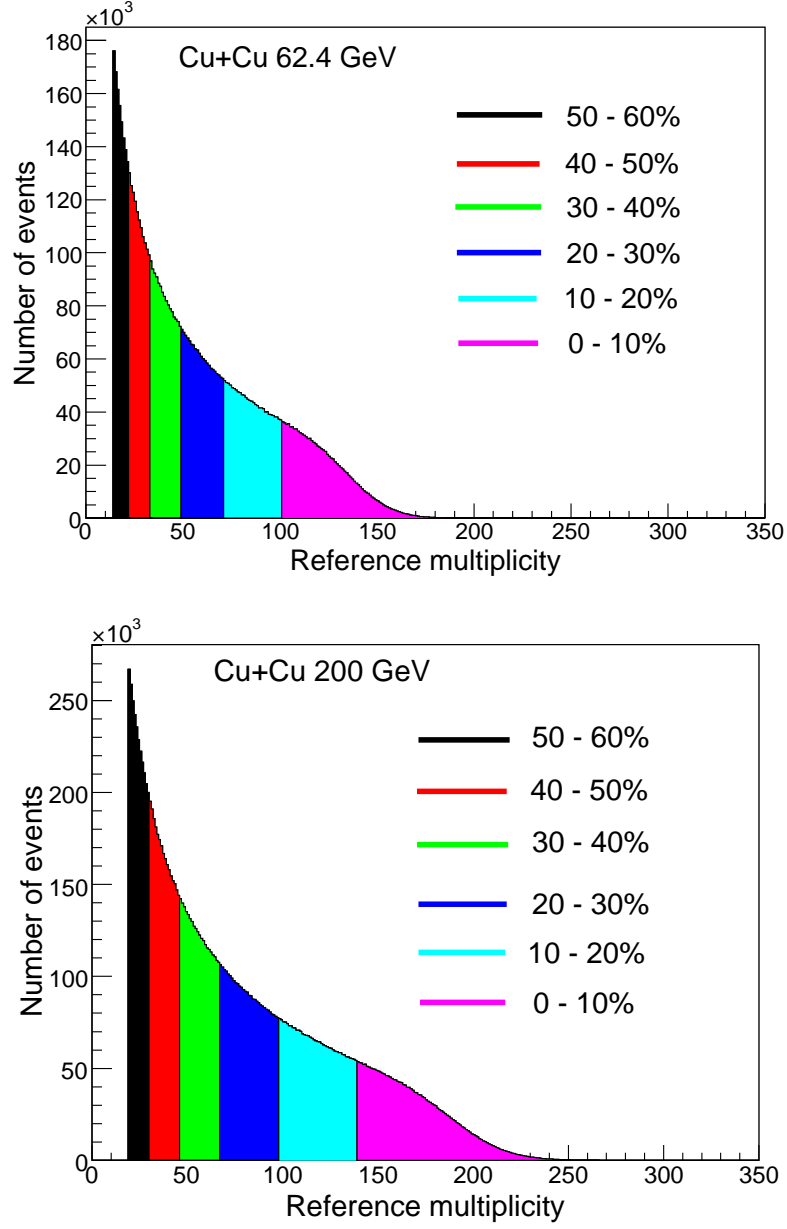


Figure 5.2: Uncorrected charged track multiplicity (reference multiplicity) distributions for Cu+Cu collisions at $\sqrt{s_{NN}} = 62.4$ (top) and 200 GeV (bottom). Various centralities used for the analysis are shown with different colors. The plots are STAR preliminary.

Table 5.1: The $N_{\text{ch}}^{\text{TPC}}$ values, average number of participating nucleons ($\langle N_{\text{part}} \rangle$) and average number of binary collisions ($\langle N_{\text{coll}} \rangle$) for various collision centralities in Cu+Cu collisions at $\sqrt{s_{NN}} = 62.4$ GeV.

% cross section	$N_{\text{ch}}^{\text{TPC}}$	$\langle N_{\text{part}} \rangle$	$\langle N_{\text{coll}} \rangle$
0-10	> 101	$96.4^{+1.1}_{-2.6}$	$161.9^{+12.1}_{-13.5}$
10-20	71 – 100	$72.2^{+0.6}_{-1.9}$	$107.5^{+6.3}_{-8.6}$
20-30	49 – 70	$51.8^{+0.5}_{-1.2}$	$68.4^{+3.6}_{-4.7}$
30-40	33 – 48	$36.2^{+0.4}_{-0.8}$	$42.3^{+2.0}_{-2.6}$
40-50	22 – 32	$24.9^{+0.4}_{-0.6}$	$25.9^{+1.0}_{-1.5}$
50-60	14 – 21	$16.3^{+0.4}_{-0.3}$	$15.1^{+0.6}_{-0.6}$

calculated as a fraction of this multiplicity distribution starting at the highest multiplicities. The centrality classes for Cu+Cu collisions at $\sqrt{s_{NN}} = 62.4$ and 200 GeV are 0–10% (most central), 10–20%, 20–30%, 30–40%, 40–50% and 50–60% (most peripheral). Figure 5.2 shows the centrality selection with various centralities for Cu+Cu collisions at $\sqrt{s_{NN}} = 62.4$ and 200 GeV. Each centrality bin is associated with an average number of participating nucleons ($\langle N_{\text{part}} \rangle$), and average number of binary collisions ($\langle N_{\text{coll}} \rangle$) using the Glauber Monte Carlo simulations [41] employing the Woods-Saxon distribution for the nucleons inside the Cu nucleus. The systematic uncertainties are determined by varying the Woods-Saxon parameters. Tables 5.1 and 5.2 list the $N_{\text{ch}}^{\text{TPC}}$, $\langle N_{\text{part}} \rangle$ and $\langle N_{\text{coll}} \rangle$ values for each centrality in Cu+Cu collisions at $\sqrt{s_{NN}} = 62.4$ and 200 GeV, respectively.

In order to have uniform detector performance, a pseudorapidity cut of $|\eta| < 1.0$ is applied in the data. The selected region of the η distributions for Cu+Cu collisions at 62.4 and 200 GeV are shown in the Fig. 5.3 (top left and top right). The ϕ -distributions (bottom-left and bottom-right) for Cu+Cu collisions at two energies are also shown in this figure. It is important to avoid the admixture of tracks from a secondary vertex. This is achieved by applying a condition on distance of closest approach (DCA) between each track and the event vertex. The charged particle tracks are required to have originated

Table 5.2: The $N_{\text{ch}}^{\text{TPC}}$ values, average number of participating nucleons ($\langle N_{\text{part}} \rangle$) and average number of binary collisions ($\langle N_{\text{coll}} \rangle$) for various collision centralities in Cu+Cu collisions at $\sqrt{s_{NN}} = 200$ GeV.

% cross section	$N_{\text{ch}}^{\text{TPC}}$	$\langle N_{\text{part}} \rangle$	$\langle N_{\text{coll}} \rangle$
0-10	> 139	$99.0^{+1.5}_{-1.2}$	$188.8^{+15.4}_{-13.4}$
10-20	$98 - 138$	$74.6^{+1.3}_{-1.0}$	$123.6^{+9.4}_{-8.3}$
20-30	$67 - 97$	$53.7^{+1.0}_{-0.7}$	$77.6^{+5.4}_{-4.7}$
30-40	$46 - 66$	$37.8^{+0.7}_{-0.5}$	$47.7^{+2.8}_{-2.7}$
40-50	$30 - 45$	$26.2^{+0.5}_{-0.4}$	$29.2^{+1.6}_{-1.4}$
50-60	$19 - 29$	$17.2^{+0.4}_{-0.2}$	$16.8^{+0.9}_{-0.7}$

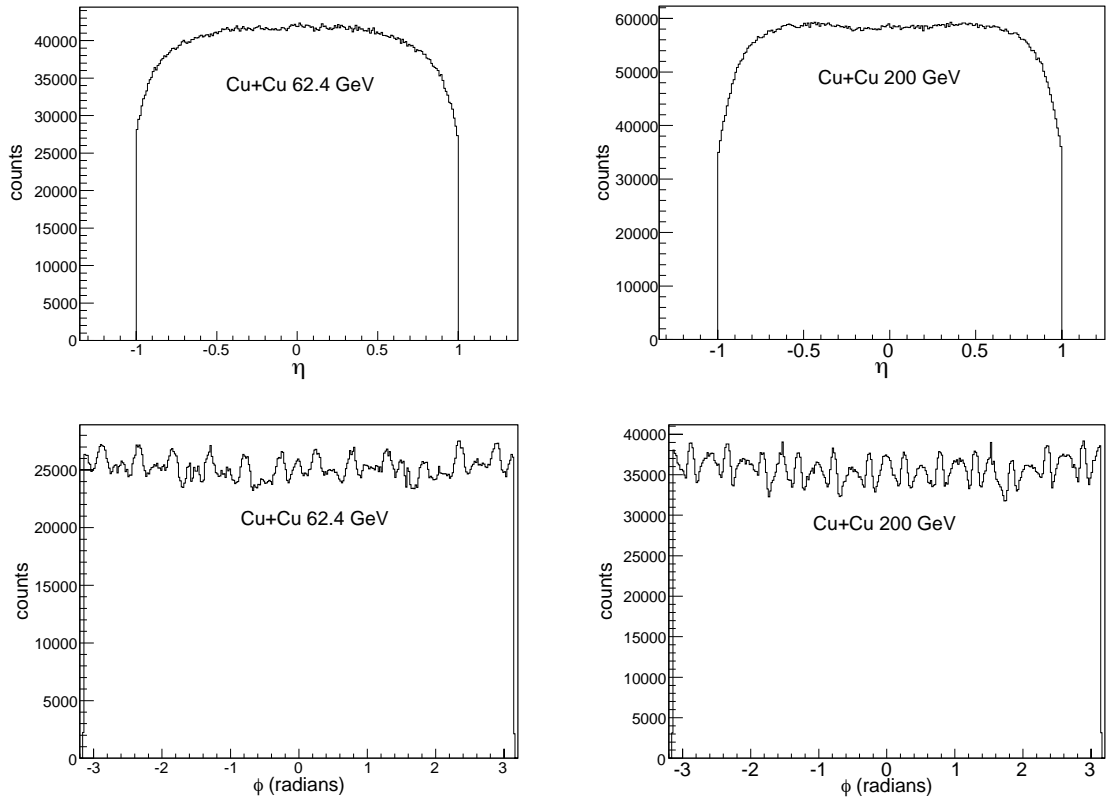


Figure 5.3: Pseudorapidity (top) and azimuthal angle (bottom) distributions for Cu+Cu collisions. The distributions on left and right are for collision energies 62.4 and 200 GeV, respectively. The plots are STAR preliminary.

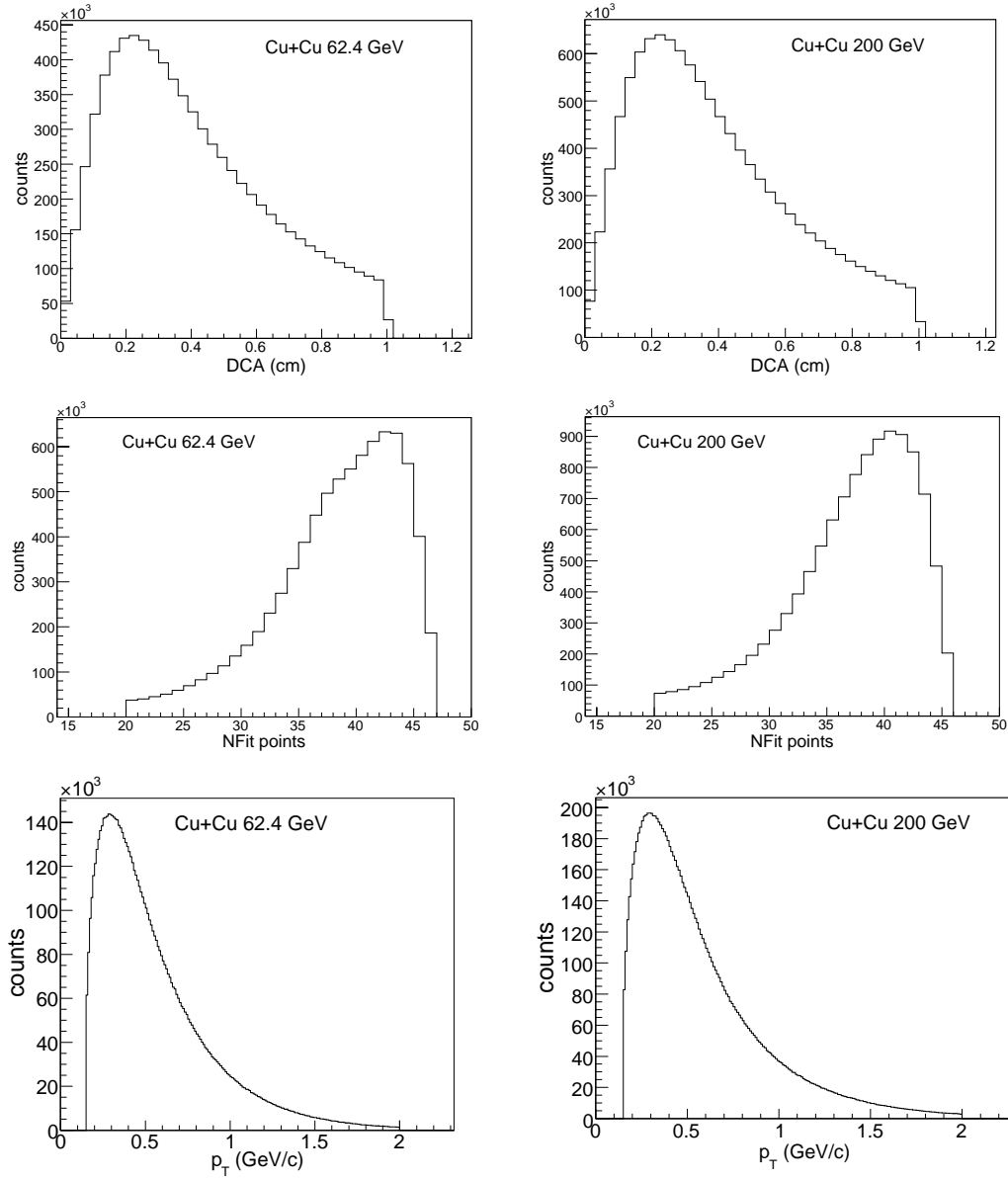


Figure 5.4: Quality assurance distributions for Cu+Cu collisions at 62.4 (left) and 200 GeV (right). Top, middle, and the bottom plots show the DCA, N_{Fit} points, and the p_T distributions, respectively. The plots are STAR preliminary.

within one cm of the measured event vertex. The multiple counting of split tracks is avoided by applying a condition on the number of track points (N_{Fit}) used in the reconstruction of the track. Those charged particle tracks are selected for the analysis which satisfy $N_{\text{Fit}} > 20$. The transverse momentum range selected for the analysis is 0.15–2.0 GeV/ c . As discussed in chapter 2, the TPC track reconstruction efficiency varies significantly below p_T value ~ 0.15 GeV/ c and then remains constant for higher p_T , so in order to minimize the effects due to varying efficiency, the above p_T range is selected for the analysis. Figure 5.4 shows the DCA (top), N_{Fit} points (middle), and p_T (bottom) distributions for the Cu+Cu collisions at $\sqrt{s_{NN}} = 62.4$ (left panels) and 200 GeV (right panels).

5.3 Transverse Momentum Fluctuations

The p_T fluctuations in high energy collisions can be measured from the distribution of the average transverse momentum of the events defined as [42]

$$\langle p_T \rangle = \frac{1}{N} \sum_{i=1}^N p_{T,i}, \quad (5.4)$$

where N is the multiplicity of accepted particles in a given event and $p_{T,i}$ is the transverse momentum of the i^{th} track. The mean p_T distribution is compared to the corresponding distribution obtained for “mixed events” [39]. Mixed events are constructed by randomly selecting one track from an event chosen from the measured events in the same centrality keeping the same event multiplicity as in the data.

Figures 5.5 and 5.6 show the event-by-event mean p_T distributions for Cu+Cu collisions at $\sqrt{s_{NN}} = 62.4$ and 200 GeV, respectively. The solid symbols represent the $\langle p_T \rangle$ distributions for data, and open symbols represent those for mixed events. The distributions corresponding to data are wider as compared to those for mixed events. This suggests the presence of non-statistical fluctuations in the data for all centralities in both Cu+Cu 62.4 and 200 GeV collisions. The mean (μ)/sigma (σ) of distributions decreases/increases from central to peripheral collisions for both data and mixed events for Cu+Cu collisions at $\sqrt{s_{NN}} = 62.4$ and 200 GeV. Tables 5.3 and 5.4 list the values of μ and σ for data and

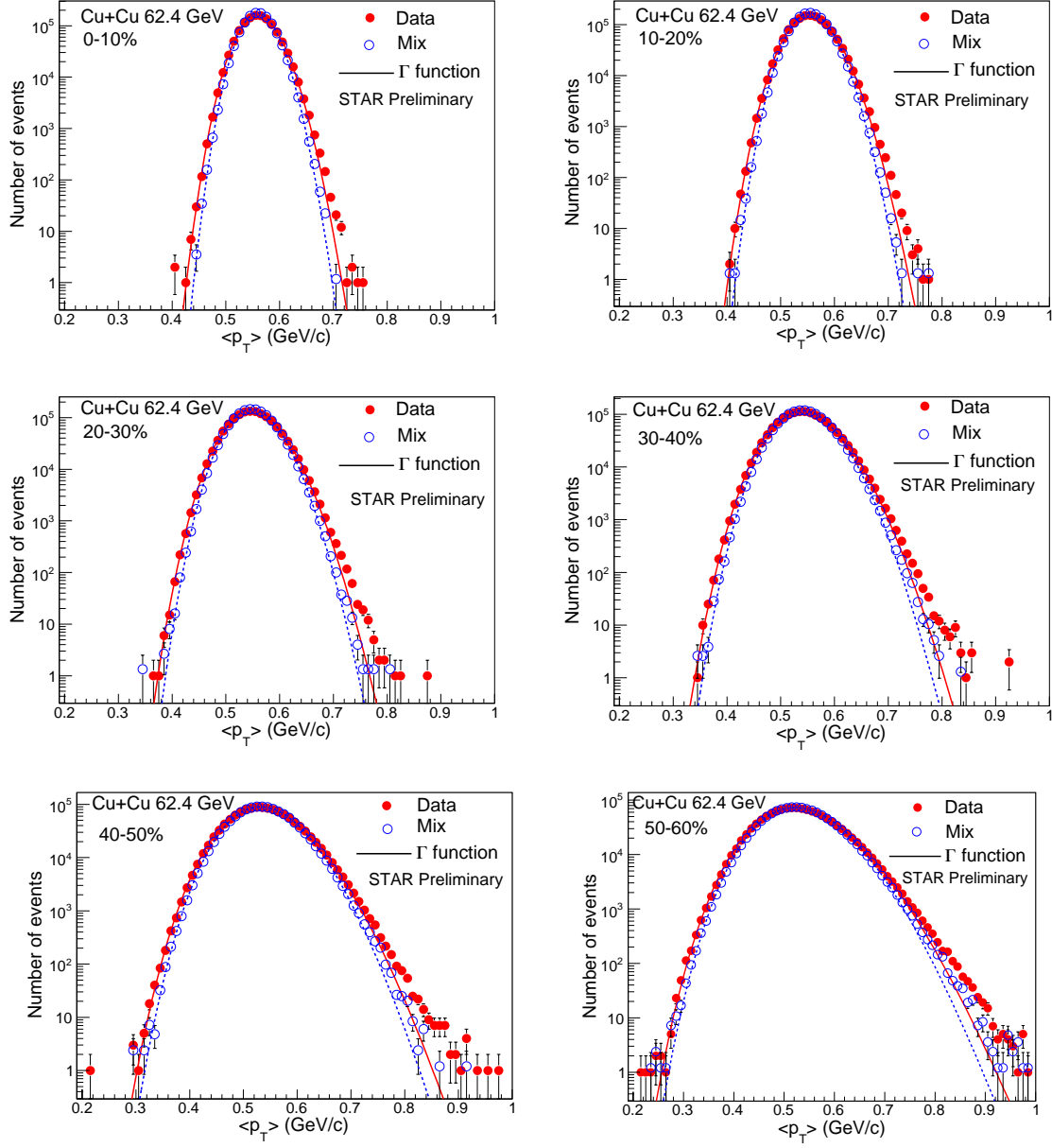


Figure 5.5: Event-by-event $\langle p_T \rangle$ distributions for various centralities for data and mixed events in Cu+Cu collisions at $\sqrt{s_{NN}} = 62.4$ GeV. The lines represent the Γ distributions. The errors shown are statistical.

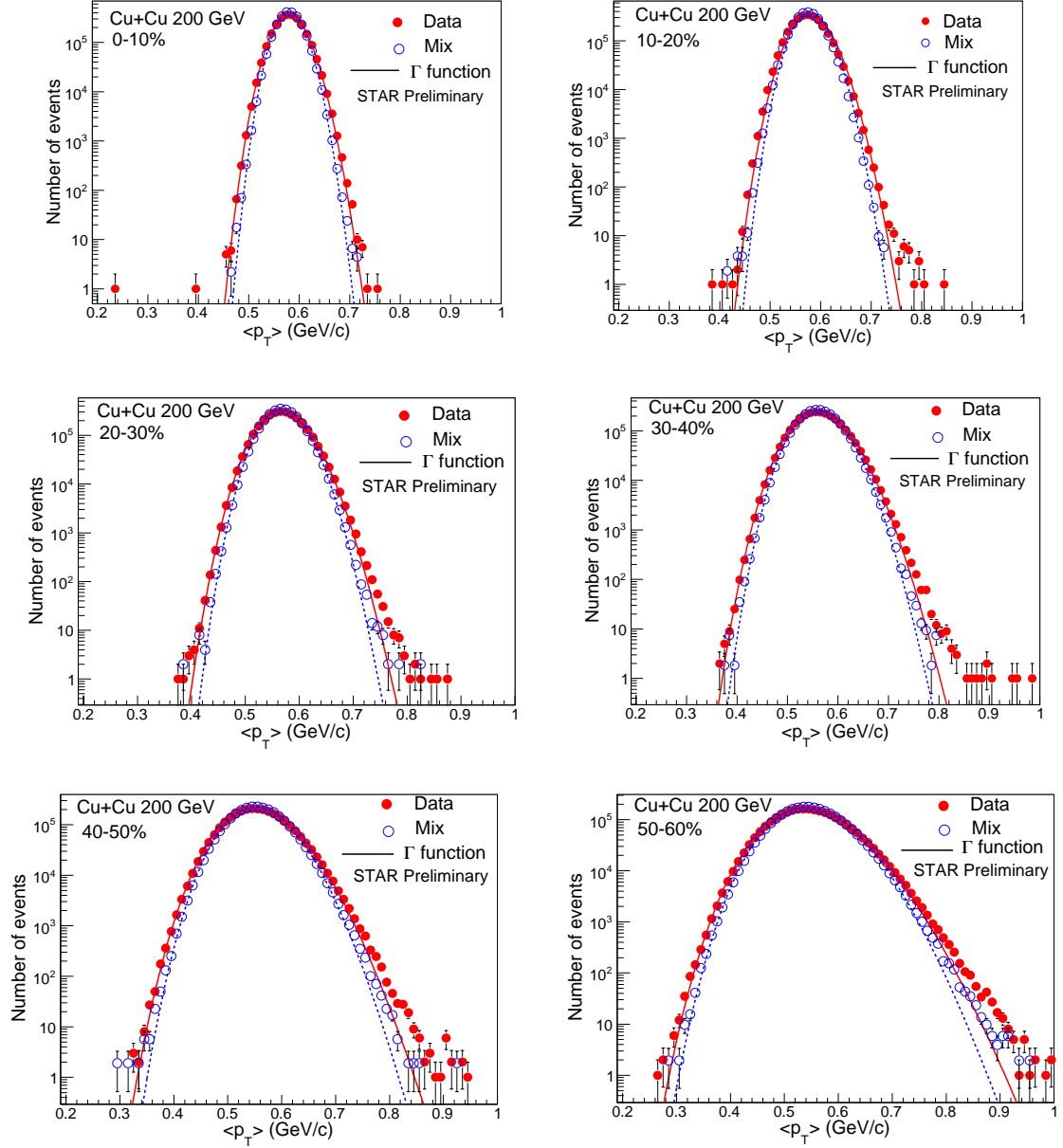


Figure 5.6: Event-by-event $\langle p_T \rangle$ distributions for various centralities for data and mixed events in Cu+Cu collisions at $\sqrt{s_{NN}} = 200$ GeV. The lines represent the Γ distributions. The errors shown are statistical.

Table 5.3: The μ and σ values in $\langle p_T \rangle$ distributions for various centralities for data and mixed events in Cu+Cu collisions at $\sqrt{s_{NN}} = 62.4$ GeV.

% cross section	μ_{data} (GeV/c)	σ_{data} (GeV/c)	μ_{mix} (GeV/c)	σ_{mix} (GeV/c)
0-10	0.560	0.0296	0.560	0.0262
10-20	0.556	0.0345	0.556	0.0310
20-30	0.550	0.0406	0.550	0.0367
30-40	0.544	0.0482	0.544	0.0442
40-50	0.537	0.0576	0.537	0.0535
50-60	0.530	0.0702	0.530	0.0658

Table 5.4: The μ and σ values in $\langle p_T \rangle$ distributions for various centralities for data and mixed events in Cu+Cu collisions at $\sqrt{s_{NN}} = 200$ GeV.

% cross section	μ_{data} (GeV/c)	σ_{data} (GeV/c)	μ_{mix} (GeV/c)	σ_{mix} (GeV/c)
0-10	0.581	0.0266	0.581	0.0231
10-20	0.575	0.0310	0.575	0.0272
20-30	0.569	0.0366	0.569	0.0323
30-40	0.562	0.0433	0.562	0.0387
40-50	0.555	0.0519	0.555	0.0469
50-60	0.546	0.0635	0.547	0.0581

Table 5.5: $\langle N_{\text{ch}} \rangle$, α and β parameters of Γ distributions for various centralities for data and mixed events in Cu+Cu collisions at $\sqrt{s_{NN}} = 62.4$ GeV.

% cross section	$\langle N_{\text{ch}} \rangle$	α_{data}	β_{data} ($\times 10^{-3} \text{GeV}/c$)	α_{mix}	β_{mix} ($\times 10^{-3} \text{GeV}/c$)
0-10	164	358.3	1.56	456.8	1.23
10-20	116	259.0	2.15	322.0	1.73
20-30	81	184.0	2.99	224.2	2.45
30-40	56	127.5	4.27	151.5	3.59
40-50	38	86.8	6.19	100.9	5.32
50-60	25	56.8	9.31	64.8	8.18

mixed events for all centralities in Cu+Cu collisions at 62.4 and 200 GeV, respectively.

The curves in Fig. 5.5 and 5.6 represent the Gamma (Γ) distributions for data (solid lines) and mixed events (dotted lines). The Γ distribution is given by

$$f(x) = \frac{x^{\alpha-1} e^{-x/\beta}}{\Gamma(\alpha) \beta^\alpha}, \quad (5.5)$$

where $\alpha = \mu^2/\sigma^2$, and $\beta = \sigma^2/\mu$ are the parameters of the Γ function. According to Ref. [43], Γ distribution is one of the standard representations of the inclusive single particle p_T distribution. It is suggested that without p_T cuts, the quantity $\alpha/\langle N_{\text{ch}} \rangle$, should be ~ 2 , and the quantity $\beta \times \langle N_{\text{ch}} \rangle$ representing inverse slope parameter may be referred to as the temperature of the system. Here $\langle N_{\text{ch}} \rangle$ is the average charged particle multiplicity in a given centrality bin. Table 5.5 and 5.6 list the values corresponding to $\langle N_{\text{ch}} \rangle$, α and β parameters for each centrality for data and mixed events in Cu+Cu collisions at $\sqrt{s_{NN}} = 62.4$ and 200 GeV, respectively.

Figure 5.7 shows the comparisons between parameters of $\langle p_T \rangle$ and Γ distributions for data and mixed events as function of $\langle N_{\text{part}} \rangle$ in Cu+Cu collisions at $\sqrt{s_{NN}} = 62.4$ and 200 GeV. Top left (right) plot shows the μ (σ) plotted as a function of $\langle N_{\text{part}} \rangle$ for data and mixed events for Cu+Cu collisions at $\sqrt{s_{NN}} = 62.4$ and 200 GeV. The plots show

Table 5.6: $\langle N_{\text{ch}} \rangle$, α and β parameters of Γ distributions for various centralities for data and mixed events in Cu+Cu collisions at $\sqrt{s_{NN}} = 200$ GeV.

% cross section	$\langle N_{\text{ch}} \rangle$	α_{data}	β_{data} ($\times 10^{-3} \text{GeV}/c$)	α_{mix}	β_{mix} ($\times 10^{-3} \text{GeV}/c$)
0-10	233	476.3	1.22	634.1	0.92
10-20	165	345.2	1.67	446.2	1.29
20-30	116	241.2	2.36	309.7	1.84
30-40	80	168.5	3.34	210.8	2.67
40-50	54	114.0	4.86	140.1	3.96
50-60	35	74.1	7.37	88.6	6.17

that μ (σ) increases (decreases) with increasing $\langle N_{\text{part}} \rangle$ for both data and mixed events in Cu+Cu collisions at 62.4 and 200 GeV. The values of μ for data and mixed events are similar for all collision centralities for both Cu+Cu at 62.4 and 200 GeV. At 200 GeV, μ values are larger compared to those at 62.4 GeV in Cu+Cu collisions. However, σ for data are larger than that for mixed events, indicating the presence of non-statistical fluctuations in the data for both Cu+Cu at 62.4 and 200 GeV. It can also be seen that σ at 62.4 GeV have larger values compared to those at 200 GeV, suggesting that lower energy has more fluctuations. Bottom-left (right) plot in Fig. 5.7 shows α (β) plotted as a function of $\langle N_{\text{part}} \rangle$ for data and mixed events for Cu+Cu collisions at $\sqrt{s_{NN}} = 62.4$ and 200 GeV. The Γ parameters α (β) increase (decrease) with increasing $\langle N_{\text{part}} \rangle$ for both data and mixed events in Cu+Cu collisions at 62.4 and 200 GeV.

We now discuss the effect of η acceptance on the parameters μ and σ obtained from the $\langle p_T \rangle$ distributions. Fig. 5.8 (top panels) shows the μ parameter and bottom panels show the σ plotted as a function of $\langle N_{\text{part}} \rangle$, for different η acceptances. Left (right) panels show the results for Cu+Cu collisions at 62.4 GeV (200 GeV). We observe that μ is independent of the variation in the η region and is found to be similar for the three measured η regions for both 62.4 and 200 GeV Cu+Cu collisions. The bottom panels

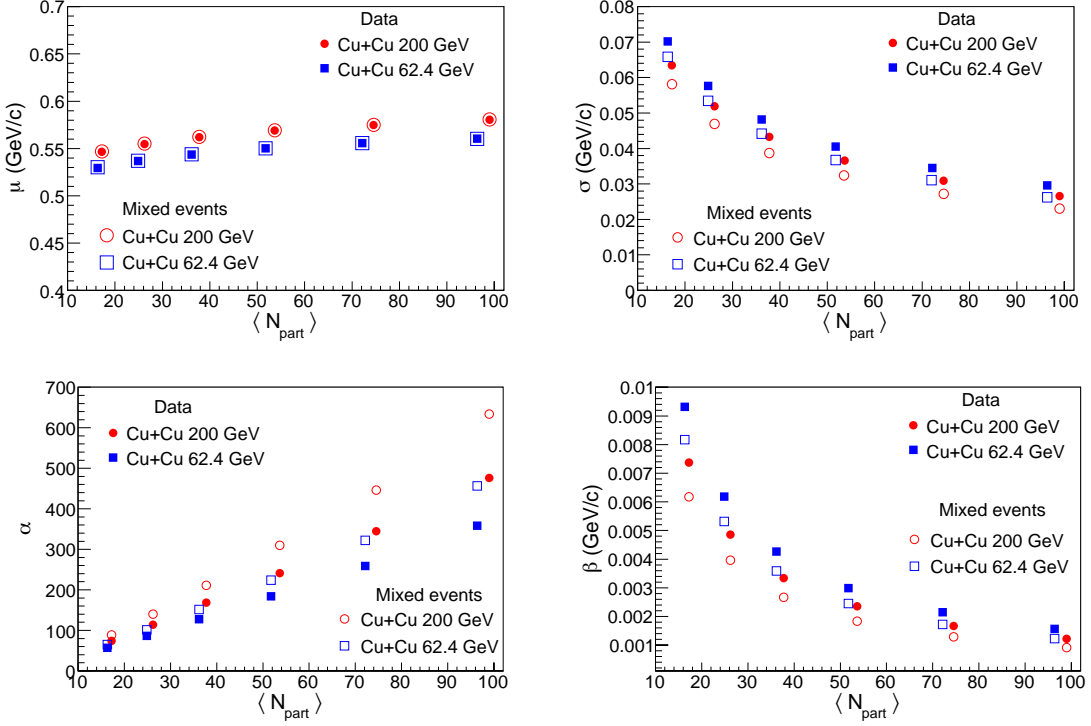


Figure 5.7: The μ (top-left) and σ (top-right) from $\langle p_T \rangle$ distributions; α (bottom-left) and β (bottom-right) parameters in Γ distributions, plotted as a function of $\langle N_{\text{part}} \rangle$ for data and mixed events in Cu+Cu collisions at $\sqrt{s_{NN}} = 62.4$ and 200 GeV. The results are STAR preliminary.

show that σ decreases as we increase the η acceptance.

To quantify the non-statistical or dynamical fluctuations present in data, we use a variable σ_{dyn} defined as

$$\sigma_{\text{dyn}} = \sqrt{\left(\frac{\sigma_{\text{data}}}{\mu_{\text{data}}}\right)^2 - \left(\frac{\sigma_{\text{mix}}}{\mu_{\text{mix}}}\right)^2}, \quad (5.6)$$

where μ_{data} and μ_{mix} are the means of the event-by-event $\langle p_T \rangle$ distributions for data and mixed events, respectively. Similarly, σ_{data} and σ_{mix} are respectively the root mean square deviations in $\langle p_T \rangle$ distributions for data and mixed events. Figure 5.9 shows the dynamical fluctuations in p_T plotted as a function of $\langle N_{\text{part}} \rangle$. The results are shown for Cu+Cu collisions at $\sqrt{s_{NN}} = 62.4$ and 200 GeV, and are compared with the results from Au+Au collisions at $\sqrt{s_{NN}} = 200$ GeV. We observe that the dynamical fluctuations are similar for Cu+Cu and Au+Au collisions. The dynamical fluctuations are also independent of the collision energy and found to vary from ~ 2 to $\sim 5\%$ as we go from central to peripheral

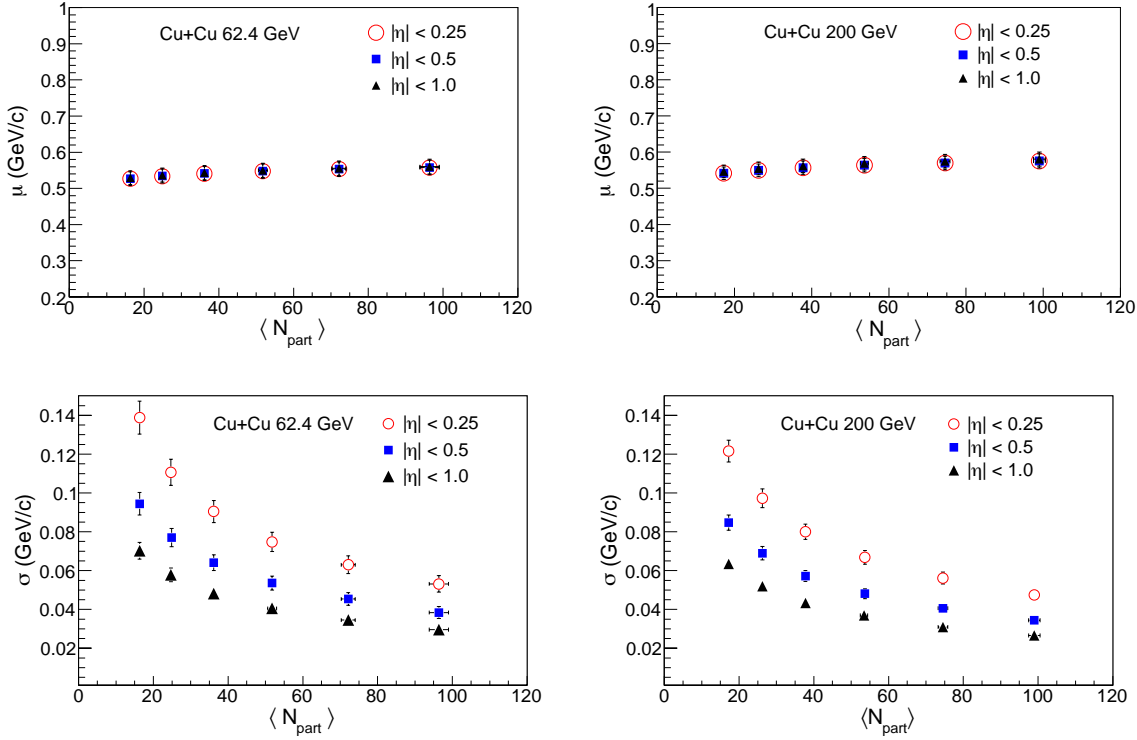


Figure 5.8: Effect of η acceptance on parameters μ (top panels) and σ (bottom panels) in the $\langle p_T \rangle$ distributions for Cu+Cu collisions at 62.4 (left panels) and 200 GeV (right panels). The errors shown are systematic. The results are STAR preliminary.

collisions in Cu+Cu system.

5.4 Transverse Momentum Correlations

The non-monotonic or dynamic fluctuations can be analyzed by using the two-particle transverse momentum correlations [39]. It is proposed that non-monotonic change in p_T correlations as a function of centrality and/or incident energy could be one of the possible signals of QGP formation [3]. Alternatively, analyses at RHIC based on p_T auto-correlations have indicated that basic correlation mechanism could be dominated by the process of parton fragmentation [44]. The two-particle p_T correlations are studied using the following equation [39]:

$$\langle \Delta p_{T,i} \Delta p_{T,j} \rangle = \frac{1}{N_{\text{event}}} \sum_{k=1}^{N_{\text{event}}} \frac{C_k}{N_k(N_k - 1)}, \quad (5.7)$$

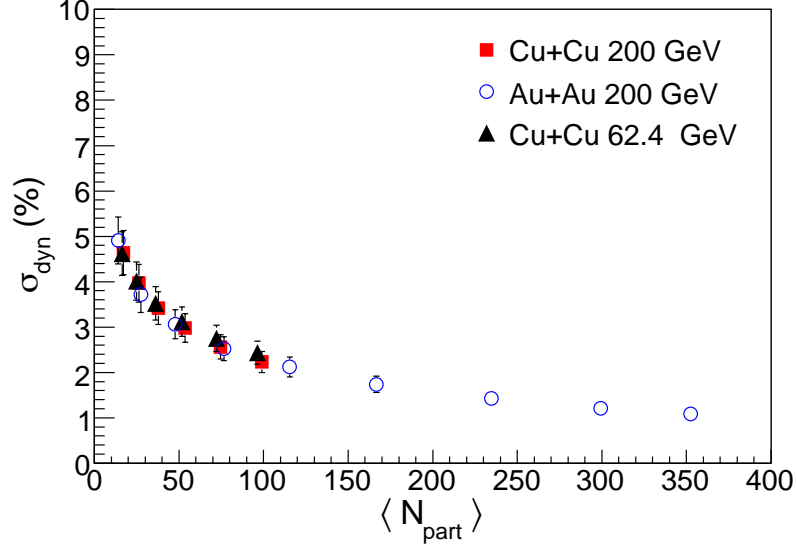


Figure 5.9: Dynamical fluctuations in $\langle p_T \rangle$ as a function of $\langle N_{\text{part}} \rangle$ for Cu+Cu collisions at $\sqrt{s_{NN}} = 62.4$ and 200 GeV. Also shown are the results for Au+Au collisions at $\sqrt{s_{NN}} = 200$ GeV. The errors shown are systematic. The results are STAR preliminary.

where C_k is the two-particle transverse momentum covariance

$$C_k = \sum_{i=1}^{N_k} \sum_{j=1, i \neq j}^{N_k} (p_{T,i} - \langle \langle p_T \rangle \rangle) (p_{T,j} - \langle \langle p_T \rangle \rangle), \quad (5.8)$$

and N_{event} is the number of events, $p_{T,i}$ is the transverse momentum of the i^{th} track in each event, N_k is the number of tracks in the k^{th} event. The overall event average transverse momentum ($\langle \langle p_T \rangle \rangle$) is given by

$$\langle \langle p_T \rangle \rangle = \left(\sum_{k=1}^{N_{\text{event}}} \langle p_T \rangle_k \right) / N_{\text{event}}, \quad (5.9)$$

where $\langle p_T \rangle_k$ is the average transverse momentum in the k^{th} event. Equation (5.7) is used to obtain the p_T correlations in Cu+Cu collisions at $\sqrt{s_{NN}} = 62.4$ and 200 GeV. These results are compared with the published results from Au+Au collisions at similar energies [39] to investigate the system-size and collision energy dependence of the p_T correlations in heavy-ion collisions at RHIC.

The $\langle \langle p_T \rangle \rangle$ is calculated as a function of $\langle N_{\text{ch}} \rangle$ in order to take care of the dependence of correlation on the size of centrality bin and changes induced due to change in

$\langle\langle p_T \rangle\rangle$. The distribution is then fitted with a polynomial. The parameters obtained from the fit are used to calculate $\langle\langle p_T \rangle\rangle$ in Eq. (5.8) on event-by-event basis as a function of $\langle N_{\text{ch}} \rangle$. Figure 5.10 shows the $\langle\langle p_T \rangle\rangle$ as function of $\langle N_{\text{ch}} \rangle$ for Cu+Cu collisions at 62.4 (left) and 200 GeV (right). The red lines in the figure are the fit polynomials. A fourth order polynomial is used for fitting in Cu+Cu 62.4 GeV. For Cu+Cu 200 GeV, polynomial of order nine is used for fitting.

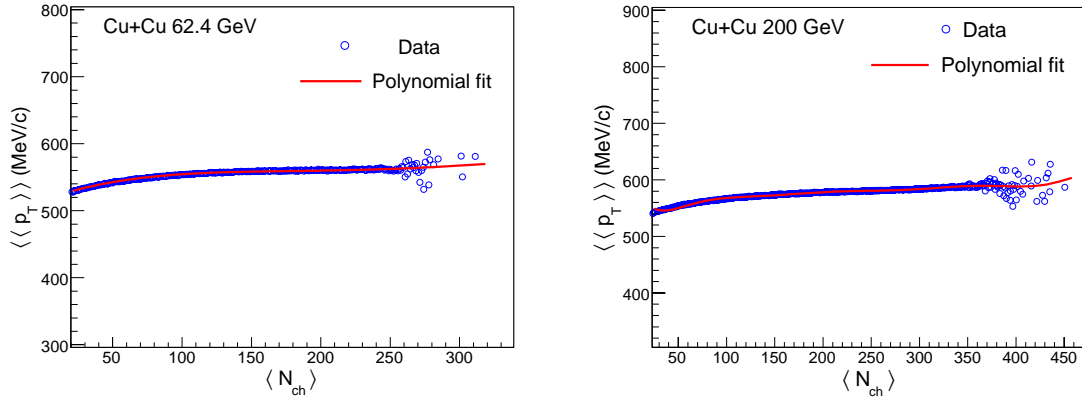


Figure 5.10: Left panel: The $\langle\langle p_T \rangle\rangle$ as a function of average charged particle multiplicity, $\langle N_{\text{ch}} \rangle$ for Cu+Cu collisions at $\sqrt{s_{NN}} = 62.4$ GeV. Right panel: Same as above but for Cu+Cu collisions at $\sqrt{s_{NN}} = 200$ GeV. The results are STAR preliminary.

Figure 5.11 shows the p_T correlations plotted as function of $\langle N_{\text{part}} \rangle$ for various cases as explained below. Top panels show Cu+Cu collisions at $\sqrt{s_{NN}} = 62.4$ (left) and 200 GeV (right). We observe finite p_T correlations that decrease with increasing $\langle N_{\text{part}} \rangle$ for both the energies. Similar behavior is observed for the Au+Au collisions at similar energies [39]. The decrease in correlations with increasing participating nucleons could be due to the fact that correlations are dominated by pairs of particles that originate from the same nucleon-nucleon collisions, and they get diluted when the the number of participating nucleons increase [39].

The collision system size dependence of p_T correlation is studied by comparing correlations obtained for Cu+Cu collisions with those obtained for Au+Au collisions at two energies. Middle panels in Fig. 5.11 show the p_T correlations plotted as a function of $\langle N_{\text{part}} \rangle$ for Cu+Cu and Au+Au collisions at $\sqrt{s_{NN}} = 62.4$ (left) and 200 GeV (right). We

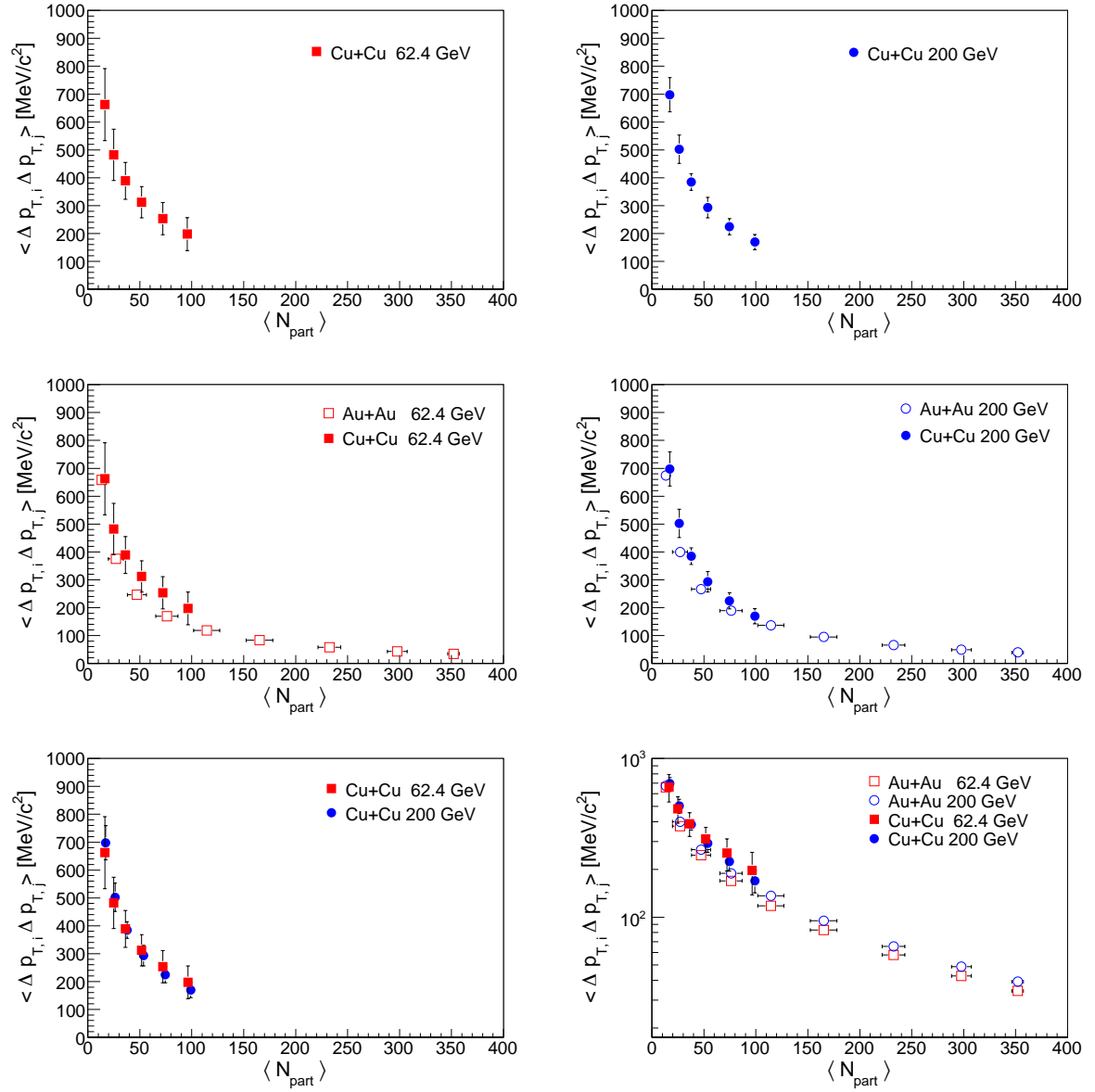


Figure 5.11: The p_T correlations as function of average number of participating nucleons. Top panels: Correlations shown for Cu+Cu collisions at 62.4 (left) and 200 GeV (right). Middle panels: Comparison of correlations in Cu+Cu collisions with those in Au+Au collisions at 62.4 (left) and 200 GeV (right). Bottom panels: Left plot shows the correlations in Cu+Cu collisions compared between 62.4 and 200 GeV. Right plot shows correlations as function of $\langle N_{\text{part}} \rangle$ for Au+Au and Cu+Cu collisions at 62.4 and 200 GeV.

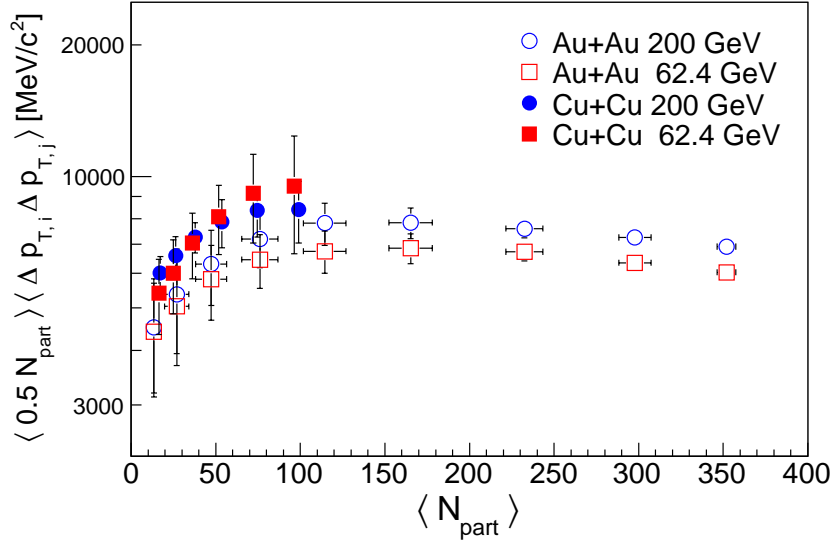


Figure 5.12: The p_T correlations multiplied by $\langle N_{\text{part}} \rangle / 2$ as function of average number of participating nucleons for Cu+Cu and Au+Au collision at $\sqrt{s_{NN}} = 62.4$ and 200 GeV.

observe that the correlations for smaller system (Cu+Cu) are slightly large compared to those for larger system, though the correlations for two collisions systems are comparable within errors. Large correlation in Cu+Cu collisions compared to that in Au+Au is more clearly observed for $\sqrt{s_{NN}} = 62.4$ GeV (left plot).

The energy dependence of p_T correlation is studied by comparing the correlations for Cu+Cu collisions at 62.4 and 200 GeV. Bottom-left plot in Fig. 5.11 shows the p_T correlations plotted as a function of $\langle N_{\text{part}} \rangle$ for Cu+Cu collisions at 62.4 and 200 GeV. It is observed that correlations for two energies are comparable within the systematic errors. Similar results are observed for Au+Au collisions at similar energies [39]. Thus, the correlations are independent of the collision energies. Bottom right plot in Fig. 5.11 shows the comparison of p_T correlations between Cu+Cu and Au+Au collisions at $\sqrt{s_{NN}} = 62.4$ and 200 GeV. It can be seen that for all the cases, correlations decrease from peripheral to central collisions.

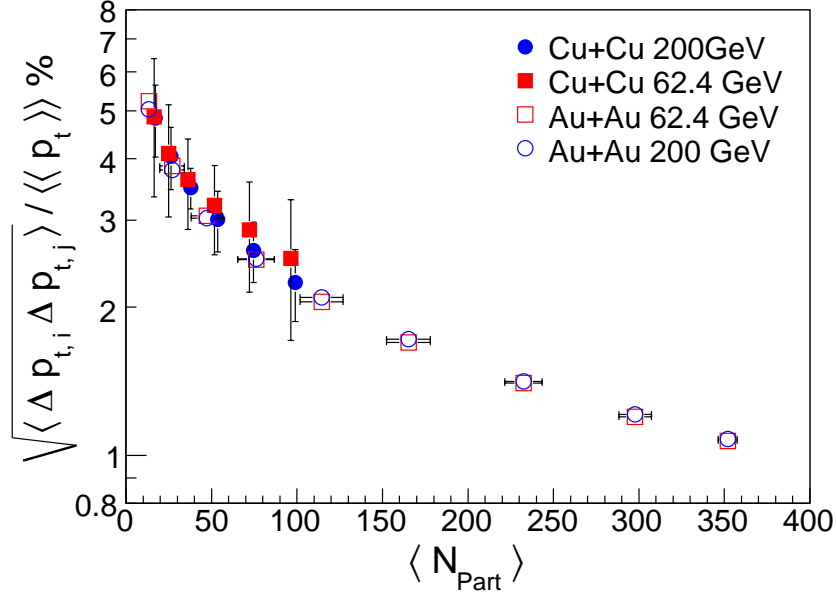


Figure 5.13: Square root of p_T correlations scaled by $\langle p_T \rangle$ as function of average number of participating nucleons for Cu+Cu and Au+Au collision at $\sqrt{s_{NN}} = 62.4$ and 200 GeV.

5.4.1 Scaling of p_T Correlations

Figure 5.12 shows the p_T correlations multiplied by $\langle N_{\text{part}} \rangle / 2$ as a function of $\langle N_{\text{part}} \rangle$. The results are shown for Cu+Cu and Au+Au collisions at $\sqrt{s_{NN}} = 62.4$ and 200 GeV. It is observed that this measure of correlations increases quickly with increasing collision centrality for both Cu+Cu and Au+Au collisions and saturates for central Au+Au collisions. The saturation of this quantity might indicate effects such as onset of thermalization [45], onset of jet quenching [46, 47], the saturation of transverse flow in central collisions [48], or other processes. It is also observed that for Cu+Cu collisions this quantity is larger than for Au+Au collisions, indicating more correlations for the smaller systems.

The correlation measure $\langle \Delta p_{T,i} \Delta p_{T,j} \rangle$ may change due any changes in $\langle p_T \rangle$ with incident energy and/or collision centrality. To take care of these changes, we study the square root of the measured correlations scaled by $\langle p_T \rangle$. Figure 5.13 shows the corresponding quantity $\sqrt{\langle \Delta p_{T,i} \Delta p_{T,j} \rangle} / \langle p_T \rangle$ plotted as a function of collision centrality for Cu+Cu and Au+Au collisions at $\sqrt{s_{NN}} = 62.4$ and 200 GeV. It is observed that the correlation scaled by $\langle p_T \rangle$ is independent of collision system size and energy but decreases

with increasing collision centrality.

5.5 Systematic Errors

Systematic errors on the mean (μ) and root mean square deviations (σ) in the $\langle p_T \rangle$ distributions, and p_T correlations are mainly calculated by varying the analysis cuts. The v_z is varied to ± 50 cm from its default (± 30 cm) value used for the analysis in order to obtain uncertainty due to the acceptance effect. We do not observe any change in $\langle p_T \rangle$ and correlations by varying v_z . The DCA cut is varied from default (< 1 cm) to DCA < 1.5 cm, to see the systematic effect of the background tracks. N_{Fit} points condition is also changed to $N_{\text{Fit}} > 15$, to observe the systematic effect due to N_{Fit} points used for the reconstruction of tracks. In order to remove the dependence of p_T correlations on the size of centrality bin and correlations induced due to change in $\langle \langle p_T \rangle \rangle$ within the experimental centrality bin, $\langle \langle p_T \rangle \rangle$ is calculated as a function of $\langle N_{\text{ch}} \rangle$, and fitted with a polynomial (as discussed in section 5.4). The parameters obtained from this fit are used to calculate $\langle \langle p_T \rangle \rangle$ (used in Eq. 5.8) on an event-by-event basis as a function of $\langle N_{\text{ch}} \rangle$. The uncertainty in determination of $\langle \langle p_T \rangle \rangle$ as a function of N_{ch} is also estimated. The systematic effect of lower p_T cut is also studied by removing the lower p_T cut in HIJING [49]. Tables 5.7 and 5.8 list the systematic errors on μ and σ in the $\langle p_T \rangle$ distributions for different centralities in Cu+Cu collisions at $\sqrt{s_{NN}} = 62.4$ and 200 GeV, respectively, due to various sources discussed above. Tables 5.9 and 5.10 list the systematic errors on p_T correlation for different centralities in Cu+Cu collisions at $\sqrt{s_{NN}} = 62.4$ and 200 GeV, respectively, due to various sources.

The p_T correlations may also include the short range correlations such as Coulomb interactions and Hanbury Brown-Twiss (HBT) correlations. These correlations usually dominate between the pairs of particles having relative transverse momentum less than 100 MeV/ c . The effect of these sources on p_T correlations is also seen by calculating p_T correlations removing the pairs of particles with relative momentum $(p_i - p_j)$, less than 0.1 GeV/ c . The p_T correlations reduce by maximum of 6% by excluding short range correlations, but are within the systematic errors as shown in Fig. 5.14 (top panel). The

Table 5.7: Systematic errors on μ and σ in event-wise $\langle p_T \rangle$ distributions due to different sources for various collision centralities in Cu+Cu collisions at $\sqrt{s_{NN}} = 62.4$ GeV.

% cross section	DCA μ (%)	N_{Fit} μ (%)	DCA σ (%)	N_{Fit} σ (%)
0-10	3.6	0.4	7.9	1.0
10-20	3.6	0.4	7.1	1.0
20-30	3.6	0.4	6.6	1.0
30-40	3.6	0.4	6.2	1.0
40-50	3.6	0.4	6.0	1.0
50-60	3.6	0.4	6.0	1.0

Table 5.8: Systematic errors on μ and σ in event-wise $\langle p_T \rangle$ distributions due to different sources for various collision centralities in Cu+Cu collisions at $\sqrt{s_{NN}} = 200$ GeV.

% cross section	DCA μ (%)	N_{Fit} μ (%)	DCA σ (%)	N_{Fit} σ (%)
0-10	3.4	0.24	5.7	1.2
10-20	3.3	0.23	5.2	1.2
20-30	3.3	0.23	5.2	1.1
30-40	3.3	0.20	4.7	1.2
40-50	3.2	0.20	4.9	1.1
50-60	3.2	0.22	4.4	1.2

Table 5.9: Systematic errors on p_T correlations due to different sources for various collision centralities in Cu+Cu collisions at $\sqrt{s_{NN}} = 62.4$ GeV.

% cross section	DCA (%)	N_{Fit} (%)	Polynomial fit (%)	Low p_T (%)
0-10	30	1.4	1.9	7.2
10-20	23	0.8	3.6	13.1
20-30	18	0.6	1.9	3.4
30-40	17	1.0	0.004	9.0
40-50	19	3.0	0.009	1.0
50-60	20	3.6	0.009	4.0

Table 5.10: Systematic errors on p_T correlations due to different sources for various collision centralities in Cu+Cu collisions at $\sqrt{s_{NN}} = 200$ GeV.

% cross section	DCA (%)	N_{Fit} (%)	Polynomial fit (%)	Low p_T (%)
0-10	16	0.05	1.9	22
10-20	13	0.09	3.6	3.2
20-30	13	1.1	1.9	12.3
30-40	8	1.2	0.004	9.7
40-50	10	2.0	0.009	8.4
50-60	7	5.0	0.009	8.3

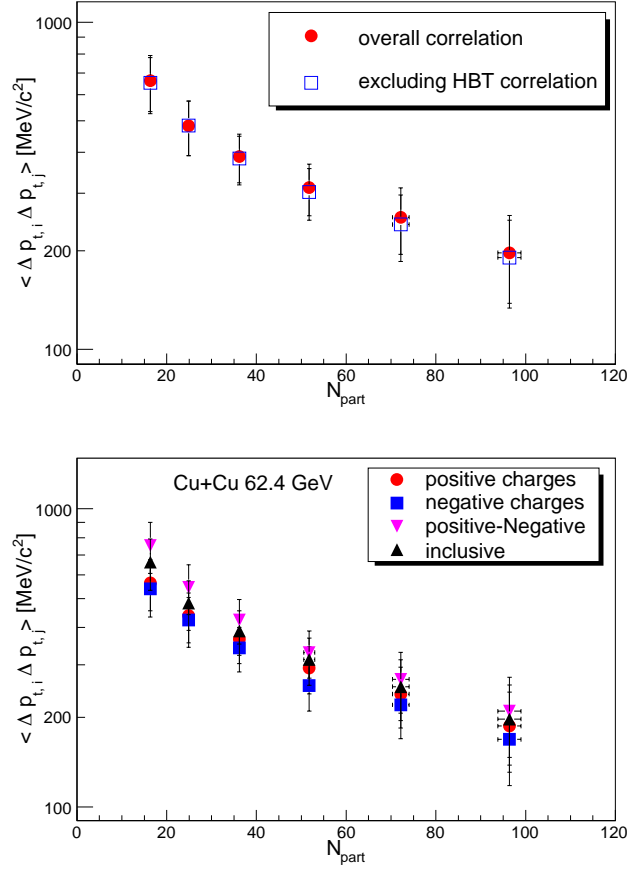


Figure 5.14: Top panel: Comparison of HBT correlations with the overall p_T correlations. Bottom panel: Correlations between particle pairs with different charge combinations compared with correlation for inclusive charged particles to see the resonance effect on p_T correlations. The plots are shown for Cu+Cu collisions at $\sqrt{s_{NN}} = 62.4$ GeV. The results are STAR preliminary.

results are shown for Cu+Cu collisions at 62.4 GeV. Similar results are obtained for Cu+Cu collisions at 200 GeV.

The contribution of resonance decays and charge ordering are also present in p_T correlations. These correlations are obtained for pairs of particles having like ($++$ or $--$) and unlike charges ($+-$) with respect to inclusive charged particles. A maximum of 15% decrease in the correlations is observed for pairs of particles with like charges and about 12% increase is observed for pairs with unlike charges with respect to the correlations for inclusive charged particle pairs for Cu+Cu collisions at $\sqrt{s_{NN}} = 62.4$ GeV and 200 GeV. The comparison for various cases is shown in bottom panel in Fig. 5.14 for Cu+Cu

collisions at $\sqrt{s_{NN}} = 62.4$ GeV. We obtained similar results for Cu+Cu collisions at 200 GeV.

5.6 η and ϕ -Dependence

The effect of η and ϕ -dependence on p_T correlations is also studied. Figure 5.15 (top-left panel) shows the correlations plotted as function of N_{part} for Cu+Cu collisions at $\sqrt{s_{NN}} = 62.4$ GeV for different η acceptances, $|\eta| < 0.25$, $|\eta| < 0.5$, and $|\eta| < 1.0$. We observe that the correlations are maximum for the narrow η window in peripheral collisions but tends to become similar to the wider η window, as the collisions become more central (see top-right panel). Similar behavior is observed for Cu+Cu collisions at $\sqrt{s_{NN}} = 200$ GeV, as shown in bottom panels in Fig. 5.15. Figure 5.16 shows the p_T correlations plotted as function of N_{part} for different ϕ -acceptances in Cu+Cu collisions at $\sqrt{s_{NN}} = 62.4$ (left panel) and 200 GeV (right panel). The various ϕ -acceptances studied are $\Delta\phi = 15^\circ, 30^\circ, 60^\circ, 90^\circ$, and 180° . We observe that correlations decrease with increase in ϕ -acceptance.

5.7 Correlations in Forward and Backward η Regions

The p_T correlations in forward ($\eta > 0$) and backward ($\eta < 0$) regions are compared to those with the combined η region. The η regions studied are the following. Backward region: $-1.0 < \eta < -0.5$ and $-0.5 < \eta < -0.0$, forward region: $0.0 < \eta < 0.5$ and $0.5 < \eta < 1.0$, and over all η region: $-0.5 < \eta < 0.5$ and $-1.0 < \eta < 1.0$. Figure 5.17 shows the correlations for these η regions as function of N_{part} for Cu+Cu collisions at $\sqrt{s_{NN}} = 62.4$ (top panel) and 200 GeV (bottom panel). It is observed that correlations for the most backward region ($-1.0 < \eta < -0.5$) and most forward region ($0.5 < \eta < 1.0$) are large compared to other η regions. This suggests that the correlation mechanisms are different in most forward and backward η regions as compared to other regions.

We try to investigate this behavior by studying the dependence of forward-backward correlations on the vertex- z acceptance. The vertex range used in the Fig. 5.17 is $|v_z| < 30$ cm. We study the correlations for similar η regions as above, but by narrowing the v_z acceptance. Figure 5.18 (top panel) shows the similar plot as in Fig. 5.17, but with

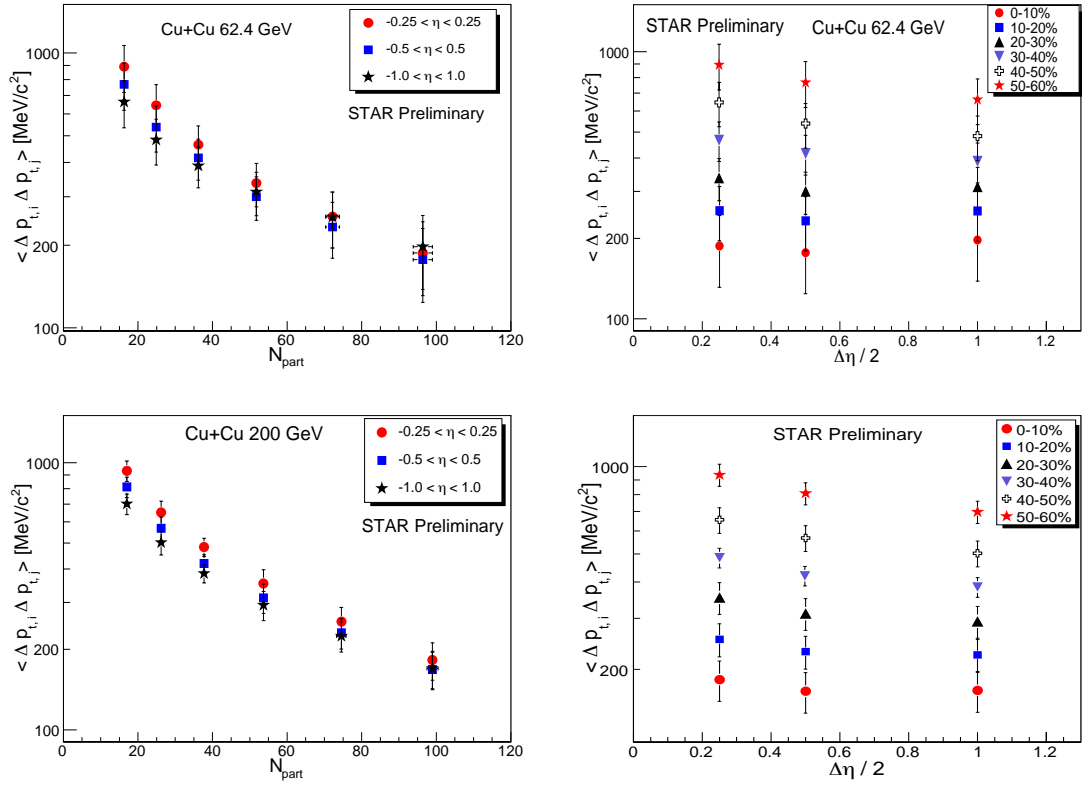


Figure 5.15: Left panels: The p_T correlations as function of collision centrality for different η regions. Right panels: Correlations plotted as function of $\Delta\eta$ for different collision centralities. Results are shown for Cu+Cu collisions at $\sqrt{s_{NN}} = 62.4$ (top panels) and 200 GeV (bottom panels). Results are STAR preliminary.

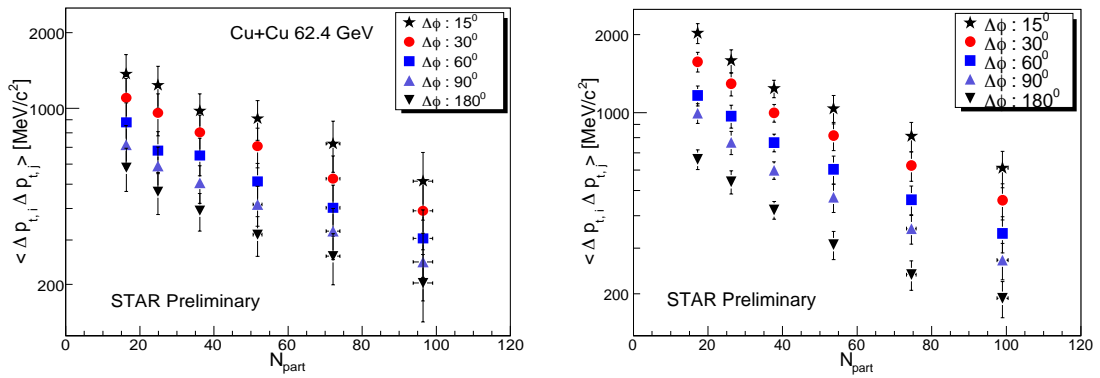


Figure 5.16: The p_T correlations as function of collision centrality for different ϕ acceptances. Results are shown for Cu+Cu collisions at $\sqrt{s_{NN}} = 62.4$ (left panel) and 200 GeV (right panel). Results are STAR preliminary.

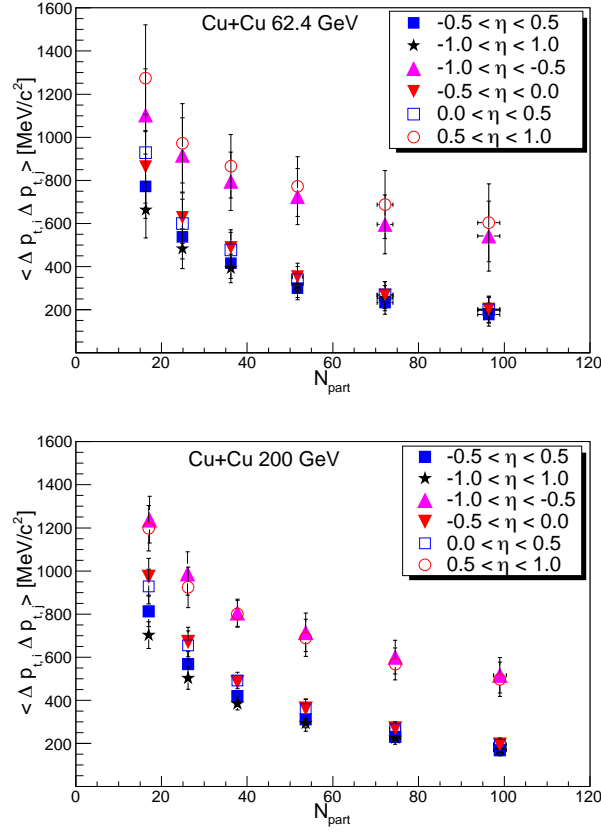


Figure 5.17: The p_T correlations as function of collision centrality for different forward ($\eta > 0$), backward ($\eta < 0$), and combined η regions. Results are shown with $|v_z| < 30$ cm for Cu+Cu collisions at $\sqrt{s_{NN}} = 62.4$ (top panel) and 200 GeV (bottom panel). Results are STAR preliminary.

$|v_z| < 10$ cm for Cu+Cu collisions at $\sqrt{s_{NN}} = 62.4$ GeV. It is observed that correlations agree for all the η regions within the systematic errors. This suggests that the effect observed in Fig. 5.17 could be due to the different v_z acceptances. Figure 5.18 (bottom panel) shows correlations within vertex ranges $|v_z| < 30$ cm and $|v_z| < 10$ cm as function of N_{part} in $|\eta| < 1$ for Cu+Cu collisions at $\sqrt{s_{NN}} = 62.4$ GeV. We observe that the correlation for $|\eta| < 1$ is independent of the vertex cuts studied, within the systematic uncertainty.

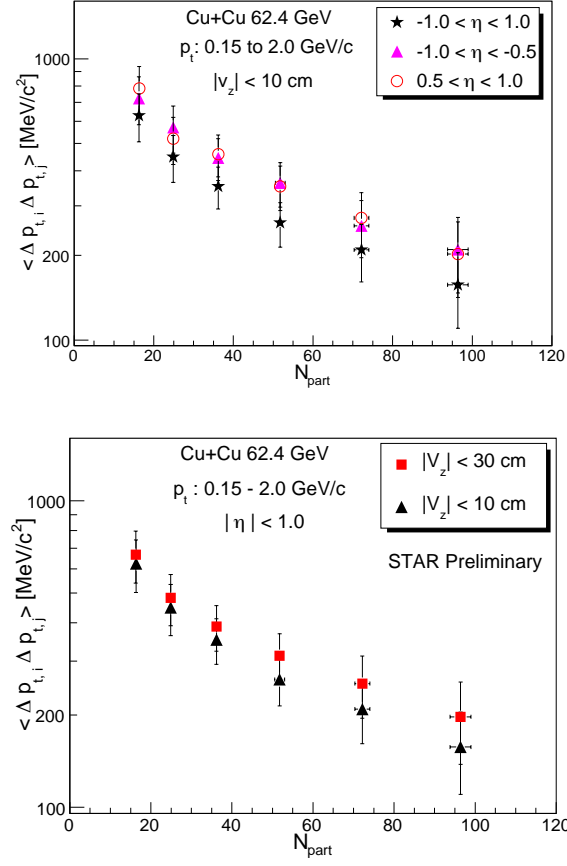


Figure 5.18: Top panel: Same as Fig. 5.17, but for $|v_z| < 10$ cm. Bottom panel: Correlations as function of N_{part} for $|v_z| < 30$ cm and $|v_z| < 10$ cm with $|\eta| < 1.0$. Results are shown for Cu+Cu collisions at $\sqrt{s_{NN}} = 62.4$ and are STAR preliminary.

5.8 Correlations for Different p_T Bins

Figure 5.19 shows the correlations as function of collision centrality for different p_T regions for Cu+Cu collisions at $\sqrt{s_{NN}} = 62.4$, and Fig. 5.20 shows the same for $\sqrt{s_{NN}} = 200$ GeV. The different p_T bins (in GeV/c) used are $0.15 < p_T < 0.35$, $0.15 < p_T < 0.4$, $0.15 < p_T < 0.5$, $0.15 < p_T < 0.8$, $0.35 < p_T < 2.0$, $0.4 < p_T < 2.0$, $0.5 < p_T < 2.0$, $0.8 < p_T < 2.0$, and default is $0.15 < p_T < 2.0$. The selection of these p_T intervals is arbitrary. We observe that correlation is maximum for charged particles having $0.15 < p_T < 2.0$ GeV/c, and minimum for particles with $0.15 < p_T < 0.35$ GeV/c. Further, it is noticed that the correlation is weak when lower p_T cut is fixed and the upper p_T cut is increased from 350 MeV/c up to 500 MeV/c. Whereas the correlation decreases when the

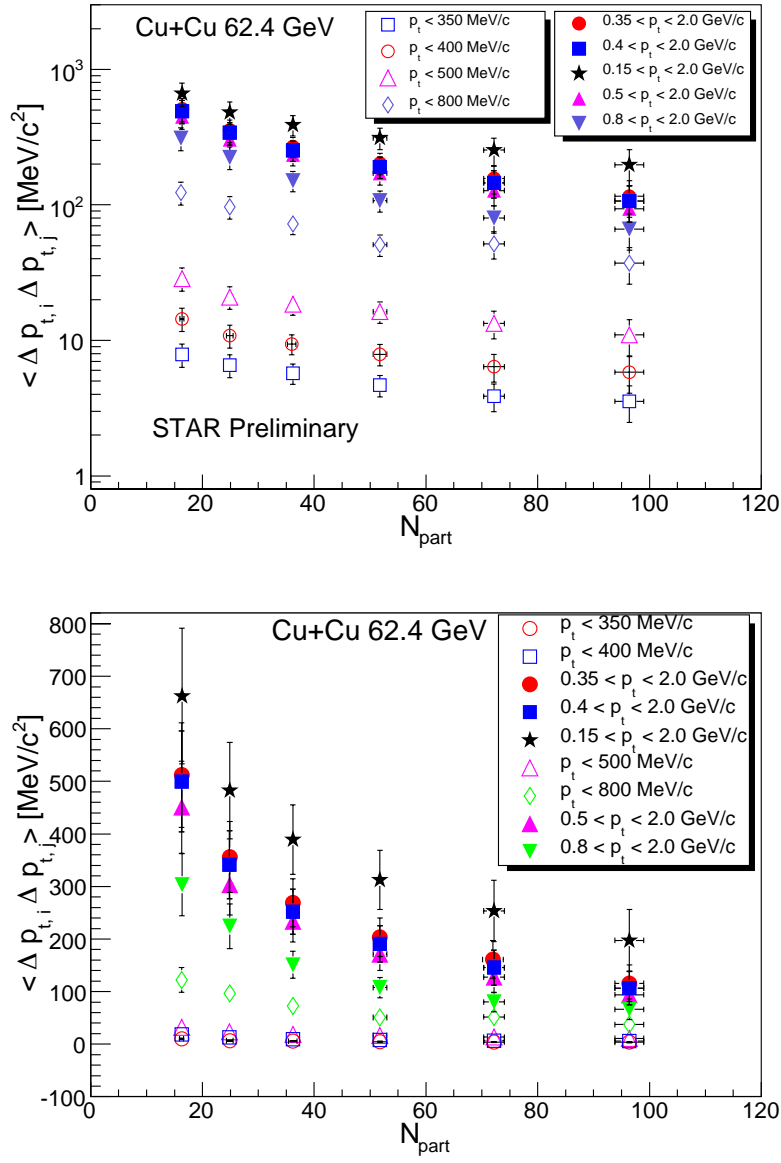


Figure 5.19: Top panel: p_T correlations for different p_T bins for Cu+Cu collisions at $\sqrt{s_{NN}} = 62.4$ GeV. Bottom panel: Same as above but shown in linear scale for clarity.

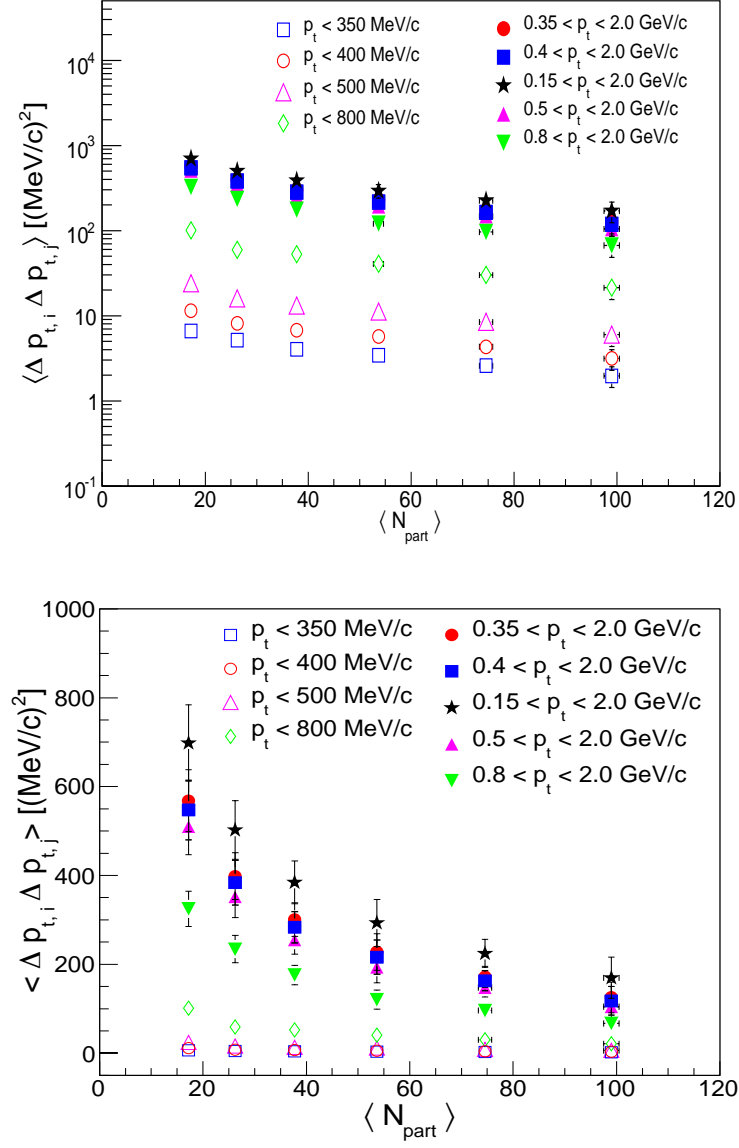


Figure 5.20: Top panel: p_T correlations for different p_T bins for Cu+Cu collisions at $\sqrt{s_{NN}} = 200$ GeV. Bottom panel: Same as above but shown in linear scale for clarity.

lower p_T cut is increased from 350 MeV/c up to 800 MeV/c, keeping the upper p_T cut of 2.0 GeV/c fixed. Thus, we observed that the low p_T particles are weakly correlated and exhibit weak dependence on $\langle N_{\text{part}} \rangle$. This could be due to the fact that low p_T particles suffer multiple scattering while coming out of the interaction medium.

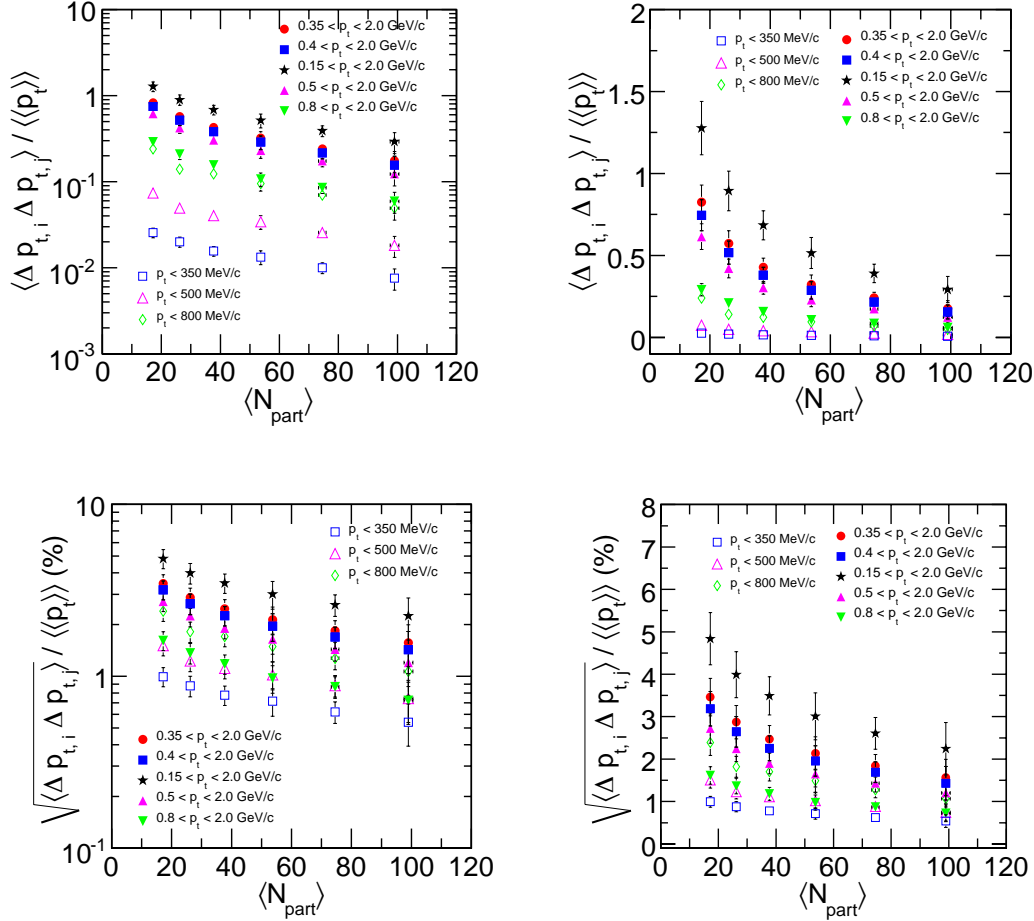


Figure 5.21: Top panel: The p_T correlations scaled by $\langle \langle p_T \rangle \rangle$ for different p_T bins in Cu+Cu collisions at $\sqrt{s_{NN}} = 200$ GeV. Bottom panel: same as above but y -axis is square root of correlations scaled by $\langle \langle p_T \rangle \rangle$. Left panels are shown in semi-log scale whereas right panels are in linear scale.

5.8.1 p_T Bin Effect Study

Since we are calculating correlations for different p_T acceptances, we need to check if there is any p_T acceptance effect on the observed correlations. These checks are done for

Cu+Cu collisions at 200 GeV and similar conclusions are drawn for Cu+Cu collisions at 62.4 GeV. The following different methods were applied:

(a) **Dividing correlation by $\langle\langle p_T \rangle\rangle$:**

We divide correlations for different bins by $\langle\langle p_T \rangle\rangle$ from corresponding p_T bins. The resulting quantity plotted as function of $\langle N_{\text{part}} \rangle$ is shown in top panels in Fig. 5.21. The trend of correlations for different p_T bins remains unchanged (top panels) and is similar to as observed in Figs. 5.19 and 5.20. Similarly, when square root of correlations are divided by $\langle\langle p_T \rangle\rangle$, the behavior of the resultant quantity remains unchanged as seen in bottom panels in Fig. 5.21.

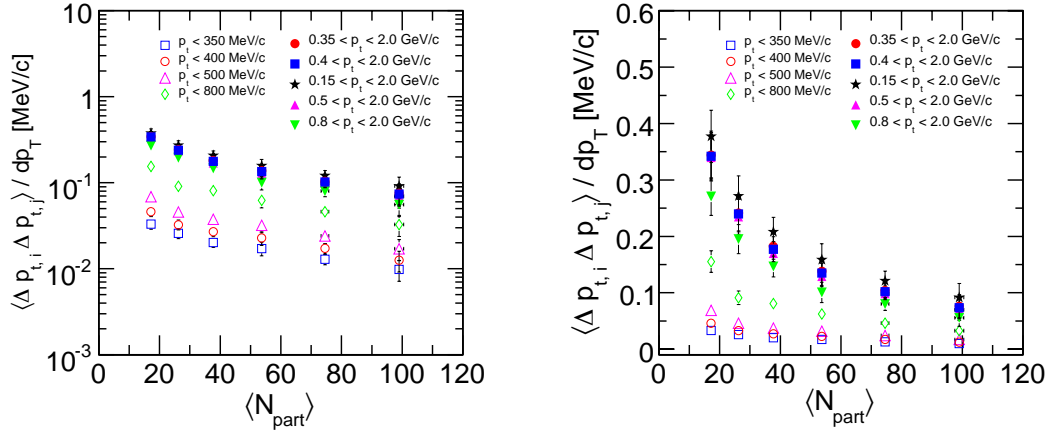


Figure 5.22: The p_T correlations scaled by the p_T bin sizes for different p_T bins in Cu+Cu collisions at $\sqrt{s_{NN}} = 200$ GeV. Left panel is shown in semi-log axis whereas right panel is in linear scale.

(b) **Dividing correlation by the corresponding p_T bin sizes:**

In this case, correlations obtained in different p_T bins are divided by the corresponding bin sizes. The resultant quantity is shown in Fig. 5.22. It also shows different values for different p_T bins and the trend is similar to that observed in Figs. 5.19 and 5.20.

(c) **Multiply by $\langle N_{ch} \rangle$:**

In this case, correlation values for different p_T bins are multiplied by the corre-

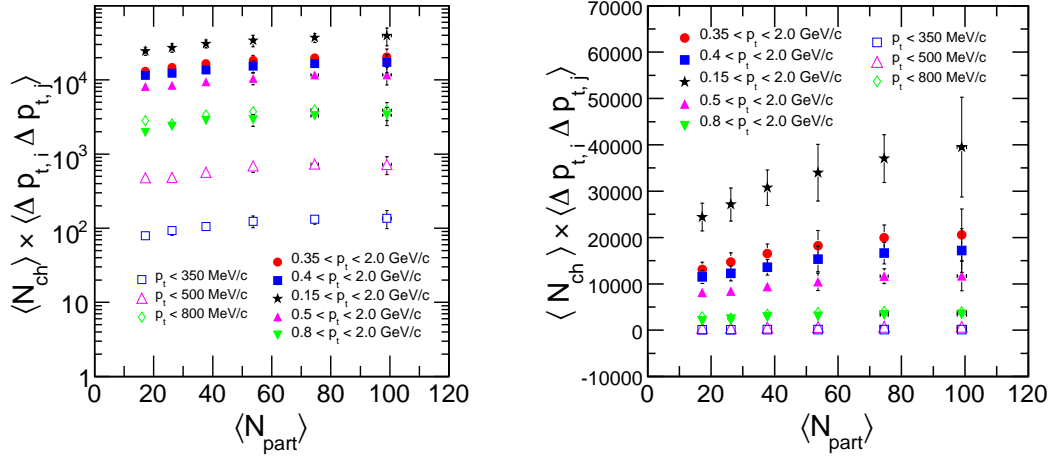


Figure 5.23: p_T correlations multiplied by $\langle N_{\text{ch}} \rangle$ for different p_T bins in Cu+Cu collisions at $\sqrt{s_{NN}} = 200$ GeV. Left panel is shown in semi-log axis whereas right panel is in linear scale.

sponding $\langle N_{\text{ch}} \rangle$ values. The resulting quantity is plotted as a function of $\langle N_{\text{part}} \rangle$ for different p_T bins as shown in Fig. 5.23. We observe that this quantity increases with $\langle N_{\text{part}} \rangle$ for all the p_T bins. However, for the lower p_T bins, the increase is relatively small. But in this case also, we observe different values for different p_T bins.

5.8.2 p_T Bin Effect Study using p_T Spectra

The checks for the p_T bin effect study discussed above, involved corrections due to the characteristic variable in that p_T bin, like $\langle \langle p_T \rangle \rangle$, bin size, and $\langle N_{\text{ch}} \rangle$. But these corrections involve the effect of both p_T bin size and the temperature fluctuations in that p_T bin. So it is important to separate the temperature fluctuations from the p_T bin effect. The p_T correlations can be formulated in terms of the temperature fluctuations by the following relation [50]:

$$\langle \Delta p_T \Delta p_T \rangle \approx \left[\frac{d\langle p_T \rangle}{dT} \right]^2 d\sigma^2. \quad (5.10)$$

This method used to correct the correlations for different p_T bins involves the following steps:

- Obtain the inclusive p_T -spectra and fit the spectra with a suitable function,

- Obtain the inverse slope parameters (T),
- Calculate the $\langle p_T \rangle$ and hence $[d\langle p_T \rangle/dT]^2$ analytically from the function used to fit the p_T -spectra, and
- Finally, divide p_T correlation values by $[d\langle p_T \rangle/dT]^2$ for each p_T bin.

We try different functions to fit the inclusive p_T spectra. We will discuss these in the following subsections.

5.8.2.1 Function - I, $F(p_T) = e^{-p_T/T}$

The inclusive p_T spectra for 0–10% centrality class fitted with this function in Cu+Cu collisions at $\sqrt{s_{NN}} = 200$ GeV, is shown in Fig. 5.24. The function fits well for p_T range 0.2 to 2.0 GeV/c. The errors shown are statistical. Similarly, we fit the inclusive p_T spectra for other centrality classes in Cu+Cu collisions at $\sqrt{s_{NN}} = 200$ GeV. The inverse slope parameters obtained from these fits are listed in Table 5.11 for various centralities.

Table 5.11: The inverse slope parameters obtained by fitting function - I to the inclusive p_T spectra for all the centralities.

Centrality (%)	0–10	10–20	20–30	30–40	40–50	50–60
T (MeV)	263.0	259.5	255.8	251.7	247.1	242.3

The $\langle p_T \rangle$ is obtained analytically by using the following equation:

$$\langle p_T \rangle = \frac{\int_a^b p_T^2 F(p_T) dp_T}{\int_a^b p_T F(p_T) dp_T}, \quad (5.11)$$

i.e.,

$$\langle p_T \rangle = 2T + \frac{a^2 e^{-a/T} - b^2 e^{-b/T}}{(a+T)e^{-a/T} - (b+T)e^{-b/T}}. \quad (5.12)$$

Here, a and b are respectively the lower and upper limits of a given p_T bin. The derivative of $\langle p_T \rangle$ with respect to T is obtained as:

$$\frac{d\langle p_T \rangle}{dT} = 2 - \frac{Ae^{-(a+b)/T} + a^2 e^{-2a/T} + b^2 e^{-2b/T}}{[(a+T)e^{-a/T} - (b+T)e^{-b/T}]^2}, \quad (5.13)$$

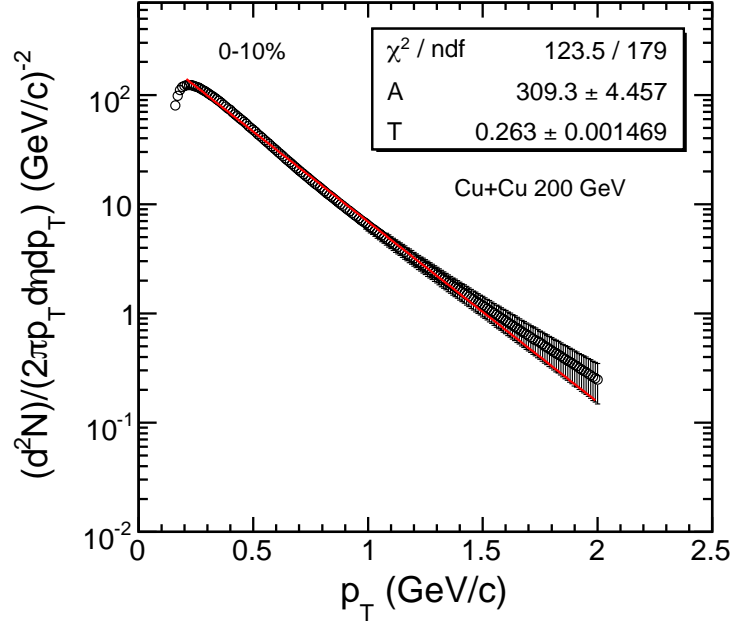


Figure 5.24: Inclusive p_T -spectra for 0–10% central Cu+Cu collisions at $\sqrt{s_{NN}} = 200$ GeV. Spectra is fitted with the function, $F(p_T) = e^{-p_T/T}$ (red line), for the p_T range 0.2–2.0 GeV/c. The errors are statistical.

where

$$A = \frac{ab(b-a)^2}{T^2} + \frac{(b^2 - a^2)(b-a)}{T} - (a^2 + b^2). \quad (5.14)$$

The results of correlations scaled by $[d\langle p_T \rangle/dT]^2$ are shown in Fig. 5.25. We observe that the trend of scaled correlations is reversed to those observed in Figs. 5.19 and 5.20. The difference of this quantity among different p_T bins is reduced for higher p_T bins. However, the difference is still there for lower p_T bins. This difference may be due to the fact that the spectra at lower p_T is not well described by the function (see Fig. 5.24). The difference may also be due to some physical phenomena. We also used different functions that could fit well in the lower p_T part of the spectra as discussed below.

5.8.2.2 Function - II, $F(p_T) = p_T e^{-p_T/T}$

This function describes the p_T -spectra comparatively well for the p_T range 0.15–0.8 GeV/c as shown in the Fig 5.26. Table 5.12 shows the inverse slope parameters obtained by fitting

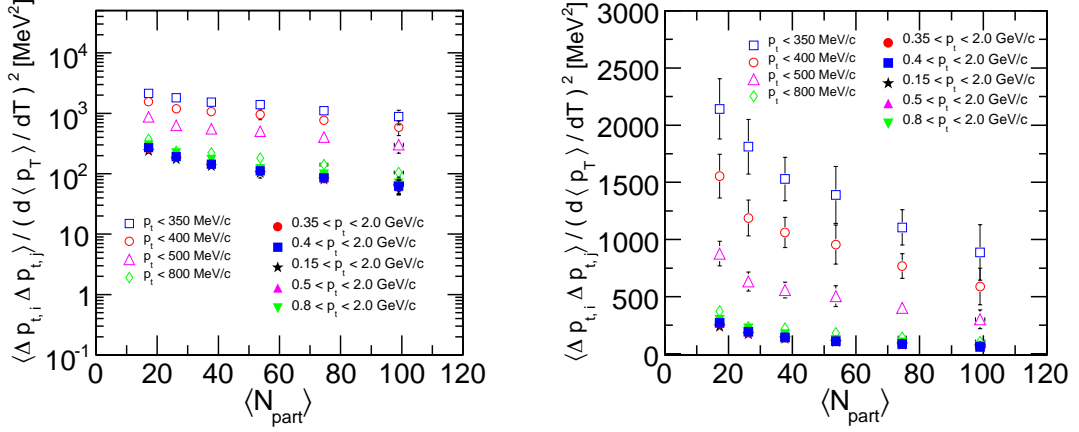


Figure 5.25: p_T correlations divided by $[d\langle p_T \rangle / dT]^2$ for different p_T bins as function of $\langle N_{part} \rangle$ for Cu+Cu collisions at $\sqrt{s_{NN}} = 200$ GeV. Left panel is shown in semi-log axis whereas right panel is in linear scale.

the above function for different centralities to the inclusive p_T -spectra.

Table 5.12: The inverse slope parameters obtained by fitting function - II to the inclusive p_T spectra for all the centralities.

Centrality (%)	0–10	10–20	20–30	30–40	40–50	50–60
T (MeV)	165.8	163.7	161.7	159.5	157.4	155.2

Following expressions can be obtained for $\langle p_T \rangle$:

$$\langle p_T \rangle = \frac{\int_a^b p_T^3 F(p_T) dp_T}{\int_a^b p_T^2 F(p_T) dp_T}, \quad (5.15)$$

$$\langle p_T \rangle = 3T + \frac{a^3 e^{-a/T} - b^3 e^{-b/T}}{(a^2 + 2aT + 2T^2)e^{-a/T} - (b^2 + 2bT + 2T^2)e^{-b/T}}. \quad (5.16)$$

The $d\langle p_T \rangle / dT$ can be obtained as:

$$\frac{d\langle p_T \rangle}{dT} = 3 - \frac{Ae^{-(a+b)/T} + 2\{(a^4 + 2a^3T)e^{-2a/T} + (b^4 + 2b^3T)e^{-2b/T}\}}{[(a^2 + 2aT + 2T^2)e^{-a/T} - (b^2 + 2bT + 2T^2)e^{-b/T}]^2}, \quad (5.17)$$

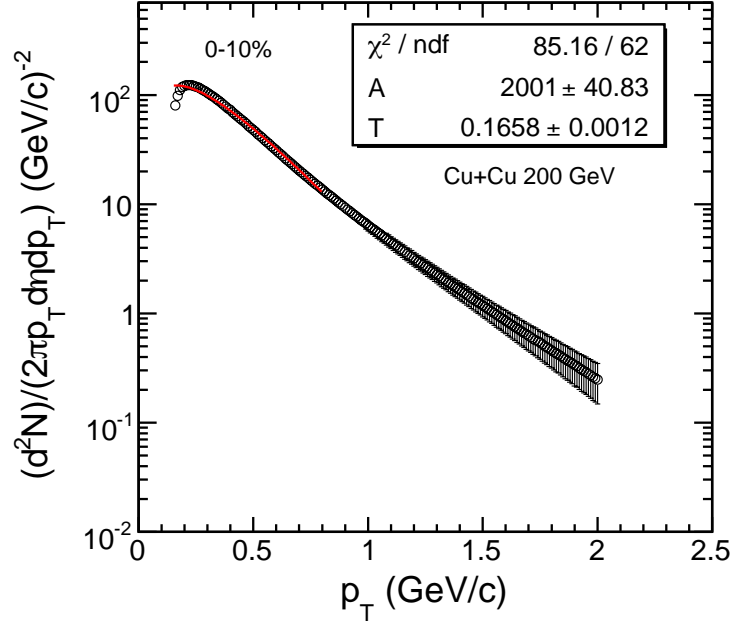


Figure 5.26: Inclusive p_T -spectra for 0–10% central Cu+Cu collisions at $\sqrt{s_{NN}} = 200$ GeV. Spectra is fitted with the function, $F(p_T) = p_T e^{-p_T/T}$ (red line), for the p_T range 0.15–0.8 GeV/ c . The errors are statistical.

where

$$A = \frac{a^2 b^2 (b-a)^2}{T^2} + \frac{2ab(b^2 - a^2)(b-a)}{T} + 2(a^4 + b^4 - 2a^3b - 2ab^3) - 4T(a^3 + b^3).$$

Figure 5.27 shows the result dividing the correlations by $[d\langle p_T \rangle/dT]^2$ for different p_T bins. Since the function in the spectra is well fitted only for p_T range 0.15–0.8 GeV/ c (see Fig. 5.26), the results are shown for the p_T bins covering this range. The trend of the scaled correlations for different bins remains unchanged, however, the dependence on p_T bin is reduced slightly. Since the function-II does not describe the data well at very low p_T of the spectra, we fit function-III, to take care of the lower p_T part of the spectra.

5.8.2.3 Function - III, $F(p_T) = p_T^2 e^{-p_T/T}$

As shown in Fig. 5.28, Function - III describes the lower p_T part of the p_T spectra better than the functions discussed above. But the p_T range of the fit is only from 0.15–0.6

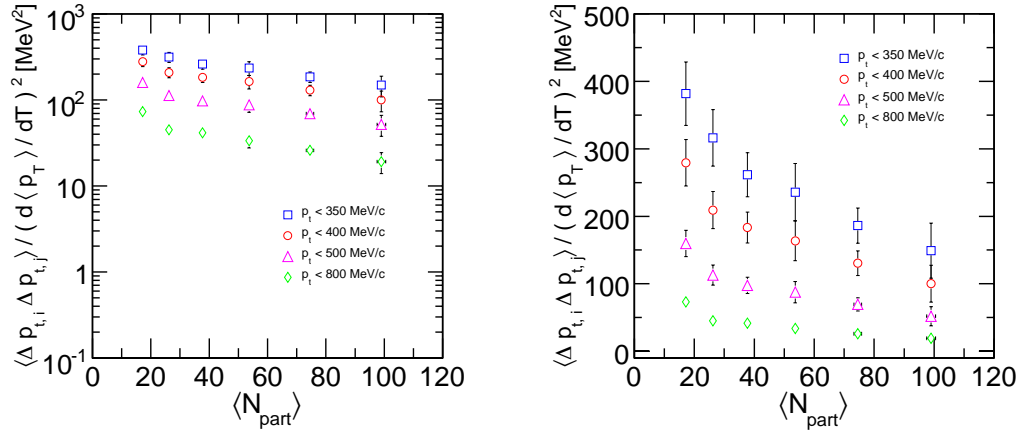


Figure 5.27: p_T correlations divided by $[d\langle p_T \rangle/dT]^2$ for different p_T bins as function of $\langle N_{\text{part}} \rangle$ for Cu+Cu collisions at $\sqrt{s_{NN}} = 200$ GeV. Left panel is shown in semi-log axis whereas right panel is in linear scale.

GeV/c. Inverse slope parameters (T) obtained by fitting spectra with this function for different centralities are given in Table 5.13.

Table 5.13: The inverse slope parameters obtained by fitting function - III to the inclusive p_T spectra for all the centralities.

Centrality (%)	0–10	10–20	20–30	30–40	40–50	50–60
T (MeV)	111.8	110.6	109.5	108.3	107.3	106.2

Following expressions are obtained for the $\langle p_T \rangle$:

$$\langle p_T \rangle = \frac{\int_a^b p_T^4 F(p_T) dp_T}{\int_a^b p_T^3 F(p_T) dp_T}, \quad (5.18)$$

$$\langle p_T \rangle = 4T + \frac{a^4 e^{-a/T} - b^4 e^{-b/T}}{C}, \quad (5.19)$$

where,

$$C = (a^3 + 3a^2T + 6aT^2 + 6T^3)e^{-a/T} - (b^3 + 3b^2T + 6bT^2 + 6T^3)e^{-b/T}. \quad (5.20)$$

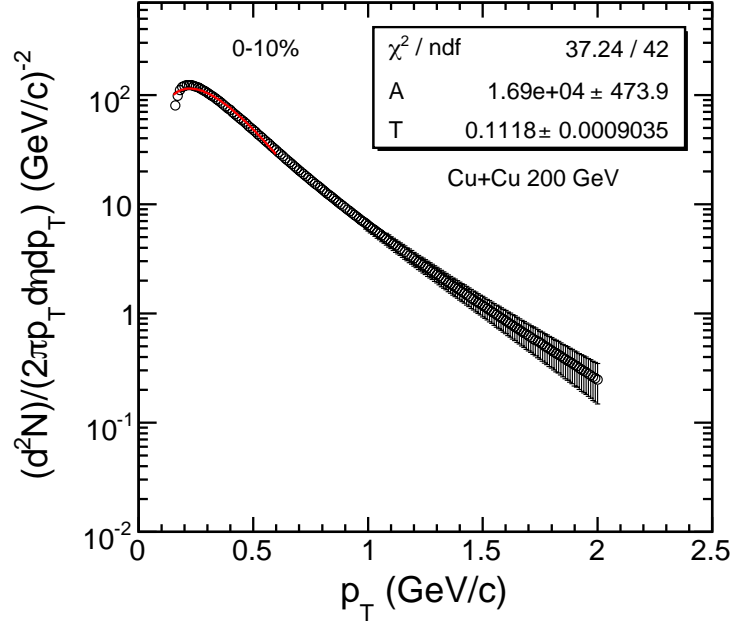


Figure 5.28: Inclusive p_T -spectra for 0–10% central Cu+Cu collisions at $\sqrt{s_{NN}} = 200$ GeV. Spectra is fitted with the function, $F(p_T) = p_T^2 e^{-p_T/T}$ (red line), for the p_T range 0.15–0.6 GeV/ c . The errors are statistical.

The $d\langle p_T \rangle / dT$ can be obtained as:

$$\frac{d\langle p_T \rangle}{dT} = 4 - \frac{e^{-(a+b)/T}(A + B + Y + D - E) + 3F}{C^2}, \quad (5.21)$$

where ,

$$\begin{aligned} A &= \frac{a^3 b^3 (b-a)^2}{T^2}, \\ B &= \frac{3a^2 b^2 (b^2 - a^2)(b-a)}{T}, \\ Y &= 3ab(2a^4 + 2b^4 - 3a^3b - 3ab^3) \\ D &= 6T(a^5 + b^5 - 3ab^4 - 3a^4b), \\ E &= 18T^2(a^4 + b^4), \text{ and} \\ F &= a^4(a^2 + 4aT + 6T^2)e^{-2a/T} + b^4(b^2 + 4bT + 6T^2)e^{-2b/T} \end{aligned}$$

Figure 5.29 shows the results when correlations for different p_T bins are divided

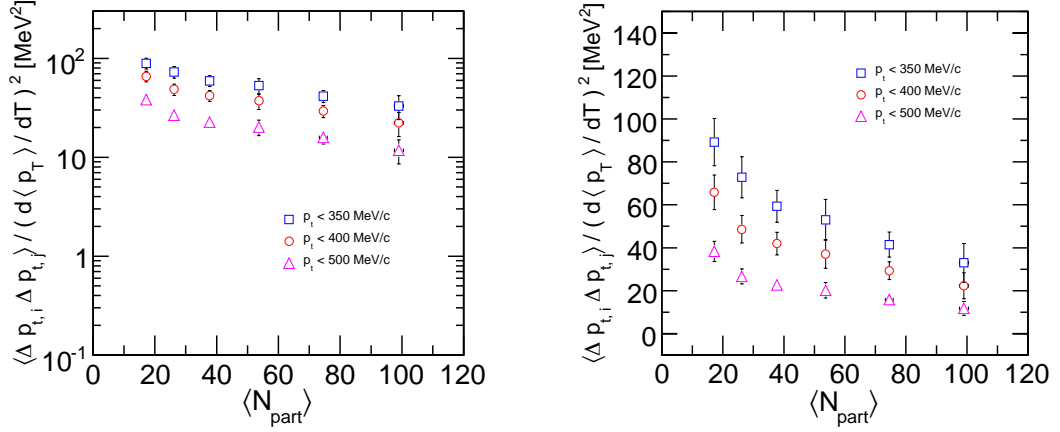


Figure 5.29: p_T correlations divided by $[d\langle p_T \rangle/dT]^2$ for different p_T bins as function of $\langle N_{\text{part}} \rangle$ for Cu+Cu collisions at $\sqrt{s_{NN}} = 200$ GeV. Left panel is shown in semi-log axis whereas right panel is in linear scale.

by the $[d\langle p_T \rangle/dT]^2$ (using Eqn.(5.21)). We observe that the difference of the resultant quantity between different p_T bins is still there but reduced compared to Fig. 5.27.

In summary, we observe finite non-statistical/dynamical fluctuations in $\langle p_T \rangle$ in the data. The p_T correlations decrease with increasing number of participating nucleons, pseudorapidity width, and azimuthal acceptance. This indicates that the correlations could be dominantly due to the pairs of particles from the same nucleon-nucleon collisions which get diluted when the number of participating nucleons increase. Correlations multiplied by $\langle N_{\text{part}} \rangle/2$ increase with the number of participating nucleons for all beam energies and collision systems, and saturate for Au+Au collisions for $\langle N_{\text{part}} \rangle$ greater than ~ 100 . This saturation may indicate the signs of effects such as thermalization, onset of jet suppression, saturation of transverse expansion in central collisions, or other processes. The scaled correlations, $\sqrt{\langle \Delta p_{T,i} \Delta p_{T,j} \rangle} / \langle \langle p_T \rangle \rangle$, are found to be independent of collision energy and system size. It is observed that the low p_T particles are weakly correlated and exhibit weak dependence on $\langle N_{\text{part}} \rangle$. This could be due to the fact that low p_T particles suffer multiple scattering while coming out of the interaction medium. We do not see any p_T acceptance effect on correlations in different p_T bins.

Bibliography

- [1] J. C. Collins and M. J. Perry, Phys. Rev. Lett. **34**, 1353 (1975).
- [2] E. V. Shuryak, Phys. Rept. **61**, 71 (1980); *ibid.* **115**, 151 (1984).
- [3] H. Heiselberg, Phys. Rep. **351**, 161 (2001).
- [4] K. Adcox *et al.* (PHENIX Collaboration), Phys. Rev. C **66**, 024901 (2002).
- [5] M. Stephanov, K. Rajagopal and E. Shuryak, Phys. Rev. Lett. **81**, 4816 (1998).
- [6] M. Stephanov, K. Rajagopal and E. Shuryak, Phys. Rev. D **60**, 114028 (1999).
- [7] M. Stephanov, Phys. Rev. D **65**, 096008 (2002).
- [8] Q. Liu and T. A. Trainor, Phys. Lett. B **567**, 184 (2003).
- [9] J. D. Bjorken and E. A. Paschos, Phys. Rev. **185**, 1975 (1969).
- [10] M. M. Aggarwal *et al.* (WA98 Collaboration), Phys. Rev. C **65**, 054912 (2002).
- [11] D. Adamova *et al.* (CERES Collaboration), Nucl. Phys. A **727**, 97 (2003).
- [12] H. Appelshauser *et al.* (NA49 Collaboration), Phys. Lett. B **459**, 679 (1999).
- [13] J. Adams *et al.* (STAR Collaboration), Phys. Rev. Lett. **90**, 172301 (2003).
- [14] J. Adams *et al.* (STAR Collaboration), Phys. Rev. C **71**, 064906 (2005) [arXiv:nucl-ex/0308033].
- [15] J. Adams *et al.* (STAR Collaboration), Phys. Rev. C **68**, 044905 (2003) [arXiv:nucl-ex/0307007].

- [16] K. Adcox *et al.* (PHENIX Collaboration), Phys. Rev. Lett. **89**, 212301 (2002).
- [17] S. S. Adler *et al.* (PHENIX Collaboration), Phys. Rev. Lett. **93**, 092301 (2004).
- [18] S. V. Afanasiev *et al.* (NA49 Collaboration), Phys. Rev. Lett. **86**, 1965 (2001).
- [19] S. A. Voloshin, V. Koch and H. G. Ritter, Phys. Rev. C **60**, 024901 (1999).
- [20] S. A. Bass, M. Gyulassy, H. Stöcker and W. Greiner, J. Phys. G **25**, R1 (1999).
- [21] S. A. Bass, P. Danielewicz and S. Pratt, Phys. Rev. Lett. **85**, 2689 (2000).
- [22] S. Jeon and V. Koch, Phys. Rev. Lett. **85**, 2076 (2000).
- [23] M. Asakawa, U. Heinz and B. Müller, Phys. Rev. Lett. **85**, 2072 (2000).
- [24] Z.-W. Lin and C. M. Ko, Phys. Rev. C **64**, 041901(R) (2001).
- [25] H. Heiselberg and A. D. Jackson, Phys. Rev. C **63**, 064904 (2001).
- [26] E. V. Shuryak and M. A. Stephanov, Phys. Rev. C **63**, 064903 (2001).
- [27] C. Pruneau, S. Gavin and S. Voloshin, Phys. Rev. C **66**, 044904 (2002).
- [28] S. Gavin, Phys. Rev. Lett. **92**, 162301 (2004).
- [29] L. Stodolsky, Phys. Rev. Lett. **75**, 1044 (1995).
- [30] E. V. Shuryak, Phys. Lett. B **430**, 9 (1998).
- [31] K. Rajagopal, proc. of the Minnesota conference on Continuous Advances in QCD 1998 (hep-ph/9808348).
- [32] B. Berdnikov and K. Rajagopal, Phys. Rev. D. **61**, 105017 (2000); K. Rajagopal, Nucl. Phys. A **680**, 211 (2000) [arXiv:hep-ph/0005101].
- [33] G. Roland *et al.* (NA49 collaboration), Nucl. Phys. A **638**, 91c (1998); H. Appelshauser *et al.* (NA49 collaboration), Phys. Lett. B **459**, 679 (1999); J.G. Reid *et al.* (NA49 collaboration), Nucl. Phys. A **661**, 407c (1999); K. Perl, NA49 note 244.

- [34] T. A. Trainor, hep-ph/0001148; T. A. Trainor and J.G. Reid, hep-ph/0004258.
- [35] T. Akesson *et al.* (Helios collaboration), Z. Phys. C **38**, 383 (1988).
- [36] H. Heiselberg, G. A. Baym, B. Blattel, L.L. Frankfurt and M. Strikman, Phys. Rev. Lett. **67**, 2946 (1991); B. Blattel, G.A. Baym, L.L. Frankfurt, H. Heiselberg and M. Strikman, Nucl. Phys. A **544**, 479c (1992).
- [37] A. Bialas, M. Bleszynski and W. Czyz, Nucl. Phys. B **111**, 461 (1976).
- [38] K. H. Ackermann *et al.* (STAR Collaboration), Nucl. Instr. Meth. A **499**, 624 (2003).
- [39] J. Adams *et al.* (STAR Collaboration), Phys. Rev. C **72**, 044902 (2005).
- [40] F. S. Bieser *et al.*, Nucl. Instr. Meth. A **499**, 766 (2003).
- [41] B. I. Abelev *et al.* (STAR Collaboration), Phys. Rev. C **79**, 034909 (2009); D. Kharzeev and M. Nardi, Phys. Lett. B **507**, 121 (2001).
- [42] T. Anticic *et al.* (NA49 Collaboration), Phys. Rev. C **70**, 034902 (2004).
- [43] M. J. Tannenbaum, Phys. Lett. B **498**, 29 (2001).
- [44] J. Adams *et al.* (STAR Collaboration), J. Phys. G **33**, 451 (2007); J. Phys. G **32**, L37 (2006).
- [45] S. Gavin, Phys. Rev. Lett. **92**, 162301 (2004).
- [46] Q. Liu and T. A. Trainor, Phys. Lett. B **567**, 184 (2003).
- [47] S. S. Adler *et al.* (PHENIX Collaboration), Phys. Rev. Lett. **93**, 092301 (2004).
- [48] S. A. Voloshin, Phys. Lett. B **632**, 490 (2006) [arXiv:nucl-th/0312065].
- [49] X. N. Wang and M. Gyulassy, Phys. Rev. D **44**, 3501 (1991).
- [50] S. Voloshin, private communication.

Chapter 6

CONCLUSIONS

The experiments at the Relativistic Heavy Ion Collider are designed to study the properties of the matter formed in nucleus-nucleus collisions at various center of mass energies ranging from 9.2 GeV to 200 GeV. The present work deals with the first measurement of identified hadron production at $\sqrt{s_{NN}} = 9.2$ GeV, photon production at $\sqrt{s_{NN}} = 200$ GeV, and p_T fluctuations and correlations between the produced particles at $\sqrt{s_{NN}} = 62.4$ and 200 GeV collisions in the STAR experiment at RHIC. The identified hadrons are measured using the Time Projection Chamber (TPC) for Au+Au collisions at midrapidity. The photon multiplicity is measured using the Photon Multiplicity Detector (PMD) for Au+Au and Cu+Cu collisions in forward rapidity. The p_T correlations between the produced charged particles in Cu+Cu collisions are compared to the results from Au+Au collisions using the data from TPC at midrapidity.

The photon multiplicity distributions are measured at forward rapidity ($-3.7 < \eta < -2.3$) for Au+Au collisions at $\sqrt{s_{NN}} = 200$ GeV. The results are compared with the measurements from Cu+Cu collisions at $\sqrt{s_{NN}} = 62.4$ and 200 GeV, and Au+Au collisions at $\sqrt{s_{NN}} = 62.4$ GeV. The photons are measured using the Photon Multiplicity Detector in the STAR experiment at RHIC. As expected, the photon yield increases with decreasing $|\eta|$ (towards midrapidity), and is larger for collisions at higher energies. The photon multiplicity per participating nucleon pair is observed to be independent of collision centrality indicating that photon production is dominated by soft processes. A similar observation is made for charged particles, although their production is slightly higher. This slightly higher production of charged particles than photons could be due

to the contribution of baryons to the charged particles, which may come from baryon transport and contribution from beam protons. On the other hand, photons are mainly from the decay of mesons (π^0). In the present work, it is also shown that for collisions with similar average number of participating nucleons, the photon yields are similar for Au+Au and Cu+Cu collisions for a given colliding beam energy. The photon production per unit rapidity per average number of participating nucleon pair vs. $\eta - y_{\text{beam}}$ shows longitudinal scaling which is independent of beam energy, collision centrality and colliding ion species.

In this thesis, we have presented measurements related to identified hadron production in Au+Au collisions at $\sqrt{s_{NN}} = 9.2$ GeV. The midrapidity results are from only ~ 3000 good events from this lowest beam energy run at the RHIC facility. The transverse momentum spectra of pions, kaons, and protons are presented for 0–10%, 10–30%, 30–60%, and 0–60% collision centrality classes. The bulk properties are studied by measuring the identified hadron dN/dy , $\langle p_T \rangle$, $\langle m_T \rangle$, and particle ratios. The centrality dependence of dN/dy , $\langle p_T \rangle$, and ratios at 9.2 GeV is similar to that observed in Au+Au collisions at $\sqrt{s_{NN}} = 62.4$ and 200 GeV. All measurements are consistent with previous measurements from fixed target experiments at similar center of mass beam energies and follow the established beam energy dependence trend.

The $\langle p_T \rangle$ of protons is higher than those of pions, indicating some degree of collectivity in radial direction. However, the difference between $\langle p_T \rangle$ for protons and kaons is considerably smaller at $\sqrt{s_{NN}} = 9.2$ GeV, compared to $\sqrt{s_{NN}} = 62.4$ and 200 GeV at RHIC. This suggests the collectivity in radial direction at the lower beam energies are smaller compared to 62.4 and 200 GeV collisions.

The \bar{p}/p ratio at midrapidity is 0.010 ± 0.001 (stat.) ± 0.003 (sys.), for $\sqrt{s_{NN}} = 9.2$ GeV collisions. This value is much smaller compared to Au+Au collisions at $\sqrt{s_{NN}} = 200$ GeV. However, p/π^+ ratio is larger at $\sqrt{s_{NN}} = 9.2$ GeV compared to that at $\sqrt{s_{NN}} = 200$ GeV. These measurements indicate large baryon stopping and hence large net-baryon density at midrapidity in collisions at $\sqrt{s_{NN}} = 9.2$ GeV. The K^-/K^+ ratio has a value of 0.38 ± 0.05 (stat.) ± 0.09 (sys.) indicating a significant contribution to kaon production from associated production at lower collision energies. The K^+/π^+ ratio at $\sqrt{s_{NN}} = 9.2$

GeV is comparable to collisions at $\sqrt{s_{NN}} = 200$ GeV.

The kinetic freeze-out parameters are extracted from a blast-wave model fit to pion, kaon, and proton p_T spectra. The $T_{\text{kin}} = 105 \pm 10$ (stat.) ± 16 (sys.) MeV and $\langle\beta_T\rangle = 0.46c \pm 0.01c$ (stat.) $\pm 0.04c$ (sys.), for 0–10% central Au+Au collisions at $\sqrt{s_{NN}} = 9.2$ GeV. The chemical freeze-out parameters are extracted from a thermal model fit to the particle ratios at midrapidity. The $T_{\text{ch}} = 151 \pm 2$ (stat.) ± 7 (sys.) MeV and $\mu_B = 354 \pm 7$ (stat.) ± 30 (sys.) MeV, for 0–10% central Au+Au collisions at $\sqrt{s_{NN}} = 9.2$ GeV. These results from the lowest energy collisions at RHIC demonstrate the capabilities of the STAR detector to pursue the proposed QCD critical point search program at RHIC and locate the onset of several interesting observations at the highest RHIC energy point.

We also studied the p_T fluctuations and correlations in Cu+Cu collisions at $\sqrt{s_{NN}} = 62.4$ and 200 GeV. In p_T correlations, we have compared our results with published results from Au+Au collisions at similar beam energies. We observe that event-by-event $\langle p_T \rangle$ distributions in data are broader than those for mixed events for all the cases. This indicates that there are non-statistical or dynamical fluctuations present in data. The dynamical fluctuations decrease with increase in centrality and are independent of the collision energy and colliding ion type. The $\langle p_T \rangle$ distributions are observed to follow the Γ distributions as the value of α/N_{ch} is close to 2.

It is observed that p_T correlations decrease with increasing number of participating nucleons, pseudorapidity width, and azimuthal acceptance, indicating that the correlations could be dominantly due to the pairs of particles coming from the same nucleon-nucleon collisions which get diluted when the number of participating nucleons increase. Correlations multiplied by half the number of participating nucleons increase for all beam energies and collision systems, but saturate for Au+Au collisions for $\langle N_{\text{part}} \rangle$ greater than ~ 100 . This saturation may indicate the signs of effects such as thermalization, onset of jet suppression, saturation of transverse expansion in central collisions, or other processes. The quantity $\sqrt{\langle \Delta p_{T,i} \Delta p_{T,j} \rangle} / \langle p_T \rangle$ seems to be independent of collision energy and collision system size. We observe that correlations in forward ($\eta > 0$), backward ($\eta < 0$) and full ($|\eta| < -1$) region are similar.

It is observed that the correlations are different for different p_T acceptances. We

observe that correlation is maximum for charged particles having $0.15 < p_T < 2.0$ GeV/ c , and minimum for particles with $0.15 < p_T < 0.35$ GeV/ c . Further, it is noticed that the correlation is weak when lower p_T cut is fixed and the upper p_T cut is increased from 350 MeV/ c up to 500 MeV/ c . Whereas the correlation decreases when the lower p_T cut is increased from 350 MeV/ c up to 800 MeV/ c , keeping the upper p_T cut of 2.0 GeV/ c fixed. Thus, we observed that the low p_T particles are weakly correlated and exhibit weak dependence on $\langle N_{\text{part}} \rangle$. This could be due to the fact that low p_T particles suffer multiple scattering while coming out of the interaction medium. The p_T bin effect study is done to see the dependence of correlations on different p_T acceptances. We do not observe any p_T acceptance effect on correlations in different p_T bins.